UNIVERSITÈ DE LILLE

Présentée pour l'obtention du grade de:
Docteur de l'Université de Lille

Spécialité :
Sciences de la Matière, du Rayonnement et de l'Environnement

Par:
Yuliia Yukhymchuk

Caractéristiques et évolution des particules d'aérosol dans l'atmosphère au-dessus de l'Ukraine: Impact sur le bilan énergétique et la qualité de l'air

Thèse soutenue le 20/02/2024 devant le jury composé de:

C. Toledano	Professeur	Science Faculty, University of Valladolid, Spain	Président du Jury Rapporteur
S. Krakovska	Chercheur	UHMI, National Academy of Sciences of Ukraine, Ukraine	Rapportrice
Y. Derimian	Doctor, HDR	Laboratoire d'Optique Atmosphèrique, Universitè de Lille, France	Examinateur
O. Ivaniha	Doctor	Physics faculty, Complutense University of Madrid, Spain	Examinatrice
G. Milinevsky	Professeur	ICFS, Jilin University, China	Directeur
P. Goloub	Professeur	Laboratoire d'Optique Atmosphèrique, Universitè de Lille, France	Directeur

Laboratoire d'Optique Atmosphèrique
U.F.R. de Physique
Universitè de Lille
59655 Villeneuve d'Ascq
France

UNIVERSITÈ DE LILLE

Abstract

U.F.R. de Physique

Docteur de l'Université de Lille

Characteristics and Evolution of Aerosol Particles in the Atmosphere over Ukraine: Impact on the Energy Balance and Air Quality

by Yuliia Yukhymchuk

The atmosphere over Kyiv, Ukraine, is influenced by various sources of aerosols, originating from both urban emissions and distant sources due to the movement of air masses. The last factor often leads to an increase in the quantity of aerosol particles, contributing to the occurrence of severe smog and reduced visibility. Additionally, elevated concentrations of aerosols can have adverse effects on human health, particularly among vulnerable population groups such as children, the elderly, and individuals with respiratory conditions or allergies. Therefore, monitoring such situations is significant for both scientific investigation of aerosol particles and informing the public about potential hazards associated with air quality.

In September 2015, extensive peat fires up north caused severe smog in Kyiv, prompting a state of emergency. For the analysis of aerosol particles from these events, data from the AERONET Kyiv sun photometer network and lidar observations were used. The field lidar campaign in Kyiv was supported by the Laboratoire d'Optique Atmospherique, Université de Lille. Using these data and HYSPLIT air mass transport calculations, the evolution of biomass burning particles and their influence from the movement of air masses was explored. Furthermore, a similar event occurred in the spring of 2020, but involved the burning of a different type of vegetation. The analysis utilized data from AERONET Kyiv and HYSPLIT, alongside information on $PM_{2.5}$ concentrations and the Air Quality Index from the AirVisual network observations.

The AERONET network has been conducting observations in Kyiv since 2008. Data on Aerosol Optical Depth, Ångström Exponent, and Radiative Forcing have been used to describe the long-term evolution of these parameters over Kyiv. To analyze these characteristics, as well as the evolution of other atmospheric components (such as black carbon, $PM_{2.5}$, SO_2, SO_4), the MERRA-2 reanalysis has been applied across the entire territory of Ukraine. Furthermore, MERRA-2 modeling has been applied to assess the impact of the full-scale Russian incursion on Ukrainian territory. AERONET observations have indicated alterations in aerosol optical properties throughout 2022, and the provided GRASP analysis has substantiated changes in the chemical composition.

Keywords: aerosols, radiative forcing, biomass burning, air quality, $PM_{2.5}$, war impact on atmospheric components.

Caractéristiques et évolution des particules d'aérosol dans l'atmosphère au-dessus de l'Ukraine : Impact sur le bilan énergétique et la qualité de l'air

L'atmosphère au-dessus de Kyiv, en Ukraine, est influencée par diverses sources d'aérosols, provenant à la fois des émissions urbaines et du transport longue distance. Ce dernier processus entraîne souvent une augmentation de la quantité de particules aérosol, contribuant à la formation de smogs sévères et à une réduction de la visibilité. De plus, des concentrations élevées d'aérosols ont une influence néfaste sur la santé humaine, notamment parmi les groupes de population vulnérables et les individus souffrant de troubles respiratoires ou d'allergies. Par conséquent, surveiller de telles situations est crucial à la fois pour l'investigation scientifique des particules d'aérosol et pour informer le public sur les dangers potentiels liés à la qualité de l'air.

En septembre 2015, d'importants incendies de tourbières dans le nord ont provoqué un smog sévère à Kyiv, entraînant un état d'urgence. Pour l'analyse de ces événements, des données du réseau de photomètres solaires AERONET de Kyiv et des observations lidar ont été utilisées. Une campagne de terrain organisée à Kyiv et embarquant un lidar a été soutenue par le Laboratoire d'Optique Atmosphérique de l'Université de Lille. En utilisant ces données et les trajectographie des masses d’air fournie par HYSPLIT, l'évolution des particules issues de la combustion de biomasse et leur influence par le déplacement des masses d'air ont été explorées.

De plus, un événement similaire s'est produit au printemps 2020, mais impliquait la combustion d'un type différent de végétation. L'analyse s'est ici encore appuyée sur les données d'AERONET de Kyiv et de HYSPLIT, ainsi que des mesures sur les concentrations de $PM_{2.5}$ et l'Indice de Qualité de l'Air provenant des observations du réseau AirVisual.

Au-delà de l'étude d'évènements aérosols intenses, le réseau AERONET mène des observations à Kyiv depuis 2008. Les données sur l'épaisseur optique en aérosols, l'exposant d'Ångström et le forçage radiatif ont été utilisées pour décrire l'évolution sur la période 2008-2023 de ces paramètres au-dessus de Kyiv. Pour analyser ces caractéristiques, ainsi que l'évolution d'autres composants atmosphériques comme le black Carbon (BC), les $PM_{2.5}$, le SO_2, et le SO_4, la réanalyse MERRA-2 a été appliquée sur l'ensemble du territoire de l'Ukraine. De plus, la modélisation MERRA-2 a été utilisée pour évaluer l'impact de l'invasion russe à grande échelle sur le territoire ukrainien. Les observations d'AERONET ont indiqué des altérations dans les propriétés optiques des aérosols tout au long de l'année 2022, et l'analyse de la composition de l'aérosols dérivée de GRASP-CHEM indique une évolution significative de cette composition..

Mots-clés: aérosols, forçage radiatif, combustion de biomasse, qualité de l'air, $PM_{2,5}$, impact de la guerre sur les composants atmosphérique

AKNOWLEGMENTS

First and foremost, I would like to express my sincere gratitude to everyone who supported me on this journey to obtain a PhD degree. I am grateful to my supervisors, Prof. Gennadi Milinevsky and Prof. Philippe Goloub, for their unwavering assistance, incredible patience, and invaluable advice. Special thanks are due to the Laboratoire d'Optique Atmosphèrique for providing the invaluable opportunity to complete my thesis and to all the personnel of the laboratory for their support and encouragement throughout this academic journey.

I also wish to thank Anne Prime, Prof. Frédéric Parol, Prof. Philippe Dubuisson, Prof. Isabelle Jankowiak, and Christophe Van-Brussel for their assistance, including in administrative and organizational matters. Additionally, I would like to thank Dr. Derimian and Philippe Lesueur for their assistance in processing GRASP data, and I look forward to further collaboration. My heartfelt thanks go to my friends Maria Fernanda Sanchez, Smita Panda, Yuyang Chang, William Boissiere, Souichiro Hioki, Gabriel Chesnoiu, Mégane Ventura and Raphael Peroni for their support and for fostering a wonderful, friendly atmosphere in the laboratory and office.

I am sincerely grateful for the financial support from the Institute of Physics, Laboratoire d'Optique Atmosphèrique, the MOBLILEX program, and the PAUSE program. I also express gratitude to the people of France for supporting Ukraine and condemning Russian aggression against our country.

CONTENTS

LIST OF FIGURES

LIST OF TABLES

LIST OF ABBREVIATIONS

LOA	Laboratoire d'Optique Atmosphérique
OC	Organic Carbon
BC	Black Carbon
AERONET	Aerosol RObotic NETwork
IPCC	Intergovernmental Panel on Climate Change
PM	Particulate Matter
WHO	World Health Organization
AQI	Air Quality Index
EPA	United States Environmental Protection Agency
CCN	Cloud Condensation Nuclei
AOD, AOT	Aerosol Optical Depth/Thickness
NASA	National Aeronautics and Space Administration
GEOS	Goddard Earth Observing System
AE	Angstrom Exponent
SSA	Single Scattering Albedo
AAOD	Absorption aerosol optical depth
AAE	Absorption Angstrom Exponent
RF	Radiative Forcing
EFR	Effective Radiative Forcing
BOA	Bottom of the Atmosphere
TOA	Top of the Atmosphere
DARF	Direct Aerosol Radiative Forcing
EFR_{ari}	Effective Radiative Forcing of Aerosol-Radiation Interactions
EFR_{aci}	Effective Radiative Forcing of Aerosol-Cloud Interactions
ACTRIS	Aerosols, Clouds and Trace gases Research Infrastructure
EARLINET	European Aerosol Research Lidar Network
GEOSS	Global Earth Observation System of Systems
GAW	Global Atmosphere Watch Programme
MODIS	Moderate Resolution Imaging Spectroradiometer
VIIRS	Visible Infrared Imaging Radiometer Suite
HYSPLIT	Hybrid Single Particle Lagrangian Integrated Trajectory Model

ARL	Air Resources Laboratory
NOAA	National Oceanic and Atmospheric Administration's
GDAS	Global Data Assimilation System
GFS	Global Forecast System
GARRLiC	Generalized Aerosol Retrieval from Radiometer and LIDAR Combined data
GRASP	Generalized Retrieval of Atmosphere and Surface Properties
AGL	Above Ground Level
STD	Standard deviation
MERRA-2	Modern-Era Retrospective analysis for Research and Applications version 2

LIST OF SYMBOLS

C	concentration of the pollutant	µg m^{-3}, ppm, ppb
C_{low}	concentration at the lower control point	µg m^{-3}, ppm, ppb
C_{high}	concentration at the higher control point	µg m^{-3}, ppm, ppb
I_{low}	index corresponding to C_{low}	
I_{high}	index corresponding to C_{high}.	
λ	wavelength	nm
F_λ	spectral flux	W nm^{-2}
L_λ	spectral radiance	W m^{-2} sr^{-2} nm^{-1}
ω	solid angle	sr
θ	zenith angle	°, deg
$F^{\uparrow}$	upward flux	W m^{-2}
$F^{\downarrow}$	downward flux	W m^{-2}
F^{net}	net flux	W m^{-2}
σ_a	absorption coefficient	m^{-1}
σ_e	extinction coefficient	m^{-1}
σ_s	scattering coefficient	m^{-1}
S	geometric distance	m
t	atmospheric transmittance	
AOD, τ_{aer}	aerosol optical depth	
Q_e	extinction efficiency	
N	number concentration	m^{-3}
$B_\lambda(T)$	Planck function	

p	phase function	
$\widetilde{\omega}$	single scattering albedo	
α	Angstrom Exponent	
$N(r)$	particle size distribution	μm^{-2}
$S(r)$	surface area distribution	$m^2\,\mu m^{-2}$
$V(r)$	volume size distribution	$\mu m^3\,\mu m^{-2}$
F_S	solar radiation flux	$W\,m^{-2}$
E_s	solar constant	$W\,m^{-2}$
A_E	Earth's surface albedo	
σ_{bol}	Stefan-Boltzmann constant	$kg\,m^{-2}\,K^{-4}$
T_E	effective temperature	K
ΔF_{BOA}	RF at the bottom of the atmosphere	$W\,m^{-2}$
ΔF_{TOA}	RF at the top of the atmosphere	$W\,m^{-2}$
$DARF_{ATM}$	Direct Aerosol Radiative Forcing	$W\,m^{-2}$
ΔF^{eff}	efficiency of aerosol radiative forcing	$W\,m^{-2}$
$P(R)$	power of backscattered radiation from distance R	mV
K	factor of LiDAR performance	
$G(R)$	factor of range dependent geometry	
$\beta(R)$	backscatter coefficient	$m^{-1}\,sr^{-1}$
$T(R)$	atmosphere transmittance	
P_{bg}	power of background noise	mV
LR_{aer}	lidar ratio	

Chapter 1

1. INTRODUCTION

1.1 Introduction

Microscopic particles present in the air come in various types: from natural sources such as mineral dust, pollen, sea salt particles, and small fragments of vegetation, to anthropogenic sources resulting from human activities such as vehicle emissions, industrial processes, waste incineration, building heating, power generation, warfare, and others. Some aerosols can form directly in the atmosphere through chemical reactions with precursor gases. All of the aforementioned particles differ significantly in their origin, chemical composition, size, and ability to impact visibility, climate, human health, and overall quality of life. These airborne particles are examples of atmospheric aerosols. In their simplest form, aerosols are defined as a mixture of solid or liquid particles suspended in a gas. Aerosols are two-phase systems consisting of the solid or liquid particles and the gas in which they are suspended, in this case, the air.

Atmospheric aerosols are among the least understood components of the atmosphere, with their properties rapidly changing in space and time, influencing human health and the global climate. Tropospheric aerosols primarily function as a cooling agent for the climate system, directly reflecting solar radiation and indirectly enhancing cloud reflectance (Arias et al., 2021). Regional issues associated with aerosols include environmental effects, such as reduced visibility, and potential impacts on human health. According to the WHO, atmospheric pollution is one of the key factors that impact human health. Special attention is given to the concentration of particulate matter (PM), specifically particles with a diameter of 10 μm or less, which can penetrate the respiratory system and lungs. Particles with a diameter of up to 10 μm are classified as PM_{10}, while a finer fraction with a size of up to 2.5 μm is classified as $PM_{2.5}$.

Aerosols, including PM, exhibit a wide range of sizes. A comparison of sizes for different types of substances is shown on Figure 1.1. The image represents various particles

such as soot and smoke particles, viruses, pet dander, microorganisms, red blood cells, pollen particles, mineral dust, and others. It is notable that in the context of this image, the mentioned objects appear miniature, as human hair seems gigantic compared to them. From this, one can conclude that many particles can enter the respiratory tract and bloodstream since their sizes are smaller than blood cells. Additionally, the size of aerosol particles is crucial for their dispersion in the atmosphere (as it determines their transport and lifetime), their impact on human health and ecosystems, and their interactions with other atmospheric components.

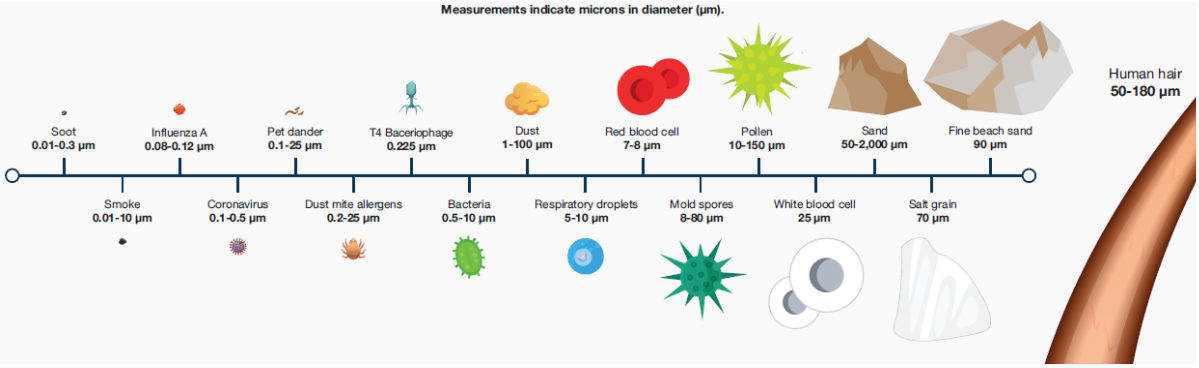

Figure 2.1. Comparative sizes of selected particles. Figure adapted from the 2021 World Air Quality Report.

How can PM enter the bloodstream? Firstly, the ability of particles to penetrate the respiratory system depends on their size, as illustrated in Figure 1.2. In more detail, particles ranging in size from 10 to 100 µm are capable of entering the upper respiratory tract. Particles in the size range of 1 to 10 µm can reach the lower respiratory tract, while smaller particles in the size range of 0.1 to 1 µm can penetrate the alveoli. The smallest particles, smaller than 1 µm, can enter the bloodstream from the alveoli and distribute throughout the body and organs (see Fig. 1.2). Smaller particles pose greater risks to human health, as their removal from the circulatory system is nearly impossible, for instance.

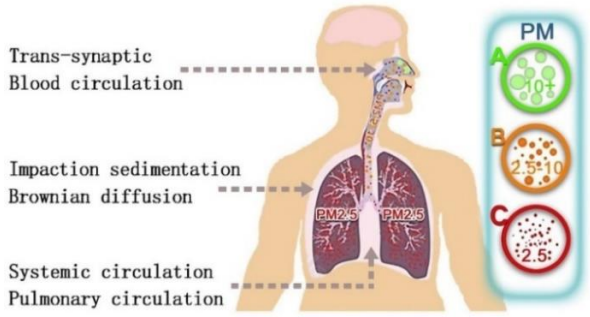

Figure 1.2. Ability of particles of different sizes to penetrate the human body (Source: Li et al., 2018).

Besides the negative effect on human health, the impact of aerosols on climate remains an important issue that concerns scientists worldwide. According to the Technical Report of the Intergovernmental Panel on Climate Change (Arias et al., 2021), the impact of aerosols on effective radiative forcing for the period from 1750 to 2014 is estimated to be –1.3 [–2.0 to –0.6] W m^{-2}. Within this, the contribution resulting from aerosol-cloud interactions is the most significant and is assessed at –1.0 [–1.7 to –0.3] W m^{-2}. The interaction of aerosols with radiation is estimated at –0.3 [–0.6 to 0.0] W m^{-2}.

The direct aerosol effect on Earth's atmospheric energy balance occurs through the scattering and absorption of solar radiation (Li et al., 2021; Sokolik & Toon, 1996; Li & Sokolik, 2018). The indirect effect involves the interaction between aerosols and clouds, where aerosol particles act as cloud condensation nuclei and ice nuclei (DeMott et al., 2003; Lohmann & Feichter, 2005; Connolly et al., 2009).

Nevertheless, evaluating the impact of aerosols on climate presents several challenges. Solar radiation spans wavelengths up to 4 μm, whereas thermal radiation emitted by the Earth's surface occurs in the range of 4 to 20 μm. Since the majority of aerosols have sizes smaller than 4 μm, it is logical that aerosol particles scatter radiation most effectively at wavelengths close to their size. Thus, a significant portion of radiation scattering by atmospheric aerosols occurs in the solar visible spectrum (Penner, 2001). However, for certain compounds such as elemental carbon, substantial absorption of solar radiation can occur. Additionally, aerosols with diameters larger than 2 μm, such as sea salt and mineral dust particles, can absorb infrared radiation (Penner, 2001).

In summary, aerosol particles can interact with solar radiation in various ways in the Earth's atmosphere: they can scatter solar light, resulting in atmospheric cooling, or they can absorb solar radiation, leading to the warming of the surrounding environment (see Fig. 1.3a). The interaction of aerosols with solar radiation through scattering and absorption is referred to as the direct aerosol effect (Li, 2021; Sokolik & Toon, 1996; Li & Sokolik, 2018). In addition to the direct aerosol effect, there is also the indirect aerosol effect (DeMott, 2003; Connolly, 2009). These phenomena are associated with the interaction of aerosols with cloud cover (see Fig. 1.3b). The radiative impact of aerosols on clouds primarily results in a reduction in precipitation, as the particles decrease the amount of solar radiation reaching the Earth's surface (thereby providing less heat for water evaporation and sustaining convective rain clouds) (Rosenfeld et al., 2008).

A significant portion of the radiation that is not reflected back into space is absorbed by aerosols in the atmosphere, primarily carbonaceous aerosols. This leads to the heating of the lower troposphere and further suppresses the generation of convective clouds (Rosenfeld et al., 2008). Additionally, particles can alter the cloud albedo. Increasing the cloud brightness through aerosol-induced changes in albedo results in an increase in the number of rain droplets and a decrease in precipitation. Therefore, aerosols can contribute to drought conditions in certain regions.

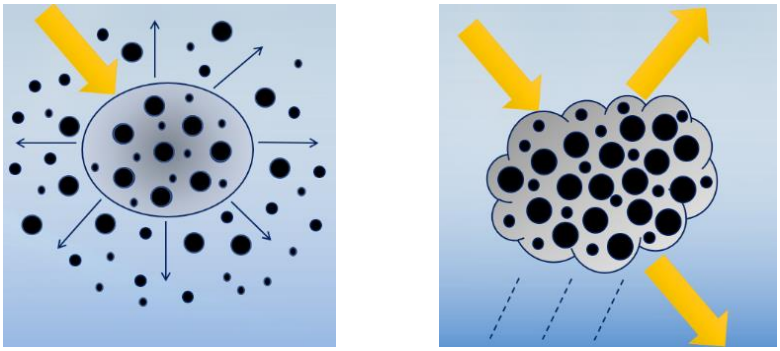

a b

Figure 1.3. Interaction of aerosols with the atmosphere: a) Direct Radiative Effect: absorption and scattering of solar radiation by aerosol particles; b) Indirect Radiative Effect: interaction of aerosols with clouds, including changes in albedo and the formation of cloud condensation nuclei.

However, another scenario of the indirect aerosol effect is possible, namely the formation of cloud condensation nuclei (CCN) by aerosol particles. In "typical" boundary layer clouds, particles need to grow to 50–100 nm in diameter to become cloud condensation nuclei (through processes of coagulation and condensation). The efficiency with which aerosols form CCN primarily depends on their initial growth rate and the background aerosol loading. Essentially, the global precipitation should be balanced with evaporation. Thus, the suppression of precipitation from low-level clouds by aerosols should be compensated by increased precipitation from high-level clouds.

This compensation can occur on both global and local scales, where clouds can grow to heights where aerosols no longer hinder rainfall (Rosenfeld et al., 2008). All of these findings align with the conceptual model of the impact of high aerosol concentration on the clean (upper) and polluted (lower) atmospheres, as shown in Figure 1.4. Cloud droplets merge into raindrops that fall from aerosol-free clouds. In polluted air, smaller droplets do not precipitate before

reaching supercooled levels where they freeze and transform into ice precipitation, which subsequently falls and melts at lower levels (Rosenfeld et al., 2008).

The additional release of latent heat during freezing aloft and the reabsorption of heat at lower levels during ice melting result in greater upward heat transport for the same amount of surface precipitation in a more polluted atmosphere (Rosenfeld et al., 2008). This signifies an increase in energy perturbations for the same amount of precipitation, leading to the acceleration of convective cloud evolution and additional rainfall, despite slower conversion of cloud droplets into raindrops (Rosenfeld et al., 2008).

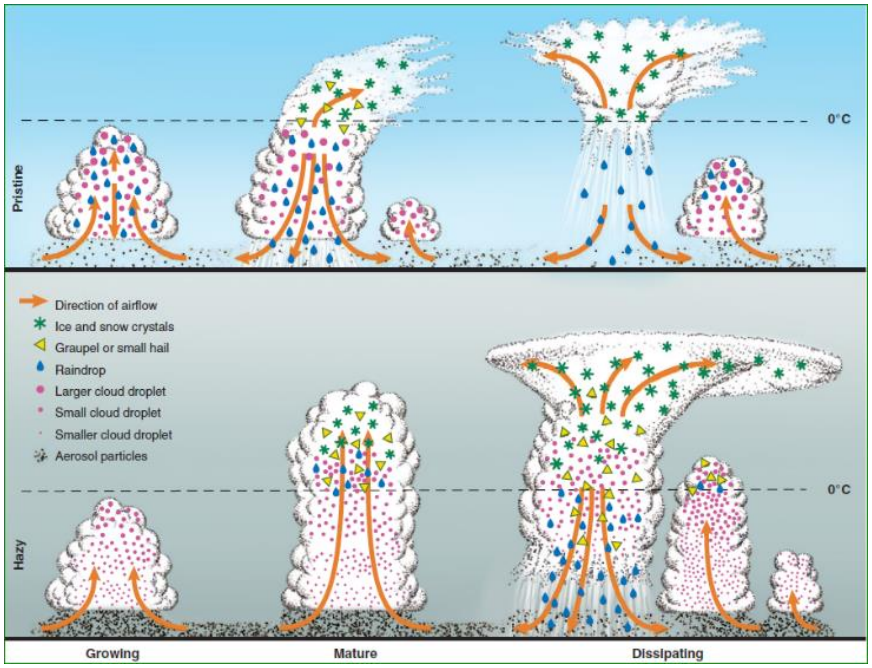

Figure 1.4. Impact of high aerosol concentration on the evolution of convective clouds (Source: Rosenfeld et al., 2008).

Based on the above, it is clear that the study of aerosols remains a pertinent topic. Ground-based and satellite observation methods are employed to monitor and study the content, distribution, and optical and microphysical characteristics of aerosols in the Earth's atmosphere (Chin et al., 2014). These methods complement each other. Ground-based instruments allow for more accurate determination of aerosol particle characteristics compared to satellite measurements, and are used to validate satellite results. For instance, to validate future results of the aerosol research space project Aerosol-UA (Yatskiv et al., 2012; Milinevsky et al., 2016), the data from ground-based sun photometers of the international network AERONET (Aerosol Robotic Network, http://aeronet.gsfc.nasa.gov/) and lidar networks, which provide information on the vertical distribution of aerosol particles in the atmosphere, are utilized.

The AERONET network is managed by NASA (USA) and the French and Spanish branches of ACTRIS (Aerosols Clouds and TRace gas InfraStructure, https://www.actris.eu/). The ACTRIS is dedicated to generating top-quality data and insights regarding short-lived atmospheric components and the mechanisms responsible for their fluctuations in both natural and controlled atmospheric conditions.

One such network is the European Aerosol Research Lidar Network (EARLINET, www.earlinet.org), comprising approximately 30 lidar stations in various European countries. However, these mentioned ground-based instruments also serve as independent and effective means for aerosol research in the Earth's atmosphere, with simultaneous measurements using solar photometers and lidars proving particularly effective.

1.2 Objectives and outline of the thesis

As previously mentioned, atmospheric aerosols have the ability to influence climate, radiative forcing, human health, and ecosystem conditions. Hence, that these particles represent a significant focal point for research. Using different methods to analyze aerosols, including combining sun photometer, lidar observations and air quality monitoring, has enabled a detailed understanding of aerosol characteristics resulting from biomass burning. The lidar campaign held in Kyiv in 2015 represented the initial measurements of aerosol spatial distribution for both Kyiv and Ukraine. This study analyzes these observations to investigate aerosol properties during the lidar campaign and the peatland burning event near Kyiv in autumn 2015.

Furthermore, this study involves concurrent investigation into aerosol properties and air quality in Kyiv using AERONET data and the recently established AirVisual network, specifically emphasizing the effects of forest fires in spring 2020. Both studies offer comprehensive insights into the optical and microphysical properties of aerosols within urban areas affected by background pollution and during episodes of biomass burning. The findings of this research can serve as a foundation for further investigations of similar occurrences in Kyiv and the region, as it demonstrates the variations in aerosol properties during biomass burning, the influence of air mass transport from emission sources to the city, and the disparities caused by different vegetation types.

Moreover, the work provides assessments of long-term variations of AOD, AE, RF, black carbon, $PM_{2.5}$, CO, SO_2, SO_4, and organic carbon. This analysis encompasses both the

processing of observations and the application of modeling. Such an approach enables the identification of seasonal regularities, the detection of anomalies, and enables the prediction of the further evolution of atmospheric constituents and their properties.

Certainly, the Russian-Ukrainian war has also had an impact on the atmosphere of Ukraine. The research involves an analysis of aerosol characteristics observed in 2022 and 2023, researching their deviations from previous years. Additionally, it explores the war's impact on the concentrations of $PM_{2.5}$, SO_2, SO_4, and Black Carbon over the Ukraine before and after the Russian invasion.

The thesis report is organized as followed:

- Chapter 2 provides an overview of fundamental concepts related to aerosols, including a discussion on light scattering and radiative transfer equations.
- Chapter 3 describes the instruments and methods employed in the analysis. It also includes information about the observational sites.
- Chapter 4 outlines the findings of the analysis concerning aerosol properties during periods of notable aerosol concentration, such as the peat fires in 2015 and the forest fires in 2020. The former case emphasizes simultaneous observations using sun photometer and lidar, while the latter focuses on air quality and $PM_{2.5}$ concentrations obtained through the AirVisual network, in conjunction with AERONET observations. In both instances, the impact of air mass transportation (calculated via HYSPLIT) and fire mapping by MODIS were integral. The results of this chapter are detailed in Bovchaliuk et al. (2017) and Zhang et al. (2022). The methodology employed in this research is further outlined in Yukhymchuk et al. (2022).
- Chapter 5 describes and discuss the variations in Aerosol Optical Thickness and Angstrom exponent over the past 15 years of observations (2008–2023) of the AERONET network in Kyiv. An assessment of the impact of aerosols on radiative forcing is provided. The chapter also investigates the evolution of black carbon, $PM_{2.5}$, CO, SO_2, SO_4, and organic carbon in the atmosphere over. The results are presented in following conference: IAMA (2022), ILRC 29 (2019), ILRC 30 (2022), YSC (2022), AGU (2022), Astronomy and Space physics (2023).

- Chapter 6 compares the levels of $PM_{2.5}$, SO_2, SO_4, and Black Carbon across Ukraine before and after the beginning of Russian aggression, exploring the war's impact on monthly, seasonal and annual variations. Additionally, the study demonstrates changes in the chemical composition during 2020. Fluctuations in the complex refractive index, as observed by AERONET, were substantiated by chemical analyses provided through GRASP. The results are presented in Astronomy and Space physics conference (2023).
- The manuscript ends with conclusions and perspectives.

Chapter 2

2. ATMOSPHERIC AEROSOLS

2.1 Sources of atmospheric aerosols

Every second, a multitude of substances, both anthropogenic and of natural origin, enter the Earth's atmosphere. This section provides a description of the major sources of aerosols on both a global and local scale.

2.1.1 Primary and secondary sources of atmospheric aerosols

Aerosols in the atmosphere can originate from both natural and anthropogenic sources. Natural aerosols include mineral dust, particularly from deserts and soil, sea salt particles, biogenic particles such as pollen and plant-emitted substances, sulfides released through the activity of the world's oceans, and volcanic emissions. Anthropogenic activities also contribute significant aerosols to the atmosphere, including emissions from transportation, industrial processes, large-scale forest fires, and waste incineration. When entering the atmosphere, some particles may already be formed, while others are generated through chemical reactions. Based on this property, aerosols can be divided into primary and secondary aerosols.

Primary aerosols consist of both inorganic and organic components (Myhre et al., 2013). Inorganic primary aerosols are relatively large, often exceeding 1 μm, and originate from sea spray, mineral dust, and volcanic eruptions and they have a short atmospheric lifetime, typically lasting only a few days (Myhre et al., 2013). Combustion processes, biomass burning, and plant/microbial materials are sources of carbonaceous aerosols, including organic carbon (OC) and black carbon (BC), which usually have sizes smaller than 1 μm (Myhre et al., 2013).

Secondary aerosols are formed through the condensation of precursor gases onto existing particles or by nucleation of new particles (Myhre et al., 2013). Their sizes range from a few nanometers to 1 μm, and their lifetimes span from days to weeks (Myhre et al., 2013). Key precursor gases such as nitrogen dioxide (NO_2), sulfur dioxide (SO_2), carbon monoxide (CO), formaldehyde (HCHO), and ammonia (NH_3) are released from burning fossil fuels or fires. Additionally, biogenic emissions of volatile organic compounds (VOCs) make a significant contribution. Furthermore, volcanic eruptions can lead to the formation of large quantities of primary and secondary aerosols both on the Earth's surface and in the stratosphere (Boulon et al., 2011).

2.1.2 Fires as a source of aerosol particles in the atmosphere above Kyiv

The content of aerosol in the atmosphere above Kyiv is influenced by numerous local sources of aerosol pollution, such as intensive urban transportation and heavy industry, as well as the transport of aerosol from distant sources, mainly natural and artificial forest and peat fires, and grass burning. The potential impact of these local and distant sources of aerosol particles on air quality and seasonal and local changes in the content and properties of aerosols in the atmosphere above Kyiv was investigated in (Milinevsky et al., 2014). The three-dimensional backward trajectories and cluster analysis determined the dominant particle transport directions and possible aerosol origins.

Emissions of aerosol particles from vegetation fires have a significant impact on both climate and air quality (IPCC, 2021). Biomass burning plays a crucial role in the climate system. Aerosols from forest, grass, and peat fires can be transported over long distances, affecting aerosol content, properties, and air quality in populated areas. For example, aerosols from a forest fire in Canada that occurred from July 2 to July 7, 2013, were observed over Central and Eastern Europe (Markowicz et al., 2016).

Forest, grass, and peat fires generate so-called biomass burning aerosols, which consist of various particles containing substances such as black carbon (soot), sulfates, nitrates, ammonium, and dust (Reid et al., 2005). The mixture of different types of particles in a smoke plume determine the microphysical and optical properties of the observed aerosol at the measurement site. The size distribution of biomass burning (BB) aerosol particles influences

the concentrations of fine particles ($PM_{2.5}$) and inhalable particles (PM_{10}), which are air quality indicators (Shelestov et al., 2020).

Special studies have emphasized the adverse effects of fine particulate matter on human health (see, for example, Haënninen et al., 2009; Lanzinger et al., 2016). It is important to accurately identify and quantitatively assess the specific pollution from biomass burning aerosol particles, especially in urban areas. On-site measurements of particulate matter concentrations are a common technique for assessing air pollution in different regions worldwide (Putaud et al., 2010; Amaral et al., 2015; Huang et al., 2018; Samek et al., 2020), including the use of inexpensive devices for air quality monitoring networks (Abera et al., 2020; Fattoruso et al., 2020). Remote sensing (Schaap et al., 2009; Van Donkelaar et al., 2011; Bovchaliuk et al., 2013; Gao et al., 2018), modeling (Huang et al., 2018; Chu et al., 2016), and the synergy of different methodologies (Lennartson et al., 2018) are also employed. Specifically, modeling the transport of air masses is necessary to assess the impact of forest fire aerosols on air quality, which depends on meteorological parameters (Yang et al., 2020; Zhao et al., 2020).

The most dangerous grass and forest fires occur in radioactively contaminated areas, such as the Chernobyl exclusion zone (Evangeliou et al., 2015). During such events, biomass containing radioactive elements can burn and spread over long distances through the air. An increase in aerosol amount was observed at the AERONET Kyiv station in April–May each year. This is primarily caused by agricultural biomass burning and forest/peat fires, which determine the seasonal properties of aerosols over Ukrainian agricultural and urban-industrial regions (Milinevsky et al., 2014).

2.1.3 Aerosols in different parts of the world

The chemical composition of aerosols can vary significantly across different locations on Earth's surface due to various factors such as regional industrialization, natural aerosol sources, proximity to major cities, and others. Therefore, in order to gain a more accurate understanding of the chemical composition of aerosols and their impact on human health and climate, extensive research is necessary in different regions of the world. The detailed chemical composition of aerosols can be studied through direct atmospheric air sampling and laboratory analysis.

For example, the study by Zhang et al. (2007) presents the observations of 37 field campaigns (using aerosol mass spectrometry) investigating organic and other aerosols in various regions worldwide, including industrial, rural, and remote areas. Some results of this research, such as the distribution and concentration of organic compounds, sulfates, nitrates, ammonium, and chlorides based on measurements from aerosol mass spectrometers in different cities all around the world (see Fig. 2.1).

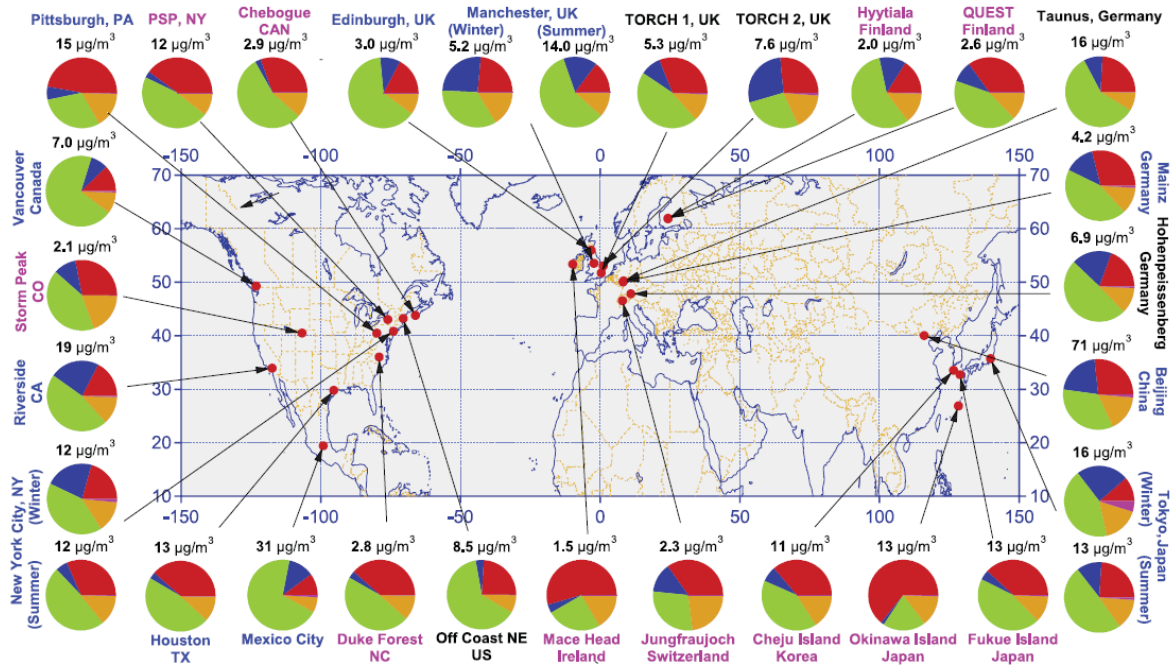

Figure 2.1. Distribution and concentration of organic compounds, sulfates, nitrates, ammonium, and chlorides based on measurements from aerosol mass spectrometers in different parts of the world. The locations of aerosol mass spectrometers are indicated by red dots on the map. The colors of the labels indicate the sampling locations: urban areas (blue), within 100 miles downwind of major cities (black), and rural/remote areas more than 100 miles downwind (pink). The pie charts represent the average mass concentration and chemical composition: organic compounds (green), sulfates (red), nitrates (blue), ammonium (orange), and chlorides (purple). The study focused on the non-refractory submicron fraction. (Source: Zhang et al., 2007).

Depending on their source, aerosol particles can have diverse compositions and may contain inorganic ions, organic compounds, black carbon, soil compounds, trace elements, radioactive isotopes, formaldehydes, hydrocarbons, and aromatic compounds. Consequently, many aerosols can pose potential hazards to human health if they enter in the body.

2.2 Air Quality and Ukraine

2.2.1 Air Quality Index

How can the air quality that humans breathe be assessed? In addition to the obvious answer related to visibility (which is logical since a high concentration of particles in the atmosphere reduces its transparency), there are more precise methods of investigation. We can demonstrate the impact of a high concentration of aerosol particles using two photographs shown in Figure 2.2, specifically on April 7 and 8, 2020. As clear from this example, within just one day, atmospheric pollution significantly reduced visibility several times over. The cause of such deterioration was the large-scale forest fires in the northern and northwestern regions of Ukraine, including the outskirts of Kyiv (Zhang et al., 2022). During this period, the city topped the rankings for pollution levels worldwide.

a b

Figure 2.2. Atmosphere conditions: a) April 7 and b) April 8, 2020. Photos taken on Chornobylska Street in the suburbs of Kyiv. (Photos are taken by Gennadi Milinevsky).

Changes in the concentration of atmospheric aerosols not only impact human health but also increase the risk of traffic accidents, pose a danger to aviation, can impair device functionality, and affect industrial operations. It is not surprising that there exists a specific scale, known as the Air Quality Index (AQI), for assessing air quality. The AQI is defined as (Technical Assistance Document for the Reporting of Daily Air Quality, 2018):

$$AQI = \frac{(I_{high} - I_{low})}{(C_{high} - C_{low})}(C - C_{low}) + I_{low} \quad (2.1)$$

where *AQI* is the Air Quality Index, *C* is the concentration of the pollutant, C_{low} is the concentration at the lower control point, C_{high} is the concentration at the higher control point, I_{low} is the index corresponding to C_{low}, and I_{high} is the index corresponding to C_{high}.

2.2.2 Air Pollution in the world and Ukraine

Solid particles are not individual pollutants; rather, their composition consists of a mixture of many chemical substances. This complex mixture of solid substances and aerosols is composed of small liquid droplets, dry solid fragments, and solid cores with liquid coatings. The particles vary widely in size, shape, and chemical composition and may contain inorganic ions, metallic compounds, elemental carbon, organic compounds, and compounds from the Earth's crust (source: https://ww2.arb.ca.gov/resources/inhalable-particulate-matter-and-health). When entering the human body, these particles can have various effects. It is not only the chemical composition and size that are important, but also the quantity of particles that periodically or continuously enter the human body. Figure 2.3 presents the results of mortality statistics attributed to air pollution by the World Health Organization as of 2016 (Source: https://www.who.int/data/gho/map-gallery).

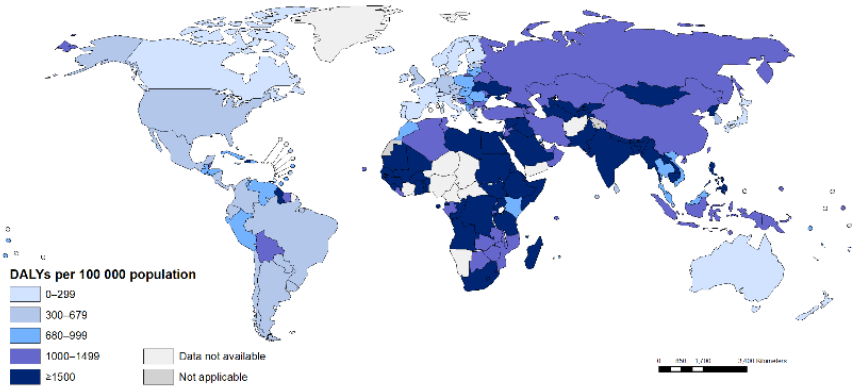

Figure 2.3. Additional daily mortality attributable to air pollution as of 2016, per 100 000 population (Source: https://www.who.int/data/gho/map-gallery).

Figure 2.3 shows the findings that Ukraine has a high mortality rate due to poor air quality. It is also apparent that higher mortality corresponds to regions with high levels of air pollution. It is not surprising that due to the danger of PM, the issue of air quality monitoring becomes more acute worldwide with each passing year. According to the European

Environment Agency (EEA), the World Health Organization recommends a daily $PM_{2.5}$ concentration of 15 µg m^{-3} and an annual average of 5 µg m^{-3}. For PM_{10}, the corresponding recommendations are 45 µg m^{-3} for daily averages and 15 µg m^{-3} for annual averages (https://www.eea.europa.eu/en).

In various countries, recommended PM concentrations may vary (examples can be found in the provided references: https://www.canada.ca/en.html, https://healthandsafetyinshanghai.com). Furthermore, the concentration of $PM_{2.5}$ and, consequently, the Air Quality Index (AQI) value differentiate the potential impact on human health. Table 1.1 presents Daily $PM_{2.5}$ Concentrations and Corresponding Air Quality Index (AQI) Levels along with Health Risk Levels for Humans, utilizing the respective color scale following U.S. Standards.

Table 1.1. Daily $PM_{2.5}$ Concentrations and Corresponding Air Quality Index (AQI) Levels and Health Risk Levels for Humans with the respective color scale (Source: https://www.iqair.com/us/). U.S. Standards.

$PM_{2.5}$ Concentration (µg m^{-3}), 24–hour	AQI	Health Risk Level
0.0–12.0	0–50	Low
12.1–35.4	51–100	Moderate
35.5–55.4	101–150	Unhealthy for Sensitive Groups
55.5–150.4	151–200	Unhealthy
150.5–250.4	201–300	Very Unhealthy
250.5+	301+	Hazardous

Based on the Air Quality Index (AQI), rankings of countries and cities can be established based on the cleanliness of air quality. According to the World Air Quality Report 2021, Ukraine ranked 56th globally in air pollution in 2021 with an AQI of 18.5 and 9th in Europe. In turn, Kyiv ranked 48th among observed cities with an AQI of 18.8 (here, it takes into account the annual concentration of $PM_{2.5}$, according to WHO – recommended levels of up to 5 µg m^{-3}, corresponding to an AQI of 0 – 5. More details can be found in the WHO global air quality guidelines). Considering this information and the high mortality rate, air quality monitoring in Kyiv and Ukraine is an important issue for both researchers and residents.

2.3 General equations of radiative transfer

It is known that the distance from the Earth to the Sun is approximately 150 million kilometers, and it takes light only about 8 minutes to reach the planet. Before reaching the Earth's surface, solar radiation passes through the atmosphere, which contains various components that can absorb or scatter radiation. In certain spectral regions, the atmosphere is transparent to solar radiation, while it is opaque in others. Figure 2.4 illustrates the atmospheric transmittance in different radiation ranges for incoming (from the Sun) and outgoing (radiation from the Earth into space) radiation fluxes.

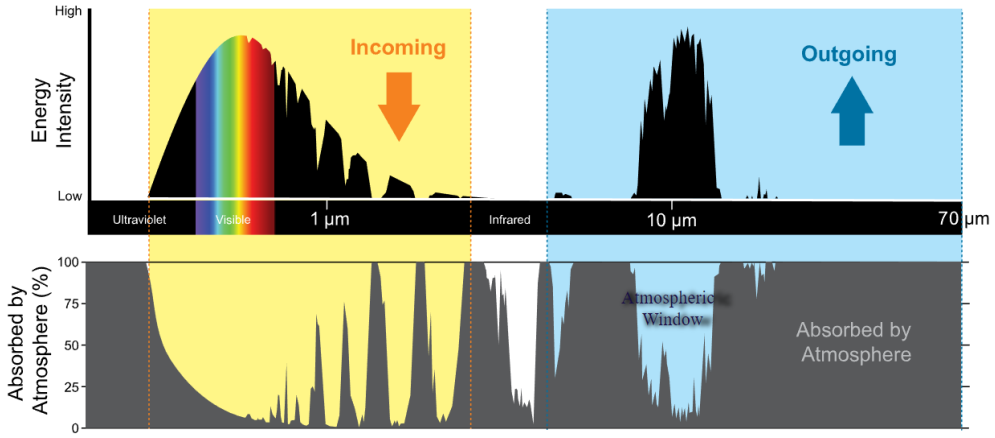

Figure 2.4. Atmospheric transmittance in different radiation ranges. (Source: https://www.weather.gov/jetstream/absorb).

Scattering of sunlight by molecules is described by the Rayleigh theory, which explains why the sky appears blue in the absence of aerosols (Rayleigh scattering). The scattering of spherical aerosol particles is described by Mie scattering theory. The atmospheric component known as ozone (specifically, stratospheric ozone) protects us from short-wavelength ultraviolet radiation, which is highly dangerous as it can damage DNA molecules and cause irreversible changes (https://earthobservatory.nasa.gov/features/UVB). Unfortunately, tropospheric ozone has a negative impact on living organisms (https://www.epa.gov/ground-level-ozone-pollution/health-effects-ozone-pollution). Other components, such as greenhouse gases and aerosols, the pollution of which has significantly increased in recent decades, have an impact on global temperature and climate. This section provides a brief description of the main processes and physical quantities associated with radiation transfer in the atmosphere and

the characteristics of aerosols. It shows how scattering and absorption processes influence the propagation of radiation.

2.3.1 Flux and Radiance

Flux is defined as the total energy carried by electromagnetic waves per unit area per unit time. Radiance is also an important characteristic of electromagnetic waves. The flux of incoherent radiation is expressed in watts per square meter (W m^{-2}) and includes fluxes at all wavelengths. In the case of monochromatic flux (also referred to as spectral flux), denoted as F_λ (Petty, 1958):

$$F_\lambda = \lim_{\Delta\lambda \to 0} \frac{F(\lambda, \lambda+\Delta\lambda)}{\Delta\lambda} \tag{2.2}$$

Where $F(\lambda, \lambda + \Delta\lambda)$ represents the flux created by radiation with wavelengths ranging from λ to $\lambda + \Delta\lambda$. Monochromatic flux is measured in watts per square meter per micrometer (W m^{-2} μm). Therefore, the flux in the wavelength range $[\lambda_1, \lambda_2]$ can be obtained by integrating the previous expression (1.2) (Petty, 1958):

$$F(\lambda_1, \lambda_2) = \int_{\lambda_1}^{\lambda_2} F_\lambda d\lambda \tag{2.3}$$

Another important characteristic of electromagnetic radiation is its radiance. For the visible range, radiance can be loosely compared to "brightness." By definition, the radiance of radiation $L(\vec{\Omega})$ is the flux passing through a solid angle $\partial\omega$ in a specific direction $\vec{\Omega}$. The flux is measured on a surface perpendicular to the direction of incident radiation. The radiance in a given direction is measured as (Petty, 1958):

$$L(\vec{\Omega}) = \frac{\partial F}{\partial \omega} \tag{2.4}$$

Let's consider the upward flux from a horizontal surface (see Fig. 2.5). This flux should be an integral of $L(\vec{\Omega})$ over all possible directions $\vec{\Omega}$ through a solid angle of 2π, corresponding to the upper hemisphere (see Fig. 2.5). However, there is one slight complication: since for a horizontal surface dS, only one direction is perpendicular (normal $\vec{n}$), while other directions are at certain angles, we need to take into account the cosine of the angle between the direction of incident radiation and the normal $\vec{n}$ (Petty, 1958).

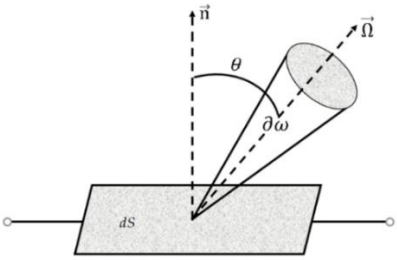

Figure 2.5. Flux carried by a beam in the direction $\vec{\Omega}$ through the surface element dS.

For the upward flux, we obtain the following equation (Petty, 1958):

$$F^{\uparrow} = \int_{2\pi} L^{\uparrow}\left(\vec{\Omega}\right) \cdot \vec{n} \cdot \vec{\Omega} \cdot d\omega \tag{2.5}$$

This is the general expression, which in the spherical coordinate system (where the z-axis is the normal direction, and the solid angle $d\omega = sin\theta d\theta d\varphi$, as shown in Fig. 2.6) takes the form of equation (1.5).

$$F^{\uparrow} = \int_0^{2\pi} \int_0^{\pi/2} L^{\uparrow}(\theta, \varphi) cos\theta sin\theta d\theta d\varphi \tag{2.6}$$

For the downward flux, and as a result, integrating over the lower hemisphere, we obtain the following expression (Petty, 1958):

$$F^{\downarrow} = -\int_0^{2\pi} \int_{\pi/2}^{\pi} L^{\downarrow}(\theta, \varphi) cos\theta sin\theta d\theta d\varphi \tag{2.7}$$

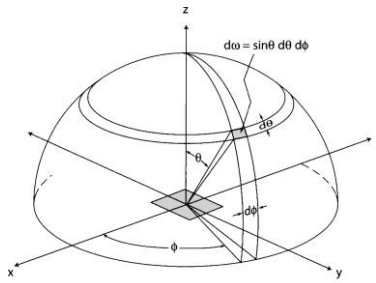

Figure 2.6. Solid angle in polar coordinate system (adapted from Petty, 1958).

In the case of isotropic radiation ($L = const$ in all directions) over a hemisphere, integration yields the following result (Petty, 1958):

$$F = \pi L \tag{2.8}$$

The net flux, or the difference in flux between upward and downward components, is determined as the difference between the upward and downward fluxes (Petty, 1958):

$$F^{net} = F^{\uparrow} - F^{\downarrow} \tag{2.9}$$

what can be expressed as (Petty, 1958):

$$F^{net} = \int_0^{2\pi} \int_0^{\pi} L(\theta, \varphi) cos\theta sin\theta d\theta d\varphi = \int_{4\pi} L\left(\vec{\Omega}\right) \cdot \vec{n} \cdot \vec{\Omega} \cdot \partial\omega \quad (2.10)$$

The change in one value results in a change in the other. Additionally, it is important to know the angles of light incidence as they have a significant influence on both the radiance and the magnitude of the flux.

2.3.2 Extinction and Beer's law. Optical thickness

Let's consider the propagation of electromagnetic waves in an absorbing homogeneous medium with a refractive index m (imaginary part is not zero). Then, the radiance L_λ will decrease exponentially with distance x (Petty, 1958):

$$L_\lambda(x) = L_{\lambda,0} \exp(-\sigma_a \, dx) \quad (2.11)$$

where σ_a is the absorption coefficient, which depends on the physical medium and the wavelength of radiation. For simplicity, we will make two additional assumptions (Petty, 1958):

1) Radiation is attenuated not only due to absorption but also due to scattering. During absorption, the energy of radiation is converted into heat or chemical energy. During scattering, the energy is re-emitted in all directions. This typically occurs through interaction with particles. Taking this assumption into account, the absorption coefficient σ_a should be replaced by the extinction coefficient, which includes both absorption and scattering.

2) The probability that the absorption or scattering strength will vary significantly along the path such that the starting point should be a differential equivalent of equation (2.11), in which we initially consider the change in radiation radiance as it traverses an infinitesimally small distance ds, where the extinction coefficient can be assumed constant. As mentioned earlier, the extinction coefficient σ_e includes contributions from both absorption and scattering and can be expressed as (Petty, 1958):

$$\sigma_e = \sigma_a + \sigma_s \quad (2.12)$$

where σ_a is the absorption coefficient and σ_s is the scattering coefficient.

Since the extinction coefficient varies with distance in the real atmosphere, by generalizing equation (2.11) and replacing x with the geometric distance s along the ray in any

direction (as shown in Fig. 2.7). Next, let's consider the attenuation of radiation over an infinitesimally small path ds, which is chosen to be small enough for the extinction coefficient σ_e to be effectively constant within the interval, and the decreasing radiation is attenuated by an infinitesimal amount dL_λ. Then, we can express it as (Petty, 1958):

$$dL_\lambda = L_\lambda(s + ds) - L(s) = -L(s)\sigma_e(s)ds \tag{2.13}$$

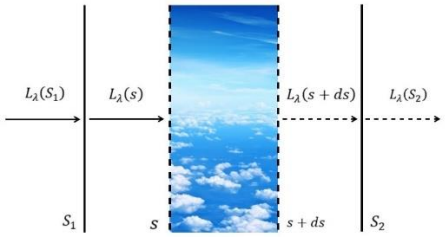

Figure 2.7. Propagation of light in the atmosphere with varying extinction coefficient.

Rearranging the last equation (1.13), we can write it as follows:

$$\frac{dL_\lambda}{L_\lambda} = d\ logL_\lambda = -\sigma_e ds \tag{2.14}$$

In other words, the infinitesimal decrease in radiance dL_λ, expressed as the fraction of the incident intensity, is equal to the product of the local extinction coefficient multiplied by the infinitesimal path length ds. To compute the extinction along a path between points s_1 and s_2 (where $s_2 > s_1$), it is necessary to integrate equation (2.14) (Petty, 1958):

$$\log[L_\lambda(s_2)] - \log[L(s_1)] = -\int_{s_1}^{s_2} \sigma_e(s)ds \tag{2.15}$$

In this regard, equation (1.15) can be expressed in the following form:

$$I_\lambda(s_2) = I_\lambda(s_1)\exp[-\int_{s_1}^{s_2} \sigma_e(s)ds] \tag{2.16}$$

The last equation (1.16) is known as Beer's law, and it leads to several important consequences. In particular, the quantity within square brackets is known as the extinction optical path or optical thickness (Petty, 1958).

$$\tau_e(s_1, s_2) = \int_{s_1}^{s_2} \sigma_e(s)ds \tag{2.17}$$

Optical thickness is a dimensionless quantity that can only take positive values. It can be equal to zero only when $s_1 = s_2$ or when $\sigma_e = 0$. Taking the exponential of τ_e yields atmospheric transmittance (or atmospheric transmission) between points s_1 and s_2 (Petty, 1958):

$$t(s_1, s_2) = e^{-\tau_e(s_1, s_2)} \tag{2.18}$$

Atmospheric transmittance is also a dimensionless quantity that varies from 0 (when $\tau_e \to \infty$) to 1 (when $\tau_e = 0$). In this case, equation (1.16) can be expressed as follows (Petty, 1958):

$$\tau_e = t(s_1, s_2) L_\lambda(s_1) \tag{2.19}$$

Under the condition of $\sigma_e = const$ over the interval $[s_1, s_2]$, equation (1.17) simplifies to the following:

$$\tau_e = \sigma_e (s_2 - s_1) \tag{2.20}$$

If we consider the propagation of radiation along a path from s_1 to s_N, then on each subinterval, as described in Petty (1958):

$$\tau_e(s_1, s_N) = \tau_e(s_1, s_2) + \tau_e(s_2, s_3) + \cdots + \tau_e(s_{N-1}, s_N) \tag{2.21}$$

$$t(s_1, s_N) = t(s_1, s_2) t(s_2, s_3) \ldots t(s_{N-1}, s_N) \tag{2.22}$$

Thus, the total optical thickness is equal to the sum of individual optical thicknesses over all intervals along the path, and the total atmospheric transmittance is the product of individual atmospheric transmittances along the same path. The extinction caused by a single particle is a function of the particle's extinction efficiency Q_e (Hinds, 1999).

2.3.3 Absorbing atmosphere. Schwarzschild equation.

Let's consider the propagation of radiation at a wavelength λ in an air layer with an infinitesimally small width ds in the direction of propagation. Then, the decrease in radiance due to absorption can be expressed as (Petty, 1958):

$$dL = -\sigma_e L ds \tag{2.23}$$

According to Kirchhoff's law, the absorption of any amount of material in a zone of local thermodynamic equilibrium is equal to the emission of that same material. Therefore, this emission can be expressed as:

$$dL_{emit} = \sigma_a B ds \tag{2.24}$$

$B_\lambda(T)$ – is the Planck function. The change in radiance can be expressed as follows:

$$dL = dL_{abs} + dL_{emit} = \sigma_a(B - L)ds \tag{2.25}$$

By rewriting the last equation, we obtain the following expression (Petty, 1958):

$$\frac{dL}{ds} = \sigma_a(B - L) \tag{2.26}$$

Equation (2.26) is known as the Schwarzschild equation. This fundamental equation describes the propagation of radiation in a non-scattering medium. It can be solved in the approximation of a plane-parallel atmosphere, where the optical path is given by (Petty, 1958):

$$\tau(s)_a = \int_s^S \sigma_a(s')\, ds' \tag{2.27}$$

Here, s represents an arbitrary point, and S denotes the position of the sensor. It is also worth noting that, by definition:

$$d\tau_a = -\sigma_a ds \tag{2.28}$$

By substituting equation (2.28) into the Schwarzschild equation (2.26), multiplying by the integrating factor $e^{-\tau}$, and integrating from $\tau_a = 0$ to $\tau_a = \tau'$, we obtain the following expression:

$$L(0) = L(\tau')e^{-\tau'} + \int_0^{\tau'} Be^{-\tau} d\tau \tag{2.29}$$

The first term in this equation describes the contribution of attenuation from any radiation source, while the second term represents the thermal radiation from each point τ along the line of sight between the sensor and the point τ'.

2.3.4 Radiative transfer equation with scattering

Assuming neglect of scattering, the radiance changes dL along an infinitesimal path ds was expressed in eq. 2.26. The attenuation of radiation occurs due to absorption. (Petty, 1958).

$$dL_{abs} = -\sigma_a L ds \tag{2.30}$$

The radiation source:

$$dL_{emit} = \sigma_a B(T) ds \tag{2.31}$$

By incorporating scattering processes, including both absorption and scattering in various directions, into equation (2.31), we obtain:

$$dL = dL_{ext} + dL_{emit} + dL_{scat} \tag{2.32}$$

where

$$dL_{ext} = -\sigma_e L ds \tag{2.33}$$

The term dL_{scat} should be proportional to the scattering coefficient σ_s. Additionally, radiation passing through an infinitesimal volume and in any direction $\vec{\Omega}'$ can potentially contribute by scattering the radiation in the given direction $\vec{\Omega}'$. Furthermore, all contributions from all directions add up linearly, meaning that the path of a photon coming from one direction is not influenced by the presence of other photons or the paths they have taken (Petty, 1958). Mathematically, this can be expressed as:

$$dL_{scat} = \frac{\sigma_s}{4\pi} \int_{4\pi} p(\vec{\Omega}', \vec{\Omega}) L(\vec{\Omega}') d\omega' ds \tag{2.34}$$

The integration is performed over the entire solid angle 4π, and the phase function $p(\Omega', \Omega)$, which describes the scattering, must satisfy the normalization condition (Petty, 1958):

$$\frac{1}{4\pi} \int_{4\pi} p(\vec{\Omega}', \vec{\Omega}) d\omega' = 1 \tag{2.35}$$

The complete differential form of the radiation transport equation can be written as (Petty, 1958):

$$dL = -\sigma_e L ds + \sigma_a B ds + \frac{\sigma_s}{4\pi} \int_{4\pi} p(\vec{\Omega}', \vec{\Omega}) L(\vec{\Omega}') d\omega' ds \tag{2.36}$$

By dividing by $d\tau = -\sigma_e ds$, equation (2.36) can be expressed as:

$$\frac{dL(\vec{\Omega})}{d\tau} = L(\vec{\Omega}) - (1 - \tilde{\omega}) + \frac{\tilde{\omega}}{4\pi} \int_{4\pi} p(\vec{\Omega}', \vec{\Omega}) L(\vec{\Omega}') d\omega' \tag{2.37}$$

In this equation, $\tilde{\omega}$ represents the single scattering albedo, which can be expressed as:

$$\tilde{\omega} = \frac{\sigma_s}{\sigma_e} = \frac{\sigma_s}{\sigma_s + \sigma_a} \tag{2.38}$$

In equation (2.43), the dependence of L on the propagation direction $\vec{\Omega}$ is clearly notable. This expression represents the most general and complete form of the radiative transfer equation. Sometimes it is convenient to combine the terms and express the equation in the form of:

$$\frac{dL(\vec{\Omega})}{d\tau} = L(\vec{\Omega}) - J(\vec{\Omega}) \tag{2.39}$$

where $J(\vec{\Omega})$ is the source function, which can be expressed as follows:

$$J(\vec{\Omega}) = (1-\tilde{\omega})B + \frac{\tilde{\omega}}{4\pi}\int_{4\pi} p(\vec{\Omega}', \vec{\Omega})L(\vec{\Omega}')d\omega' \tag{2.40}$$

It should also be noted that in this case, $d\tau$ has been defined as a negative quantity, corresponding to the propagation of radiation towards the detector. Therefore, negative terms on the right-hand side are associated with the radiation source, while negative terms describe attenuation. Sometimes, opposite conventions are used in the literature. Additionally, from equation (2.40), it follows that the radiation source is a combination of thermal emission and scattering from other directions. When $\tilde{\omega} = 0$, the terms corresponding to scattering vanish, and when $\tilde{\omega} = 1$, the component of thermal emission disappears.

2.4. Optical and physical characteristics of aerosols

This section provides a description of the optical and physical properties of aerosols, including Aerosol Optical Depth, Angstrom Exponent, Single Scattering Albedo, absorption parameters, size distributions, and complex refractive index. Furthermore, the relationship between these properties and aerosol types analyzed.

2.4.1. Aerosol Optical Depth

Aerosol Optical Depth (AOD) is defined as the integral of the extinction coefficient between two points (z_1, z_2) in the medium through which radiation propagates.

$$AOD(\lambda, z_1, z_2) = \int_{z_1}^{z_2} \sigma(\lambda, z)\mathrm{d}z \tag{2.41}$$

Another term commonly used is Aerosol Optical Thickness (AOT). However, the term Aerosol Optical Depth is more widely used, so we will preferentially use AOD.

$$\tau_\lambda = \tau_{mol,\lambda} + \tau_{aer,\lambda} \tag{2.42}$$

$\tau_{mol,\lambda}$, $\tau_{aer,\lambda}$ are the optical depths for molecules and aerosols at a wavelength λ. In addition to $\tau_{mol,\lambda}$, the total optical depth includes the sum of all relevant molecular components in the atmosphere.

2.4.2 Angstrom Exponent

The spectral optical thickness can be expressed using the empirical Angstrom formula (1929):

$$AOD(\lambda) = \lambda^{-\alpha} \tag{2.43}$$

where α is the Angstrom exponent (AE), which characterizes the wavelength dependence and provides basic information about the influence of aerosol particle size. In equation (2.42), it is assumed that AOD and α are independent and constant with changing wavelength, meaning that each interval can be used to determine them. However, in reality, these coefficients are not independent and also exhibit wavelength dependence (Kaskaoutis & Kambezidis, 2006). Therefore, Angstrom Exponent can be expressed as follows:

$$\alpha = -\frac{d\ln(AOD)}{d\ln\lambda} = -\frac{\ln(\frac{AOD(\lambda_1)}{AOD(\lambda_2)})}{\ln(\frac{\lambda_1}{\lambda_2})} \tag{2.44}$$

where λ_1 and λ_2 are the wavelengths of two waves, $AOD(\lambda_1)$ and $AOD(\lambda_2)$ are the aerosol optical depths at the respective wavelengths. The Angstrom exponent can be used to describe the size of aerosol particles. In practice, AE provides derivative information about the particle size distribution in the vertical column of the atmosphere. By knowing this parameter, conclusions can be drawn about the dominant aerosol type. Small values typically indicate the presence of larger particles (mineral dust, sea salt), while larger values suggest the presence of anthropogenic contributions.

2.4.3 Single Scattering Albedo

The Single Scattering Albedo (SSA) is defined as the ratio of the scattering coefficient to the extinction coefficient and was already mentioned in section 2.3.4, equation (2.38). SSA defines the ratio of scattering to absorption processes of radiation in the atmosphere and is

therefore associated with the type of aerosol particles (see Fig. 2.8). When $\tilde{\omega} = 1$, there is no absorption, whereas $\tilde{\omega} = 0$ indicates pure scattering. Large particles such as sea salt and mineral dust, which scatter solar radiation, have an SSA approaching unity, while small and ultrafine particles like smoke and urban aerosols are capable of absorbing solar radiation, resulting in an SSA of less than 0.95 (see Fig. 2.8).

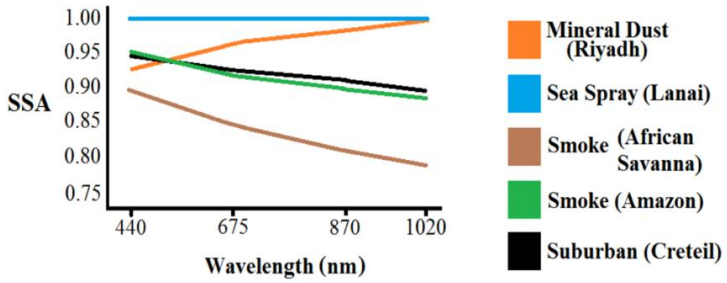

Figure 2.8. Single Scattering Albedo for various types of aerosols (source: https://earth.gsfc.nasa.gov/climate/data/deep-blue/science)

2.4.4 The absorption characteristics of aerosols

In addition to aerosol optical depth (AOD), there is a concept called absorption aerosol optical depth (AAOD) that is defined as (Che et al., 2018; Khan et al., 2019):

$$AAOD = AOD(1 - SSA) \tag{2.45}$$

This characteristic represents the contribution of absorbing particles to the aerosol optical depth. However, it is not a unique parameter specific to a particular aerosol type, especially when multiple types of absorbing aerosols, such as soot and mineral dust, are present in the air. The contribution of mineral dust to the total light absorption by aerosols is particularly important at ultraviolet wavelengths (Shin et al., 2019). Based on AAOD, it is possible to define the absorption Angstrom exponent (Khamala et al., 2023)

$$AAE = -\frac{dln(AAOD_{\lambda})}{dln(\lambda)} \tag{2.46}$$

Knowing the AAE can help determine the aerosol type more accurately, for example, for small spherical particles of black carbon (with a radius of approximately 0.01 mm), the AAE is within the range of 1 (Bergstrom et al., 2007). For more detailed information on AAOD and

AAE studies, you can refer to the works of Khamala et al. (2023), Bergstrom et al. (2007), Lack & Cappa (2010), Shin et al. (2019), and Che et al. (2018).

2.4.5 Complex Refractive Index

The complex refractive index is composed of real and imaginary parts. In the case of aerosol particles, the real part depends on the chemical nature of the aerosol and varies according to the aerosol type. As for the imaginary part, it also depends on the composition and is responsible for the aerosol's absorbing properties. Therefore, if this part is equal to zero, it indicates particles that are unable to absorb solar radiation.

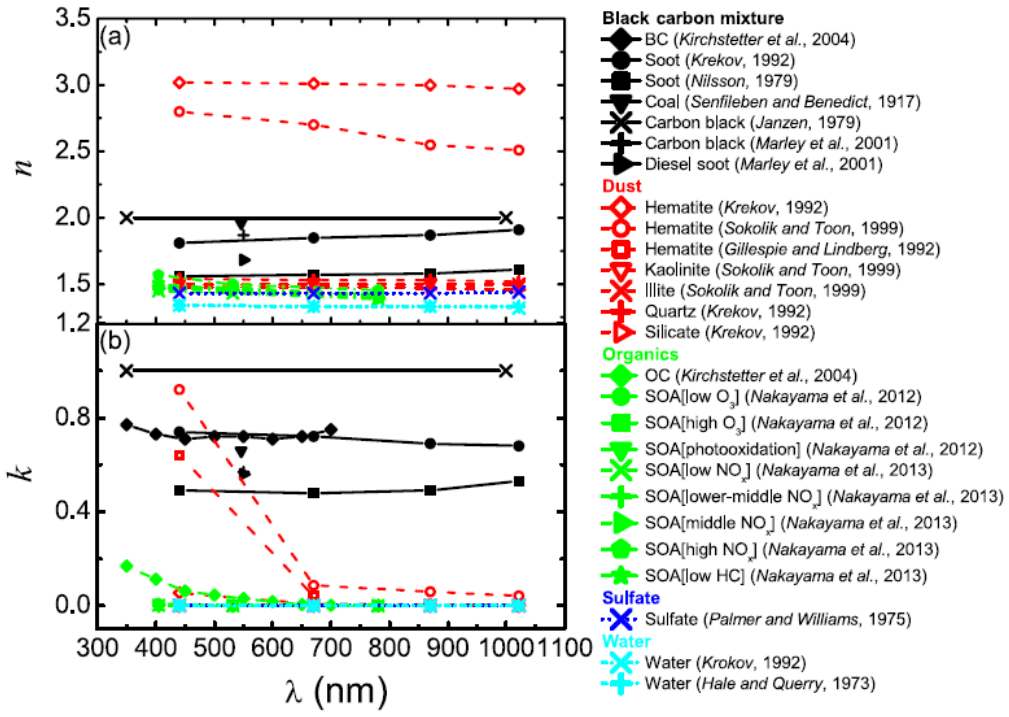

Figure 2.9. Complex refractive indices (real part: a; imaginary part: b) reported in the literature. Abbreviations are as follow: BC (black carbon), OC (organic carbon), SOA (secondary organic aerosol). Source: Zhang et al., 2017.

In Figure 2.9, the complex refractive index values for various aerosol types are depicted, encompassing black carbon, mineral dust, organic aerosols, sulfates, and water droplets (adapted from Zhang et al., 2017). The graph reveals the diverse refractive index values across

these aerosol categories, while demonstrating striking similarities in both the range and shape of the curves associated with each aerosol type.

Understanding the complex refractive index of aerosol particles is crucial in studying their interactions with light and their impact on atmospheric processes. By studying the values of the real and imaginary parts of the refractive index across different aerosol types, researchers can gain insights into the optical properties and behavior of these particles. This information is valuable for various applications, such as climate modeling, remote sensing, and air quality assessments. Additionally, the observed similarities in the refractive index curves within each aerosol category suggest common optical characteristics and provide a basis for developing parameterizations and models to accurately represent aerosol behavior in atmospheric studies.

2.4.6. Size distributions

Due to the wide range of particle sizes in aerosols (from 10^{-3} to 10^{2} μm in radius), it is convenient to represent particle distributions using a logarithmic scale. In this case, the particle size distribution within the radius range $[\ln r, \ln r, + d\ln r]$ can be expressed as:

$$N(r) = \frac{dN}{d\ln r} \tag{2.48}$$

The surface area distribution (the area of particles per unit volume) will have the following form:

$$S(r) = \frac{dS}{d\ln r} = 4\pi r^2 N(r) \tag{2.49}$$

The volume distribution represents the volume of aerosol particles in a unit cross-sectional column:

$$V(r) = \frac{dV}{d\ln r} = \frac{4\pi r^3 N(r)}{3} \tag{2.50}$$

The total number of particles in the distributions is obtained by integration:

$$N = \int_0^\infty N(r)\, d\ln r \tag{2.51}$$

$$S = \int_0^\infty S(r)\, d\ln r \tag{2.52}$$

$$V = \int_0^\infty V(r)\, d\ln r \tag{2.53}$$

The size distribution can be used to determine the AOD:

$$\mathrm{AOD} = \int_{r_1}^{r_2} \pi r^2 Q(r,\lambda) N(r) dr \qquad (2.54)$$

The particle distribution depends on the type of aerosol, and different particles have different shapes (see Fig. 2.10). For mineral dust, the distribution is dominated by large particle concentrations, while the opposite is observed for biomass burning aerosols, where the fine fraction prevails. Knowing the size distribution of aerosol particles allows us to determine the dominant aerosol type.

Many previous studies of the global aerosol system (e.g., Rasch et al., 2000) have modeled the global distribution of one or several major aerosol components: sulfates, elemental carbon, organic matter, sea salt, and mineral dust. Typically, in such studies, aerosols are represented as an external mixture, which means a mixture of particles, each composed of only one compound, or an internal mixture (particles containing a homogeneous mixture of individual components) with fixed ratios of the individual components. However, observations indicate (Seinfeld et al., 2004) that the state of mixing in the global aerosol system is highly variable, with significant internal mixing effects and different component ratios (Stier et al., 2005).

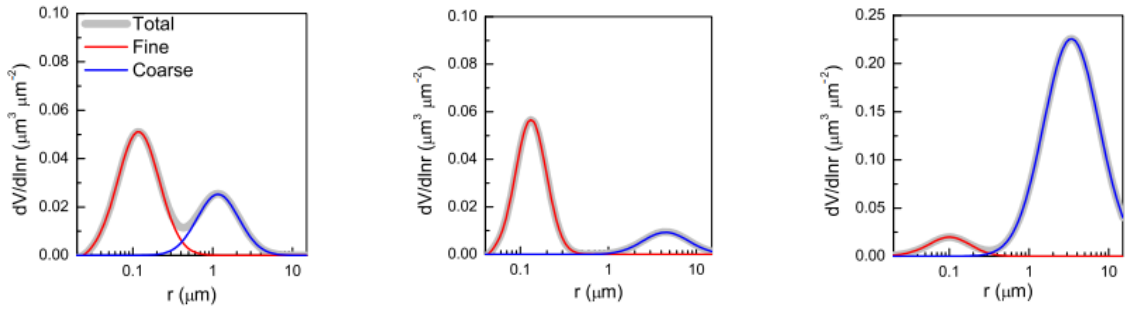

Figure 2.10. Particle size distribution for different aerosol types (Source: Zhang et al., 2017): a) water-soluble aerosol; b) biomass burning aerosol; and c) mineral dust. The red and blue colors represent the fine-mode and coarse-mode, respectively. The gray includes the distribution considering both modes.

A comprehensive analysis of aerosol-climate interactions requires knowledge of the size distribution, composition, and mixing state, thus necessitating the use of size-resolved, multi-component aerosol modules suitable for long-term integration in models (Stier et al., 2005).

2.5. Energy Exchange in the Earth's Atmosphere

This section delves into the intricate relationship between aerosols, radiative forcing, and climate, while presenting the fundamental equations essential for describing radiative forcing. Furthermore, it explores the intricate mechanisms through which aerosols interact with radiation, leading to changes in radiative forcing and subsequently influencing the Earth's climate system.

2.5.1 Radiative Forcing

Radiative Forcing (RF) and Effective Radiative Forcing (ERF) concepts are used to assess changes in the Earth's energy balance resulting from the influence of various atmospheric pollutants. Radiative Forcing can be defined as the change in the net downward flux (shortwave + longwave) at the tropopause after the stratospheric temperatures have reached radiative equilibrium (with water vapor, cloud cover, and tropospheric temperature being fixed values in this case) (Boucher et al., 2013). Therefore, RF does not include the impact of certain short-term changes in the atmosphere. The ERF concept allows for the inclusion and evaluation of rapid perturbations for all variables (except global mean surface temperature, ocean temperature, and sea ice extent) (Boucher et al., 2013).

Since aerosols are short-lived components of the atmosphere, when discussing aerosol radiative forcing, we refer to effective radiative forcing. Both terms are widely used, but the term effective radiative forcing is more commonly employed in articles after 2013. In the latest IPCC report (2021), the term RF is used more broadly to refer to the overall impact, while ERF specifically relates to the assessment of aerosols and other components. In this dissertation, when referring to aerosol radiative forcing, we will be considering effective radiative forcing. Furthermore, the next section will discuss direct and indirect RF according to the internationally recognized terminology that is widely used today.

The concept of radiative forcing in terms of changes in the energy balance of the atmosphere, is as follows. The incoming solar radiation flux to the Earth over a day is defined as follows:

$$F_S = \frac{E_S}{4}(1 - A_E) \tag{2.55}$$

where E_s is the solar constant (solar irradiance at the top of the Earth's atmosphere) and A_E is the Earth's surface albedo. The outgoing radiation flux from the Earth can be described by the Stefan-Boltzmann law.

$$F_E = \sigma_{bol} T_E^4, \tag{2.56}$$

where σ_{bol} is the Stefan-Boltzmann constant and T_E is the effective temperature of the Earth's climate system. The total flux at the boundary of the climate system can be described by the following equation.

$$F = F_S - F_E \tag{2.57}$$

In the case of energy equilibrium, $F = 0$. However, if the equilibrium is disturbed, it is possible to estimate the change in the total flux.

$$\Delta F = \Delta F_S - \Delta F_E \tag{2.58}$$

Based on the last equation, we can observe that changes in this flux can be caused by alterations in both the incoming and outgoing radiative fluxes. These changes in the climate system are induced by external factors known as forcing. Consequently, these factors can modify the solar irradiance (solar constant), albedo, and/or effective temperature of the climate system. A positive RF leads to system warming, while a negative RF results in cooling of the system.

Radiative forcing defined at the Earth's surface is referred to as BOA (Bottom of the Atmosphere) at an altitude of approximately 1 km, and at the top boundary of the atmosphere, it is referred to as TOA (Top of the Atmosphere) at an altitude of approximately 100 km. For aerosol-induced RF at the boundary between the upper and lower atmosphere, equation (2.58) takes the following form (Khamala, 2023):

$$\Delta F_{BOA} = \Delta F_{BOA}^a - \Delta F_{BOA}^b \tag{2.59}$$

$$\Delta F_{TOA} = \Delta F_{TOA}^a - \Delta F_{TOA}^b \tag{2.60}$$

Where ΔF^a and ΔF^b represent the net fluxes with and without aerosols, respectively. Since ΔF is the difference between the downward flux $F_\downarrow$ (denoted as F_S for clarity) and the upward flux $F_\uparrow$ (denoted as F_E), the RF at the bottom (ΔF_{BOA}) and top (ΔF_{TOA}) boundaries of the atmosphere can be calculated as follows (Khamala, 2023):

$$\Delta F_{BOA} = (F_{\downarrow,BOA}^a - \Delta F_{\uparrow,BOA}^a) - (F_{\downarrow,BOA}^b - \Delta F_{\uparrow,BOA}^b) \tag{2.61}$$

$$\Delta F_{TOA} = (F^{a}_{\downarrow,TOA} - \Delta F^{a}_{\uparrow,TOA}) - (F^{b}_{\downarrow,TOA} - \Delta F^{b}_{\uparrow,TOA}) \quad (2.62)$$

ΔF is also referred to as Direct Aerosol Radiative Forcing (DARF). Since at the top boundary of the atmosphere $F^{a}_{\downarrow,TOA} = F^{b}_{\downarrow,TOA}$, equation (2.62) can be written as follows (Khamala, 2023):

$$\Delta F_{TOA} = \Delta F^{b}_{\uparrow,TOA} - \Delta F^{a}_{\uparrow,TOA} \quad (2.63)$$

The net atmospheric radiative forcing caused by aerosols represents the amount of solar energy trapped in the atmosphere due to aerosol absorption and is calculated as the difference between the RF at the top boundary ($DARF_{TOA}$) and the bottom boundary ($DARF_{BOA}$) of the atmosphere (Khamala, 2023):

$$DARF_{ATM} = DARF_{TOA} - DARF_{BOA} \quad (2.64)$$

$DARF_{BOA}$ represents the combined effect of aerosol scattering and absorption of solar radiation on the net flux at the surface, $DARF_{TOA}$ accounts for the aerosol-induced reflection of solar radiation back to space, and $DARF_{ATM}$ indicates the absorption of solar radiation in the atmosphere (Khamala, 2023). Aerosol radiative forcing provides valuable information about the energy impact of atmospheric aerosols. However, for a meaningful comparison, the so-called radiative forcing efficiency is applied, which is defined as the ratio of RF to AOD at a wavelength of 500 nm (Garcia et al., 2012) at either the lower or upper boundary of the atmosphere.

$$\Delta F^{eff} = \frac{DARF_{ATM}}{AOD} \quad (2.65)$$

The efficiency of aerosol radiative forcing is evaluated as the change in radiative forcing resulting from a unit change in aerosol concentration in the air. Its value depends on various factors, including the size and chemical composition of aerosols, their distribution in the atmosphere, the amount of solar radiation, and the state of the Earth's surface. Research on aerosol radiative forcing and its efficiency based on observations from the AERONET network was provided by Garcia et al. (2012).

2.5.2 Direct and indirect aerosol radiative forcing

The previous section introduced the concept of direct radiative forcing, which refers to the alterations in atmospheric energy resulting from the interaction between solar radiation and

various constituents of Earth's atmosphere. These alterations are brought about through the scattering and absorption of solar radiation by aerosols and other atmospheric components. Specific aerosols such as mineral dust, organic carbon, sulfate, and nitrate aerosols contribute to negative radiative forcing (see Fig. 2.11).

Black carbon and contrails (white trails in the sky from aircraft, consisting of a mixture of water vapor and fuel combustion products) contribute to positive RF (see Fig. 2.11). In addition to direct RF, there is also indirect radiative forcing. This effect involves the interaction between aerosols and clouds: aerosol particles act as cloud condensation nuclei and ice nuclei (Lohmann & Feichter, 2005). Aerosols can alter cloud droplet size, droplet concentration within the cloud, modify cloud radiative properties, and influence their albedo.

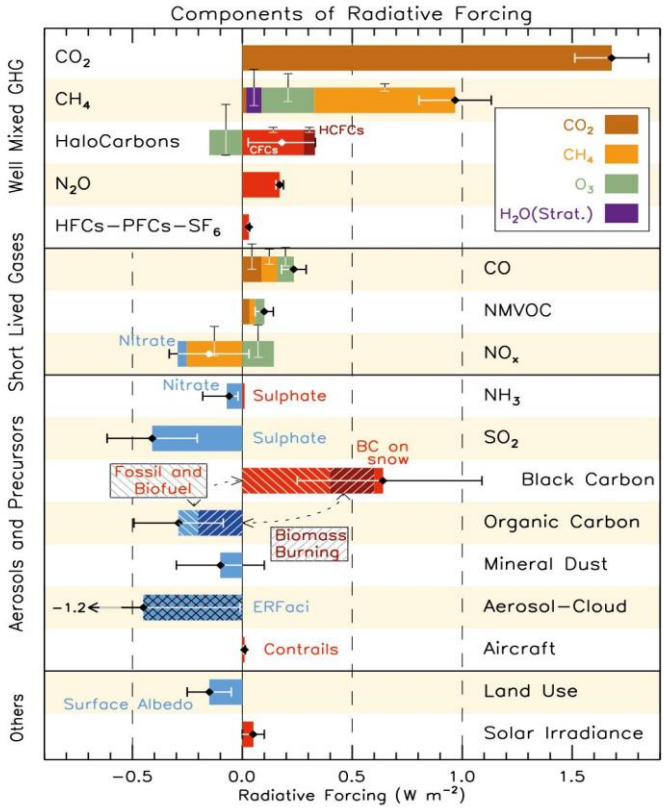

Figure 2.11. Assessment of radiative forcing for various components of the atmosphere, including greenhouse gases and different types of aerosols (Source: IPCC, https://www.ipcc.ch/report/ar5/wg1/anthropogenic-and-natural-radiative-forcing/).

According to IPCC (2014), the interaction between aerosols and clouds exhibits the highest uncertainty, reaching up to 0.5 W m^{-2} (see Fig. 2.11). Figure 2.12 (Boucher et al., 2013) schematically illustrates the impact of aerosols on solar radiation and aerosol-cloud interactions, using both the new and old terminology for comparison. Blue arrows represent

incoming solar radiation. Gray arrows represent the longwave radiation emitted from the Earth's surface, which results from the absorption of incoming shortwave radiation. Radiation from the heated upper layers of the atmosphere, along with a small amount from the Earth's surface, is emitted back into space. The majority of emitted longwave radiation heats the lower layers of the atmosphere. The brown arrow indicates the importance of the connection between the surface and the cloud cover.

In order to clarify the terminology and avoid confusion, we have the following summary: Figure 2.12 links the former terminology of direct, semi-direct, and indirect aerosol effects with the current widely used terminology. The Effective Radiative Forcing of Aerosol-Radiation Interactions (EFR_{ari}) encompasses the radiative effects of anthropogenic aerosols and corresponds to what was previously referred to as direct aerosol radiative forcing (Boucher et al., 2013). Rapid changes induced by the aerosol-induced perturbation of the surface energy balance, atmospheric profile, and cloudiness also contribute to ERF through aerosol-radiation interactions (Boucher et al., 2013). Particles capable of absorbing solar radiation contribute to heating the atmosphere relative to the surface temperature. Such processes involve what was previously known as semi-direct effects. The Effective Radiative Forcing of Aerosol-Cloud Interactions (EFR_{aci}) refers to the instantaneous impact on cloud albedo through changes in cloud condensation and ice nuclei concentrations (also known as the Twomey effect) (Boucher et al., 2013). Changes in cloud lifetime and thermodynamics represent rapid impacts that contribute to ERF from aerosol-cloud interactions (Boucher et al., 2013). EFR_{aci} is a theoretical construct that is challenging to separate from other aerosol-cloud interactions.

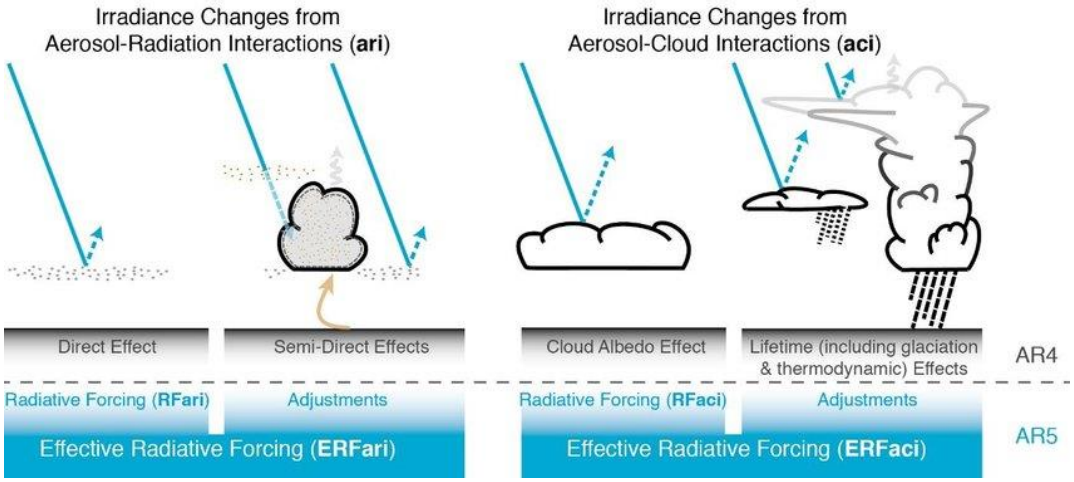

Figure 2.12. Impact of aerosols and aerosol-cloud interactions on solar radiation (Source: Boucher et al., 2013).

Chapter 3

3. INSTRUMENTS AND METHODS

This chapter introduces the tools and methods used for aerosol observations. Ground-based measurements, such as those from the AERONET network, CE 370 lidar, and AirVisual AirPro network, provide precise local data. Satellite-based observations, like MODIS and VIIRS, offer a global perspective, tracking aerosol properties and content on a large scale. Both approaches play a vital role in understanding aerosol behavior, including their sources, transport, and impact on the environment.

Furthermore, the application of modeling techniques enhances the comprehensive analysis of aerosol evolution and its influence across different spatial and temporal scales. The section describes the HYSPLIT air mass transport model and the MERRA-2 reanalysis, enabling assessments of both aerosols and other atmospheric constituents. In this context, the GIOVANNI platform was used to access MERRA-2 data. Additionally, the section references the GRASP algorithm, which is applicable for chemical analyses of aerosols.

3.1. Ground-based Networks and Instruments for Aerosol Research

Ground-based observations of aerosols provide continuous and long-term datasets for a specific area. Such measurements are more accurate compared to satellite-based observations, but they are limited to local scales. In this study, observations from sun photometers of the international AERONET network are used. The CE 370 lidar, provided by Université Lille as a component of the collaborative project between France and Ukraine, played a crucial role in the field campaign from July to September 2015. Additionally, particle counters from the AirVisual AirPro network were used for measurements. This section describes the working principles and placement of the aforementioned tools.

3.1.1. Sun photometers and the AERONET Network

a) Sun photometers

The working principle of a sun photometer is based on the application of the Beer-Lambert-Bouguer law, which involves solving an inverse problem (Dubovik et al., 2002):

$$F(\lambda) = F_0(\lambda)e^{(-\tau(\lambda)m)} \tag{3.1}$$

Where $F(\lambda)$ represents the measured flux at the Earth's surface, $F_0(\lambda)$ is the extraterrestrial solar flux adjusted for the Earth-Sun distance, m is the optical air mass along the measurement path, and $\tau(\lambda)$ denotes the optical thickness in the direction of the sun, which includes contributions from atmospheric molecular components, absorbing gases, and aerosols.

$$F(\lambda) = F_0(\lambda)e^{-(\tau_{mol}m_{mol}+\tau_{gas}m_{gas}+\tau_{aer}m_{aer})} \tag{3.2}$$

Taking into account that certain quantities can be easily calculated from this equation, namely the Rayleigh optical thickness (τ_{mol}) corrected for local pressure and gas absorption (τ_{gas}) the aerosol optical thickness (AOD or τ_{aer}):

$$\tau_{aer} = \frac{[Ln\left(\frac{F_0(\lambda)}{F(\lambda)}\right)-\tau_{mol}m_{mol}-\tau_{gas}m_{gas}]}{m_{aer}} \tag{3.3}$$

The channels used for aerosol research are located in spectral regions with weak absorption by atmospheric gases. To adjust for the low absorption by O_3, NO_2, and other components, effective absorption coefficients for each channel are calculated using filter transmittance curves. This information could be obtained from various sources, including satellites, ground-based measurements, climatological data (Giles et al., 2019).

b) Sun photometer observations in Kyiv

The main characteristic measured by a sun photometer is the spectral irradiance of direct solar radiation at the observation site. This measurement is used to determine aerosol, including the aerosol optical depth for each of the photometer's spectral channels, the Angstrom Exponent for the specified spectral range, and the content of atmospheric condensed water vapor above

the observation site. In this study, measurements from the CIMEL-318 sun photometer (see Fig. 3.1a) are used. Instrument is located at the Main Astronomical Observatory of the National Academy of Sciences of Ukraine, in Golosiiv Forest, on the southern outskirts of Kyiv, approximately 10 km away from the city center (see Fig. 3.1b). The Cimel CE-318-2 is a portable sun photometer with automatic tracking capability. It measures the brightness of the sun and sky in 8 spectral channels in the visible and near-infrared ranges. The CE-318-2 is equipped with filters at 340 nm, 380 nm, 440 nm, 500 nm, 675 nm, 870 nm, and 1020 nm for measuring the optical depth of atmospheric aerosols, as well as a filter at 939 nm for measuring atmospheric water vapor.

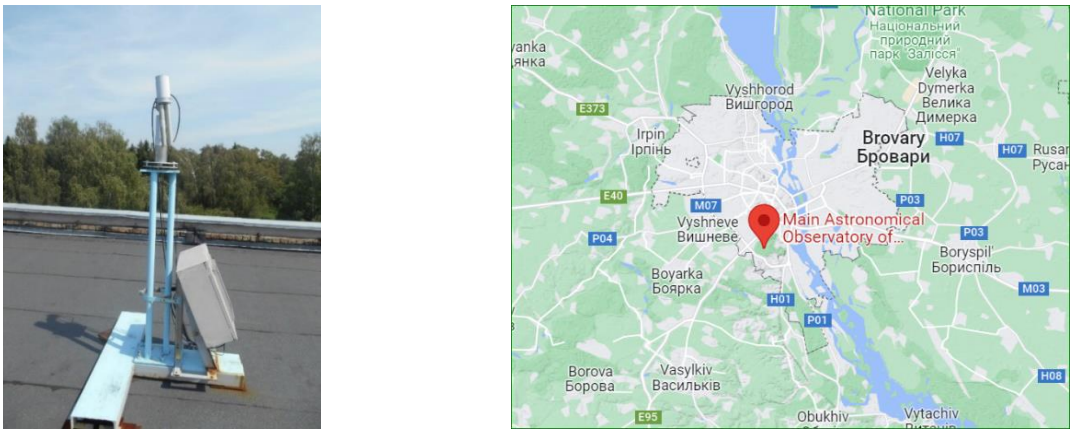

a b

Figure 3.1. a) The sun photometer on the roof of the Main Astronomical Observatory of the National Academy of Sciences of Ukraine and b) its location on the map, Kyiv, Ukraine.

Measurements with the sun photometer are performed every 15 minutes (within the range of sun zenith angles of 75° and less) under the control of a microprocessor using a dedicated program. According to this program, for consecutive time intervals corresponding to specific sun zenith angles, the photometer measures the irradiance of direct solar radiation at the observation site at the specified wavelengths and the sky radiance distribution along the sun almucantar and its height circle, using two optical channels (Dubovik et al., 2002).

c) AERONET network

The International Network of Automated Sun Photometers, AERONET (Aerosol RObotic NETwork), utilizes CIMEL CE318 instruments (www.cimel.fr) and is recognized as

one of the most advanced aerosol remote sensing systems (Holben et al., 1998, 2018, http://aeronet.gsfc.nasa.gov/). The Europe AERONET network is managed by French and Spanish branches of ACTRIS (Aerosols Clouds and TRace gas InfraStructure, https://www.actris.eu/). The instruments within this network enable the retrieval of long-term accurate aerosol properties, which can be utilized for analyzing aerosol variations (Dubovik et al., 2020, 2002, 2006) and studying seasonal dynamics and local aerosol behavior. The accuracy of aerosol optical depth determination is approximately 0.01 at wavelengths above 440 nm and is dependent on the calibration of the sun photometer (Holben et al., 2001). This calibration consists of two components: AOD calibration and sky radiance measurements (Giles et al., 2019, Sinyuk et al., 2020). The AERONET system's software provides three levels of data quality: Level 1.0 (unscreened), Level 1.5 (cloud-screened), and Level 2.0 (highest accuracy). Level 1.0 observations include all measurements. Subsequently, error filtering and cloud correction are applied, resulting in the Level 1.5 dataset.

3.1.2 GRASP

GRASP (Generalized Retrieval of Atmosphere and Surface Properties, Dubovik and King, 2000; Dubovik et al., 2000; 2002a, b; Dubovik et al., 2014; Li et al., 2019) is recognized as the comprehensive algorithm and software package designed for the determination of atmospheric properties based on diverse remote sensing observations. These observations encompass data from satellites, ground-based, and airborne passive and active measurements of atmospheric radiation, as well as their combinations. GRASP builds upon the accumulated experience of improvements in the determination of atmospheric parameters, previously implemented within the AERONET system (Holben et al., 1998). The algorithm recognizes numerous aerosol properties, encompassing particle size distribution, refractive index, and other optical properties.

The retrieval of the aerosol refractive index in the GRASP/Components version of the algorithm (Li et al., 2019) is based on assumptions about the mixing model of different aerosol species. Thus, reconstructing aerosol components requires selecting a mixing approach. The new GRASP/Component version uses mixed aerosol components with redescribed refractive indices (Li et al., 2019). This module relies on the Maxwell-Garnett effective medium approximation, describing the optical features of aerosols consisting of various components

within liquid or solid matrices. It is grounded in the approach by Schuster et al. (2016a, 2009), but assumes independent mixed aerosol components in the fine and coarse modes and directly reconstructs radiance instead of intermediate steps of reconstructing extracted refractive indices (Li et al., 2019). Only one refractive index is utilized for each aerosol type. However, certain components cannot be distinguished from an optical standpoint. Consequently, several elements represented in the mixing model may indeed correspond to distinct aerosol components.

3.1.3 Atmospheric lidars and the EARLINET network

Atmospheric lidars are widely employed for various atmospheric research purposes, including the investigation of atmospheric aerosols. These instruments enable the spatial distribution of particles at different altitudes, their concentration, and even their type to be obtained. Additionally, lidars facilitate measurements of atmospheric profiles during both daytime and nighttime.

a) Lidar Technologies for Atmospheric Research

In its simplest form, the equation that describes lidar observations can be written as follows:

$$P(R) = KG(R)\beta(R)T(R) + P_{bg} \tag{3.4}$$

Where $P(R)$ is the received intensity at distance R measured by the detection module, K is the coefficient describing the instrument efficiency of the lidar, $G(R)$ is the coefficient describing the geometry of the observations (dependent on the relative orientation of the laser beam and the field of view of the lidar telescope), $\beta(R)$ is the backscatter coefficient, $T(R)$ is the atmospheric transmittance coefficient, and P_{bg} is the background intensity measured by the detection module. The coefficients K and $G(R)$ depend on the design of the lidar system and serve as calibration parameters, while $\beta(R)$ and $T(R)$ need to be determined from observations.

The measured signal $P(R)$ always includes the background radiation P_{bg}, which consists of the scattering of solar and terrestrial radiation by molecules and particles that enter the field

of view of the lidar. This background signal is independent of height and can be easily determined from observations. The averaged value of the measured signal from a very distant height range, where no backscattering of lidar radiation from particles and molecules is expected, represents the background value.

The instrumental coefficient *K* can be expressed in the following form:

$$K = P_0 \frac{c\tau}{2} A\eta \tag{3.5}$$

Where P_0 is the power of the laser beam, τ is the pulse duration, $\frac{c\tau}{2}$ is the height of the volume of the medium from which the backscattering is detected at a specific moment in time, *A* is the area of the telescope's entrance aperture, and η is the efficiency coefficient of the system, which includes the efficiency of the light beam passing through all optical systems of the lidar and the detection efficiency of the detectors. The geometric coefficient *G(R)* is related to the overlap function and the distance from the telescope R^2:

$$G(R) = \frac{O(R)}{R^2} \tag{3.6}$$

The overlap function *O(R)* is a characteristic of the laser beam divergence and the field of view of the telescope. It increases from zero near the telescope to unity at the distance of full overlap between the laser beam and the telescope's field of view, including all its optical components. The quadratic decrease of the intensity of the backscattered light with R^{-2} is related to the fact that the telescope's aperture is part of the surface area of a sphere with radius *R* within which the scattering occurs. The backscattering coefficient $\beta(R)$ is an atmospheric parameter that determines the intensity of light scattered back in the reverse direction by particles and molecules in the atmosphere. This coefficient depends on the type and size of particles as well as the wavelength of the emitted light. It can be expressed in terms of particle concentration $N_j(R)$ (where *j* represents the particle or molecule type) and their differential scattering cross-section ($\frac{d\sigma_j^{sca,ca}(\pi,\lambda)}{d\Omega}$, where $\sigma_j^{sca,ca}$ is the scattering cross-section, and Ω is the solid angle, for backward scattering at wavelength λ.

$$\beta(R,\lambda) = \sum N_j(R) \frac{d\sigma_j^{sca,ca}(\pi,\lambda)}{d\Omega} \tag{3.7}$$

Since the backscattering coefficient β depends on the type of particles, it is advantageous to separate it into molecular and aerosol components: $\beta = \beta_{mol} + \beta_{aer}$. The molecular component of the backscattering coefficient can be accurately determined using meteorological

data and a standard atmospheric model (Krueger et al., 1976). The atmospheric transmittance coefficient describes the energy losses of the laser beam of light along the path to the atmospheric volume at a distance *R* from the lidar and back to the telescope.

$$T(R,\lambda) = \exp[-2\int \sigma^{exp}(R,\lambda)dr] \tag{3.8}$$

This coefficient is derived from the Lambert-Beer-Bouguer law for lidars (Weitkamp, 2006). The integral includes the distance R from the lidar to the point of backscattering, and the factor of 2 arises because the light beam travels this distance twice, from the telescope to the scattering location and back to the telescope. The extinction coefficient σ^{ext} can be represented in a similar form to the backscatter coefficient.

$$\sigma^{exp}(R,\lambda) = \sum N_j(R)\sigma_j^{sca,ca}(\lambda) \tag{3.9}$$

This coefficient includes terms that account for the scattering and absorption of light by molecules and aerosols in the Earth's atmosphere.

$$\sigma^{exp} = \sigma_{mol}^{abs} + \sigma_{mol}^{sca} + \sigma_{aer}^{abs} + \sigma_{aer}^{abs} \tag{3.10}$$

The wavelengths in lidars are chosen to minimize molecular absorption. Molecular scattering can be determined using the standard atmospheric model (Krueger et al., 1976). The coefficients of aerosol absorption and scattering, which contribute to aerosol extinction, are unknown and are determined through observations. Taking into account the above, the lidar equation can be expressed as follows:

$$P(R,\lambda) = P_o \frac{c\Delta\tau}{2} A\eta \frac{O(R)}{R^2}\beta(R,\lambda)\exp[-2\int \sigma^{exp}(R,\lambda)dr] \tag{3.11}$$

This equation includes two unknown parameters: the aerosol extinction coefficient $\sigma^{exp}(R,\lambda)$ and the aerosol backscatter coefficient $\beta(R,\lambda)$. The atmospheric parameters on which the extinction and backscatter coefficients depend can be determined from a standard atmospheric model or neglected under certain conditions (for example, if the wavelength of the laser radiation is chosen such that there is no absorption by atmospheric molecules). Therefore, an analytical solution to this equation cannot be found. However, as proposed by James Klett (Klett 1981, 1985, Mortier et al., 2013), it can be solved under the assumption of a relationship between the extinction and backscatter coefficients of aerosols (the Klett method). The ratio of the extinction coefficients to the backscatter coefficients is referred to as the lidar ratio, and the equation can be written in the following form:

$$LR_{aer}(R,\lambda) = \frac{\sigma_{aer}(R,\lambda)}{\beta_{aer}(R,\lambda)} \quad (3.12)$$

In general, the lidar ratio varies with altitude because the extinction and backscatter coefficients depend on the type, size, and shape of particles, which change with altitude. In the Klett method, the lidar ratio is assumed to be constant with altitude, and then equation (eq. 3.12) can be solved iteratively for the backscatter coefficient. Assuming a constant lidar ratio at all altitudes increases the error in determining the profiles of extinction and backscatter. Additional observations (such as sun photometer) and/or additional constraints are necessary to reduce the errors in determining the aerosol extinction profile. The sun photometers of the international AERONET network measure the spectral optical thickness of aerosols in the atmospheric column above the observation site. These observations serve as additional information alongside lidar measurements if they are performed simultaneously at the same observation site.

For the analysis of similar simultaneous observations from a sun photometer and a lidar, the GARRLiC algorithm (Generalized Aerosol Retrieval from Radiometer and LIDAR Combined data) can be utilized (Lopatin et al., 2013). This algorithm is part of a more comprehensive inversion code called GRASP (Generalized Retrieval of Atmosphere and Surface Properties) (Dubovik et al., 2011, 2000), which can be accessed at https://www.grasp-sas.com/. The development of this algorithm took place at the Laboratoire d'Optique Atmosphérique (LOA, CNRS/Lille1) (Bovchaliuk et al., 2016, Lopatin 2013, Lopatin et al., 2013).

b) The EARLINET network

The European Aerosol Research Lidar Network (EARLINET) is an aerosol research network that was established in 2000 as a research project. Its objective is to create a comprehensive and statistically significant database on the horizontal, vertical, and temporal distribution of aerosols on a continental scale. Since then, EARLINET has been providing the largest amount of ground-based data on the distribution of aerosol particles in the atmosphere over Europe (source: https://www.earlinet.org/index.php?id=earlinet_homepage). Currently, there are 31 operational stations of the network in Europe. Most stations use multi-wavelength high-power lidars for their observations.

EARLINET measurements must adhere to stringent standards of stability and accuracy. To ensure this, the network has developed a rigorous quality assurance program that covers both instrument performance and algorithm evaluation (to ensure instrument standardization, coordinated lidar retrieval within the network, and standardized data exchange format). The main part of the measurements follows a fixed schedule to obtain an objective and statistically significant dataset. Additional measurements are specifically provided for important processes localized in space or time. Backward trajectories obtained from weather forecasting models are utilized to characterize the observed air masses, taking into account the vertical distribution of aerosol particles (https://www.earlinet.org/index.php?id=earlinet_homepage).

The EARLINET network is a key component of the ACTRIS infrastructure, which represents a significant step towards improved coordination of atmospheric observations in Europe and the establishment of a European component of the Integrated Global Atmospheric System as part of GEOSS (Global Earth Observation System of Systems, GEOSS, 2005). The EARLINET project is also a participant in the Global Atmosphere Watch Programme (GAW).

c) automatic lidar CIMEL CE370

The CIMEL CE370 lidar was used in this study, which is capable of monitoring aerosols and clouds up to the tropopause height 24 hours a day, 7 days a week (see Fig. 3.2). It features a large aperture (200 mm diameter) that enables measurements at high altitudes and includes a second receiving channel to extend measurements at low altitudes (starting from 50 m), while ensuring compliance with eye safety regulations. The CE370 consists of a control unit (housing the laser and receiver) connected to the main optical system using a Galilean configuration.

The CE370 lidar can be used for the following purposes (source: https://www.cimel.fr/: measurement of volcanic ash content, measurement of sand content from dust storms, air quality monitoring and forecasting, climate change studies, investigation of airport flight operations, atmospheric research in the scientific field, modeling of aerosols and cloudiness, numerical weather forecasting.

Furthermore, it provides the following features:

• High measurement performance: detection of aerosols up to the low stratosphere (above 18 km, during nighttime), direct measurement of reference optical properties, very short blind zone (<100 m), automatic extinction calibration.

• Wide range of applications and flexible implementation (compliance with eye safety regulations, automatic system, easy transportation)

• Vertical resolution of 15 m.

Figure 3.2. Installation of the CIMEL CE370 lidar at the Main Astronomical Observatory in Kyiv. The photo shows the installation being carried out by Head of the Space Physics Research Laboratory Prof. Gennadi Milinevsky

Lidar observations are processed using the BASIC code, which allows for the retrieval of the extinction profile and lidar ratio from combined lidar observations and AOD measurements. This code was developed by Augustin Mortier and Philippe Goloub at the Laboratoire d'Optique Atmosphérique (https://www.icare.univ-lille.fr/basic/, Mortier et al., 2013; Mortier, 2013). There are currently two inversion modes available. In one mode, the algorithm utilizes both the lidar profile and AOD measurements, leveraging information present in both datasets. In the other mode, the algorithm can also operate, even if only the lidar profile is available, provided certain assumptions about the lidar ratio over the time range are made.

3.1.4 Laser particle counters and AirVisual network

a) AirVisual Pro

The AirVisual Pro device is an air quality monitor that operates on the principle of advanced laser technology for aerosol particle identification, providing highly accurate

measurements of $PM_{2.5}$ particle concentration. Each AirVisual Pro device is equipped with a SenseAir S8 mini-NDIR sensor, which measures CO_2 levels in the range of 400 to 10,000 ppm, a specially designed optical aerosol concentration sensor (AVPM25b) that measures PM_1, $PM_{2.5}$, and PM_{10} concentrations in the range of 0 to 2000 µg m^{-3}, as well as temperature sensors ranging from –10 to +40°C and humidity sensors from 0 to 100%.

Data can be downloaded directly from the device, the website, or using a dedicated smartphone application. Additionally, the website and app automatically generate a measurement history that is updated hourly, provide short-term pollution forecasts, and list the most polluted cities worldwide. Moreover, the website offers useful tips and recommendations for protecting against air pollution and improving air quality in both private and public sectors. The website serves as an important tool for understanding the impact of air pollution on human health and the environment as a whole.

b) AirVisual Network in Kyiv

The AirVisual network is employed for monitoring air quality and encompasses a broad spectrum of sensors situated worldwide. These sensors routinely measure pollution levels such as $PM_{2.5}$, PM_{10}, and other harmful substances, allowing for the creation of fairly accurate depictions of air conditions in various regions. The AirVisual is owned by IQAir, a company specializing in air quality control technologies (https://www.iqair.com/).

The four stations of the AirVisual network were installed in early March 2020 in Kyiv and the fifth station was placed in the western part of the city in June 2020 (Zhang et al., 2022). The four stations of the AirVisual network, whose data were used in this study, are distributed throughout Kyiv to cover as much of the urban area as possible. All sensors are installed in specially designed and constructed meteorological shelters, which protect the sensors from direct sunlight and precipitation. The locations of the five AirVisual stations and the Popudrenka station (APDA-371 HORIBA) on the map of Kyiv city are shown in Figure 3.3.

The Artema Street station is located in the city center, approximately 2.3 km from the geographical center of Kyiv. The sensor is installed at a height of 10 m above ground level and is situated 70 m away from the busy Sichovykh Striltsiv Street (now Artema Street) with heavy traffic. There is a small park with trees up to 5 m tall between the road and the sensor.

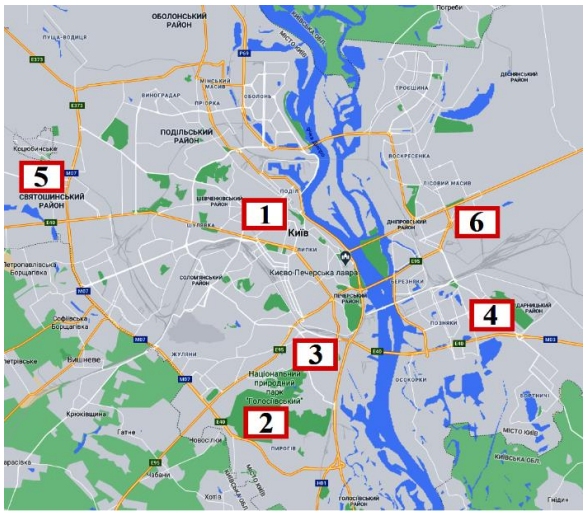

Figure 3.3. Locations of the five AirVisual stations and the Popudrenka station (APDA-371 HORIBA) on the map of Kyiv: 1 – Artema Street, 2 – Golosiiv, 3 – Nauky Avenue, 4 – Trostyanetska, 5 – Chornobylska Street, 6 – Popudrenka.

The Golosiiv station is situated within the territory of the Main Astronomical Observatory of the National Academy of Sciences of Ukraine, which is located in the "Holosiivskyi" National Park, approximately 9.7 km south of the center of Kyiv. This area is considered one of the cleanest in terms of air quality in Kyiv. Therefore, this station can be considered as a reference point.

The Nauky Avenue station is located 6.5 km south of the center of Kyiv at the intersection of the quiet Lysogirska Street and the moderately busy Nauky Avenue, at a height of 15 m. The sensor itself is positioned one meter away from the building's wall.

The Trostyanetska station is situated 10 km southeast of the center of Kyiv in the Darnytskyi district. It is surrounded by heavily trafficked roads on four sides: 300 meters northeast is the Kharkiv Highway, and 1.3 km south is the Bazhana Avenue. The "Enerhiya" waste incineration plant is located 2.7 km to the south. The nearest green area, Park Partyzanskoi Slavy, is located 600 m to the northeast.

The Chornobylska Street station is positioned at a height of 30 m on the western outskirts of the city, 12.7 km from the city center and 600 m from Palladina Avenue with heavy vehicular traffic.

The parameters of air quality status according to the AQI index include the concentration of $PM_{2.5}$ particles, air temperature, wind direction and speed, relative humidity, and the current concentration of carbon dioxide (CO_2). Additionally, the forecast for these

parameters for the upcoming week, including cloudiness and the possibility of precipitation, is provided. Each resident of Kyiv can access this information online from their smartphone for each station (corresponding to their district) through links such as https://www.airvisual.com/invitation/T8nZek2N2. By following this link, users can download the iQAir AirVisual application and gain access to data from our AirVisual network.

The Popudrenka station, which meets the requirements for $PM_{2.5}$ and PM_{10} determination methods according to the Resolution of the Cabinet of Ministers of Ukraine dated August 14, 2019, No. 827, EU Directive 2008/50/EC, and the standards of the US Environmental Protection Agency (EPA), belongs to the State Institution "O.M. Marzeev National Academy of Medical Sciences of Ukraine". It is located 8 km east of the center of Kyiv in the Desnianskyi district (50.4593N, 30.6337E). The sampling location meets the requirements for representativeness, where the sensor is placed away from local sources of pollution and is free from aerodynamic turbulence (Turos et al., 2019).

Mass concentrations of $PM_{2.5}$ and PM_{10} are measured in situ using the HORIBA APDA-371 (Air Pollution Dust Analyzer), which consists of a detector, pump, and sampling probe (https://www.environmental-expert.com/products/horiba-model-apda-371-ambient-dust-monitor-151228). The HORIBA APDA-371 model has been recognized by the United States Environmental Protection Agency (EPA) as a Federal Equivalent Method for continuous monitoring of PM_{10} particulate matter. Additionally, the APDA-371 is the world's first instrument to receive EPA recognition for continuous monitoring of $PM_{2.5}$ when configured with the appropriate accessories. The measurement principle is approved in accordance with European Union standards and EPA regulations.

3.2 Satellite methodology for aerosol research

Both satellite and ground-based methods are utilized for the study of aerosols. The advantage of satellite observations is their ability to track atmospheric changes on a global scale, including aerosol dynamics and content. The high spatial and temporal resolution of remote sensing satellites is crucial for most atmospheric research. Information derived from such aerosol observations, such as spatial and vertical distribution, temporal variations, fine and coarse aerosol fractions, light absorption, and certain spectral characteristics, can be used to determine the sources of major aerosol emissions, aerosol transport, and the interaction between

aerosols and energy and water cycles. Since the late 1970s, a series of space missions with instruments capable of observing backscattered solar radiation at the upper boundary of the atmosphere have been launched (Verma et al., 2018). This section describes the role of satellite methods in the study of aerosols, specifically focusing on MODIS and VIIRS.

3.2.1. MODIS

MODIS (Moderate Resolution Imaging Spectroradiometer) is a key instrument on board the Terra (formerly known as EOS AM-1) and Aqua (formerly known as EOS PM-1) satellites. The Terra satellite orbits the Earth from north to south across the equator in the morning, while Aqua passes from south to north over the equator in the afternoon (https://modis.gsfc.nasa.gov/about). Terra MODIS and Aqua MODIS observe the entire Earth's surface every 1 to 2 days, collecting data in 36 spectral bands or wavelength groups. The instrument has a swath width of 2330 km, and it captures Earth's radiance in the range of 0.405 to 14.385 μm in 36 spectral bands or wavelength groups. It acquires data at three spatial resolutions: 250, 500, and 1000 meters.

Using physical and empirical algorithms, high-speed computers process MODIS data to derive 44 global data products ranging from surface temperature of land and ocean to physical properties of clouds. Each MODIS instrument has a designed lifespan of five years. These data enhance our understanding of global dynamics and processes occurring on land, in oceans, and in the lower atmosphere. MODIS plays a crucial role in the development of validated global interactive models of the Earth system, capable of predicting global changes with sufficient accuracy to assist policymakers in making informed decisions regarding environmental protection.

3.2.2. VIIRS

The Visible Infrared Imaging Radiometer Suite (VIIRS) observes and collects global satellite data in the visible and infrared ranges over land, ocean, and atmosphere. The instrument is onboarding the joint NASA/NOAA Suomi National Polar-Orbiting Partnership (Suomi NPP) satellite and NOAA-20. VIIRS Corrected Reflectance Imagery is generated nearly in real-time,

ensuring continuity with MODIS Corrected Reflectance imagery (https://www.earthdata.nasa.gov/learn/find-data/near-real-time/viirs). VIIRS has a spectral coverage ranging from 412 nm to 12 μm in 22 bands, providing nadir imagery with a resolution of ~375 m in 5 bands and radiometric data with a moderate resolution of ~750 m (https://www.ospo.noaa.gov/Products/Suites/satellite_instruments.html).

With the instrument, it is possible to obtain infrared images of hurricanes, detect fires, smoke, and aerosols, monitor land, ocean, and ice temperatures. Additionally, VIIRS products have various other applications (https://www.nesdis.noaa.gov/current-satellite-missions/currently-flying/joint-polar-satellite-system/visible-infrared-imaging).

3.3. Modeling the spatial distribution of aerosols

Predicting atmospheric aerosol is an important area of research for various fields, including climate modeling, to better understand climate changes. Aerosols have been found to not only impact climate but also influence weather patterns and precipitation. Based on measurements, global models can be created to localize and track major aerosol types, as shown in Figure 3.4. Different colors indicate different particle types: mineral dust (red), sea salt (blue), smoke (green), and sulfate particles (white).

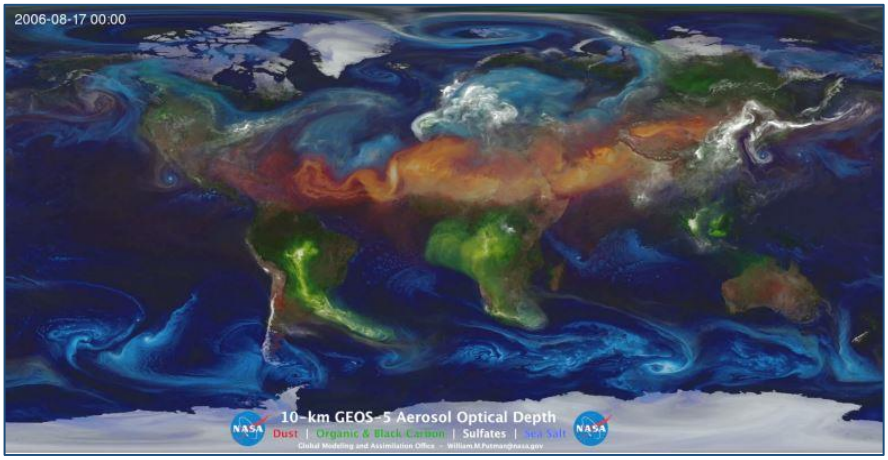

Figure 3.4. A map of global aerosols created using GEOS-5 modeling with a resolution of 10 kilometers. Mineral dust (red color) is lifted from the surface, sea salt (blue color) circulates within cyclones, smoke (green color) rises from fires, and sulfate particles (white color) emanate from volcanoes and fossil fuel emissions. (Source: https://www.nasa.gov/multimedia/imagegallery/image_feature_2393.html).

Major sources of mineral dust are located in desert regions, while sea salt enters the atmosphere from the oceans. Smoke particles originate from biomass burning and forest fires, while SO_x compounds are released from volcanic eruptions and industrial emissions. Figure 3.6 was generated using the Goddard Earth Observing System version 5 (GEOS-5), which is capable of simulating global weather with a resolution ranging from 10 to 3.5 kilometers (source: https://www.nasa.gov/multimedia/imagegallery/image_feature_2393.html). The modeling of aerosols plays a crucial role not only in their global-scale study but also at the local level. This section describes the application of the MERRA-2 reanalysis and the calculation of air mass movement using HYSPLIT. Additionally, the section mentions the scientific platform GIOVANNI, which facilitates access to scientific data.

3.3.1 HYSPLIT

HYSPLIT (Hybrid Single Particle Lagrangian Integrated Trajectory Model) is a model that simulates the dispersion and trajectory of substances transported and dispersed through our atmosphere, ranging from local to global scales (https://www.arl.noaa.gov/hysplit/, Stein et al., 2015). This model can be applied to calculate the transport of air masses to or from a specific area. It allows both forecasting and utilizing an existing database for calculating archival trajectories. HYSPLIT was developed by the Air Resources Laboratory (ARL) of the National Oceanic and Atmospheric Administration (NOAA).

The computational method of the model is a hybrid between the Lagrangian approach and the Eulerian methodology. The former uses a moving reference frame for advection and diffusion calculations as trajectories or air parcels move from their initial positions. The latter employs a fixed three-dimensional grid as the reference frame for calculating the concentration of pollutants in the air. This model can be run in an interactive mode online through the ARL READY system or downloaded as a program for Windows or Mac PCs. The web version has been configured with some limitations to avoid computational overload on the ARL web server. The registered PC version has no computational restrictions, except that users need to obtain their own meteorological data files.

In this study, the web version of HYSPLIT was used with the GDAS (Global Data Assimilation System) meteorological dataset. GDAS is a system that uses the Global Forecast System (GFS) model to assimilate observations into a gridded model space for weather

forecasting initialization. GDAS incorporates various types of observations into the three-dimensional gridded model space, including surface observations, radiosonde data, wind profiler data, aircraft information, buoy observations, radar data, and satellite observations.

3.3.2 GIOVANNI

GIOVANNI is a web application owned by the NASA Goddard Earth Science Data and Information Services Center (GES DISC) Distributed Active Archive Center (DISC). It serves as a valuable tool for researchers, offering accessible to users interface to visualize, analyze, and access remote sensing data, including satellite data, without the requirement of data download (https://www.earthdata.nasa.gov/). This platform greatly simplifies the exploration and utilization of Earth science data, facilitating the efficient extraction of valuable insights for scientific investigations. Furthermore, the Earth Science Data Systems (ESDS) program plays a significant role in ensuring comprehensive and unrestricted access to NASA's extensive Earth science data collection.

3.3.3 MERRA-2

The Modern-Era Retrospective analysis for Research and Applications, Version 2 (MERRA-2), is an updated dataset that extends back to 1980, replacing the original MERRA dataset. The development of MERRA-2 was necessitated by advancements in the assimilation system, enabling the integration of modern hyperspectral radiance, microwave observations, and GPS-Radio Occultation datasets (https://gmao.gsfc.nasa.gov/reanalysis/MERRA-2/). Notably, MERRA-2 incorporates NASA's ozone profile observations, which were initiated in late 2004. Moreover, MERRA-2 introduces further enhancements in the GEOS model and the GSI assimilation system, enhancing the accuracy and quality of the reanalysis.

In terms of spatial resolution, MERRA-2 maintains a similar scale to its predecessor, with an approximate resolution of 50 km in the latitudinal direction. This resolution provides valuable insights into atmospheric processes and allows for the investigation of large-scale phenomena and their regional variations. Researchers can leverage the MERRA-2 dataset to

study long-term climate patterns, atmospheric dynamics, and other Earth system phenomena with improved precision and comprehensive data coverage.

Chapter 4

4. CHANGES IN AEROSOL CHARACTERISTICS DURING EVENTS OF WILDFIRES

In this chapter, the research results on the properties of aerosol particles during the autumn 2015 and spring 2020 peat and forest fires events are presented.

4.1 Lidar Campaign in Kyiv and Wildfires in Autumn 2015

This section presents the results of the analysis of optical and microphysical properties of aerosol particles and their distribution in the atmosphere over Kyiv during the lidar campaign from July to September 2015, as well as during the atmospheric pollution caused by forest and peatland fires in early September 2015. The observations were performed using the CIMEL370 lidar provided by the Laboratoire d'Optique Atmosphérique of the University of Lille and the sun photometer of the AERONET station located on the rooftop of the Main Astronomical Observatory of the National Academy of Sciences of Ukraine in Kyiv.

4.1.1 Vegetation Cover of Ukraine and Its Impact on Biomass Burning Products

Despite a significant portion of Ukraine's primary vegetation cover being cleared for agricultural use, three main zones of natural vegetation are still distinguished: the mixed forest zone (forest-swampy), the forest-steppe zone, and the steppe zone (see Fig. 4.1). In the northwestern and northern regions, the zone of mixed forests is located. Over 1/3 of this area is occupied by arable land, and nearly 1/4 is covered by mixed forests consisting of tree species such as oak, ash, birch, hornbeam, ash-leaved maple, pine, linden, alder, poplar, willow, and beech. Peatlands and marshes account for less than 5 percent of the total area (source:

Britannica.com). The forest-steppe zone is located beyond the zone of mixed forests. It consists of agricultural lands (2/3 of the region's territory) and forests, but it occupies only about 1/8 of Ukraine's territory. Further south is the steppe zone. Many flat and forestless plains in this region are also cultivated. Natural reserves not only protect diverse fauna but also preserve the natural steppe vegetation, such as feather grass and steppe grass (source: Britannica.com, Encyclopedia Britannica, established in 1768 in Edinburgh, Scotland, remains a trusted English-language encyclopedia, upheld by expert contributors, rigorous fact-checking, and regular updates, now headquartered in Chicago with global contributors). Additionally, various species of grasses and shrubs grow in the steppe zone.

Figure 4.1. Natural vegetation zones of Ukraine (Source: Müller et al., 2016).

It is important to note that the vegetation in Ukraine also varies depending on the season. March and April are periods when the snow cover typically melts, and new greenery begins to grow and bloom. Therefore, the main components of the vegetation cover consist of last year's leaves, grasses, and shrubs. With increasing temperature and sunny days, this vegetation dries up and becomes highly flammable. In August and September, trees start to lose their leaves, and grasses and shrubs wither and dry up. When this coincides with a dry and sunny weather period, it leads to an increased risk of wildfires and forest fires. Moreover, a significant number of fires during these two periods are related to the outdated approach of some farmers to the disposal of fallen leaves and agricultural waste, as well as vandalism associated with burning dry grass in the fields. The differences associated with the influence of different property types were analyzed in Shi et al. (2019) and are shown in Figure 4.2.

During biomass burning, various substances are released into the air, including black carbon, which is a major component of soot. According to Shi et al. (2019), the amount of BC emissions is higher when burning grass and shrub biomass (almost 4%) compared to burning

forests and peat (approximately 1%) within the first 24 hours of formation (see Fig. 4.2). Over time, this concentration degrades (see Fig. 4.2, 72 hours after formation). In this case, the single scattering albedo for shrubs and bushes is lower and ranges within 0.85 at a wavelength of 440 nm. A different situation is observed for the combustion products of forests and peat, where the SSA (at 440 nm) is approximately 0.95. The magnitude of SSA may increase over time (see Fig. 4.2, 72 hours after formation).

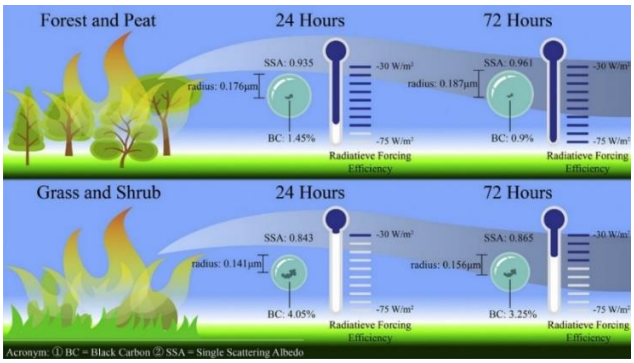

Figure 4.2. Temporal evolution of aerosol properties at a wavelength of 440 nm from biomass burning for different vegetation types (forest and peat, grass and shrub). Source: Shi et al., 2019 (Graphical Abstract).

Additionally, as seen in Figure 4.2 the sizes of aerosol particles differ, with smaller sizes observed for grass and shrub burning, which influences the radiative forcing efficiency. For forest and peat burning, the radiative forcing contribution ranges from –35 W m^{-2} to –75 W m^{-2}, whereas for grass and shrub burning, it is smaller, ranging from –35 W m^{-2} to –45 W m^{-2}. Both characteristics, particle size and radiative forcing efficiency, increase over time, as indicated by the results at 24 and 72 hours after particle formation shown in Figure 4.2 (Shi et al., 2019).

4.1.2 Wildfires in forests and peatlands near Kyiv in autumn 2015

During September 1–6, 2015, significant atmospheric haze was observed in the city of Kyiv (see Fig. 4.3a). On the morning of September 3, it was difficult to breathe, and classes in schools and kindergartens were canceled. The haze was caused by spontaneous forest fires near Kyiv, as well as the transport of air masses from northwestern regions of Ukraine (see Fig. 4.3b, Fig. 4.4), where a considerable number of forest and peatland fires were also occurring (see Fig. 4.3b, Fig. 4.5).

According to the State Emergency Service of Ukraine, the forest fire near the villages of Koblytsia and Velykyi Lis (located in the north-northwest direction from Kyiv) lasted from September 1 to 4, 2015, and affected an area of 24 hectares. From September 2 to 4, there was a fire in the territory of the Bilodubravne Forestry of the Darnytske Forest and Park Management (in the northeast part of Kyiv), covering an area of 32 hectares.

a b

Figure 4.3. a) Haze in Kyiv on September 3, 2015, and b) MODIS satellite image: red dots indicate fires, and the blue circle indicates Kyiv.

Based on the backward trajectories of air masses (see Fig. 4.4), the map of forest fires (see Fig. 4.5), and information from the State Emergency Service, a preliminary conclusion can be drawn that during the initial period of intense fires (September 1–2), the haze was observed to a minor extent (not visible to the naked eye) due to the inflow of northwestern air masses. However, on September 3, the haze was caused by peat fires near the villages of Koblytsia and Velykyi Lis and was visible to the naked eye (see Fig. 4.3a). As the intensity of fires near Kyiv decreased, the haze in the city also diminished.

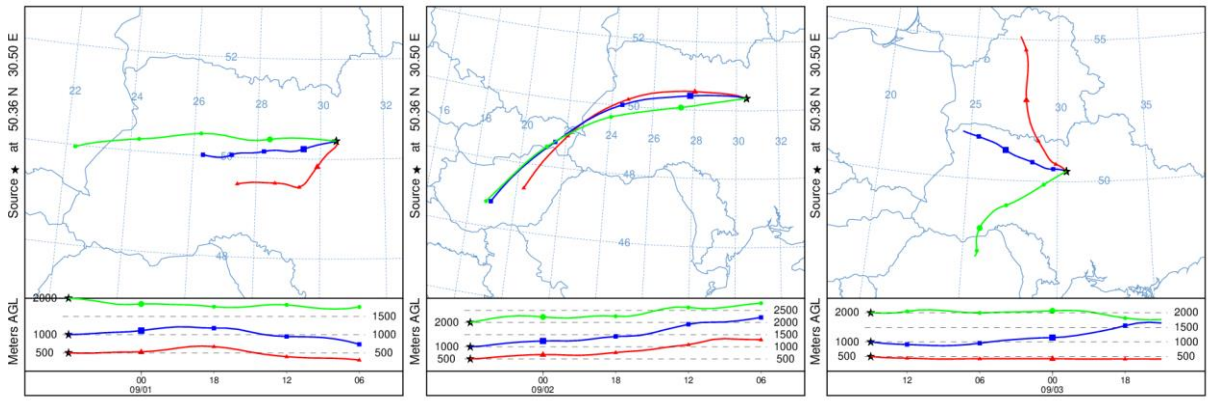

a b c

Figure 4.4. Backward trajectories of air masses: a) September 1, 06:00 UT; b) September 2, 06:00 UT; c) September 3, 15:00 UT. The scale at the bottom indicates the horizontal displacement of air masses and the time of travel.

According to the map of fires recorded in Ukraine from September 1 to 3, 2015 (see Fig. 4.5) by the VIIRS instrument, the majority of thermal anomalies were detected in the northern and northwestern regions (north of Zhytomyr, Kyiv, and Volyn oblasts).

Figure 4.5. Fires (red dots) detected during September 1–3, 2015 by the VIIRS instrument (source: https://firms.modaps.eosdis.nasa.gov/map/).

Since on September 1 and 2, the backward trajectories (see Fig. 4.4) did not directly pass through these regions, significant atmospheric smoke was not observed. However, on the following day, September 3, the trajectories at altitudes of 500 and 1000 meters (see Fig. 4.4c, red and blue trajectories) directly passed through the fire-affected regions, facilitating the transport of aerosol particles to Kyiv and causing the city's haze. The backward trajectories were calculated using the online version of the HYSPLIT model (Draxler & Hess, 1998, Stein et al., 2015; Stohl, 1998; https://aeronet.gsfc.nasa.gov/cgi-bin/bamgomas_interactive). Consequently, the smoke event can be divided into three periods:

1) September 1–2: Typical atmospheric conditions for Kyiv with particles from combustion products, possibly transported from the northwestern regions of Ukraine (Yatskiv & Milinevsky, 2015). Average aerosol pollution during the day: Aerosol Optical Depth at a wavelength of 440 nm was approximately 0.4; Angstrom Exponent for the wavelength pair 440–870 nm was around 1.8.

2) September 3: High-level aerosol pollution event (wildfire near Kyiv). Average aerosol pollution during the day: AOD at 440 nm was approximately 0.8; AE was around 1.8. After September 3, the first simultaneous observations of the lidar and sun photometer were conducted.

3) September 7: Atmosphere with low aerosol pollution levels (after rain): AOD at 440 nm was approximately 0.1; AE at 440–870 nm was around 1.6. In this case, AERONET measurements are not analyzed due to the low AOD values, as aerosol properties are poorly reproduced under such low AOD conditions (Dubovik et al., 2011; Dubovik & King, 2000).

4.1.3 AERONET observations in Kyiv

a) Aerosol Optical Depth, Ångström Exponent and Single Scattering Albedo

Based on measurements from the AERONET station in Kyiv, aerosol characteristics can be studied throughout the year, specific months, or days. Figure 4.6 illustrates the variation in AOD at a wavelength of 500 nm and the Ångström Exponent (440–870 nm) from August 25 to September 15, 2015. The graph presents daily averaged data. It is clear from the graph that on September 3, the AOD reaches a value of 0.75, which is the highest observed value during the given period and generally for Kyiv, where the climatological value AOD for August is 0.225 and for September is 0.19. As for the Ångström Exponent, its value shows significant variability, and on September 3, it decreases compared to previous days.

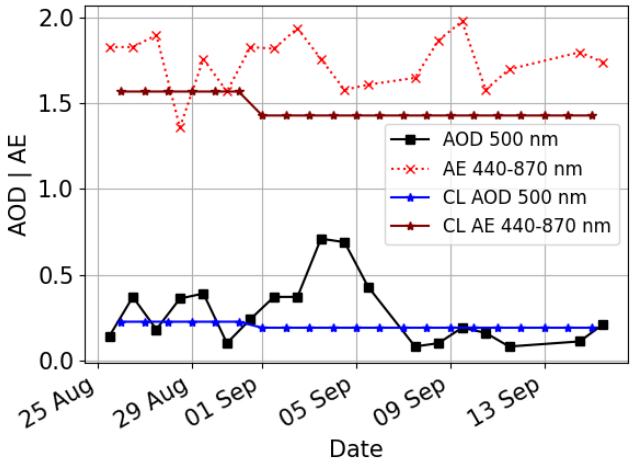

Figure 4.6. Daily variations in Aerosol Optical Depth (AOD) and Climatological Aerosol Optical Depth (CL AOD) at 500 nm, Ångström Exponent (AE) and Climatological Ångström Exponent (CL AE) at 440-870 nm based on the sun photometer observations from AERONET Kyiv, 2015.

Between September 4 and 8, rainfall occurred, resulting in some gaps in the AERONET measurements during certain time intervals. The climatological values of AE (440–870) for August and September are 1.57 and 1.43 respectively (by climatological the typical values are meant). Throughout the day, slightly different values of AOD and AE may be observed. Figure 4.7 illustrates the variation in AOD and AE on September 2nd and 3rd, 2015. In the morning of September 2nd, a typical range of aerosol optical depth was observed over Kyiv, ranging from 0.2 to 0.4, with Ångström Exponent values close to 2. After 10:00 UTC, there was an increase in AOD and a decrease in AE (hereafter, AERONET time is indicated in UTC). It was during this time that biomass burning emissions started reaching Kyiv (see Fig. 4.7a).

By the morning of September 3rd, around 4:20 AM, as the photometric measurements began, AOD values reached approximately 0.9, and at a certain point during the measurements (around 7:00 AM), even reached 1.25, indicating a significant aerosol layer. Throughout the afternoon, AOD values fluctuated between 0.5 and 0.75 and increased again towards the evening (see Fig. 4.7b), indicating the arrival of air masses with high aerosol particle concentrations.

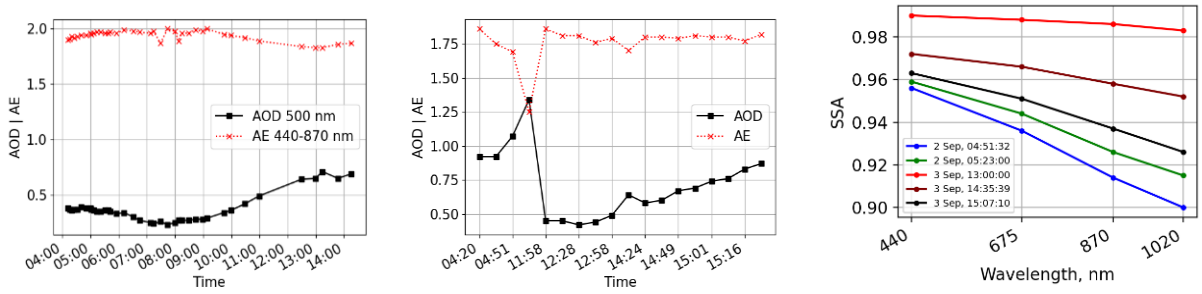

a b c

Figure 4.7. Aerosol Optical Depth (AOD, 500 nm, black line) and Ångström Exponent (AE, 440–870 nm, red line) for a) September 2nd and b) September 3rd, 2015. c) Single Scattering Albedo (SSA) changes during 2–3 September 2015. AERONET data from Kyiv. Data level 2.0.

As for the Ångström Exponent parameter, its value during September 3rd remains relatively constant, ranging around 1.75 (see Fig. 4.7b). However, it is worth noting that the previous day, its value was higher (see Fig. 4.7a) and started to decrease with the arrival of combustion products into the atmosphere of Kyiv. On September 3rd, only the measurement at 7:00 am showed a significant decrease in AE to a value of 1.25. Such a decrease in AE and an increase in AOD indicate the presence of particles larger than the background, potentially

including smoke with relatively large ash particles. There may also be traces of mineral dust that could be transported from burned areas.

Single Scattering Albedo is a quantity that depends on the particle's ability to scatter and absorb solar radiation. There are limitations in accurately determining the SSA from sky radiances inversion, especially under conditions of low solar zenith angles (SZA) or low AOD. Dubovik et al. (2000) indicated that errors in SSA could be at least 0.03. Conversely, Sinyuk et al. (2020) proposed narrower SSA uncertainties, ranging from 0.017 to 0.023 at 440 nm and from 0.015 to 0.026 at 675 nm, specifically for an AOD of 0.6 at 440 nm. Typically, for Kyiv, the Single Scattering Albedo (SSA) at 440 nm varies in the range of 0.9–0.99, while it ranges from 0.85 to 0.99 for 675 nm and 870 nm, and from 0.8 to 0.97 for 1020 nm.

Since biomass burning particles, including black carbon and soot, have the ability to absorb light, they reduce the value of SSA. The changes in the Single Scattering Albedo (SSA) on September 2 and 3 (Fig. 4.7c) demonstrate a transition from more absorbing particles to less absorbing ones. This shows that the SSA values on September 3 exceed those of the previous day. For instance, at a wavelength of 440 nm, on September 2, the SSA does not exceed 0.96, whereas on September 3, the values at the same wavelength are higher, reaching a maximum of 0.99. The following figure (see Fig. 4.8) shows the variation of SSA with wavelength for September 1–3, 2015. The data values are averaged over the course of each day. The graphs provide interesting information, as the lowest SSA values are observed not on September 3 as expected, but on September 2, a day earlier. The values on September 3 are close in magnitude to those observed on September 1.

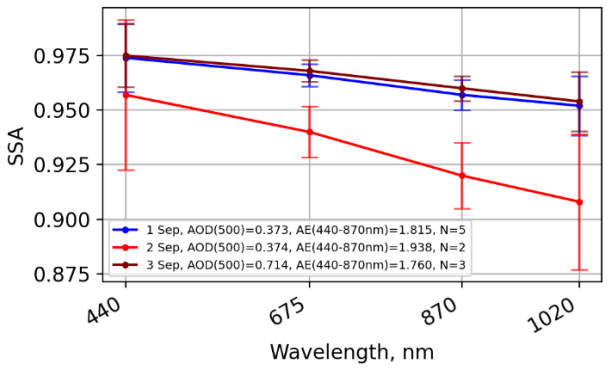

Figure 4.8. Spectral Single Scattering Albedo (SSA) in the atmosphere above the AERONET Kyiv station based on sun photometer observations during September 1–3, 2015. Data from AERONET Kyiv. Data level 2. The colors indicate the observation day, and the data are averaged over a 24-hour period. N is number of measurements.

However, as described in the previous section, the SSA from biomass burning depends on the vegetation type and ranges from 0.93 for peatlands and forests for fresh biomass burning products (within 24 hours of formation) to higher values of approximately 0.96 on the third day after formation. It should be noted that the single scattering albedo is not dependent on particle concentration but only on the scattering and absorption characteristics of the particle. Since AOD in Kyiv started to increase from the second half of the day on September 2 (see Fig. 4.7a), and the air mass trajectories during this period pass through fire-affected areas, it can be concluded that biomass burning products, formed relatively recently, began to enter Kyiv with the increasing AOD. Therefore, the SSA curve for September 2 in Figure 4.8 (red line) corresponds to the presence of absorbing particles in the atmosphere above Kyiv, specifically the products of peatland and forest burning, which were very likely formed within 24 hours prior to reaching Kyiv, as indicated by their SSA values.

On the following day, September 3, 2015, the particle concentration increased, as evidenced by a significant change in AOD (above 0.5 throughout the day, see Fig. 4.7b). However, these were no longer freshly formed biomass burning products but particles that had entered the atmosphere more than 24 hours earlier (2–3 days based on fire activity maps and air mass trajectories).

b) Particle Size Distribution

The particles from biomass burning belong to the fine fraction of the aerosol. The next figure (see Fig. 4.9) illustrates the particle size distribution during September 1–3 and 7–8, 2015. For September 1 and 2, the distributions are similar in both magnitude and shape (see Fig. 4.9, green and blue lines). On the following day, September 3, the concentration of the fine fraction increases, while the coarse fraction decreases compared to the previous two days (see Fig. 4.9, red line).

Since it rained in Kyiv on September 4 and 5, AERONET data is unavailable for this period. For September 7 and 8, the particle distributions noticeably differ from the early days of September. Firstly, the particle concentration is much lower than in the preceding days, and secondly, the contributions from the fine and coarse fractions are nearly identical. This situation is attributed not only to the decrease and cessation of fires in forests and peatlands but also to

the "cleaning" of the atmosphere by rainfall. The distribution predominantly dominated by the fine mode is characteristic of aerosol resulting from biomass burning. A similar shape is also typical for urban aerosol, which consists primarily of fine and ultrafine particles (emissions from vehicles, factories, burning of wood and coal).

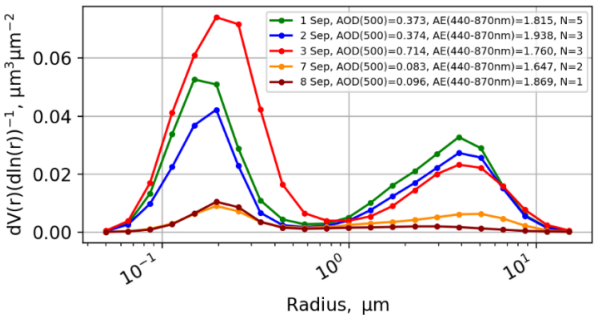

Figure 4.9. Distribution of aerosol particles by volume size in the atmospheric column above AERONET station in Kyiv, based on sun photometer observations during September 1–3, 7, and 8, 2015. Data from AERONET Kyiv. Data level 2.0. Each color represents a different observation day, and the data is averaged over a day, numbers of measurements indicates in N.

c) Complex Refractive Index

Figure 4.10 illustrates the changes in the real and imaginary parts of the complex refractive index for aerosols during September 1–3, 2015. According to the changes in the real part (see Fig. 4.10a, red line), the chemical composition of the aerosol over atmosphere of Kyiv differed on September 2 compared to September 1. The same can be said for September 3. Although both cases involve biomass burning aerosols, the chemical composition will differ for these two days. It should also be noted that these values are independent of aerosol concentration and solely depend on its chemical composition. Regarding the changes in the imaginary part of the refractive index during the aforementioned days, the situation is similar.

The real part of the refractive index for Kyiv during September 1–3 falls within the range of 1.44–1.54 at a wavelength of 440 nm. Such values are fairly typical for this region. Nevertheless, there are certain differences in the values on September 1 and 3 compared to September 2, where the values are slightly higher (Fig. 4.10a). While on September 1 and 3, the real part of the refractive index remains below 1.45 at a wavelength of 440 nm, on

September 2, it is 1.54. A somewhat smaller difference is observed at other wavelengths (675 nm, 870 nm, 1020 nm).

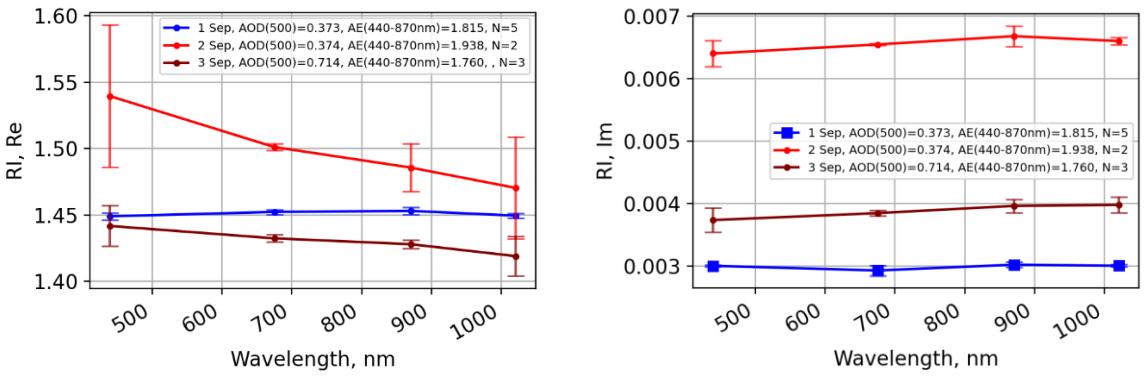

a b

Figure 4.10. a) Real and b) imaginary parts of the complex refractive index during September 1–3, 2015. AERONET data from Kyiv. Data level 2.0. Observation days are color-coded, and the data are averaged over a day. The numbers of measurements indicate in N.

As for the imaginary part of the refractive index, the values during September 1-3 are quite low for all days. However, on September 1 and 3, the range of values is between 0.003 and 0.004 (for all wavelengths: 440 nm, 675 nm, 870 nm, 1020 nm), whereas on September 2, it is approximately 0.007, indicating more absorbing properties of aerosols. Changes in the aerosol refractive index during September 2nd and 3rd correspond to the arrival of "fresh" biomass burning products in Kyiv on September 2nd and the presence of previously formed particles on the following day.

d) Absorption Aerosol Optical Depth

With an increasing number of absorbing particles in the atmosphere, the component of aerosol optical depth responsible for absorption (referred to as Absorption AOD or AAOD) increases, indicating the amount of radiation absorbed. Figure 4.11 illustrates the variation of AAOD from September 1 to September 3, 2015.

The AAOD values recorded on September 2 and 3 were nearly twice as high as those measured the previous day, specifically on September 1, 2015. The observation data confirms the increase in the number of particles in the atmosphere, particularly biomass burning products, which have the capability to absorb radiation. Although the magnitudes are relatively small,

they influenced the changes in AAOD and other aerosol characteristics. It is also worth noting that these values were recorded for aerosols that were transported to Kyiv over a period of 2–3 days and from distances of 200 km and beyond.

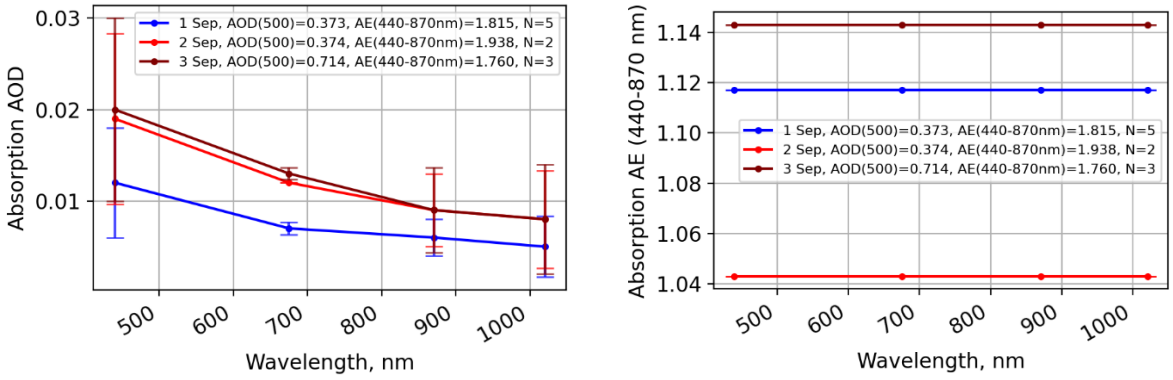

a b

Figure 4.11. a) Aerosol Absorption Optical Depth (indicated as Absorption AOD on the graph) and b) Absorption Angstrom Exponent (440–870nm) during September 1–3, 2015. Data obtained from AERONET Kyiv. Data level 2.0. Colors represent the observation days. N is number of measurements

In regards to the Absorption Angstrom Exponent (440 – 870 nm) presented in Figure 4.11b, the highest values, around 1.14, were observed on September 3, while the minimum, 1.04, was recorded on September 2. Therefore, the highest values of AAE correspond to the day with the highest concentration of biomass burning particles

4.1.4 Results of the 2015 lidar campaign

a) Temporal-altitude distribution of lidar signal during the September 2015 wildfires

The lidar campaign in Ukraine took place from July to September 2015. As part of the campaign, the Ukrainian team of scientists was provided with the CIMEL CE370 lidar. The instrument was provided by the Laboratoire d'Optique Atmospherique, Universite de Lille (Lille, France). This is a single-wavelength lidar with a laser wavelength of 532 nm (detailed principles of lidar observations and features of the CIMEL CE370 lidar are discussed in section 3.2.1). Observations were done at the Main Astronomical Observatory and various locations in Kyiv, including during smog episodes caused by wildfires (thanks to the instrument's mobility,

it can be easily transported and used even on the roof of a vehicle). The temporal-altitude distribution of aerosols is shown in Figure 4.12 and Figure 4.13.

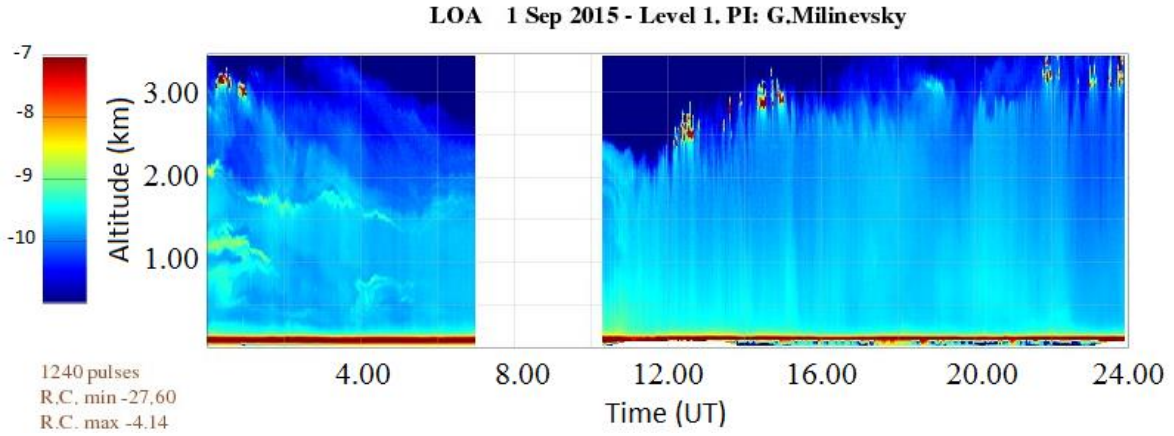

a

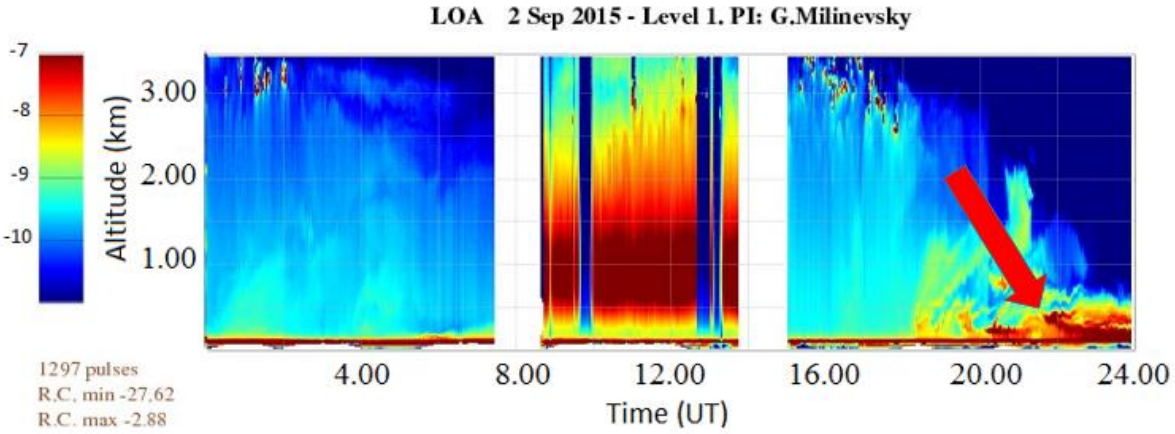

b

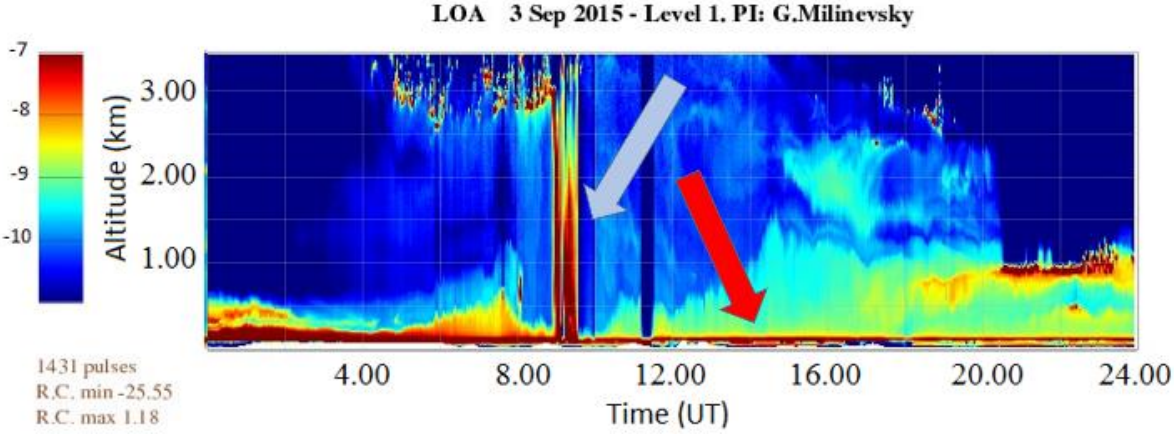

c

Figure 4.12. Temporal-vertical distribution of lidar signal from September 1st to 3rd, 2015. The color represents the natural logarithm of the height-corrected (ln PR^2, scale on the left) lidar signal.

The natural logarithm of the height-corrected ln PR^2 signal is represented by color, a parameter commonly used for visualization of raw data. On September 1st, a typical atmospheric condition for the given period and region is observed over Kyiv (see Fig. 4.12a). The main portion of aerosols is concentrated up to an altitude of 3 km, so there is no need to display the atmosphere above this level. Layered and stratocumulus clouds are also observed at this altitude (on the graph, clouds appear as zones with high signal, and they can be distinguished from aerosols based on their shape and altitude).

A dense aerosol layer above Kyiv obstructed the lidar light transmission above 500 meters on September 2nd, 2015, around 20:00 UT (hereafter, lidar measurement times are indicated in UT) (see Fig. 4.12b, red arrow).

This situation persisted throughout the night from September 2nd to 3rd. The aerosol layer's intensity decreased only after 4:00 UT on September 3rd. At 9:30 UT on September 3rd, a rainfall occurred (see Fig. 4.12c, blue arrow), which contributed to temporary atmospheric cleansing for about one hour. After 12:00 UT, smoke started to reenter, but the intensity of this aerosol layer was lower than during the night of September 2nd (see Fig. 4.12b, red arrow).

The gaps in measurements are associated with the absence of observations and the transportation of the instrument, including its installation on the roof of the vehicle for mobile measurements in the city. The lidar observations on September 4th, 5th, and 7th, 2015, are shown in Figure 4.13. Thus, on September 4th, the situation remained almost unchanged. The appearance of clouds around 1 am slightly alleviated the sense of smokiness due to the decrease in air temperature (see Fig. 4.13a, blue arrow). However, the smoke once again enveloped Kyiv at 9 pm (see Fig. 4.13a, red arrow).

This situation persisted throughout the night until September 5th, and only occasional showers that occurred after 12 pm on September 5th cleared the air above the city (see Fig. 4.13b, blue arrows). On September 6th, it rained almost all day, contributing to the cleansing of the atmosphere from smoke. As a result, on September 7th, the atmosphere was cleared of biomass burning products, and the lidar signal showed even less urban pollution than usual (see Fig. 4.13b). This is indicated by the fact that aerosols were found at an altitude of approximately 500 m, the lidar signal was not strong, and the AERONET AOD values were low (approximately 0.1).

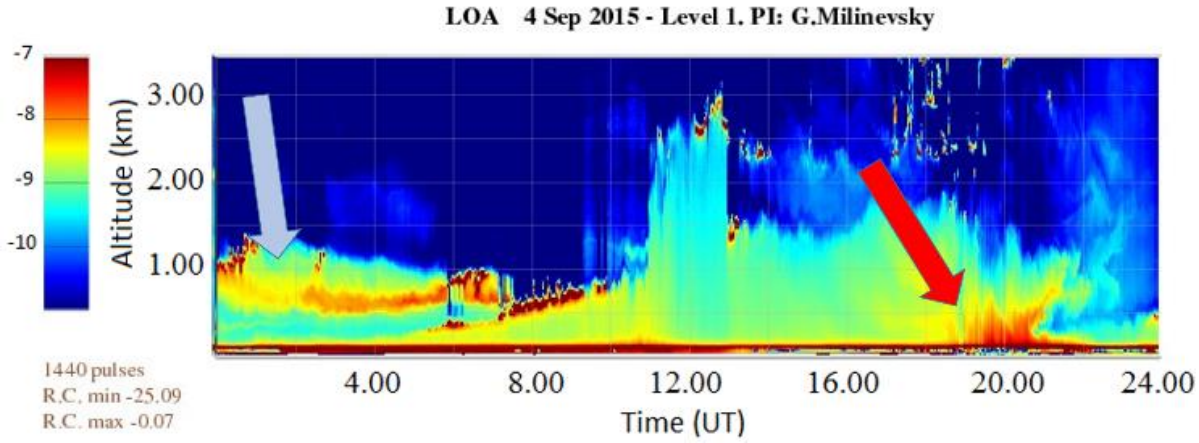

a

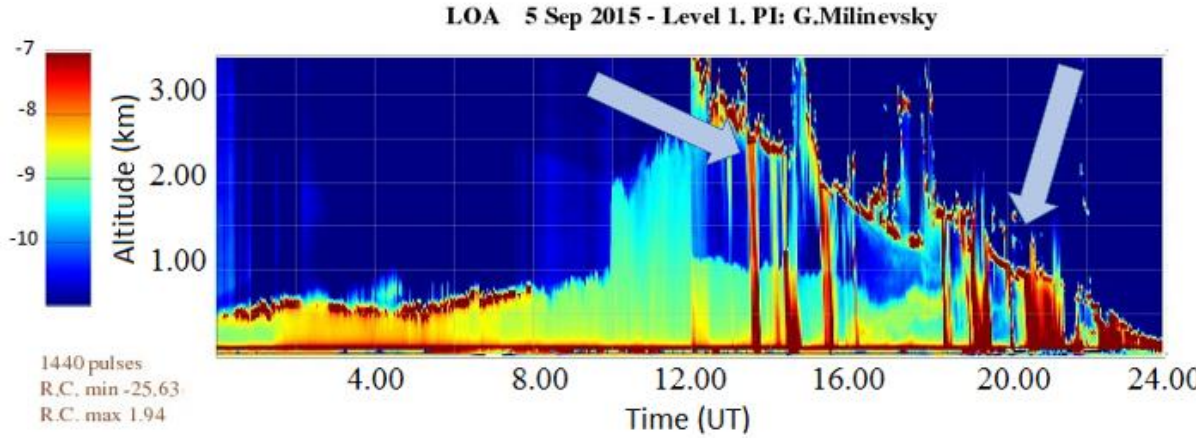

b

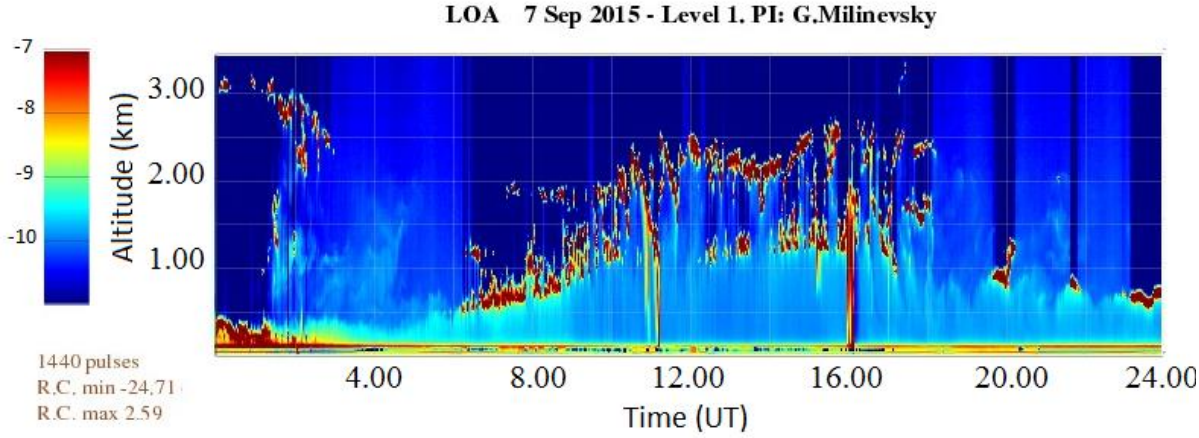

c

Figure 4.13. Temporal-vertical distribution of lidar signal for September 4th, 5th, and 7th, 2015. The color represents the natural logarithm of the height-corrected (ln PR^2, scale on the left) lidar signal.

b) The extinction profile and the average mass concentration of particles

Retrieval of extinction profile and effective lidar ratio (the extinction to backscattering ratio) are performed during daytime using methodology Leon et al. (2009), that is based on the Klett and Fernald solution (Klett et al., 1981; Fernald et al., 1984) using the BASIC algorithm (Mortier et al., 2013; Mortier, 2013), and it includes the use of the accurate AOD measurements, such as AERONET. The other AERONET observed aerosol characteristics are the particle diameter (for two modes), the proportion of fine and coarse mode, particle density, and real and imaginary parts of the refractive index, which, in synergy with the extinction profile, could be used for the calculation of aerosol mass concentration (Mortier et al., 2013). The lidar retrieval algorithm allows choosing the aerosol type model based on the above-mentioned aerosol properties: biomass burning, ash, urban–industrial, dust, sea salt, or manually defining.

During September 1 and 2, an increase in the extinction coefficient was observed at heights ranging from 0.5 to 1 km above the ground, ranging from 0.05 to 0.1 km^{-1}. At heights from 1 to 4 km, the average value of the extinction coefficient was 0.1 km^{-1} and exhibited a homogeneous distribution. During the smoky conditions in Kyiv, the vertical distribution of aerosols varied. Similar to the pre-event conditions, an increase in the extinction coefficient was observed from 0.15 to 0.2 km^{-1} within the altitude range of 0.5 to 1.5 km. Above this level, between 2 to 5 km, a small cloud of aerosol particles with an average coefficient value of 0.1 km^{-1} or less was observed.

On the day of maximum smoke pollution, September 3, the burning particles were transported up to heights of 2 km and above, but did not reach higher than 5 km (see Fig. 4.14c). For comparison, the results for August 30, 2015, are also presented. On this day, the atmosphere over Kyiv was in a typical industrial state and was practically cloud-free (see Fig. Fig. 4.14a).

To calculate the mass concentration, profiles were selected for specific time intervals on August 30 and September 3, 2015, which were filtered to avoid the influence of clouds and primarily estimate the impact of aerosols. For August 30, 2015, the extinction profiles were taken from the interval between 13:00 and 14:22 (see Fig. 4.14b). The coefficient values during this period do not fall within the range of 0.04–0.06 km^{-1}. Based on these data, the average extinction profile was calculated (see Fig. 4.15a) using the BASIC algorithm that was mentioned before.

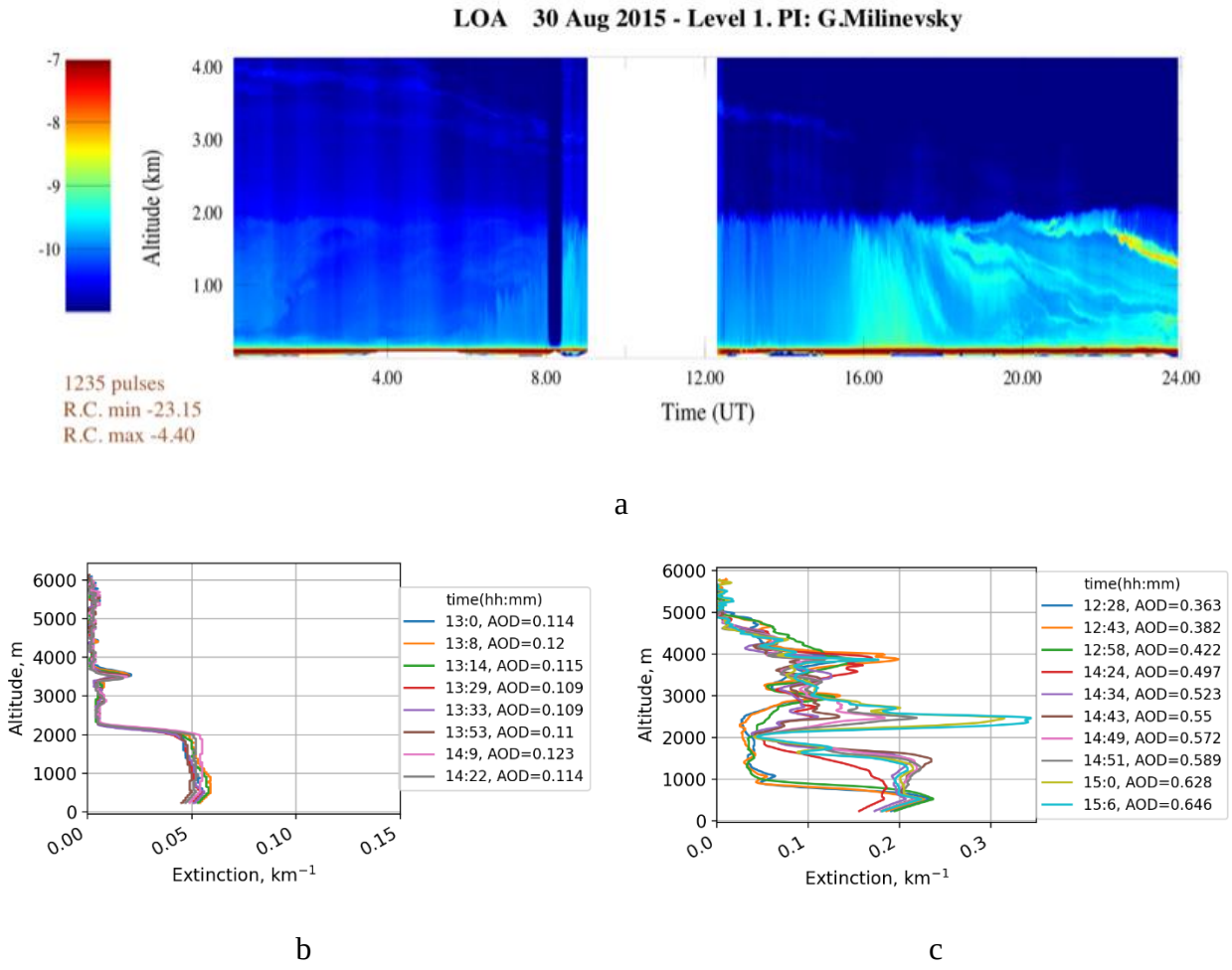

Figure 4.14. a) Temporal-vertical distribution of lidar signal for August 30, 2015. The color represents the natural logarithm of the height-corrected signal (ln PR^2, left scale) b) Vertical distribution of extinction coefficient for August 30, and c) September 3, 2015, reproduced based on lidar observations. The colors on graphs b) and c) indicate the time of lidar measurements in UT.

Similarly, the same procedure was carried out for the time interval from 12:28 to 15:06 on September 3. This time period corresponds to the arrival of biomass burning aerosols into the atmosphere above Kyiv, coinciding with the absence of cloud cover (see Fig. 4.12c), as clouds have high extinction coefficients that can introduce significant errors in the aerosol contribution estimation. Therefore, the extinction during this period is much higher than the observed values on August 30. The plot of the average extinction coefficient as a function of height is shown in Figure 4.15b.

Based on the averaged extinction profiles shown in Figure 4.14, the mass concentrations of aerosols were calculated according to their altitude. The results are presented in Figure 4.15.

The calculation was performed as follows. Using the definition of aerosol extinction σ_{aer} (equation 2.24) and assuming a homogeneous medium, the particle concentration $\overline{n(r)}$ can be determined as:

$$\overline{n(r)} = \frac{\sigma_{aer(\lambda_{532nm})}}{\pi r^2 Q_{scat}(\alpha,\overline{r},m)} \tag{4.1}$$

Where r is the particle radius, Q_{scat} is the extinction efficiency dependent on the size parameter α, and therefore on the radius. The mass concentration of aerosol particles C can then be obtained as:

$$C = \frac{\rho_{aer} V_{part} \overline{n(r)}}{V_{air}} \tag{4.2}$$

Here, V_{part} represents the volume of one particle, ρ_{aer} represents the density of aerosol, and V_{air} is the volume of air (we are interested in the number of particles per cubic meter).

For calculating the average mass concentration of aerosol particles at different altitudes on this day (at a specific time), the following assumptions and observations were used: (1) the values of the complex refractive index from AERONET observations (see Fig. 4.10); (2) according to the AERONET algorithm, the aerosol density from biomass burning is approximately 1.35 g cm^{-3} (typically ranging from 1.22 to 1.92 g cm^{-3}, as reported by Levin et al., 2010), and for urban pollution aerosol, it is 1.6 g cm^{-3} (Pitz et al., 2003); (3) based on AERONET observations of aerosol size distribution, as shown in Figure 4.9, a biomass burning and industrial aerosol model was used for this case, with an average particle radius of 0.2 μm; and (4) lidar measurements of the extinction coefficient.

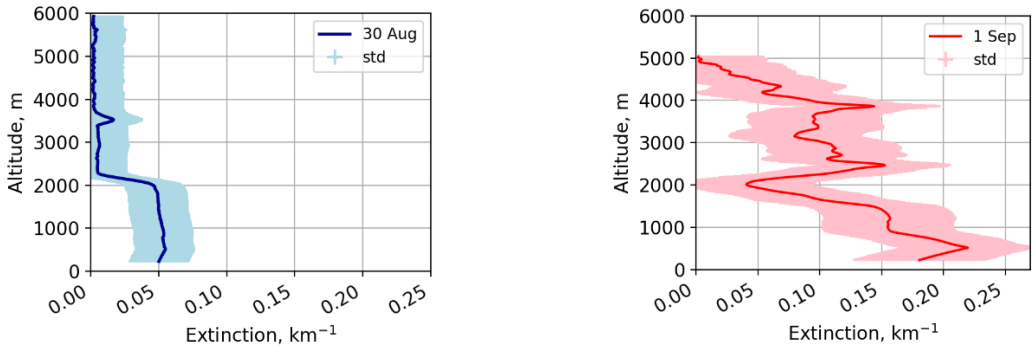

a b

Figure 4.15. Averaged vertical distributions of the extinction coefficient: a) for August 30, 2015, during the time period from 13:00 to 14:22 UT, and b) for September 3, 2015, during the time interval from 12:28 to 15:06 UT, reproduced based on lidar observations.

The calculated mass concentrations of particles for August 30, 2015, during the time period from 13:00 to 14:22, and for September 3, 2015, during the time period from 12:28 to 15:06, based on the provided measurements and assumptions, are shown in Figure 4.16. For August 30, the average particle concentration ranged from 20 to 25 μg m^{-3}, while on September 3, it exceeded 80 μg m^{-3} for altitudes below 1 km. Above 1 km, the concentration varied between 50 and 60 μg m^{-3}.

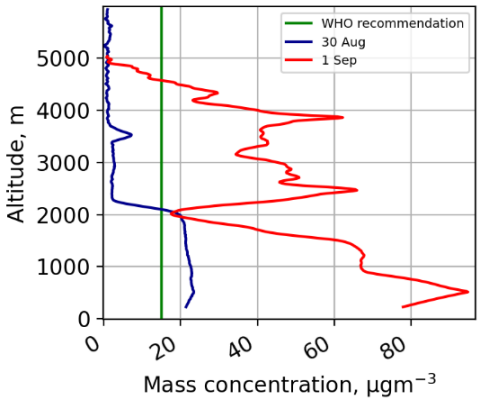

Figure 4.16. Average mass concentration of particlesmfor August 30, 2015, during the time period from 13:00 to 14:22 (UT), and for September 3, 2015, during the time period from 12:28 to 15:06 (UT).

It should be noted that the biomass burning aerosol density is lower than the industrial aerosol, and the values for both days (even for the relatively clean August 30) exceed the recommended particle concentrations by the WHO, as well as European and American standards (recall that these are 15–20 μg m^{-3}, recommendations and permissible limits are provided in section 2.2.2). Therefore, this level of aerosol loading in the atmosphere reaches the yellow category: it is hazardous for vulnerable population groups (people with allergies, asthma, bronchial diseases, children, etc.) The calculations presented above demonstrate a significant increase in the concentration of aerosol particles during biomass burning. Furthermore, by utilizing lidar measurements, it is possible to compute the spatial distribution of aerosol concentrations at various altitudes, rather than solely within the near-surface layer.

d) Results of the lidar campaign

As mentioned in the previous subsection, the lidar campaign in Ukraine took place from July 15th to September 14th, 2015, with the support of the Laboratoire d'Optique

Atmosphériquethe of University of Lille. The retrieved extinction coefficients based on Lidar measurements were used to analyze variations during the observations. For this purpose, sorted profiles (taking into account minimal cloud and rain influence) served as the basis for constructing the extinction plots for the entire observation period (see Fig. 4.17).

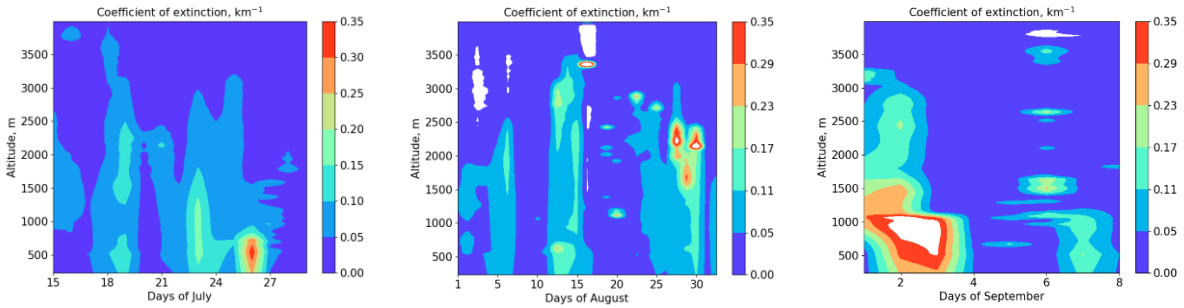

a b c

Figure 4.17. Vertical distribution of the extinction coefficient for a) July, b) August, and c) September 2015, reproduced based on lidar observations (only day). Kyiv. The magnitude of extinction is indicated by colors.

The extinction coefficient of aerosol particles in the atmosphere above Kyiv typically ranges from 0.04 to 0.07 km^{-1} in the altitude range from the ground to 2 km for July and August 2015 (see Fig. 4.17a and b). Above 2 km, the extinction decreases as the aerosol is concentrated in this region. Variations at altitudes of 3–4 km are influenced by the contribution of clouds. As for September, higher values within the range of 0.06–0.3 km^{-1} up to 2 km (see Fig. 4.17c) are associated with air pollution resulting from biomass burning. There is also a noticeable increase in extinction from 2 to 3 km compared to previous months: 0.02–0.6 km^{-1} (see Fig. 4.17c), indicating the presence of biomass burning particles at higher altitudes, different from typical urban aerosol. Additionally, September measurements cover only two weeks, which increases the uncertainty of the average calculations.

4.1.5 The impact of peat burning on radiative forcing

Radiative forcing (RF) at the top of the atmosphere (TOA) and bottom of the atmosphere (BOA) based on AERONET algorithms for July, August, and September 2015 are shown in Figure 4.18. At the TOA, RF values range from –20 to –5 W m^{-2} on average during July–August 2015 (see Fig. 4.18a). After September 6, the RF variations are similar to those of the

previous two months. A significant RF value is observed from September 1 to 6, with a minimum of –33 W m^{-2} on September 3.

The AERONET algorithm allows for the calculation of direct radiative forcing (Garcia et al., 2008), which arises from the absorption and scattering of solar radiation by atmospheric aerosol particles. The presence of BB products in the atmosphere above Kyiv in early September 2015 led to a stronger radiative forcing at the TOA and, as a result, stronger cooling of the upper atmosphere. RF at the bottom of the atmosphere (BOA) also has negative values. Throughout July to September 2015, the average RF at the BOA varied between –10 and –40 W m^{-2} (see Fig. 4.18b).

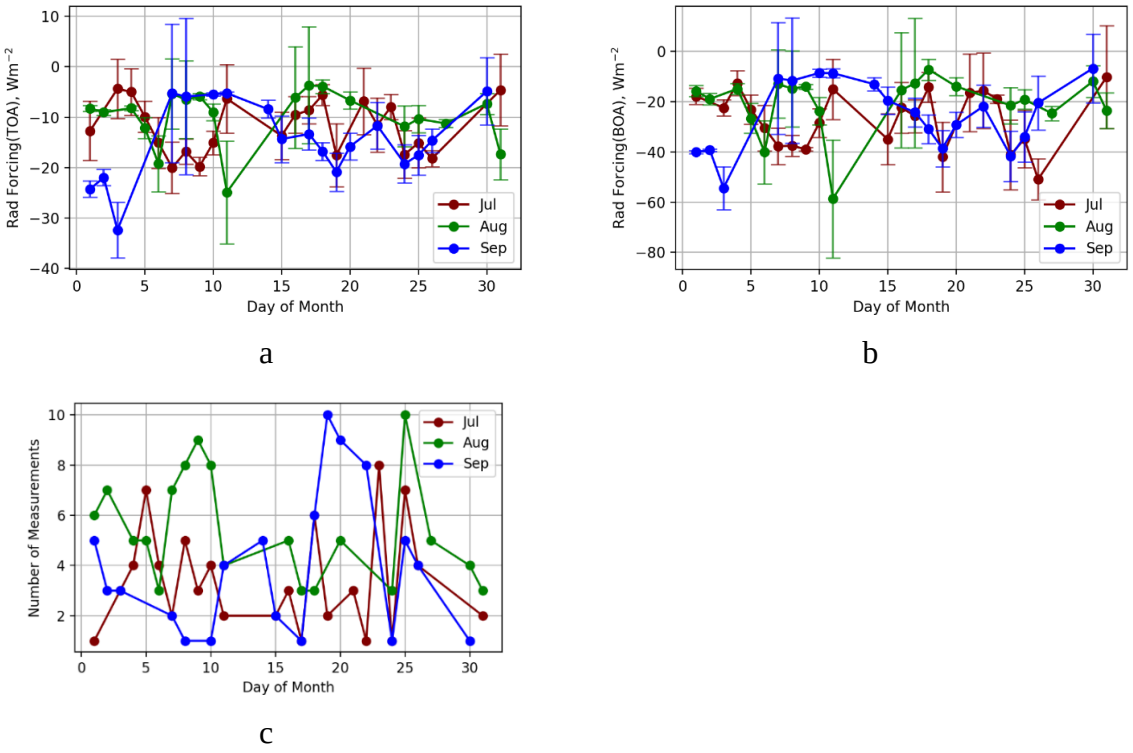

Figure 4.18. Changes in radiative forcing (RF) a) at the top of the atmosphere (TOA); b) at the bottom of the atmosphere (BOA) and c) number of measurements used for averaging. Observations from the AERONET station in Kyiv during the period of July to September 2015. Kyiv, Ukraine. AERONET data level 2.0. The colors indicate the month and year of the observations. The data is averaged daily.

However, two peaks significantly differ from the average daily variations. One peak occurs on September 3 and is associated with the presence of biomass burning aerosols, resulting lower values RF at BOA. The other peak, with RF that almost reaches –60 W m^{-2}, occurs on August 11, 2015. This case is particularly interesting to study. The AOD at 500 nm

varied between 0.3 and 0.5, and the AE (440–870 nm) varied between 1.6 and 1.8 in the early morning hours (from 3 to 5 am), and above 1.9 after 5 am on that day. The single scattering albedo at 440 nm reached value 0.89. After 5 am, the single scattering albedo varied within the range of approximately 0.95 to 0.99 (for the specific observations, direct access can be obtained from the AERONET website at https://aeronet.gsfc.nasa.gov/).

The described situation corresponds to the presence of particles with moderate absorption capacity in the atmosphere above Kyiv. These particles could include combustion products, which may consist not only of soot but also relatively larger ash particles (the Ångström Exponent initially decreased and then increased, reaching values characteristic of the dominance of fine-mode aerosols). Both on September 3 and August 11, the atmosphere above Kyiv was dominated by particles capable of absorbing solar radiation. This led to the changes of RF and, as a result, stronger cooling at the TOA and BOA. Furthermore, the behavior of radiative forcing and its efficiency during forest fires will be described. Figure 4.19 shows the change in RF and the efficiency of RF (Eff RF) at the boundary between the upper and lower atmosphere during the period from August 30 to September 10, 2015, based on the observation data from the AERONET station in Kyiv.

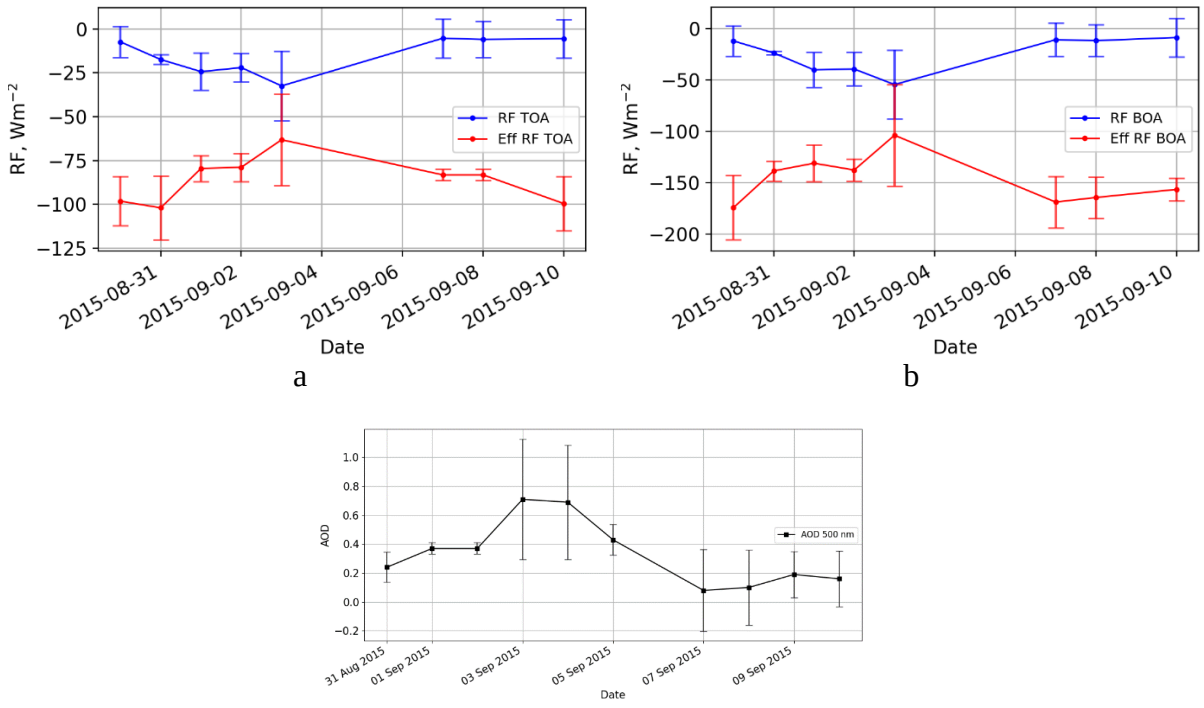

Figure 4.19. Radiative Forcing (RF) and Efficiency of Radiative Forcing (Eff RF) at a) the top of the atmosphere (TOA) and b) the bottom of the atmosphere (BOA); c) AOD (500 nm). Daily average data for the period from August 30 to September 10, 2015, from the AERONET station in Kyiv. AERONET data level 2.0.

Regarding RF at the TOA boundary (see Fig. 4.19a), on September 3, the value is approximately –30 W m^{-2}, which is lower than the preceding and subsequent days. The behavior of the efficiency of RF is opposite: on September 3, 2015, a maximum is observed compared to the preceding days. RF at the BOA boundary (see Fig. 4.19b) shows similar behavior: RF reaches its minimum on September 3, –50 W m^{-2}, while the efficiency shows a maximum.

In fact, RF is not linearly dependent on AOD, and thus the forcing efficiency actually depends on the AOD values. The efficiency of RF allows determining how effectively aerosols in the atmosphere influence the scattering and absorption of radiation. The higher the value of this ratio (see eq. 2.65), the greater the influence of aerosols on the radiation balance of the atmosphere. A situation with high AOD corresponds to lower RF, and vice versa. This is what we observed: on the day with the highest AOD, September 3 (see Fig. 4.19c), the stronger RF corresponds to the lowest efficiency RF.

4.2 The BB impact on air quality and aerosol properties

This section describes the impact of spring 2020 forest fires on the changes of aerosol properties based on AERONET observations, as well as its influence on air quality and PM2.5 concentration. Measurements from the AirVisual network are used for particulate matter analysis. Additionally, the study investigates the influence of air mass transport calculated using the HYSPLIT model.

4.2.1 The forest and field fires during the spring of 2020

The year 2020 proved to be challenging for the entire planet due to the COVID-19 coronavirus and more. Large factories and plants were being shut down worldwide, industrial production was halted, automobile traffic decreased, air travel and other transportation were canceled. As a result, air quality significantly improved in many places, smog decreased or disappeared altogether, water bodies became cleaner, and wild animals roamed deserted streets. However, the situation in Ukraine unfolded differently. The end of March and April 2020 were

marked by large-scale fires throughout the territory of the country, including the Chornobyl Exclusion Zone.

The impact of these fires was noticeable even in relatively distant areas from the ignition sources, as smoke and biomass burning products were transported by the movement of air masses for hundreds of kilometers from the formation sources. Observations of thermal anomalies and active fires using the VIIRS instrument and thermal anomalies according to MODIS provide near-real-time information on fire locations and offer imagery of the affected territory (https://earthdata.nasa.gov/firms), which caused significant aerosol pollution in the atmosphere over the city of Kyiv in spring 2020 (see Fig. 4.20). On the left, Figure 4.20a presents a map of fires during the period from March 15 to April 15.

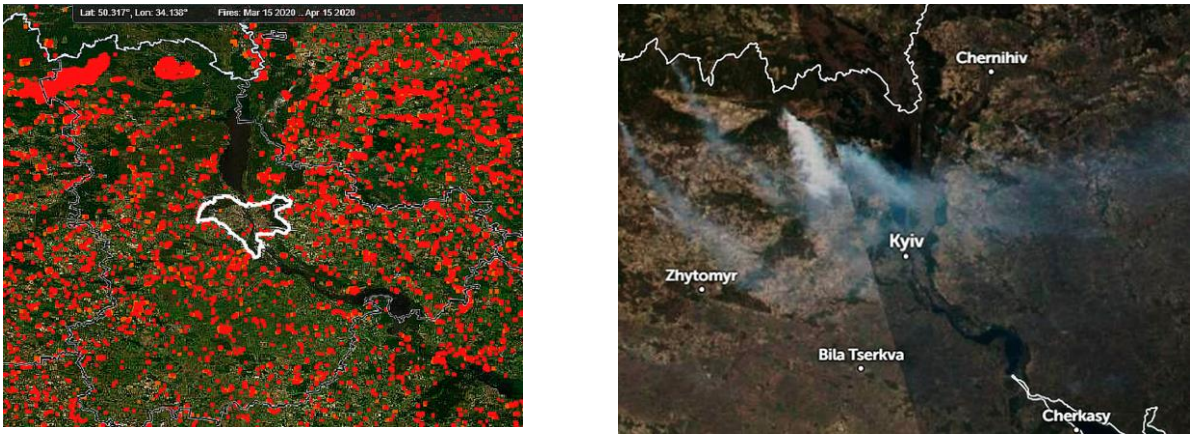

a b

Figure 4.20. a) MODIS/VIIRS fire map data March 15 – April 15, 2020, prevailed wind direction N–NW, wind speed up to 27 km h^{-1}. Two big forest fire areas were persistent at north of Chernobyl region. b) Satellite image April 8, 2020 with large forest fire in the northwest of the Kyiv region. Plots have been created using open access data from (https://zoom.earth/, https://earthdata.nasa.gov/firms). The area of the Kyiv city is marked with a white line.

The white contour indicates the boundaries of Kyiv city. Thermal anomalies were detected in all directions from the capital, with a particularly high concentration of red dots in northern Ukraine. On the right side of Figure 4.20, a satellite image taken on April 8, 2020, shows a large forest fire in the northern part of Kyiv Oblast (https://zoom.earth/). Backward air mass trajectories indicate the influence of predominantly large forest fires in northern Ukraine on the aerosol content and properties in the atmosphere over the city of Kyiv in spring 2020 (see Fig. 4.21). Similar to the previous case, backward trajectories were calculated using the

online version of the HYSPLIT model for altitudes ranging from 0.1 to 5 km above ground level (AGL). The trajectories originate from the AERONET station in Kyiv.

Increased pollution of the air in the Kyiv city on April 17–19 was caused by the large forest fires, which took place in the northern region of Ukraine, northwest of the Kyiv city. Smoke trails from the fire locations visible on the MODIS pictures (see Fig. 4.21a) show it. Also, the back trajectories from the Kyiv city of the air mass movement (see Fig. 4.21a) indicate the northwest wind and the air pass over the fires on the April 17–19 event.

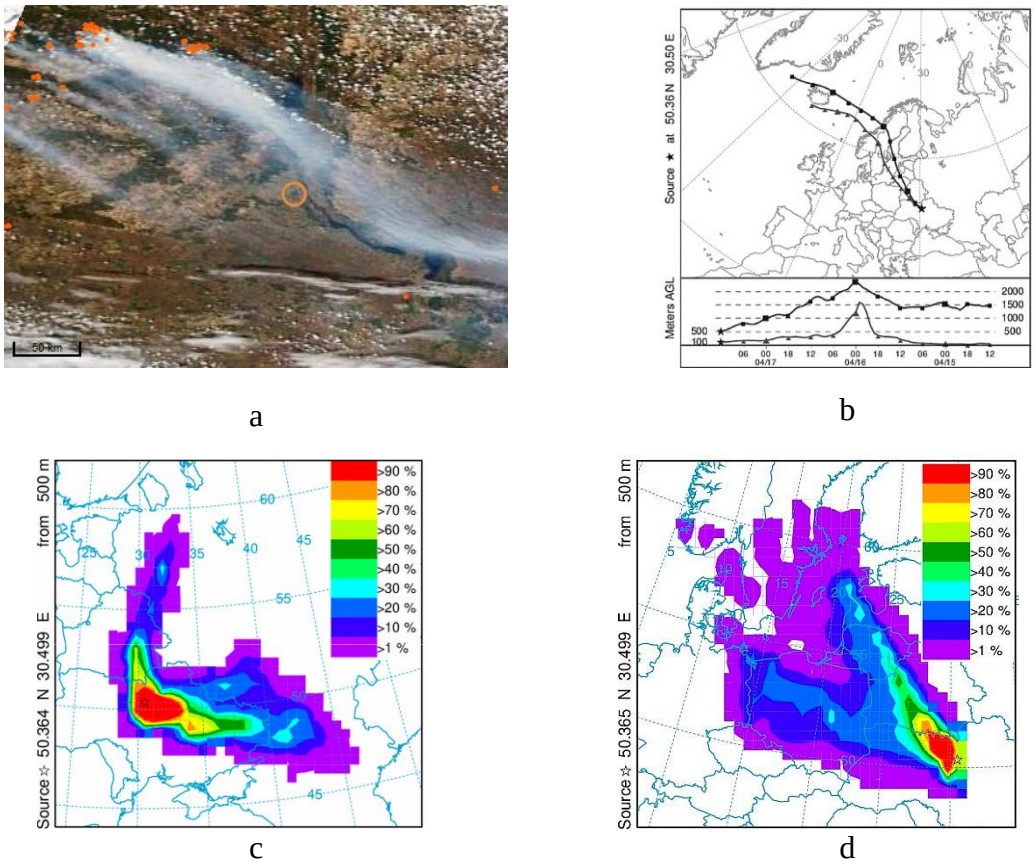

Figure 4.21. Smoke plumes of the forest fires in the north part of Ukraine on April 17, 2020: a) MODIS/Terra image, b) back trajectories on altitude 100 and 500 m AGL for the Kyiv AERONET site on April 17 passed over territories with fires. The Kyiv AERONET site and Golosiiv AirVisual station location marked with a circle in the right bottom corner of a). c) Trajectory frequencies at altitude 500 m AGL for the Kyiv AERONET site on March 30 and d) April 17 passed over territories with fires. The Kyiv AERONET site and Golosiiv AirVisual station location marked with a star.

Distances from the locations of the fires to the Golosiiv observational site ranged 90 to 240 km approximately as it can be estimated using the scale of the MODIS pictures. The largest fires were located at the distance about 200 km. The plots in Figure 4.21were created using

publicly available data from AERONET/Data Synergy Tool. The air mass moved to the Kyiv city from the azimuth direction approximately 300° with mixing the air layers in the altitude range from the surface to 1500 m AGL (see Fig. 4.21b) due to convection in the atmosphere (which originate mixing) produced by the fire. The time travel dependence on the altitude of the air mass means that the AirVisual sensors and the sun-photometer can observe different aerosol particles at the same time. It should be expected that, owing to the air mass speed dependence on altitude, the sun photometer observes "fresher" aerosol compared to AirVisual sensors.

To refine the aerosol source characterization, it was necessary to analyze the frequency plots of air backward trajectories to obtain information about the predominant wind directions and the movement of air masses over the territory of Kyiv. For this purpose, we utilized the trajectory frequency option, which allows launching trajectories from an altitude of 500 meters above ground level every 3 hours for the AERONET Kyiv station. The analysis of air backward trajectories was done for 3-day periods from the archive, as shown in Figures 4.21c and 4.21d.

Back trajectories on altitude 500 m AGL starting from the Kyiv AERONET site on March 26–30 passed over territories with fires during the previous 3 days (see Fig. 4.21c). The results for March 30 at 12 UTC include information from March 26 at 20 UTC (see Fig. 4.21c) and show that most air mass was transported to the Kyiv city from the south-east – northwest direction. Fires showed a maximum during March 26–28, which were the most probable cause of aerosol loading of the atmosphere over the Kyiv city on those days.

During this period wildfires in the East and the South parts of Ukraine were detected. Another case that contains calculation from April 14 at 20 UTC until April 18 at 12 UTC (see Fig. 4.21d), shows opposite directions of air mass transfer. For this period, the north and northwest air movements were typical. In this case, air masses with aerosol contamination from the northwest and north regions, including the Chornobyl area, achieved the Kyiv city and its suburbs.

4.2.2 AERONET and AirVisual observations

The data on $PM_{2.5}$ concentration in the atmosphere above the city of Kyiv during the period of March–April 2020 were collected using observations from four AirVisual sites and

the Popudrenka station and shown in Figures 4.22a and 4.22b. During the observation period, specifically in March four maxima of $PM_{2.5}$ were observed. The $PM_{2.5}$ concentration increased up to 80 μg m^{-3} approximately, which is three times higher than the threshold of $PM_{2.5}$ pollution according to European standards of 25 μg m^{-3} (see Fig. 4.22a). The largest pollution was observed at the Nauky Avenue site in the first half of March, and at Artema Street and Trostyanetska sites in the second half of March 2020 (see Fig. Fig. 4.22a).

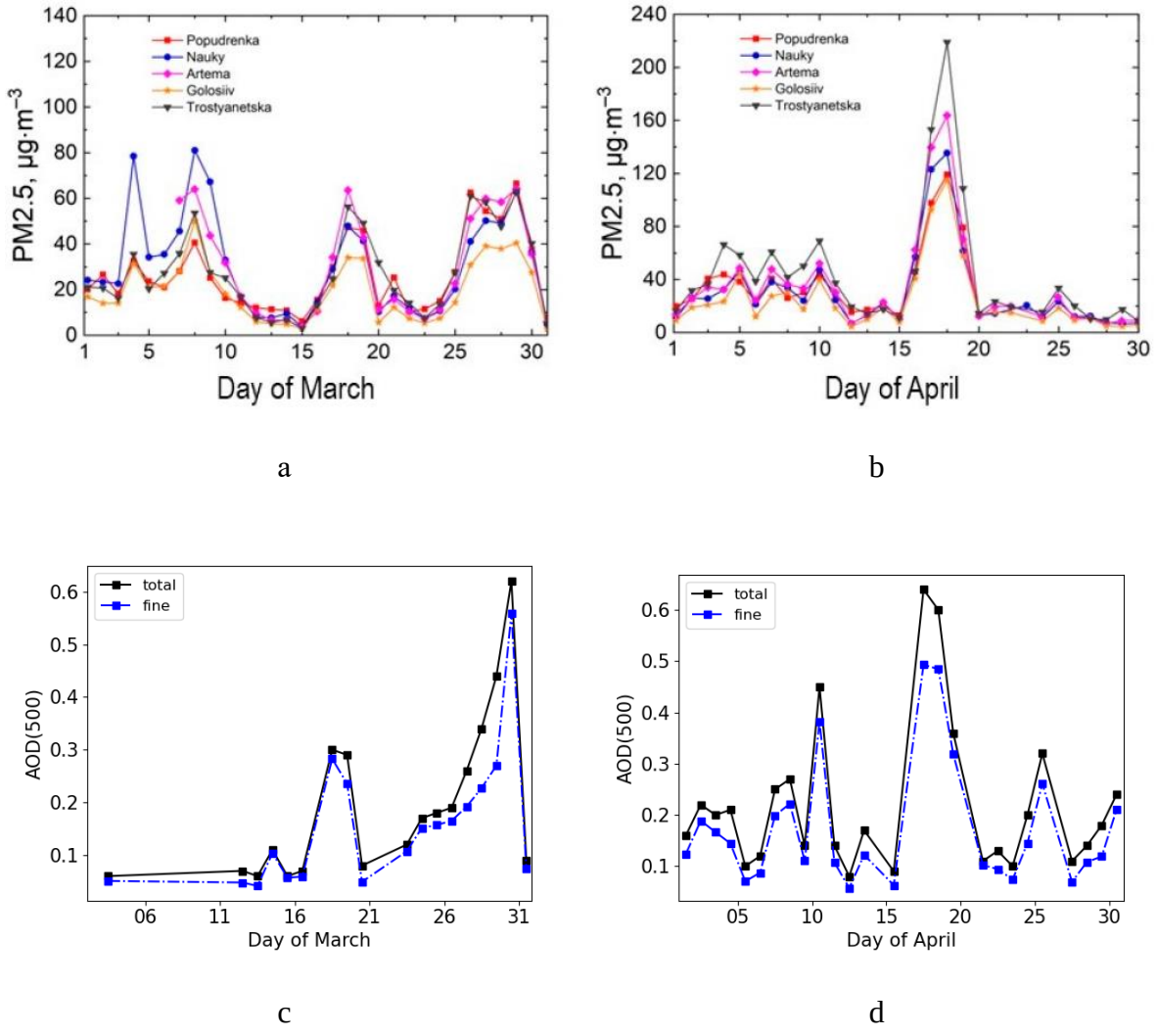

Figure 4.22. Air Visual network $PM_{2.5}$ daily averaged in situ measurements in the Kyiv city in four sites: Nauky, Artema, Trostyanetska, Golosiiv and APDA-371 Popudrenka site in a) March and b) April 2020; the daily averaged AOD of all particles (total) and AOD fine particles (fine) over the Kyiv city from observations with the AERONET Kyiv site sun photometer at 500 nm wavelength during c) March and d) April 2020.

In April, a significant increase of $PM_{2.5}$ aerosol contamination to 40–70 μg m^{-3} was registered in the first half of April with maximum detected at the Trostyanetska site. The

extreme contamination with the $PM_{2.5}$ maximum 220 μg m^{-3} was observed on April 18 (see Fig. 4.22b). Therefore, the level of pollution by $PM_{2.5}$ particles is almost 10 times higher than the EU restrictions. The extreme contamination with $PM_{2.5}$ aerosols was observed at all sites of the in situ measurement network in the Kyiv city with the largest daily averaged values at the Trostyanetska site. Some additional information, including the STD representation, is provided in Appendix 1.

The data of AirVisual stations are in good agreement with the $PM_{2.5}$ values variations at Popudrenka station (see Fig. 4.23a, b). To estimate the reliability and accuracy of the in situ measurements, we compared daily averaged $PM_{2.5}$ concentrations obtained by AirVisual stations with $PM_{2.5}$ concentrations measured by the EU-certified APDA-371 HORIBA sensor (see Fig. 4.23a). As shown in Figure 4.23a, the values of aerosol contamination obtained with the AirVisual and the APDA-371 HORIBA sensors are consistent for small concentrations of $PM_{2.5}$ (up to ~ 40 μg m^{-3}), but the divergence increases at values more than 60 μg m^{-3}.

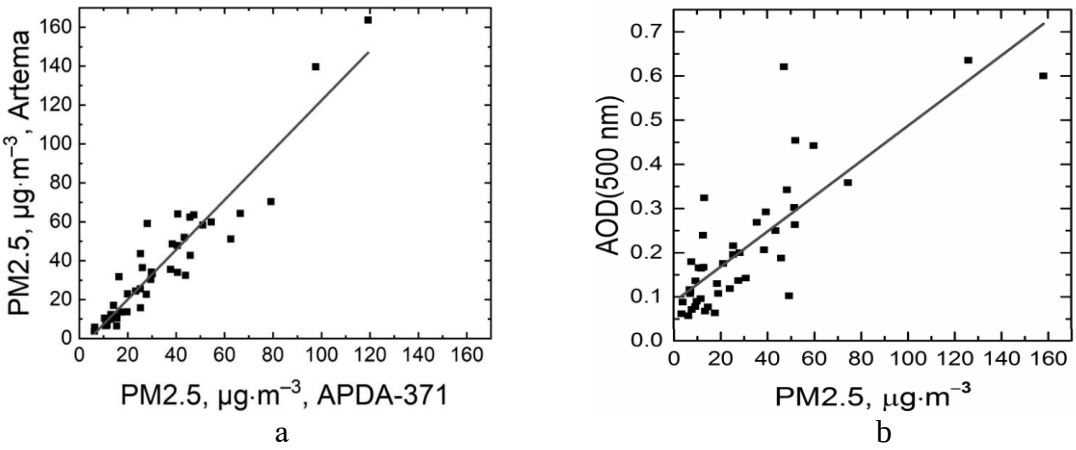

Figure 4.23. a) Comparison of AirVisual $PM_{2.5}$ data from Artema Street site with APDA-371 Popudrenka site simultaneous measurements March – April, 2020. b) Comparison of the daily averaged $PM_{2.5}$ concentration with daily total AOD (500 nm) data from the AERONET Kyiv site for March – April, 2020.

Linear regression with Pearson correlation coefficient provided a value of r = 0.94. If in March, the highest $PM_{2.5}$ values were observed at Nauky Avenue and Artema Street stations, in April the highest (extreme) pollution levels were observed at Trostyanetska station. The lowest values of $PM_{2.5}$, as expected, were observed at Golosiiv station, which is located in the forest-park zone on the outskirts of the Kyiv city. However, the time variations of $PM_{2.5}$ concentration at this station also follow the variations of $PM_{2.5}$ at other stations.

4.2.3 Aerosol characteristics based on observations from the sun photometer at the AERONET station in Kyiv

a) AOD and AE

During March–April 2020, significant events of elevated AOD were observed at the AERONET Kyiv station (see Fig. 4.22c, d). The aerosol content primarily increased due to the presence of fine mode aerosols, as indicated by the aerosol size distribution plots. For the first time in the city of Kyiv, a major aerosol pollution event was recorded simultaneously by the sun photometer and $PM_{2.5}$ measurement devices. To compare the $PM_{2.5}$ concentration data with AOD, daily average $PM_{2.5}$ data obtained from four locations (Artema, Popudrenka, Nauky, and Golosiiv) were used for the days with available AOD measurements in Kyiv during March and April 2020 (see Fig. 4.23b). The daily $PM_{2.5}$ data were averaged from four AirVisual sites and compared with the corresponding daily averaged AOD (at 500 nm).

The equation of linear regression AOD (500 nm) = $a + b \cdot PM_{2.5}$ was used to quantify the AOD versus $PM_{2.5}$ relation. Obtained parameters of regression: Pearson's correlation coefficient r = 0.81, standard deviation (STD) of 0.09; a = 0.088 ± 0.019; b = 0.004 ± 0.0004. Formally the r value indicates the close relationship between AOD and $PM_{2.5}$ parameters of the atmosphere pollution, but it is obviously caused mainly by high contamination level in the near-ground air and atmosphere column on two days on April 17 and 18. On the contrary, AOD (500 nm) of 0.62 was observed on March 29 at relatively moderate contamination at the ground level. Also very low AOD occurred at the same level of $PM_{2.5}$ (see Fig. 4.22b).

Comparison of the results of sun photometer measurements with the data from the in situ network shows that changes of AOD (500 nm) were accompanied with simultaneous changes of the $PM_{2.5}$ concentration (see Fig. 4.22). Both data series show a significant increase in air pollution over the Kyiv city on March 17–19 and 25–30, and during the April 16–19 period. The cloudiness explains the data gaps from 3 to 12 March and during some other days in March and April (see Fig. 4.22c, d). However, some discrepancies are seen between AOD and $PM_{2.5}$ data (see Fig. 4.22b and compare Fig. 4.22a and Fig. 4.22c). Thus, $PM_{2.5}$ concentration on March 17–19 was the same approximately as on March 25 – 30 (~ 40 to 70 $\mu g\ m^{-3}$), but AOD increasing was different: AOD (500 nm) was not more than 0.3 during the former period and more than 0.6 during latter.

On the contrary, on April 10 the sun photometer registered a significant increase in AOD relative to its normal values from 1 to 15 April, while ground-based PM concentration measurements showed a more or less stable but relatively high level of $PM_{2.5}$ concentrations. Apparently, this is possible due to the peculiarities of the movement of air masses at different altitudes, and the increase in AOD on this day could be caused by the transport of aerosol particles from distant sources above the surface layer of the atmosphere. During a forest fire the smoke originated near the Earth's surface can be transported by convection into the higher levels of the atmosphere depending on fire characteristics and local atmospheric conditions. However, the aerosols at ~3–5 km can be originated from elsewhere, for example, from fire free regions. That also can be a reason of the observed difference between AOD and $PM_{2.5}$ measurements.

Found that $PM_{2.5}$ varied from ~5 μg m^{-3} to ~80 μg m^{-3} during the first smoke event and from ~3 μg m^{-3} to ~220 μg m^{-3} during the second event. The results from the first event are close to findings, e.g., in Sapkota et al. (2005) for the forest fires in the province of Quebec, Canada. However, the results of $PM_{2.5}$ concentration from the second event are more than twice higher, which indicates the extremely high fire activity during April 17–19. The large scattering of points relative to the regression line can be explained by different smoke plumes observed by AirVisual devices and by the sun photometer, particularly because of the different velocities of the air mass moving at the different altitudes. However, analysis of the back trajectories and satellite data on the fire locations showed the same origin of the atmosphere contamination by the aerosols during the period under study. It was the forest fires on the large area of Ukraine and sur-rounding territories of Belarus and Russia.

The details of the change of the daily averaged AOD (500 nm) and AE (440–870 nm) variations during the period of significant pollution from March 15 to April 21, 2020 are presented in Figure 4.24. Variations of the daily AE (440–870 nm) (see Fig. 4.24) are in the range of 1.6–1.8, which indicates the presence of a fine aerosol mode in the atmosphere produced by forest fires and urban aerosols. The climatological AOD values for Kyiv in March and April, according to AERONET, are 0.179 and 0.242, respectively. The climatological AE value for both of these months is 1.39.

Starting from March 26, there was a decrease in AE values as AOD increased, suggesting the presence of coarse mode aerosols in the atmosphere above Kyiv. This trend continued until March 30, when the AOD (500 nm) reached its peak value of around 0.6, as shown in Figure 4.24. Subsequently, AE values increased again to a range of 1.6–1.7 on March

31 and fluctuated between approximately 1.7 and 1.2 while the AOD at 500 nm ranged from 0.1 to 0.3 until April 10.

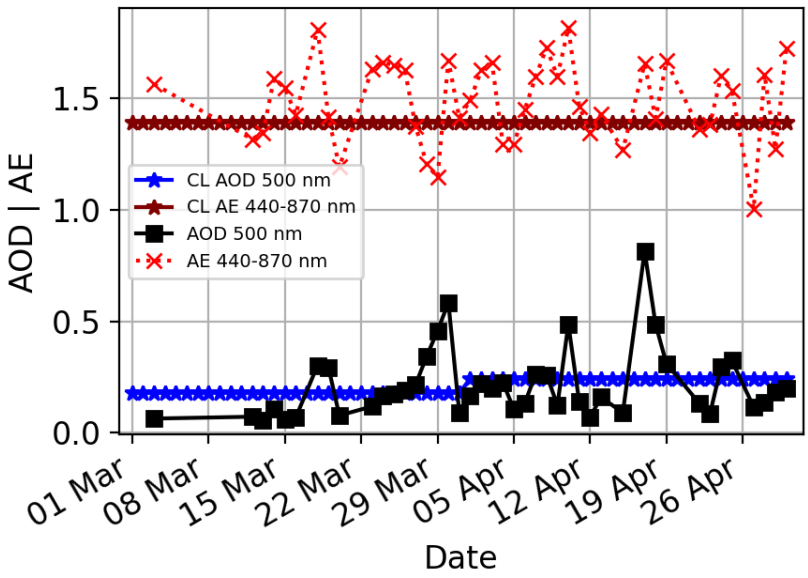

Figure 4.24. Daily variations of Aerosol Optical Depth (AOD) and Climatological Aerosol Optical Depth (CL AOD) at 500 nm, and Ångström Exponent (AE) and Climatological Ångström Exponent (CL AE) at 440–870 nm based on sun photometer observations from AERONET Kyiv during March–April 2020 Data level 1.5.

The aerosol content and properties variation during those days, as well as during the end of April and start of May, is not interesting for analysis because firstly low aerosol content was determined from the low number of observations, and secondly the AE short-time variations suggest that AOD variations were provoked by aerosol of the various origins. On April 10, the AOD increased dramatically, and AE values indicate the fine mode aerosol dominant in the atmosphere column. It is clear that the smoke plume passed over the Kyiv AERONET site on that day. Significant pollution of the atmosphere over the Kyiv city with biomass burning aerosol occurred during April 17–19. The AE increasing from 1.4 to 1.85 indicates that the fine mode particles dominated in the atmosphere column on those days.

b) Aerosol size distribution

Measurements of aerosol size distribution are an important tool for studying forest fires and their impact on the environment. Insufficient observations during periods of cloudiness can

significantly complicate data analysis and lead to inaccurate results. However, successful observations done from March 28 to April 19, 2020, provided high-quality data for determining the distribution (20 successful observations of the sky radiance were conducted). The data showed that particles size distribution was very variable (see Fig. 4.25). During 29 March, the coarse mode particles predominated over the fine mode only. In most of the other cases, the fine mode was dominant.

The time of smoke travel was estimated with the HYSPLIT model back trajectories. Location of the fires and smoke origin were determined for April 17 (see Fig. 4.25b) and the age of aerosols was not more than approximately 10 hours. In order to reach the Kyiv AERONET site on March 27–29 the air mass traveled more than 2 to 3 days over the large area where fires took place (see Fig. 4.20a). Following Alados-Arboledas et al. (2011) we can consider the aerosol observed at the Kyiv AERONET site as fresh during March and April events.

Noted that the difference in air mass movement during two smoke advection events in March 26–30 and in April 15–19 (see Fig. 4.26). While during the April 15–19 event the air masses movements is rather uniform from the northwest, the advection direction for March 26–30 event changes from east and southeast to northwest are seen in back-ward trajectories (see Fig. 4.26a). In (see Fig. 4.26a) the change in wind direction is visible from March 29 to March 30. The change of aerosol properties (the aerosol size distribution) is seen in transition from eastern (see Fig. 4.25a,c) to northwest (see Fig. 4.25e) advection. While in eastern advection the coarse mode aerosol prevails, after change to northwest advection the fine mode became prevailing.

Aerosols of coarse mode apparently predominated in the particle size distribution during March 28 and 29, when air masses arrived in the Kyiv city along the trajectories shown in Figure 4.27a from east and southeast over the burning open areas both grasses and forest-steppe fields. Some part of aerosols in smoke plumes can reach quite large sizes (Janhäll et al., 2010). After steppe vegetation fires, the wind also can lift up coarse mode particles into the air from exposed soil. In the March 28–29 case, such particles could arrive in large amount over the Kyiv city (as the back trajectories show in Figure 4.26a), while during the previous two or three days air masses moved at low altitudes over regions where vegetation fires of various types took place (see Fig. 4.20a). Therefore, soil dust, ash and unburned parts of vegetation could rise into the air by winds.

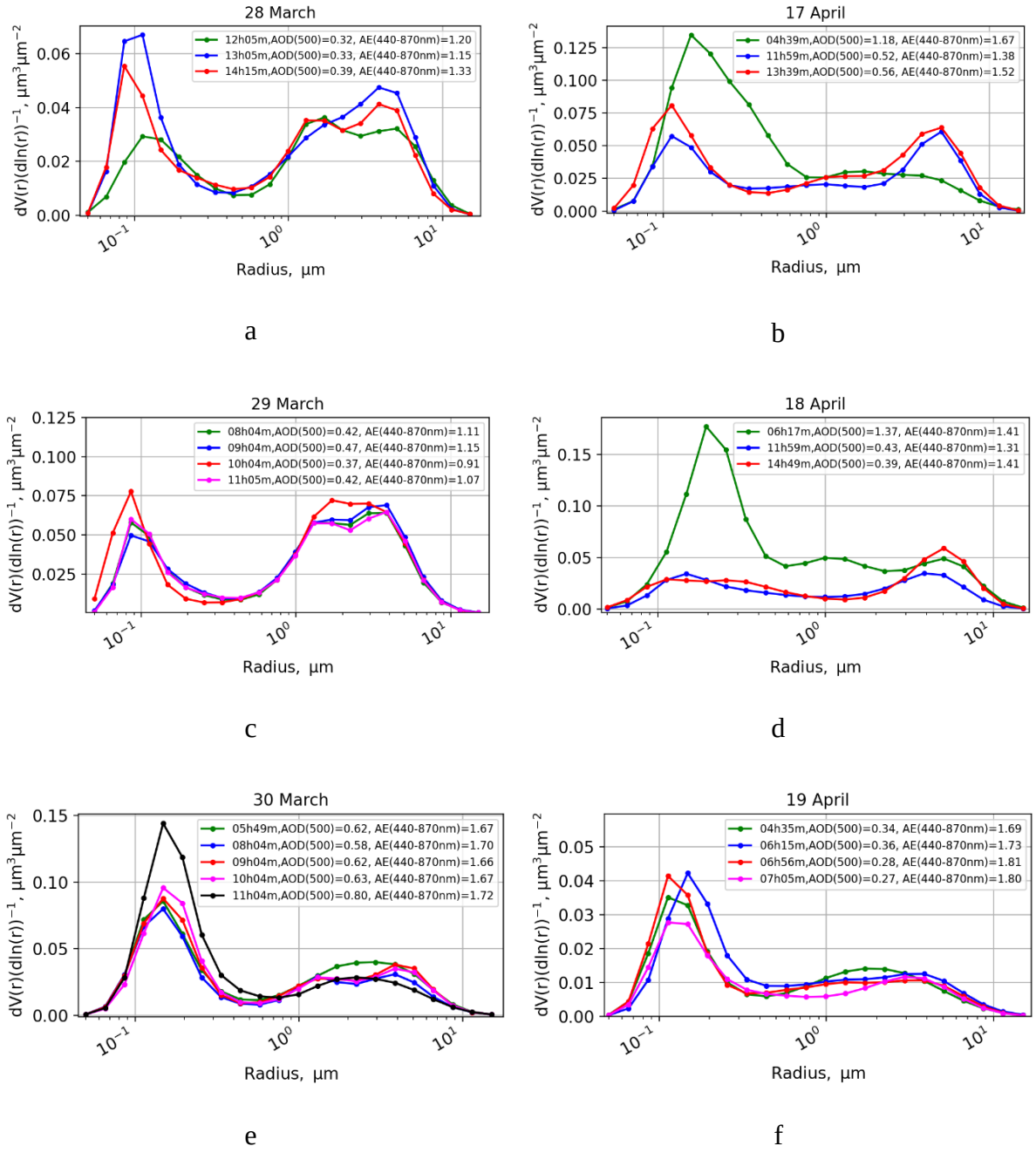

Figure 4.25. Aerosol particle distribution by volume sizes in the atmospheric column above AERONET Kyiv station: (a. c, e) March 28–30; (b, d, f) April 17–19, 2020. Colors indicate the observation time (UTC), AOD (500 nm), and AE (440–870 nm). Data level 1.5.

This process is more likely in the open areas like steppe and forest-steppe areas than in forested areas in the north, which may explain the predominance of coarse mode aerosol in the particle size distributions during March 28–29 compared to the March 30 and April 17–19 periods (compare Fig. Fig. 4.25a,c,e with Fig. Fig. 4.25b,d,f). The coarse mode aerosol in March 28–29 case was a mixture of vegetation combustion products and mineral dust from

open areas at south and southeast of Ukraine. The dust intrusion to southeast of Ukraine also was seen from the Navy Aerosol Analysis and Pre-diction System (NAAPS) data on March 27, 2020, when the increased dust concentration "tongue" moved at lower layers of the atmosphere from the regions of Central Asia (more details can be found by following link https://www.nrlmry.navy.mil/aerosol_web/Docs/nrlmryonrprop.html).

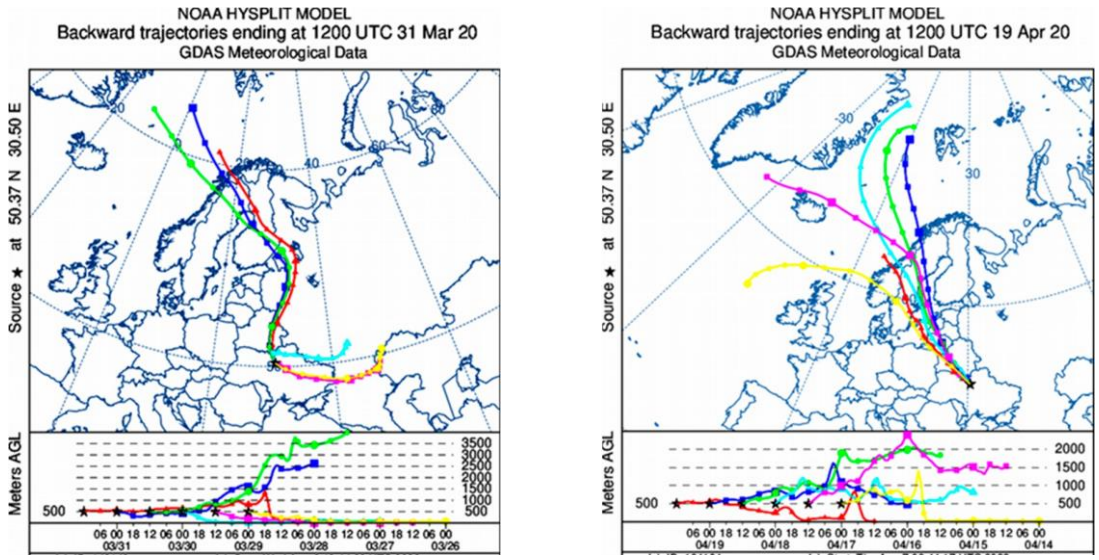

Figure 4.26. a) Backward trajectories of air mass transport at a height of 500 m above ground level from March 26–31, with the trajectory ending at the AERONET Kyiv station and for b) April 14–19. The trajectory data passed over fire-affected areas. The locations of Kyiv AERONET and AirVisual Golosiiv stations are marked with a star. The plots were generated using the HYSPLIT web service with GDAS meteorological data. Different colors correspond to the days and times when the air masses started moving along the respective trajectories: yellow – April 14, 00h UTC; pink – April 14, 12h UTC; blue – April 15, 00h UTC; green – April 15, 12h UTC; blue – April 16, 00h UTC; red – April 16, 12h UTC. Stars at a height of 500 m indicate when the corresponding air mass reached the AERONET Kyiv station.

On March 30, fine particles prevailed in the column of atmosphere over the Kyiv city (see Fig. 4.26e). This type size distribution is typical for aerosol from forest fires, see e.g. (Reid et al., 2005; Sayer et al., 2014). In that case, there is a lower content of soil dust, as air masses passed over areas with a predominance of forests (see Fig. 4.26a: red, green and blue trajectories), where fires were observed during the previous three days. Thus, these two periods of smoke transport, March 26–30, differ due to the difference in dominant vegetation types between the eastern and southeastern regions of Ukraine compared to the northern part of

Ukraine. The northern part of the country is characterized by mixed forests with wetlands and swamps. The eastern and southeastern regions are predominantly forest-steppe territories, characterized by a combination of forests and steppe vegetation, as well as significant open areas.

c) single scattering albedo and complex refractive index

As SSA depends on the complex refractive index (RI) of the aerosol particle, both parameters were analyzed together (see Fig. 4.27). The columnar SSA and RI were determined for the aerosols observed at the Kyiv AERONET site during events of significant pollution of the atmosphere in March and April 2020 were very changeable both in value and in spectral dependence (see Fig. 4.27). The SSA and RI variation is very significant both from day to day and during each day. During March 30 and the April 17–18 event, fine particles from forest fires dominated over the Kyiv city, which determined both the particle size distribution and the spectral dependence of SSA and RI (see Fig. 4.25, Fig. 4.26b).

The large values of SSA were retrieved on March 30 and April 17–18, when SSA (440 nm) varies from 0.97 to 1.0, and SSA (1020 nm) varies from 0.90 to more than 0.99. The lowest values of SSA were retrieved on March 28–29 with SSA (440 nm) and SSA (1020 nm) not more than 0.88. However, generally the SSA values were quite high during those events of the aerosol loading in the atmosphere over the Kyiv city. In addition, the prominent feature was the variation of the spectral dependence of the SSA for those events. Although SSA (440 nm) was generally larger than SSA (1020 nm), except for March 29, the slope of the wavelength dependence was various during a day. During the March 26–29 case, the effect of coarse mode aerosols appears both in the size distribution and in the spectral dependence of SSA and RI (see Fig. 4.27). The presence of the coarse mode aerosols leads to an increase SSA values with a wavelength on March 29 compared to March 30 and April 17.

The real part of RI values also increased with a wavelength, but imaginary part of the RI noticeably increased in the short wavelength part of the visible spectrum in comparison to the spectral dependence imaginary RI on April 17. On base of data from the AERONET site (Holben et al., 2018) we can estimate the uncertainties of spectral SSA for the Kyiv AERONET

site at events under study to be approximately not more than 0.025 at 440 nm, 0.030 at 675 nm, 0.035 at 870 nm and 0.045 at 1020 nm.

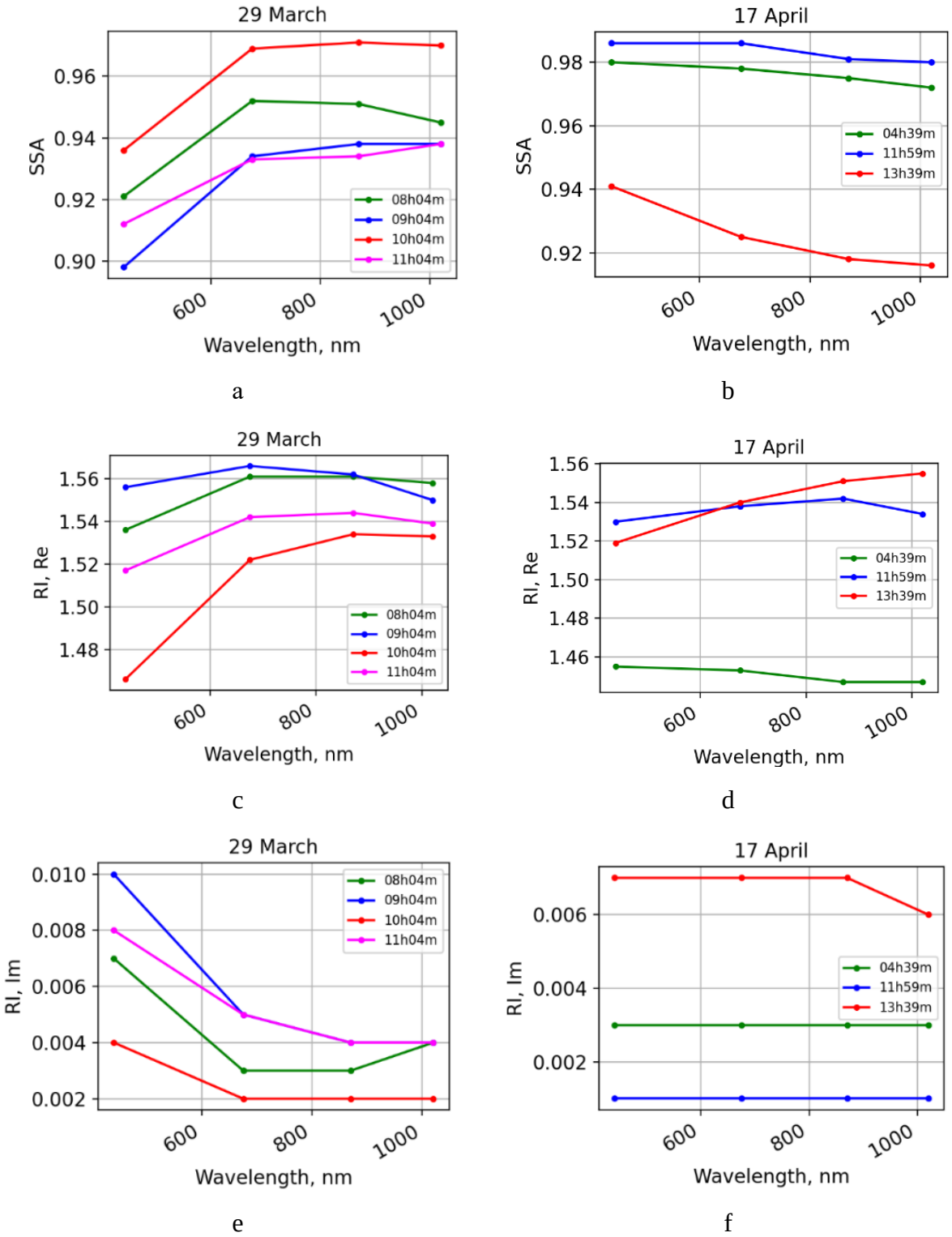

Figure 4.27. Spectral SSA and complex RI in the atmosphere over the Kyiv AERONET site from sun photometer observations at (a, c, e) March 29, 2020; (b, d, f) April 17, 2020. The legends show UTC time of observation. Data level 1.5.

The uncertainties of the real RI (440 nm) values can be estimated as less than 0.02 for AOD (500 nm) > 0.3, and the uncertainty for the imaginary RI (440 nm) values is less than 0.003, according to Sinyuk et al. (2020).

Forest areas in northern Ukraine are located within latitudes ranging from 51° to 52° N and are situated at the intersection of the temperate and boreal zones. Summarizing the research results, it can be concluded that the characteristics of aerosol particles detected above the AERONET Kyiv station during the fires caused by vegetation burning in March–April 2020 are consistent with the properties of smoke particles typical for this type of combustion.

4.3 Conclusions of Chapter 4

In this chapter, events of significant aerosol particle concentrations of various origins in the atmosphere over Kyiv (Ukraine) were analyzed. The characteristics of the particles, their transport, sources, and their impact on air quality and radiative forcing were studied.

The main results of Chapter 4 are as follows:

1) During September 1–7, a dense aerosol layer was observed over and around Kyiv, which was caused by active forest fires in different parts of Ukraine, including peatland fires. The influence of air mass movements on the smoke pollution in Kyiv was analyzed.

2) Using the CE 370 lidar, aerosol distributions with height were obtained, allowing for the study of particle evolution, vertical distribution, extinction coefficient, and mass concentration during over Kyiv during a field campaign carried out in 2015. This research initiative was made feasible through the generous support of the Laboratoire d'Optique Atmosphérique (University of Lille).

3) The study revealed that on September 2nd, the aerosol layer over Kyiv obstructed the passage of lidar light above the layer by approximately 500 meters. The extinction coefficient on September 3rd reached values exceeding 0.3 km^{-1}, and the maximum concentration on the same day was 250 μg m^{-3} at an altitude of approximately 4 km. The Angstrom Exponent exhibited high values, indicating the presence of small-sized particles typical of biomass burning. The high ratio of extinction coefficient to backscattering coefficient corresponds to a high content of small-sized aerosol particles. Image obtained using the MODIS instrument

allowed for the localization of fire sources and assessment of the extent of atmospheric smoke pollution.

4) Also, this section presents the initial results of the local AirVisual network of instruments for monitoring air quality in Kyiv, focusing on the measurement of $PM_{2.5}$ concentrations. The results of measurements from AirVisual stations, the APDA-371 HORIBA Popudrenka station, and the AERONET Kyiv station are described in detail, highlighting the air pollution by aerosol particles in Kyiv during the forest fires that affected significant areas of the city's northern region in March–April 2020.

5) The properties of aerosol particles during pollution, as indicated by measurements from the AERONET Kyiv station, are also discussed. These data enabled the assessment of variations in aerosol particle sizes and provided insights into their nature based on the Angstrom Exponent and its dependence on AOD at different wavelengths. The variability in optical properties and chemical composition of aerosol particles in smoke plumes passing over Kyiv is attributed to different burning materials and fire phases at different times. These characteristics of biomass burning aerosols are typical for the region.

The results of this section have been published in the following articles: Bovchaliuk et al. (2017), Zhang et al. (2022). Similar research involving the analysis of lidar measurements and sun photometer observations is presented in Appendix 2 and published in the work by Yukhymchuk et al., 2022.

Chapter 5

5. EVOLUTION OF ATMOSPHERIC COMPONENTS IN THE ATMOSPHERE OVER KYIV AND UKRAINE

This chapter shows the analysis of the Aerosol Optical Depth and Ångström Exponent observed within the atmospheric region above Kyiv, using data from the AERONET network. Furthermore, it presents the changes in the atmosphere over a 15-year period, focusing on changes in energy balance at the upper and lower atmosphere. Additionally, nearly five years of $PM_{2.5}$ observations in Kyiv provided by AirVisual were analyzed. Moreover, this section elaborates on the detailed shifts observed in AOD, AE, $PM_{2.5}$, CO, SO_2, and SO_4 across Ukraine's atmosphere over the past 15 years, drawing upon data from MERRA-2 reanalysis.

5.1 Long-term observations of AOD, AE, and RF at the AERONET station in Kyiv

a) Changes in AOD and AE

Observations at the AERONET station in Kyiv, located at the Main Astronomical Observatory of the National Academy of Sciences of Ukraine, have been carried out since 2008 and continue to the present, despite the ongoing state of war in Ukraine. Over this period, long-term series of nearly continuous data have been collected, which can be utilized for analyzing long-term changes in aerosol pollution in the atmosphere over Kyiv. In particular, the monthly average variations of aerosol optical depth for different seasons during the observation period, specifically from 2008 to 2023, are shown in Figure 5.1a.

As result from the provided graph (see Fig. 5.1), variations in aerosol optical depth (AOD) are seasonally dependent, with typically higher values during spring and summer. These

peaks are often associated with agricultural activities (field cultivation, other farming practices) and climate characteristics (dry grass in spring prone to burning, increased likelihood of forest fires during this period). Such events, along with aerosol characteristics, were specifically discussed in the previous chapter 4.

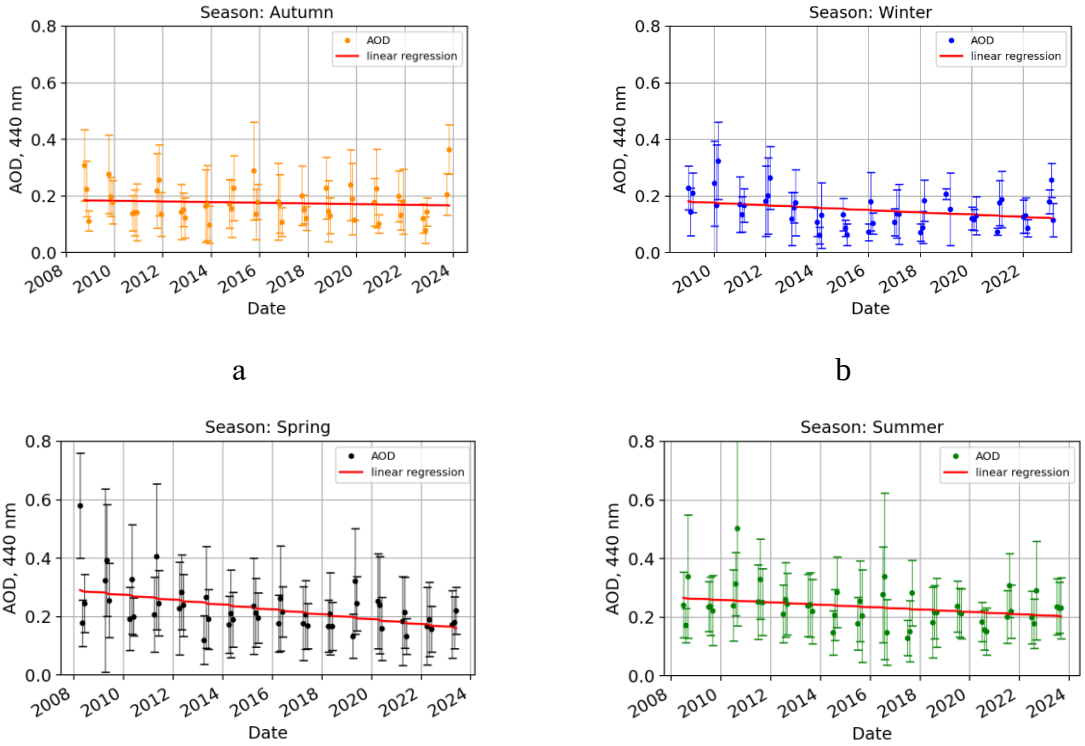

Figure 5.1. Seasonal variations of aerosol optical depth (AOD) at a wavelength of 400 nm and its standard deviation for: a) Autumn; b) Winter; c) Spring; and d) Summer during the period from 2008 to 2023, based on observations at the AERONET station in Kyiv. Data level 2.0 until 2019, from 2019 level 1.5.

In the autumn period, AOD values ranged from 0.1 to 0.2 between 2008 and 2023 (see Fig. 5.1a). Similar values are observed in the winter period (see Fig. 5.1b), although in most cases, AOD does not exceed 0.2, especially after 2012. In the spring period, as mentioned earlier, maximum AOD values are observed within the range of 0.1 to 0.4 (see Fig. 5.1c). In the summer period, AOD slightly decreases but remains within the range of spring values, although with a smaller number of months reaching 0.3 (see Fig. 5.1d).

To assess the dynamics of AOD, a linear regression was calculated, which reflects the relationship between variables and allows predicting AOD values over time. To find the parameters "a" and "b" of the linear model, the method of least squares was used. This method

seeks values of "a" and "b" that minimize the sum of squares of deviations between observed values of "y" and values predicted by the linear model. Even to the naked eye, there is a noticeable trend of decreasing AOD, especially in the case of spring. Furthermore, the slope of the line representing linear regression for this season is –0.0028, while for summer and winter, it is –0.0014, and for autumn, it is –0.0004. Based on this, one can conclude that according to AERONET observations for Kyiv from 2008 to 2023, there is a tendency of decreasing AOD values for all seasons.

The following figure (see Fig. 5.2) illustrates the variation of the Ångström Exponent during the same time period (from 2008 to 2023 inclusive) calculated at wavelengths of 440–870 nm, based on observations from the AERONET station in Kyiv. In general, the values of AE (440–870 nm) are within the range of 1.1 – 1.7 for all seasons. However, during summer and autumn, the values are slightly higher than those for winter and spring.

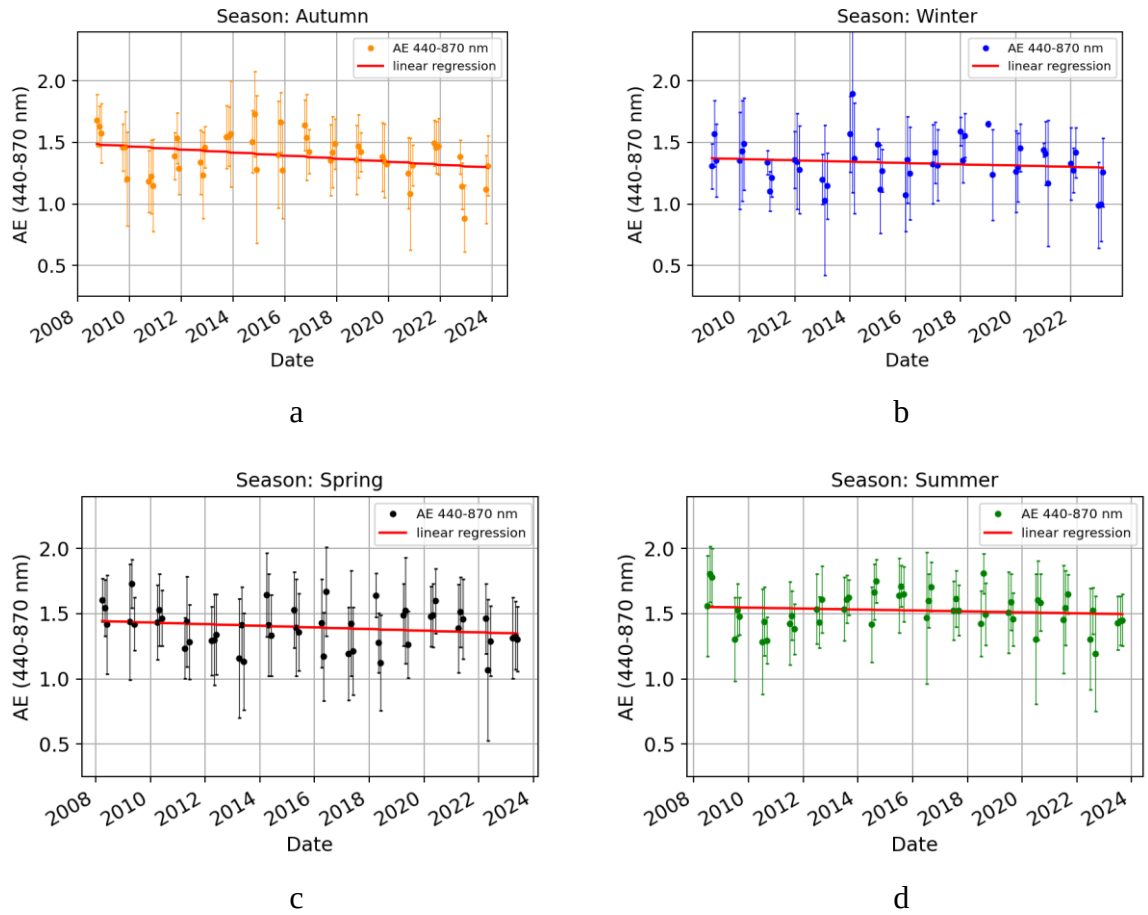

Figure 5.2. Seasonal variations of the Ångström Exponent (AE) at wavelengths of 400–870 nm and its standard deviation for: a) Autumn; b) Winter; c) Spring; and d) Summer during the period from 2008 to 2023, based on observations at the AERONET station in Kyiv. Data level 2.0 until 2019, from 2019 level 1.5.

Reduction of particles with smaller sizes in the winter period is associated with the influence of a seasonal pollution source – building heating (coal is used in boilers, many private houses can use wood and other types of fuel, which result in emissions of combustion products into the atmosphere). Weather conditions also contribute to the formation of particles with larger sizes (high humidity, low temperatures). Conversely, during summer, high temperatures, other aerosol sources (vegetation, more active formation of particles from precursor gases under the influence of solar radiation, lower humidity) contribute to the reduction in particle size and their longer atmospheric lifetime.

As in the previously discussed AOD analysis, a linear regression was also calculated for AE to assess its behavior. The slope of the curve for autumn is –0.0042, for winter –0.0018, for spring –0.0021, and –0.0012 for summer (see Fig. 5.2). This indicates a decrease in AE (400–870 nm) for all seasons. Such a trend suggests some changes in the aerosol composition in the atmosphere over Kyiv, particularly an increase in particle size. This trend is most pronounced during autumn. During this period, the situation may be associated with an increase in hot days in autumn and, as a result, a higher presence of mineral dust in the air. During summer, AE values show little variation across all years. The reasons for the decrease in AE during autumn and winter may be similar, and in the case of winter, a reduction in snow cover may also play a role. Additionally, in Kyiv, other factors such as transportation and industrial production may have an impact, requiring further investigation.

b) Long-term variations in radiative forcing

Changes in aerosol properties indicate changes, particularly in their chemical composition, which consequently impact the radiative characteristics of particles and, as a result, radiative forcing (RF) and its variations during the observation period at the AERONET Kyiv station. Figure 5.3 illustrates variations in Radiative Forcing (RF) at both the Top of the Atmosphere (TOA) and the Bottom of the Atmosphere (BOA) over Kyiv for different seasons. This data spans from 2008 to 2023 and is derived from sun photometer observations within the AERONET network. In contrast to the BOA, RF values at the TOA are generally smaller, primarily ranging from –20 to 0 W m^{-2}. Although a few data points with positive values were observed during the winter season (as seen in the blue curve in Figure 5.3b), the highest RF values at the TOA are predominantly associated with this period.

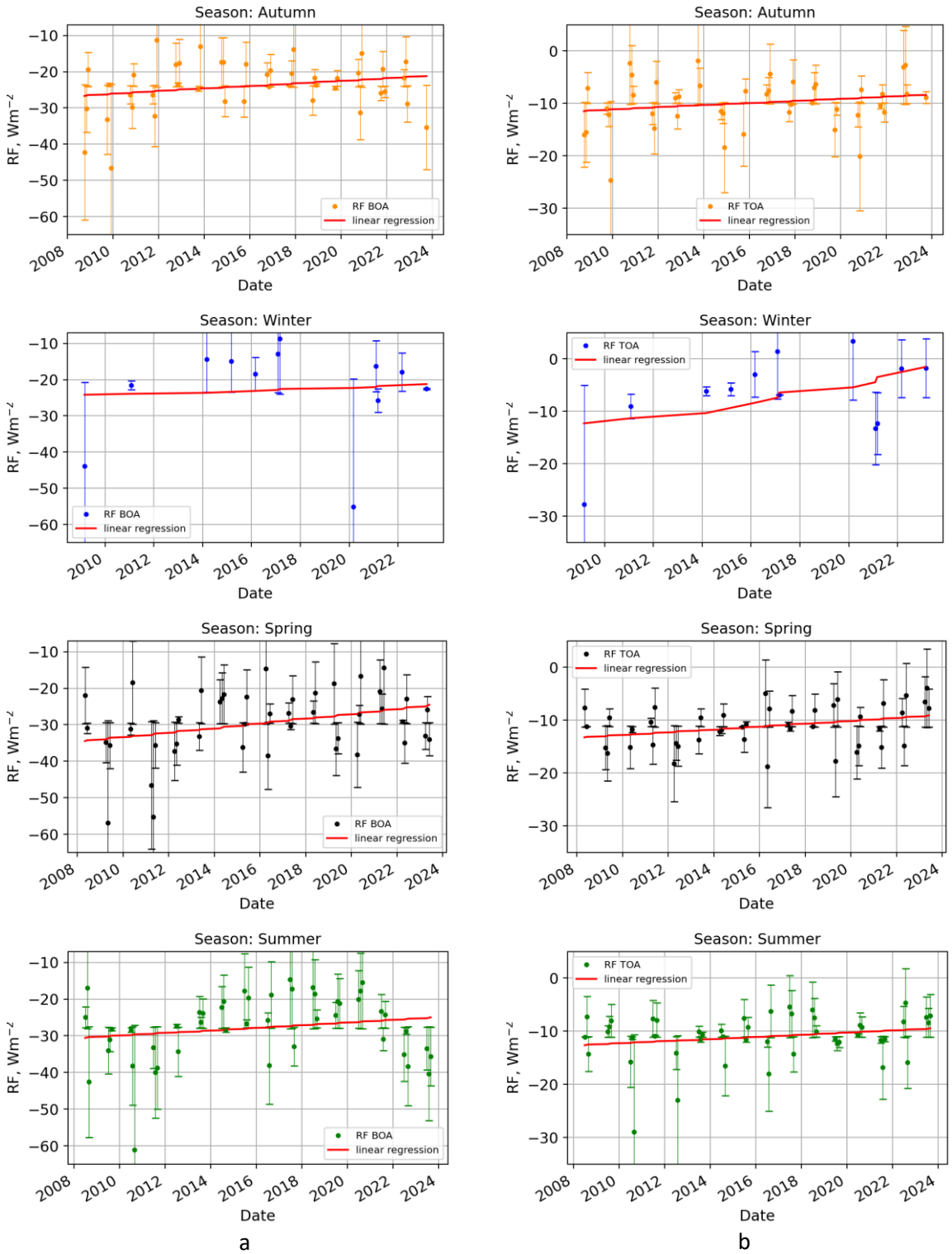

Figure 5.3. Seasonal changes in radiative forcing at the boundary a) bottom of the atmosphere (BOA) and b) top of the atmosphere the period from 2008 to 2023 based on observations from the AERONET Kyiv station. Observations are monthly averaged. Data level 2.0 until 2019, from 2019 level 1.5.

Conversely, the lowest values are characteristic of summer, falling within the range of –30 to –10 W m^{-2} (as indicated by the green curve in Figure 5.3b). The slope of the linear regression curve in this case is 0.0738 for autumn, 0.0969 for spring, 0.0689 for summer, and 0.979 for winter. In summary, aerosol radiative forcing at the TOA and BOA for all seasons from 2008 to 2023 shows a trend towards an increase. These results suggest that both the upper and lower atmospheric boundaries are experiencing a tendency towards temperature elevation.

5.2 Variations in aerosols and other components in the atmosphere over Ukraine

5.2.1 Changes in AOD and AE in the atmosphere over Ukraine during 2008–2023

To investigate the long-term variations in aerosol optical depth, Ångström Exponent, and other atmospheric components, the analysis employed the online platform GIOVANNI (https://giovanni.gsfc.nasa.gov/giovanni/). The study used the MODIS observations and MERRA-2 reanalysis such as: MODIS Atmosphere L3 Monthly Product (08_L3) and "MERRA-2 tavgM_2d_aer_Nx: 2d, Monthly mean, Time-averaged, Single-Level, Assimilation, Aerosol Diagnostics V5.12.4 (M2TMNXAER)" product. Figure 5.4 illustrates the variation of AOD (see Fig. 5.4a) and AE (see Fig 5.4b) for each season from 2008 to 2023, inclusive. The data is averaged for the territory of Ukraine. For aerosol optical depth, MODIS-Aqua observations were used (product: Average Aerosol Optical Depth 550 nm, Deep Blue, Land-only, monthly data, spatial resolution 1°). For the Angstrom Exponent parameter, MERRA-2 analysis was employed (product: Average Total Aerosol Angstrom Exponent (470–870 nm), monthly data, spatial resolution 0.5 x 0.625 degrees).

According to the results obtained from satellite observations, the values of AOD in the air over the territory of Ukraine range from 0.05 to 0.25. Specifically, the highest values are observed in summer (see Fig 5.4a, green curve), which differs from the in situ measurements for Kyiv (see Fig. 5.3a). In contrast, during autumn and spring, AOD values are practically the same and have similar magnitudes (see Fig 5.4a, orange and black curves). The lowest AOD values are characteristic of winter (see Fig 5.4a, blue curve). The higher AOD values observed in summer may be attributed to increased anthropogenic emissions and more intensive use of

transportation during this period, particularly on a country–wide scale. Additionally, there is an additional contribution from organic aerosols, including plant particles. For spring, autumn, and winter, AOD values are lower and relatively similar. In the case of the Angstrom Exponent, the results for Ukraine show better correlation (in terms of seasonality) with the observations from the AERONET station in Kyiv, although they are lower. In this case, AE varies in the range of 1 to 1.3. Depending on the season, different aerosol components dominate in the air over Ukraine. According to results, the fine mode aerosol component prevails in summer (see Fig 5.4b, green curve), while the coarse mode component is more widespread in winter (see Fig 5.4b, black curve). Spring values (see Fig 5.4b, blue curve) are closer to winter values, while autumn values (see Fig 5.4b, orange curve) are slightly lower than summer values.

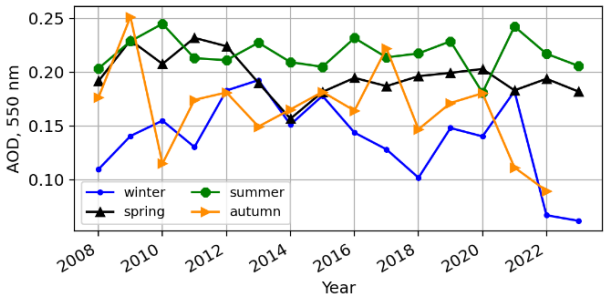

a

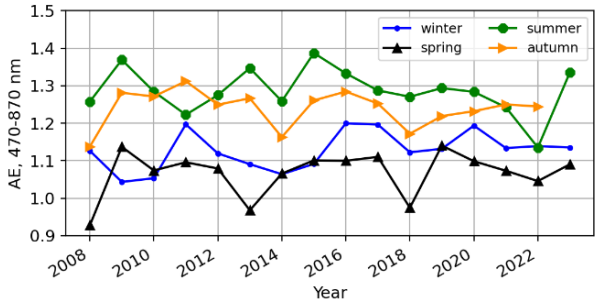

b

Figure 5.4. Seasonal variations of a) Aerosol Optical Depth (AOD) at a wavelength of 550 nm and b) Angstrom Exponent (AE) at wavelengths of 440–870 nm in the atmosphere over Ukraine during the period 2008–2023. Data from the GIOVANNI platform: a) MODIS, b) MERRA-2 reanalysis. Seasons are indicated by different colors.

Considering the geographical location and the diversity of climatic conditions and vegetation in Ukraine, the observed AOD values may differ from the in situ measurements done in the city of Kyiv. However, the range of AOD values derived from MODIS satellite observations closely aligns with the results recorded at the AERONET station in Kyiv.

Regarding the Angstrom Exponent, an important factor influencing the composition and concentration of aerosols could be the presence of mineral dust from the extensive steppe zone of Ukraine, which may contribute to a lower overall Angstrom Exponent value across the entire territory. In addition, the obtained results confirm the seasonal and spatial variability in the aerosol composition and concentration in the atmosphere over Ukraine.

5.2.2 The 15-year dynamics of black carbon, $PM_{2.5}$, CO, SO_2, SO_4 and organic carbon

The concentrations of black carbon (BC), $PM_{2.5}$, CO, SO_2, SO_4 and organic carbon over the entire territory of Ukraine from 2008 to 2023 are shown in Figure 5.5. The analysis was applied for each season (indicated by different colors) using MERRA-2 reanalysis and the GIOVANNI platform. Particularly "MERRA-2 tavgM_2d_aer_Nx: 2d, Monthly mean, Time-averaged, Single-Level, Assimilation, Aerosol Diagnostics V5.12.4 (M2TMNXAER)" product was used.

Black carbon is a constituent of particles that form as a result of incomplete combustion of coal and other fossil fuels, vehicle engine emissions, and biomass burning. The increased concentration of inorganic carbon is primarily linked to electricity generation from thermal power plants and residential heating, particularly when coal is utilized. A seasonal cycle with a peak in black carbon particles is observed over Central and Eastern Europe during the cold period when there is a high demand for household heating (Sówka et al., 2019; Zanatta et al., 2016; Kucbel et al., 2017).

Regarding the twelve-year dynamics (see Fig. 5.5a), the highest concentrations are expectedly observed during the autumn–winter period, averaging within the range of 0.5–0.7 μg m^{-3}. In the spring-summer period, the concentrations range from approximately 0.4–0.55 μg m^{-3}. However, some values deviate from these ranges, particularly the peaks in autumn concentrations in 2014 and 2015, and the high spring value in 2020, which are associated with the influence of intense forest fires, including those discussed in the study.

Figure 5.5b illustrates the change in average near-surface concentrations of $PM_{2.5}$ particles from 2008 to 2023. The concentrations range between 10–15 μg m^{-3} and exhibit interesting variations over this period. Particularly interesting is the fact that before 2014, the

maximum concentration of solid particles is observed during the winter period and decreases thereafter (see Fig. 5.5b, blue line). In contrast, the concentrations of $PM_{2.5}$ for other seasons (especially spring and summer) do not show a similar trend and demonstrate relatively stable values (see Fig. 5.5b, black and green lines, respectively).

The sharp decrease in $PM_{2.5}$ concentration during the winter period after 2014 may be associated with a change in fuel used during the heating season. The lowest values of solid particles in Ukraine are characteristic of the summer season (see Fig. 5.5b, green line). This is due to the absence of heating and less agricultural activity, with the peak of agricultural work occurring in spring and autumn. The latter factor contributes to relatively higher spring concentrations of $PM_{2.5}$ compared to summer (plus the heating season typically extends into March, and there are often fires that occur almost every year). As for the autumn variations (see Fig. 5.5b, orange line), namely low concentrations until 2013, a peak in 2014, and a decrease from 2021, in this case, additional factors are added to agricultural work and the start of the heating season: weather conditions, as well as the risk and formation of forest fires. Dry and warm weather increases the likelihood of ignition compared to cool and rainy weather. Additionally, dry weather facilitates significant transport of mineral dust from open soil due to agricultural activities.

It is advisable to consider other atmospheric pollutants in addition to black carbon and $PM_{2.5}$, including CO, SO_2, and SO_4. While carbon monoxide (CO) is not particularly effective as a direct greenhouse gas in the atmosphere, its influence becomes substantial through reactions with hydroxyl radicals (OH), leading to a decrease in their abundance. These hydroxyl radicals are instrumental in reducing the lifespan of potent greenhouse gases such as methane and carbon monoxide. Consequently, the reduction in OH levels indirectly enhances the potential for global warming caused by these gases. In addition to its atmospheric impact, carbon monoxide, also known as a toxic gas, is a colorless and odorless gas. CO is emitted during combustion, and the major sources of its emissions into the environment are vehicles and machinery burning fossil fuels such as gasoline (https://www.epa.gov/), incomplete combustion of carbon-based fuels such as coal, wood, and oil (https://earthobservatory.nasa.gov/global-maps/MOP_CO_M).

Furthermore, various household items such as unvented gas and gas heaters, chimneys, and stoves (especially those with defects and operating conditions) release CO and can affect indoor air quality (https://www.epa.gov/). Carbon monoxide is poisonous and can lead to poisoning and death (high concentrations in enclosed, unventilated spaces). More information

on the risks and dangers of CO can be found on the websites of the United States Environmental Protection Agency (https://www.epa.gov/), World Health Organization (https://www.who.int/), etc.

Seasonal variations in surface CO concentrations in Ukraine are shown in Figure 5.5b. The highest concentrations of carbon monoxide are typically observed during the winter period, averaging around 140 ppbv (see Fig. 5.5b, blue line). The lowest CO concentrations, below 120 ppbv, are observed during summer (see Fig. 5.5b, green line). According to our data, CO concentrations have remained relatively stable from 2008 to 2020. The increase in CO levels for 2022 is not surprising due to the extensive combustion of fossil fuels, petroleum products, and the occurrence of fires resulting from the Russian invasion. Additionally, the operation of generators, typically fueled by gasoline or diesel, contributed to the increased levels of CO. The reasons for the elevated carbon monoxide values in 2021 are less apparent and could be a subject for further investigation beyond the scope of this study.

Also, carbon monoxide released during the combustion of fossil fuels, particularly in power plants, another dangerous substance, sulfur dioxide (SO_2), is emitted in large quantities. Smaller sources of SO_2 emissions include industrial processes such as metal extraction from ores, natural sources like volcanoes, as well as locomotives, ships, and other vehicles and heavy equipment burning high-sulfur fuels (https://www.epa.gov/). Gaseous sulfur dioxide can oxidize to form solid sulfate particles (SO_4). Sulfate aerosol primarily consists of sulfuric acid and corresponding salts, such as ammonium sulfate. In addition to the negative health effects on humans, high concentrations of gaseous SOx can also harm trees and plants by damaging leaves and inhibiting growth (EPA, https://www.epa.gov/). Moreover, SO_2 and other sulfur oxides can contribute to the occurrence of acid rain, which can damage sensitive ecosystems (EPA, https://www.epa.gov/).

Seasonal variations of SO_2 and SO_4 are shown in Fig. 5.5d and 5.5e, respectively. The highest concentrations of these substances are observed during winter, ranging from 4.5–5.4 μg m^{-3} for SO_2 and 3–4 μg m^{-3} for SO_4. Autumn values of SO_2 exceed the minimum summer concentrations (see Fig. 5.5d), while in the case of SO_4, autumn and spring concentrations are similar and higher than summer concentrations (see Fig. 5.5e). The winter increases are once again associated with the heating season, and the concentration of SO_4 is linked to SO_2. Differences in the correlation between autumn and spring concentrations of these compounds may be attributed to the peculiarities of the chemical processes between them, as well as other factors that may not be apparent at first glance. This topic requires further investigation.

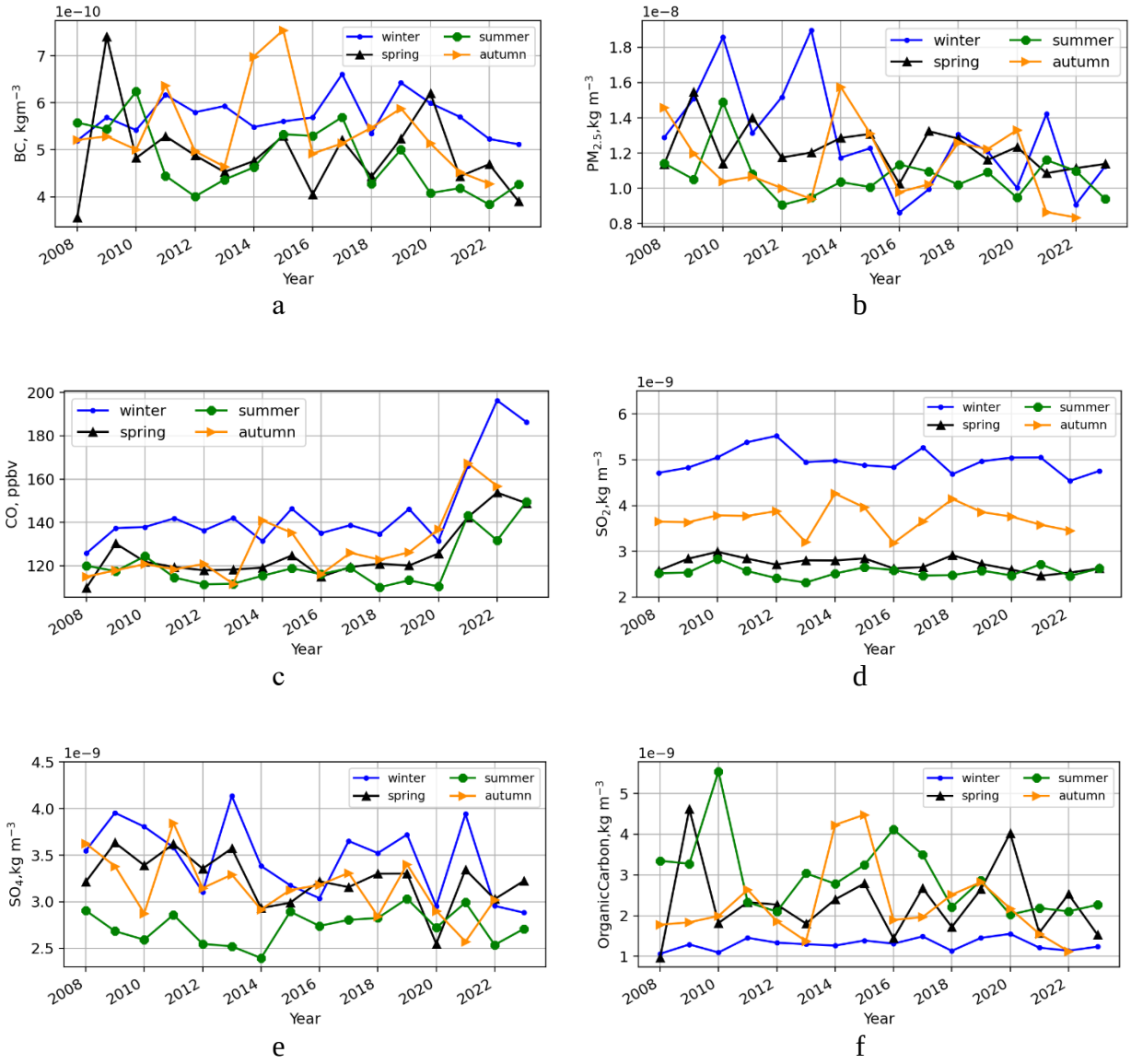

Figure 5.5. Seasonal variations in total surface mass concentrations of a) black carbon, b) $PM_{2.5}$, c) CO, d) SO_2, e) SO_4, and f) organic carbon in the atmosphere over Ukraine during 2008–2023. MERRA-2 reanalysis. Data from the GIOVANNI platform. Seasons are indicated by colors.

To this point, the types of pollutants and particles mentioned have had maximum concentrations during the winter period. The next type of aerosols, organic carbon, has the highest quantities in the atmosphere during the warm seasons, and its variations are presented in Figure 5.5e. In general, the amount of organic particles in the atmosphere ranges from 1 to 3 μg m^{-3}. The highest concentrations of SO_2 occur in autumn and summer, while the lowest concentrations are expected in winter when vegetation cover is almost absent (referring to the absence of leaves on trees and shrubs, agricultural crops, etc.). Additionally, an increase in

organic carbon content is observed during seasons associated with large-scale fires in or near Ukraine, such as the summer of 2010, autumn of 2015, spring of 2020, and others (see Fig. 5.5e).

These results indicate that changes in the concentrations of pollutants and aerosols in the atmosphere above Ukraine are influenced by seasonal variations. A significant amount of pollutants is emitted during the heating season due to the combustion of fossil fuels and firewood. Vehicle emissions, industrial activities, and agricultural practices also make a substantial contribution to increased atmospheric aerosols. In addition to industrial factors, there are natural factors that can increase the number of particles in the atmosphere, such as seasonal changes in vegetation cover and dry windy weather, which can enhance wind erosion of soil, resulting in the transport of mineral dust particles over long distances. Furthermore, weather conditions, combined with human carelessness or disregard for safety rules and behavior, can lead to large-scale forest and peat fires, the emissions of which worsen not only the air quality but also affect the energy balance in the Earth's atmosphere.

5.3 Changes in $PM_{2.5}$ in the atmosphere over Kyiv from 2019 to 2023 based on AirVisual observations

Monitoring of $PM_{2.5}$ concentration in the atmosphere over Kyiv using AirVisual air quality sensors began in July 2019 from the Nauky Avenue station. Over time, new stations were added, while the operation of certain stations was suspended. The observations of particulate matter concentration in the atmosphere over Kyiv from 2019 to 2023 for the Artema, Golosiiv, Nauky Avenue, Trosyanetska, and Chornobylska stations are shown in Figure 5.6.

Since all observation points are located within the city, it is not surprising that the obtained $PM_{2.5}$ concentration values are similar. The slight variation in values is caused by different traffic loads near the observation points, distance from park areas, and industrial facilities (the detailed placement of sensors is discussed in Section 3.1.3b).

The next figure (see Fig. 5.7) depicts the averaged concentrations of $PM_{2.5}$ based on weekly observations (across all available sensors during the given time period) and corresponding average values of the Air Quality Index (AQI). When averaging the data, it was assumed that measurements from each station have minor deviations from the mean value.

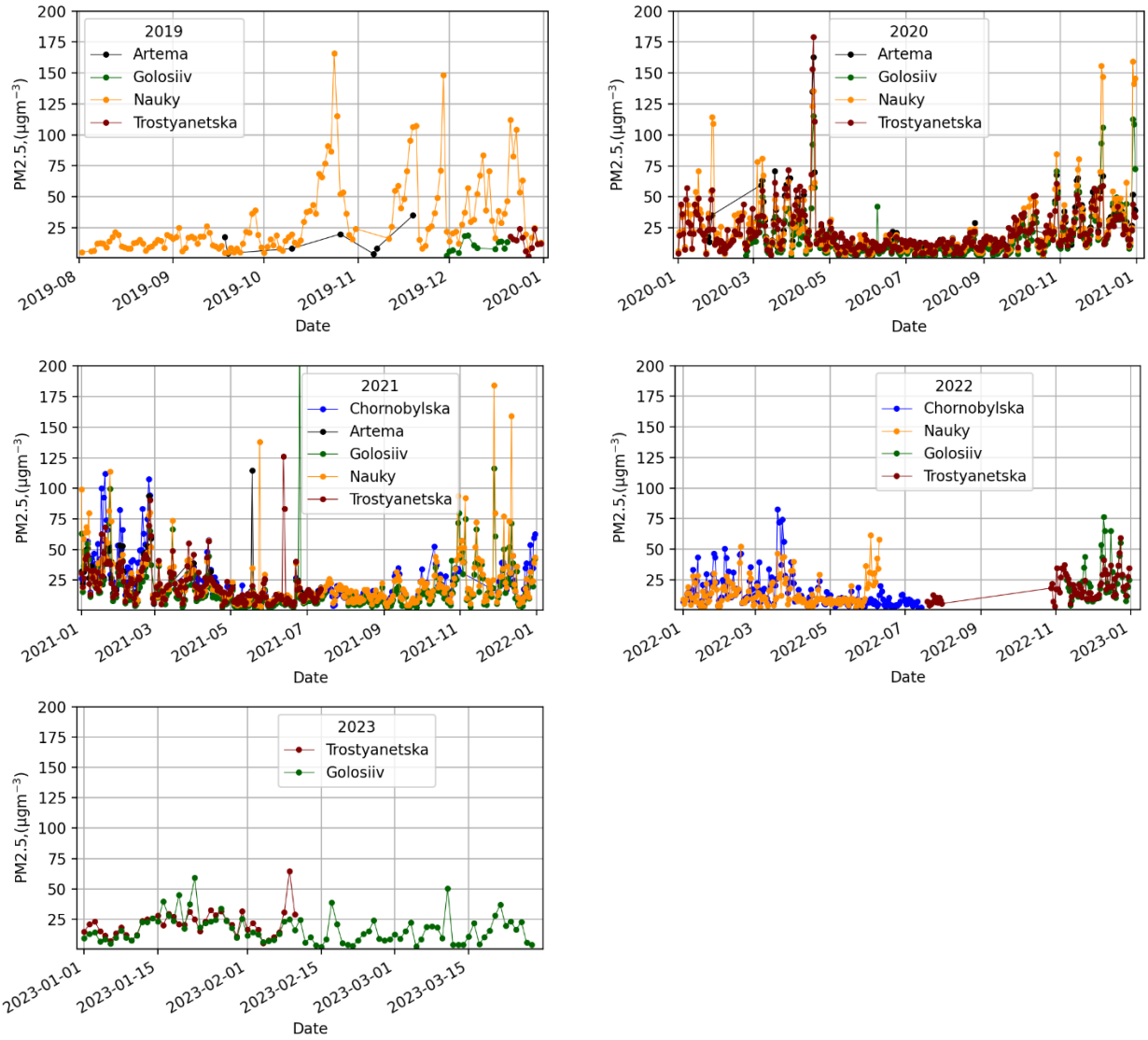

Figure 5.6. Concentration of particulate matter $PM_{2.5}$ in the atmosphere over Kyiv based on observations from AirVisual network stations: Artema, Golosiiv, Nauky, Trosyanetska, and Chornobylska, during the period of 2019–2023. The graphs indicate the year of observations and the name of the station, represented by different colors.

Therefore, it was logical to create a database that includes all measurements (considering the time of measurement). If multiple measurements were taken within a specific time interval, the average value was used. Since individual values throughout the day are not of interest for assessing seasonal changes, it is more appropriate to utilize the average values. At this stage, a 7-day period was chosen for the averaging process.

Therefore, regarding the seasonal variations of $PM_{2.5}$: the highest concentrations of these particles are observed from November to early April, corresponding to the cold season and the heating period (see Fig. 5.7a). The lowest concentrations are characteristic of the

summer period. It can be inferred that the combustion of fossil fuels significantly increases the level of $PM_{2.5}$ in the atmosphere above Kyiv. Winter values exceed summer values by 2 to 3 times. While during the warm period, $PM_{2.5}$ concentrations range from 10 to 20 μg m^{-3}, in winter they range from 15 to 40 μg m^{-3} and higher (see Fig. 5.7a).

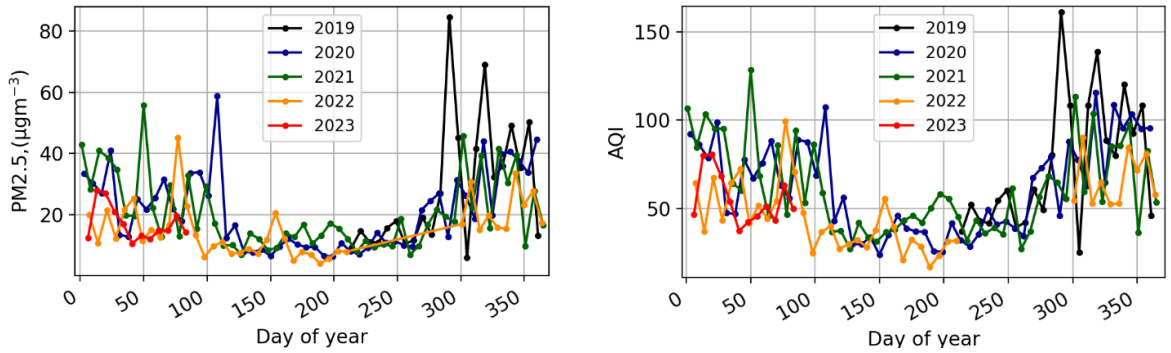

a b

Figure 5.7. Annual variations of a) $PM_{2.5}$ concentration and b) Air Quality Index (AQI) for Kyiv during 2019–2023. Observations are averaged on a weekly basis. The graphs indicate the year of observations.

The direct correlation between the Air Quality Index (AQI) and $PM_{2.5}$ concentration indicates that the lowest AQI values and hence the best air quality is observed in Kyiv from April to the end of October. Typically, during this period, the AQI does not exceed the recommended level of 50 by the WHO (see Fig. 5.7b). However, during winter, the AQI usually ranges from 50 to 100, and there are weeks when the air quality index exceeds the recommended standards by 2 to 3 times, particularly with a significant number of high values above 100 observed in the autumn periods of 2019 and 2020 (see Fig. 5.7b). The information about the number of measurements used and the standard deviation is provided in Appendix 3.

5.4 Conclusions of Chapter 5

In this chapter, long-term variations of aerosol properties (AOD, AE) and $PM_{2.5}$ based on in situ measurements from AERONET for Kyiv were analyzed, and the dynamics of aerosols and other atmospheric components based on MODIS measurements and MERRA-2 reanalysis (utilizing the GIOVANNI platform) were evaluated.

The main results of Chapter 5 are as follows:

1) Observations at the AERONET station in Kyiv, located at the Main Astronomical Observatory of the National Academy of Sciences of Ukraine, have provided nearly continuous data on aerosol pollution over Kyiv since 2008. AOD variations reflect seasonal fluctuations, with peaks often observed in late spring and autumn. This is associated with agricultural activities and climatic features such as dry grass in spring and a high likelihood of forest fires.

2) Over the observation period (2008–2023), there was a general tendency of decreasing AOD values. The monthly mean AOD values decreased from around 0.3 to 0.2, and for some months, they reached 0.1. This indicates a reduction in aerosol pollution, although it does not necessarily imply improved air quality.

3) The Angstrom Exponent, a parameter used to evaluate aerosol particle size, follows a similar pattern to AOD between 2008 and 2023. The overall trend indicates a decrease in AE, signifying an increase in the size of aerosol particles within the atmosphere over Kyiv.

4) Observations carried out at the AERONET station in Kyiv over the aforementioned time span have unveiled pronounced seasonal fluctuations and discernible inclinations toward amplified radiative forcing, both at the upper boundary of the atmosphere and at its lower boundary. These observed alterations underscore a substantial influence of aerosol particles on the energy equilibrium and a resultant escalation in atmospheric temperatures.

5) Analysis of data using the GIOVANNI platform showed that AOD values over Ukraine vary from 0.05 to 0.25, with the highest values characteristic of the summer period. AE values range from 1 to 1.3. Depending on the season, different aerosol components dominate the air over Ukraine. For example, fine aerosol components prevail in summer, while coarse components are more prevalent in winter.

6) A 12-year analysis of concentrations of black carbon, $PM_{2.5}$, CO, SO_2, SO_4, and organic carbon in the atmosphere over Ukraine from 2010 to 2022 was conducted. For black carbon, the highest concentrations are observed in the autumn-winter period. It was found that before 2014, the maximum $PM_{2.5}$ concentration occurred in winter, while after 2014, there was a noticeable sharp decrease in these particles during the winter period. $PM_{2.5}$ concentrations for other seasons remain relatively stable.

7) Carbon monoxide (CO) concentration is highest in winter. Overall, CO concentration variations are relatively stable from 2010 to 2020, and the increase in CO level in 2022 can be attributed to increased combustion of fossil fuels and the impact of the Russian invasion. The

highest levels of SO_2 and SO_4 are observed in winter, decreasing in the summer period. The increases are associated with the heating season, and the concentration of SO_4 depends on SO_2. Additionally, organic carbon, which is another type of aerosol, exhibits the highest concentrations in the atmosphere during the warm seasons.

8) It was observed that the concentrations of $PM_{2.5}$ particles over Kyiv were similar across all monitoring stations as they are located within the city. Small differences in values can be explained by variations in traffic loads, distance from green areas, and industrial sites.

9) The highest $PM_{2.5}$ concentrations are observed from November to early April, corresponding to the cold season and the heating period. The lowest concentrations are characteristic of the summer period. $PM_{2.5}$ values in the winter period exceed summer values by 2–3 times. From these data, it can be concluded that the seasonal variations of $PM_{2.5}$ in Kyiv are strongly influenced by the heating period when significant emissions of pollutants into the atmosphere occur.

The results of this chapter have been published in conference abstracts for IAMA (2022), ILRC 29 (2019), ILRC 30 (2022), YSC (2022), and AGU (2022).

Chapter 6

6. THE IMPACT OF RUSSIAN INVASION ON AEROSOLS AND ATMOSHERIC COMPONENTS IN UKRAINE AND KYIV

This chapter analyzes changes in air components such as $PM_{2.5}$, SO_2, SO_4, and black carbon across Ukraine due to the full-scale Russian military incursion using MERRA-2 modeling. It also investigates aerosol variations through AERONET data and $PM_{2.5}$ levels over Kyiv based on AirVisual observations. Additionally, the GRASP algorithm assesses changes in aerosol components like water, soluble materials, quartz, black carbon, brown carbon, and iron oxide from 2008 to 2022, studying their response to the ongoing war.

6.1 Russian invasion and occupation of Ukrainian territories

The barbaric war unleashed by Russia to seize Ukrainian territory has resulted in the loss of thousands of lives, both civilian and military, the destruction of city infrastructure, with some cities being completely devastated, and, naturally, environmental consequences. As a result of the burning of oil depots, military equipment, projectiles, and various weapons in water bodies, soil, and air, tons of different pollutants have been released. This study analyzed the impact on air quality based on available observations.

The Russian invasion of Ukrainian territory began in the night of February 24, 2022, at approximately 4 a.m. local time, with an aerial attack launching over 100 missiles (including short and medium-range ballistic missiles, cruise missiles, and sea-launched missiles) against Ukrainian air defense systems, supply depots, and airfields (https://understandingwar.org/) Russian ground forces advanced from four main directions (https://understandingwar.org/):

1) Belarusian Direction: Russian forces in Belarus are advancing towards Kyiv along both sides of the Dnieper River, presumably aiming to isolate the capital. The occupiers' troops have significantly advanced west of the Dnieper, capturing the Chernobyl Exclusion Zone.

2) Kharkiv Direction: Russian forces are conducting a frontal assault on Kharkiv from the northeast of Ukraine.

3) Donbas Direction: Russian forces are encircling through the Luhansk region rather than launching a frontal attack from the occupied Donbas.

4) Crimean Direction: Russian forces are achieving significant territorial gains by advancing north of Crimea. They have penetrated at least 60 kilometers inland and captured the city of Kherson, securing access to the Crimean Canal.

As of March 2, 2022 (see Fig. 6.1a), according to information from the Institute of War (https://understandingwar.org/), the situation regarding the advancement of the Russian army was as follows: the resumption of offensive operations against the western outskirts of Kyiv after a pause for resupply from February 27 to March 1; the initiation of an offensive operation in the Zhytomyr region; the resumption of the offensive in the northeast direction of Kyiv, reaching a line approximately 65 kilometers from the city center.

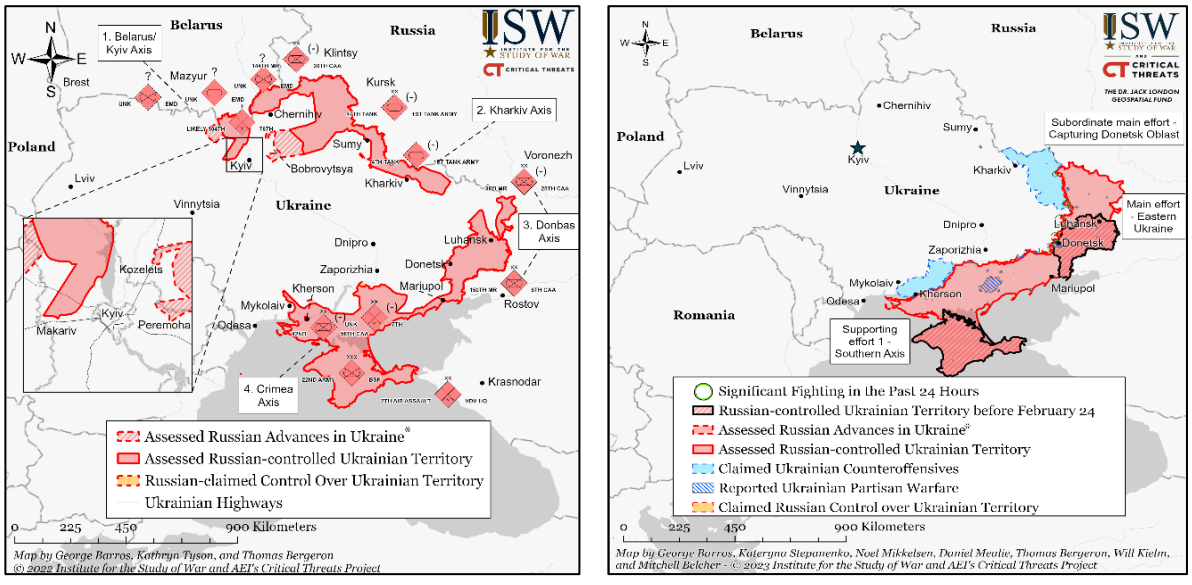

a b

Figure 6.1. Control over territories in Ukraine and main directions of Russian invasion and occupation as of a) March 2, 2022, 3:00 PM (EST) and b) March 24, 2023, 3:00 PM (ET). (Source of maps: Institute for the Study of War, https://understandingwar.org/).

Additionally, on March 2nd, Russian forces launched an attack on the center of Kharkiv and continued intensive bombardment of the city, likely resulting in an increased number of civilian casualties (https://understandingwar.org/). On the same day, Russian forces completely surrounded Mariupol and carried out a deliberate campaign to destroy critical civilian infrastructure and residential areas (https://understandingwar.org/). This information is provided to understand the extent of the Russian invasion into Ukrainian territory. Over the next few months, the Ukrainian army managed not only to halt the advancement of enemy forces but also to conduct a series of successful counteroffensives, liberating significant portions of Ukrainian territory. For more details on the movement of Russian and Ukrainian forces, as well as a map of military operations and the dynamics of territory capture and liberation in Ukraine since February 24, 2022, throughout the entire period of full-scale war, by the link: https://storymaps.arcgis.com/stories/733fe90805894bfc8562d90b106aa895.

As of March 24, 2023, there are several directions and objectives that Russia is attempting to achieve (see Fig. Fig. 6.1b, https://understandingwar.org/):

1) Luhansk Oblast. Objective: Capture the remaining territory of Luhansk Oblast and continue offensive operations in the eastern part of Kharkiv Oblast and the northern part of Donetsk Oblast.

2) Donetsk Oblast. Objective: Capture the entire territory of Donetsk Oblast, the area claimed by Russia's proxies in Donbas.

3) Supporting Operation - Southern Axis. Objective: Maintain positions on the front line and secure the rear from Ukrainian attacks.

4) Mobilization and force formation efforts. Objective: Expand combat capability without conducting a general mobilization.

5) Activities in the occupied territories. Objective: Consolidate administrative control over the annexed territories; forcibly integrate Ukrainian civilian population into the Russian sociocultural, economic, military, and governance system.

6) Significant activity in Belarus.

Operational information regarding the state of the Russian-Ukrainian war can also be found on official sources, including the General Staff of the Armed Forces of Ukraine or the Ministry of Defense (more details can be found at the following links: https://www.mil.gov.ua/, https://www.mil.gov.ua/).

6.2 The Impact of the Full-Scale Russian Invasion on BC, $PM_{2.5}$, SO_2, and SO_4 Evolution

Despite a more than one year of full-scale invasion, there is limited research dedicated to the topic of the environmental impact of war on the territory of Ukraine. Specifically, the influence of military operations on climate and pollution of the environment is analyzed in the study by Racioppi et al. (2022). Regarding aerosol characteristics, this issue remains even less explored. For instance, in the study made by Zalakeviciute et al. (2022), which focuses on the impact of the Russia-Ukraine war on air quality over Ukraine, concentrations of pollutants such as NO_2, CO, O_3, SO_2, and $PM_{2.5}$ were analyzed, averaged over various two-week periods during different years.

It is logical that in some regions, emissions have decreased, in areas affected by active combat, the amount of emissions significantly exceeds the average and includes hazardous toxic compounds, such as heavy metals, which not only enter the air but also contaminate and poison water and soil. These pollutants can have negative impacts on human health, animals, plants, and the ecological resilience of the regions. During the war, environmental pollution can be facilitated by military operations and the destruction of infrastructure, such as factories, plants, cities, and other facilities that can release hazardous substances into the environment, as well as the burning of machinery and fuel, and the chemicals released due to the detonation of projectiles, among others. The environmental consequences of the war will be felt in Ukraine for many years, including the destruction of ecosystems and various species of plants and animals. Vast territories of Ukraine are mined and pose a danger to human life and the environment. To understand the impact of the war on air quality over Ukraine, it is advisable to analyzed both short-term periods before and after the onset of full-scale invasion to assess the influence of combat operations on the local concentration of specific substances over specific regions of the country.

6.2.1 Changes of BC

As shown in previous sections, one of the main sources of atmospheric aerosol particles over Kyiv and Ukraine is the combustion processes (biomass burning, fuel combustion, heating season, transportation). One of the primary products of combustion is black carbon, the

concentration of which for different period during 2020–2023 will be discussed in this section. This time period is of interest for study because it encompasses the influence of various factors: in 2020, there was a lockdown due to the COVID-19 pandemic and large-scale forest fires in Ukraine; 2021 can be considered as a year with typical emissions, including black carbon; and in 2022 and 2023, a large-scale Russian invasion and war took place on the territory of Ukraine.

For the analysis of black carbon surface mass concentration for different periods, the MERRA-2 reanalysis was used, specifically products: "MERRA-2 tavg1_2d_aer_Nx: 2d,1-Hourly, Time-averaged, Single-Level, Assimilation, Aerosol Diagnostics V5.12.4 (M2T1NXAER)" and "MERRA-2 tavgM_2d_aer_Nx: 2d, Monthly mean, Time-averaged, Single-Level, Assimilation, Aerosol Diagnostics V5.12.4". Figure 6.2 illustrates the change in BC surface mass concentration before (see Fig. 6.2a) and after the full-scale Russian invasion (see Fig. 6.2b).

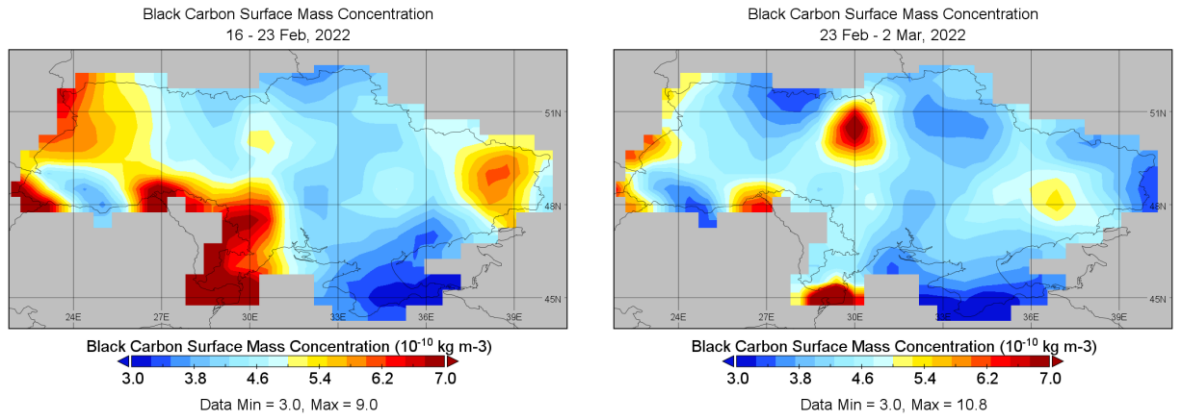

a b

Figure 6.2. Time-averaged black carbon surface mass concentration in the atmosphere over Ukraine during a) February 16–23, 2022, and b) February 24 – March 2, 2022. Modeling was provided using the MERRA-2 program. Data were obtained from the GIOVANNI platform. The unit of the color scale is 10^{-10} kg m^{-3}.

In both shown cases, BC concentrations over Ukraine range from 0.3 to 0.5 μg m^{-3}. Prior to February 24, higher concentrations between 0.5 and 0.6 μg m^{-3} are observed in eastern and western Ukraine, with the Odessa region displaying the highest values, reaching up to 0.9 μg m^{-3}. Additionally, somewhat elevated levels relative to the national average are characteristic of the Kyiv region.

Several factors contribute to the higher BC values in these regions. Emissions from industrial facilities in the east are significant, and it is worth noting that the situation along the

front line escalated even before February 24. In western regions, the widespread use of solid fuel heating also contributes to increased BC concentrations in the atmosphere. This factor, along with a significant volume of transportation, leads to higher values in the vicinity of Kyiv. Regarding the Odessa region, it should be mentioned that it serves as a major port with substantial maritime traffic, which can contribute to the highest BC values in Ukraine. With the onset of the invasion, the concentration of BC decreased across the entire territory of Ukraine, except for the Kyiv region and parts of the southern eastern areas. Notably, these directions align with the advancement of the Russian military deeper into Ukrainian territory. Concerning the decrease in BC values over a substantial portion of Ukraine, a significant role was played by the reduction in vehicular traffic and the temporary cessation of numerous industrial facilities.

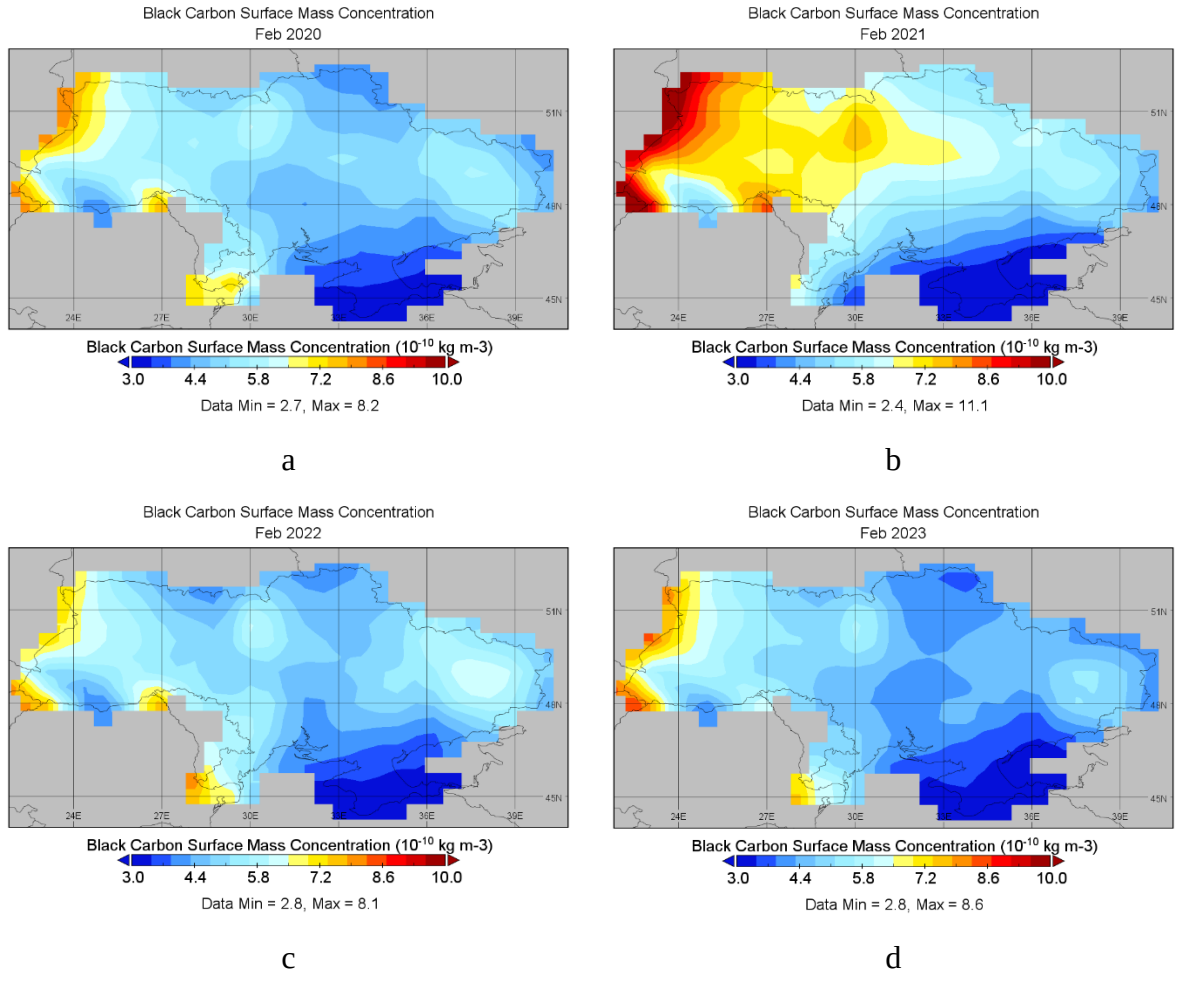

Figure 6.3. Time-averaged black carbon surface mass concentration in the atmosphere over Ukraine during a) February 2020, b) February 2021, c) February 2022 and d) February 2023. Modeling was provided using the MERRA-2 program. Data were obtained from the GIOVANNI platform. The unit of the color scale is 10^{-10} *kg* m^{-3}.

Consider the fluctuations in black carbon concentration throughout February and March of 2022 and 2023, contrasting them with preceding years, specifically 2020 and 2021. Figure 6.3 illustrates the average black carbon concentration on the surface in February from 2020 to 2023. The data indicates that a year after the full-scale invasion, the concentration in February was even lower across a significant area of Ukraine compared to previous years, ranging from 0.3 to 0.65 μg m^{-3}. For February 2022, there's also an absence of elevated values, potentially due to the invasion occurring late in the month and localized black carbon emissions having minimal impact on the overall picture. However, the situation is more complex for 2021 (see Fig. 6.3b) as the black carbon concentration values on the Western and Northwestern territories of Ukraine range from 0.65 to 10 μg m^{-3} and higher. The reasons behind these values remain unclear.

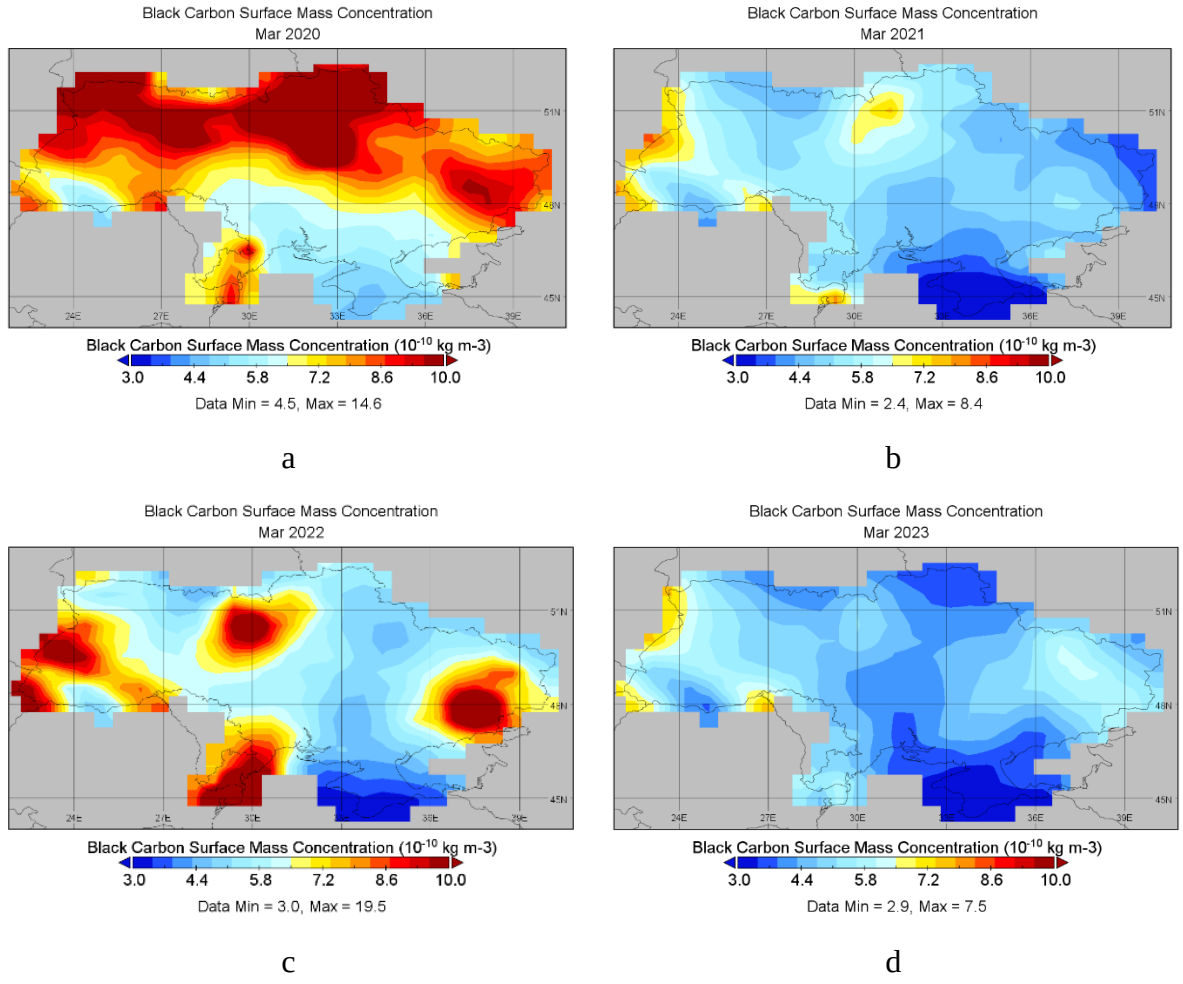

Figure 6.4. Time-averaged black carbon surface mass concentration in the atmosphere over Ukraine during a) March 2020, b) March 2021, c) March 2022 and d) March 2023. Modeling was provided using the MERRA-2 program. Data were obtained from the GIOVANNI platform. The unit of the color scale is 10^{-10} *kg* m^{-3}.

While analyzing the black carbon surface mass concentration across March from 2020 to 2023, the impact of military actions becomes clear, significantly influencing the monthly outcomes (see Fig. 6.4), similar to the period following the full-scale invasion (Fig. 6.2b). In comparison with March 2021 and 2023, notably higher concentrations were observed in March 2022, particularly in the Kyiv region and its surrounding areas, as well as in the Southwestern and Eastern parts of Ukraine. Elevated levels were also notable in the Odessa region. March 2020 also saw heightened black carbon levels across nearly the entire territory of Ukraine, reaching a peak concentration of 1.46 μg m^{-3}, while for March 2021, this figure was at 1.95 μg m^{-3}.

Figure 6.5 presents a map of surface concentrations of black carbon in the atmosphere over Ukraine during the winter periods from 2020 to 2022. It should be noted that the usually highest concentrations of black carbon are observed specifically during the winter-spring period (lower concentrations are obtained for the summer and autumn periods, see Fig. 6.7 and Fig. 6.8). The concentrations for winters are similar for the years 2020 and 2021, with higher concentrations of black carbon observed in the Western region of Ukraine, in range 0.65 – 1 μg m^{-3} (see Fig. 6.5a,b).

In the central regions of Ukraine, concentrations decrease with the lowest concentrations of black carbon observed in the south. This result may be related to small temperature differences (warmer winters in southern Ukraine) as well as different heating methods, with wood burning being more common in the western and northwestern regions. The winter of 2021–2022 shows a similar distribution of concentrations but with slightly lower values (see Fig. 6.5c). This result may be attributed to the displacement of a significant portion of the population from southern and eastern regions of Ukraine to safer areas due to the onset of full-scale Russian aggression.

During the winter of 2022–2023, black carbon concentrations are slightly higher than the previous winter but do not exceed the results for the winters of 2019–2020 and 2020–2021. In addition to the impact of heating (which, along with relatively mild winters and economic policies, may have contributed to the decrease in overall black carbon levels for the winter of 2022–2023, see Fig. 6.5d), transportation should also be mentioned. Heavy traffic congestion was observed in the early days of the full-scale invasion (as people attempted to leave for safer places outside major cities and flee the territory of Ukraine), but a significant decline occurred in the following months.

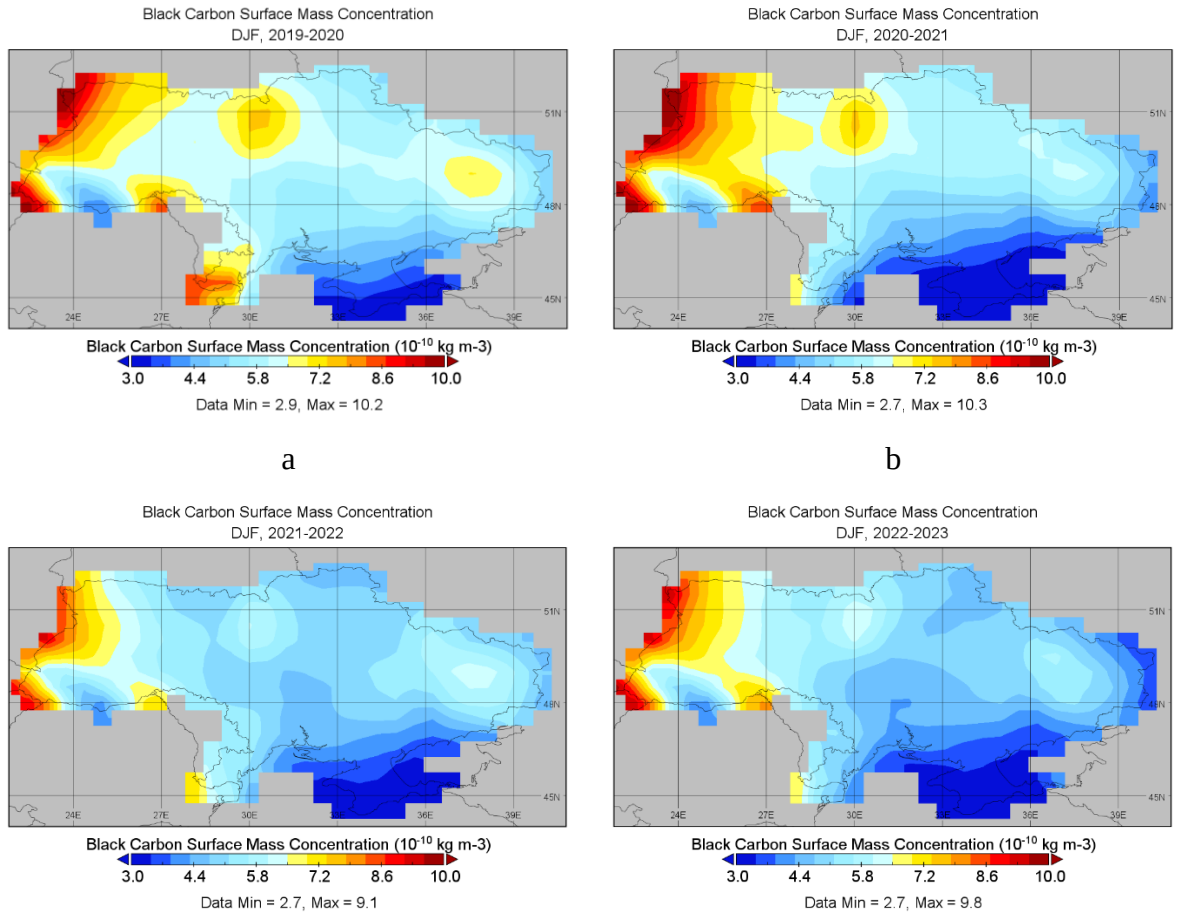

Figure 6.5. Time-averaged black carbon surface mass concentration in the atmosphere over Ukraine during a) winter 2019 – 2020, b) winter 2020 – 2021, c) winter 2021 – 2022 and d) winter 2022 – 2023. The abbreviation DJF represents the months: December, January, and February. Modeling was provided using the MERRA-2 program. Data were obtained from the GIOVANNI platform. The unit of the color scale is 10^{-10} kg m^{-3}.

Spring concentrations of black carbon are lower than winter concentrations, which can be attributed to the end of the heating season. However, significant fire risks and the practice of burning dry grass, which often leads to large-scale fires, contribute to higher concentrations. In particular, the increase in black carbon concentrations to around 1.7 µg m^{-3} in the northern regions of Ukraine, including the Kyiv region and the Chornobyl zone (see Fig. 6.6a), is associated with the spring fires in 2020 discussed in the previous section. No significant anomalies are observed in the spring of 2021, with low carbon values characteristic of the entire territory of Ukraine and slightly higher values in the western regions.

As for the spring of 2022, an increase in black carbon is observed in three additional regions compared to the previous springs of 2020 and 2021: the Kyiv region, the region

bordering Donetsk and Luhansk regions, and the Odessa region (see Fig. 6.6). This dynamic may be attributed to the increase in forest and industrial fires as a result of military actions, including the attack on Ukrainian infrastructure by Russian forces. Spring 2023 displays the lowest values of black carbon within this time frame, ranging from 0.25 to 0.65 μg m^{-3} (see Fig. 6.6d).

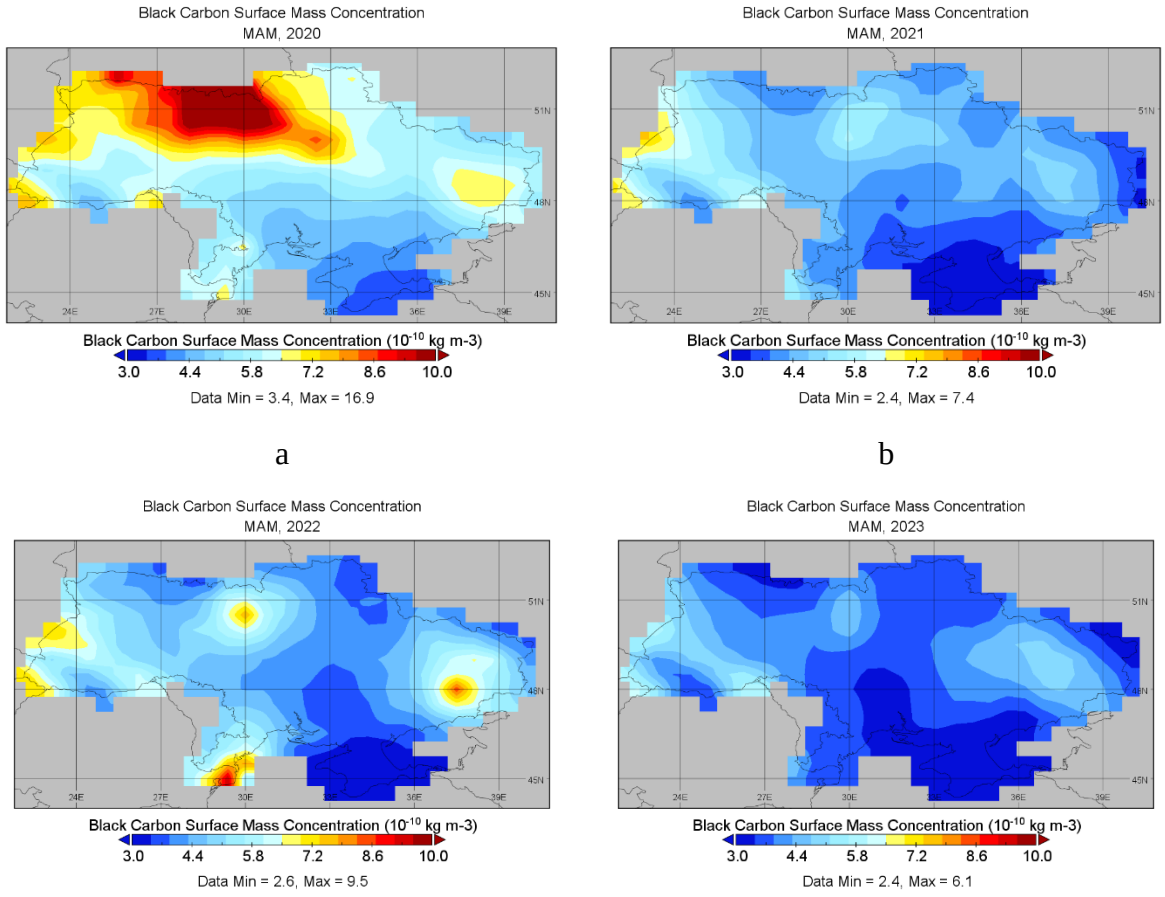

Figure 6.6. Time-averaged black carbon surface mass concentration in the atmosphere over Ukraine during a) spring 2020, b) spring 2021, c) spring 2022 and d) spring 2023. The abbreviation MAM represents the months: March, April, and May. Modeling was provided using the MERRA-2 program. Data were obtained from the GIOVANNI platform. The unit of the color scale is 10^{-10} kg m^{-3}.

The summer season is characterized by the lowest surface mass concentrations of black carbon, not exceeding 0.65 μg m^{-3} (see Fig. 6.7). For all years both the values and spatial distribution are similar, with peaks in the western, southeastern parts of Ukraine and near Kyiv regions (see Fig. 6.7).

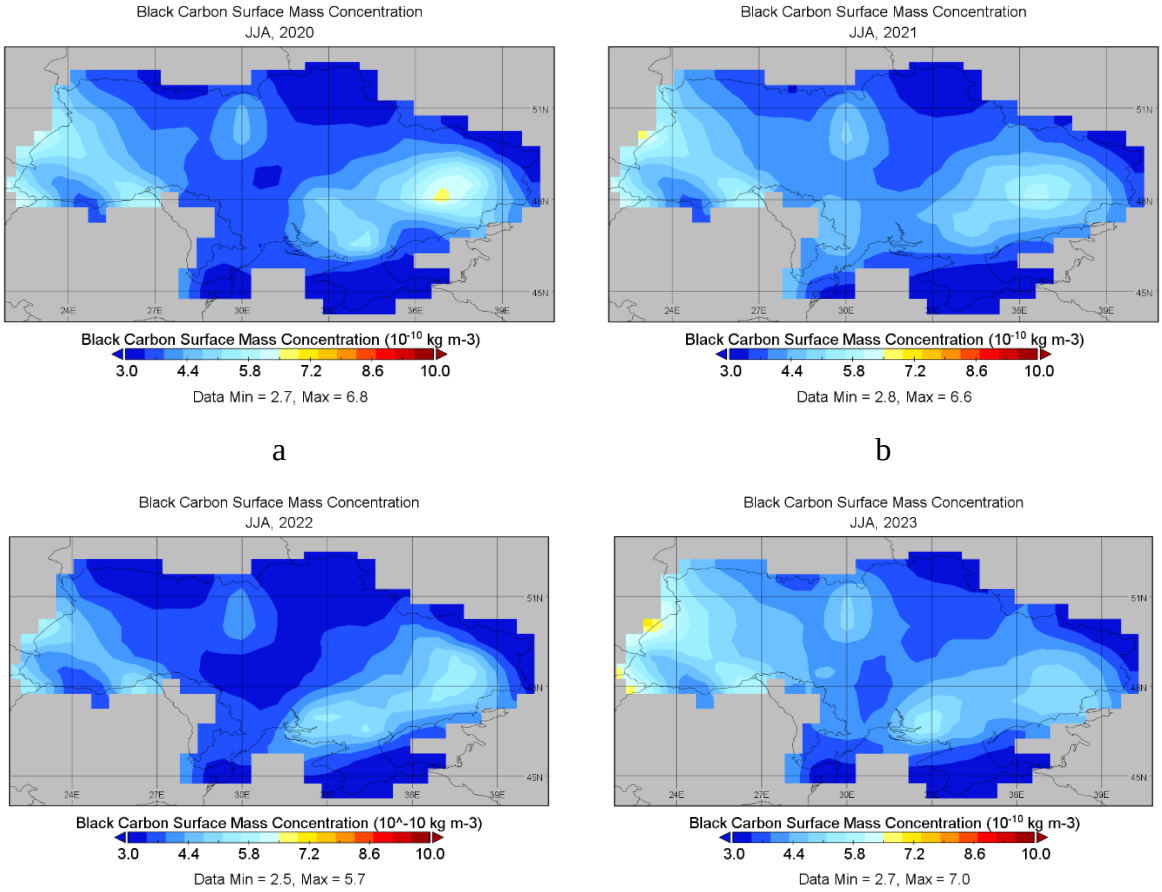

Figure 6.7. Time-averaged black carbon surface mass concentration in the atmosphere over Ukraine during a) summer 2020, b) summer 2021, c) summer 2022 and d) summer 2023. The abbreviation JJA represents the months: June, July, and August. Modeling was provided using the MERRA-2 program. Data were obtained from the GIOVANNI platform. The unit the color scale is 10^{-10} *kg* m^{-3}.

In the autumn, black carbon concentrations increase, with the highest levels recorded in autumn 2020 over the past three years (see Fig. 6.8). The following two years show a decrease in concentrations across the entire territory of Ukraine. Agricultural activities, including the burning rather than composting of plant residues from fields and farms, the start of the heating season, and the possibility of forest fires, can influence black carbon concentrations during the autumn period. The decrease in ground-level concentrations of black carbon in autumn 2022 still remains poorly understood due to ongoing military operations in Ukraine, particularly in the south and southeast regions. However, as a result of the evacuation of a significant portion of the population, heating issues, and challenges in agricultural activities, the overall concentration of black carbon throughout the autumn period does not exceed the values of previous years.

Therefore, based on the presented analysis, it can be concluded that the concentration of black carbon in the atmosphere over Kyiv and Ukraine exhibits seasonal variations, which are associated with factors such as heating, biomass burning, transportation, and fires. Additionally, the impact of military actions and population evacuation on black carbon concentration in autumn 2022 requires further investigation.

In autumn, specifically during September and October of 2023 (see Fig. 6.8d), the black carbon surface mass concentration reached its lowest levels for the analyzed period, not exceeding 0.74 µg m^{-3}. The data for this period is incomplete due to the absence of November. This month typically experiences cold weather and marks an active heating season, as temperatures often drop below freezing outdoors. Consequently, there is an increase in black carbon emissions. Therefore, the complete information might alter considering additional data.

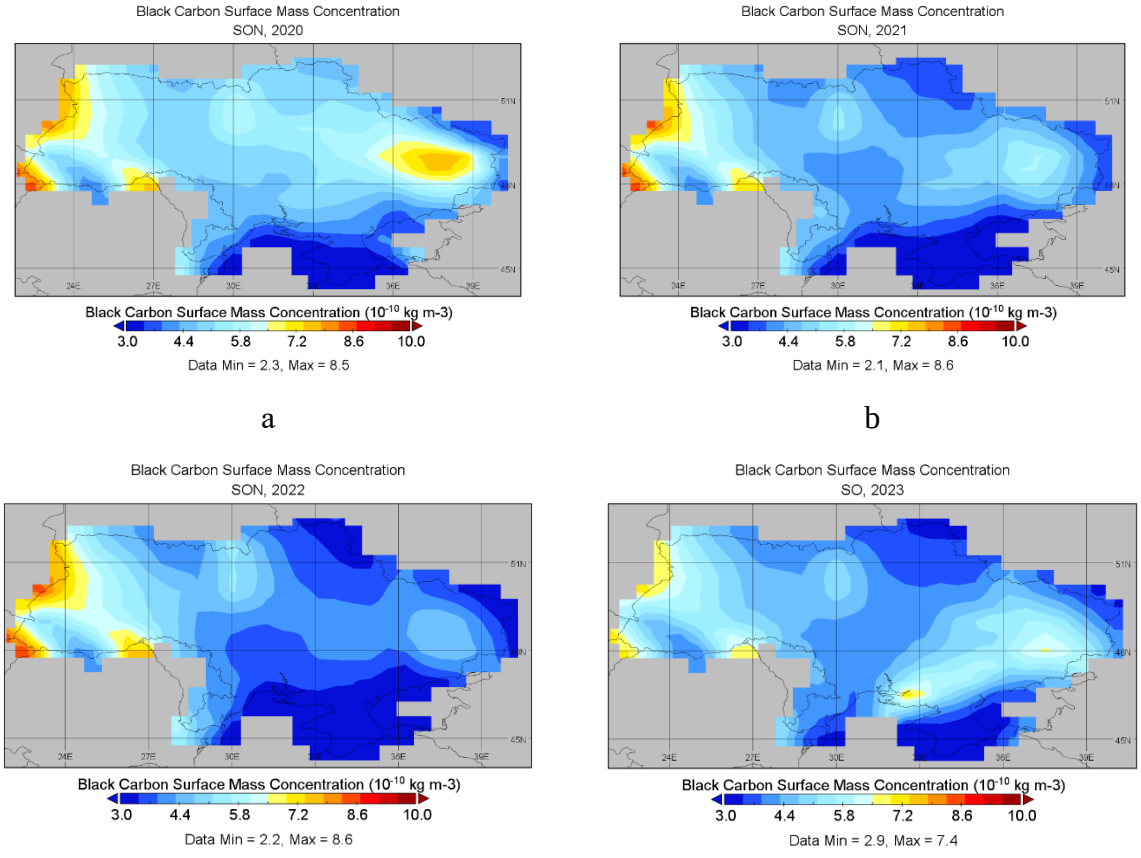

Figure 6.8. Time-averaged black carbon surface mass concentration in the atmosphere over Ukraine during a) autumn 2020, b) autumn 2021, c) autumn 2022 and c) September and October of 2023. The abbreviation SON represents the months: September, October, and November. Modeling was provided using the MERRA-2 program. Data were obtained from the GIOVANNI platform. The unit of the color scale is 10^{-10} *kg* m^{-3}.

6.2.2 Changes of $PM_{2.5}$

To gain insight into the impact of the war on atmospheric $PM_{2.5}$ levels over Ukraine, one can analyze the changes in particle concentrations before and after the initiation of a full-scale invasion. Figure 6.9 illustrates the time averaged total surface mass concentration of $PM_{2.5}$ during two distinct time intervals: the period encompassing February 16th to February 23rd (see Fig. 6.9a) and the subsequent timeframe spanning from February 24th to March 2nd, 2022 (see Fig. 6.9b). Prior to February 24th, Ukraine registered a comparatively subdued average concentration of fine $PM_{2.5}$, falling within the range of approximately 5 to 12 μg m^{-3}. For the analysis of surface mass concentration of $PM_{2.5}$ for different periods, the MERRA-2 reanalysis was used, specifically products: "MERRA-2 tavg1_2d_aer_Nx: 2d, 1-Hourly, Time-averaged, Single-Level, Assimilation, Aerosol Diagnostics V5.12.4 (M2T1NXAER)" and "MERRA-2 tavgM_2d_aer_Nx: 2d,Monthly mean, Time-averaged, Single-Level, Assimilation, Aerosol Diagnostics V5.12.4 (M2TMNXAER)".

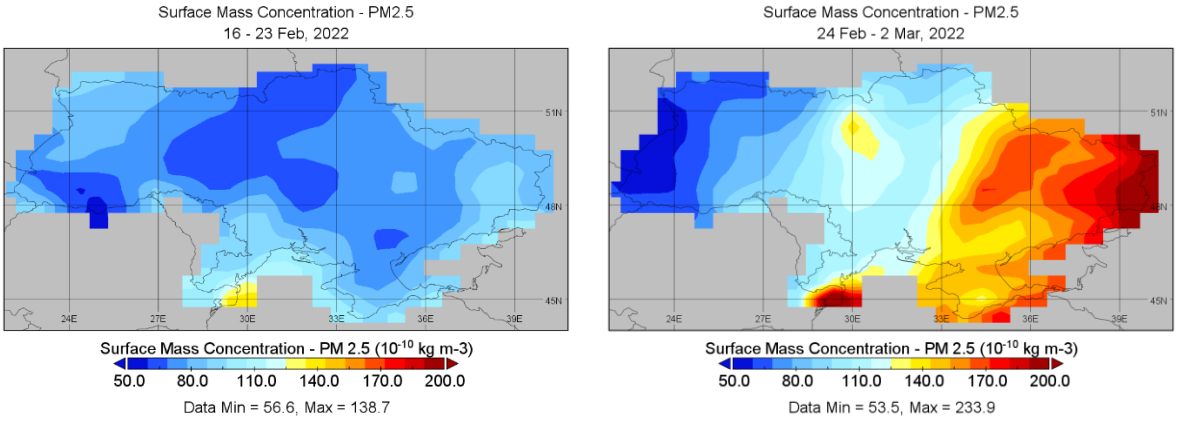

a b

Figure 6.9. Time-averaged surface mass concentration of $PM_{2.5}$ in the atmosphere over Ukraine time-averaged for the periods: a) February 16–23, 2022, and b) February 24 – March 2, 2022. Modeling was provided using the MERRA-2 program. Data were obtained from the GIOVANNI platform. The unit of the color scale is 10^{-10} kg m^{-3}.

Subsequent to February 24, a significant change occurred, leading to a considerable rise in $PM_{2.5}$ levels, as depicted in Figure 6.9b. At the commencement of the incursion, the western reaches of Ukraine recorded the most diminished $PM_{2.5}$ concentration, ranging from 5 to 9 μg m^{-3}, a value slightly below the levels in the week antecedent to the incursion (i.e., from February 16 to 23). Significant alterations in $PM_{2.5}$ concentrations were also noticed in other regions of

Ukraine. In the central and northeastern areas, $PM_{2.5}$ concentrations ranged from 12 to 14 μg m^{-3} (see Fig. 6.9b). Progressing southeastward, the concentration exhibited a heightened gradient, culminating in the maximal values observed in the eastern region, surpassing 13 μg m^{-3}, with the majority of readings falling within the range even of 15 to 24 μg m^{-3}. This pronounced escalation in $PM_{2.5}$ content aligns with military engagements and conflicts, primarily concentrated in the eastern and southern regions of Ukraine, coupled with military movements and infrastructure bombardments (see Fig. 6.1a).

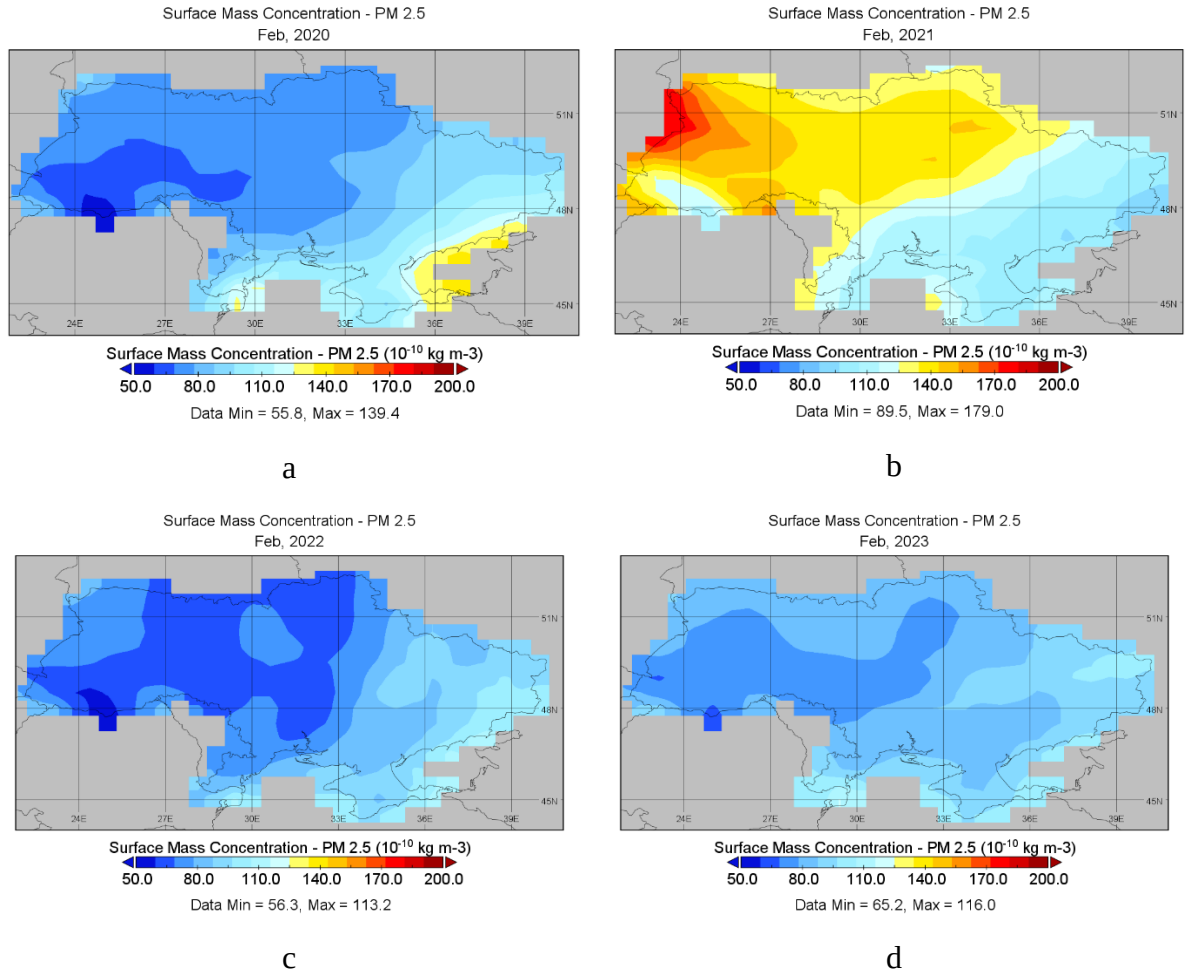

Figure 6.10. Time-averaged surface mass concentration of $PM_{2.5}$ in the atmosphere over Ukraine during a) February 2020, b) February 2021, c) February 2022 and d) February 2023. Modeling was provided using the MERRA-2 program. Data were obtained from the GIOVANNI platform. The unit of measurement for the color scale is 10^{-10} kg m^{-3}.

Similar to the previous case, the comprehensive impact of an event on the monthly averaged $PM_{2.5}$ levels for February and March will be analyzed and compared against previous years (see Fig 6.10). Consequently, the highest concentrations of $PM_{2.5}$ were observed in February 2021, ranging from 9 to 18 μg m^{-3}, whereas for analogous periods in 2020, 2022, and

2023, the values did not exceed 12 μg m^{-3}. This situation deviates from expectations and might be associated with temperature and, consequently, the intensity of the heating season, affecting the emission levels of $PM_{2.5}$ particles (as further demonstrated, $PM_{2.5}$ values for the winter of 2020–2021 are higher than in comparative winters).

In contrast to February 2022, the impact of military activities in March of this year shows a more apparent effect on the $PM_{2.5}$ concentration. Overall, March consistently demonstrates notably high $PM_{2.5}$ across all years. In 2020, concentrations ranging from 12 to 27 μg m^{-3} were observed across almost the entire territory of Ukraine (see Fig 6.11a), associated with the influence of forest fires, a topic analyzed in this study (section 4.2).

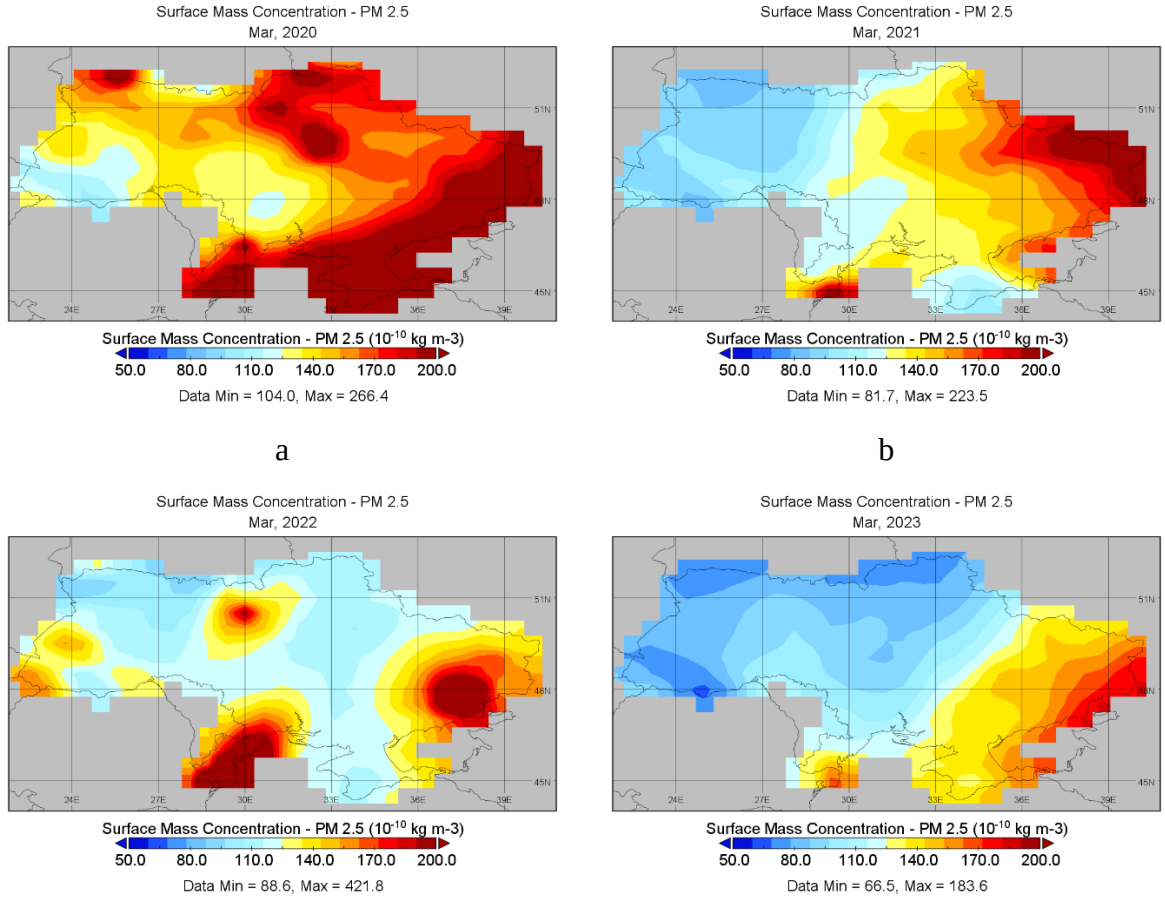

Figure 6.11. Time-averaged surface mass concentration of $PM_{2.5}$ in the atmosphere over Ukraine during a) March 2020, b) March 2021, c) March 2022 and d) March 2023. Modeling was provided using the MERRA-2 program. Data were obtained from the GIOVANNI platform. The unit of the color scale is 10^{-10} kg m^{-3}.

In March 2021 (see Fig 6.11b), concentrations of 12 – 22 μg m^{-3} were typical for the eastern part of Ukraine. Peak $PM_{2.5}$ in March 2022 align with active combat zones and are twice

as high as the typical values of the preceding two years, reaching 42 μg m^{-3} (see Fig 6.11c). For 2023, the lowest concentrations were recorded, with higher values observed in the eastern region, resembling patterns seen in 2020 and 2021 but not exceeding 18 μg m^{-3}. The next question arises regarding the impact of almost two years of war on seasonal concentrations of particulate matter. Concerning the winter changes depicted in Figure 6.12, there don't appear to be any abnormally high values for the winters of 2022 and 2023. In 2022, the lowest values, around 15 μg m^{-3}, were observed, essentially on par with those in 2020.

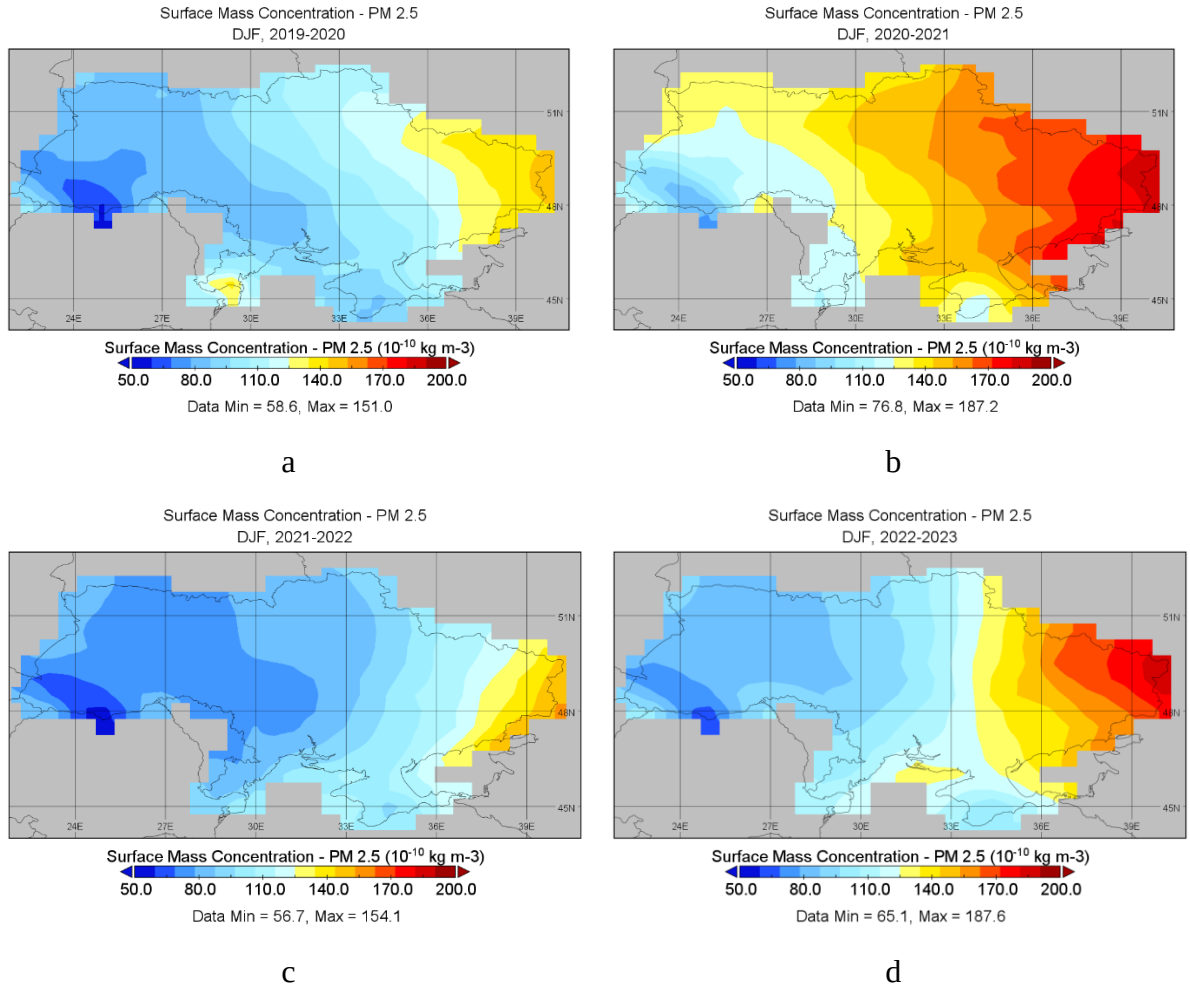

Figure 6.12. Time-averaged surface mass concentration of $PM_{2.5}$ in the atmosphere over Ukraine during a) winter 2019 – 2020, b) winter 2020 – 2021, c) winter 2021 – 2022 and d) winter 2022 – 2023. The abbreviation DJF represents the months: December, January, and February. Modeling was provided using the MERRA-2 program. Data were obtained from the GIOVANNI platform. The unit of the color scale is 10^{-10} kg m^{-3}.

For the spring season of 2022, there is a noticeable impact of Russian aggression on concentration of particulate matter: elevated $PM_{2.5}$ levels in the East, in the Odessa region, and near Kyiv, peaking at 23 μg m^{-3} (see Fig. 6.13c). In contrast, the distribution of concentrations

in other years follows a different pattern, increasing in the southeast but remaining within the range of 8 to 12 µg m^{-3} (see Fig. 6.13a, b, d). The high values observed in spring 2020, particularly in the Kyiv region and the Chernobyl zone, are clearly linked to forest fires (see Fig. 6.13a).

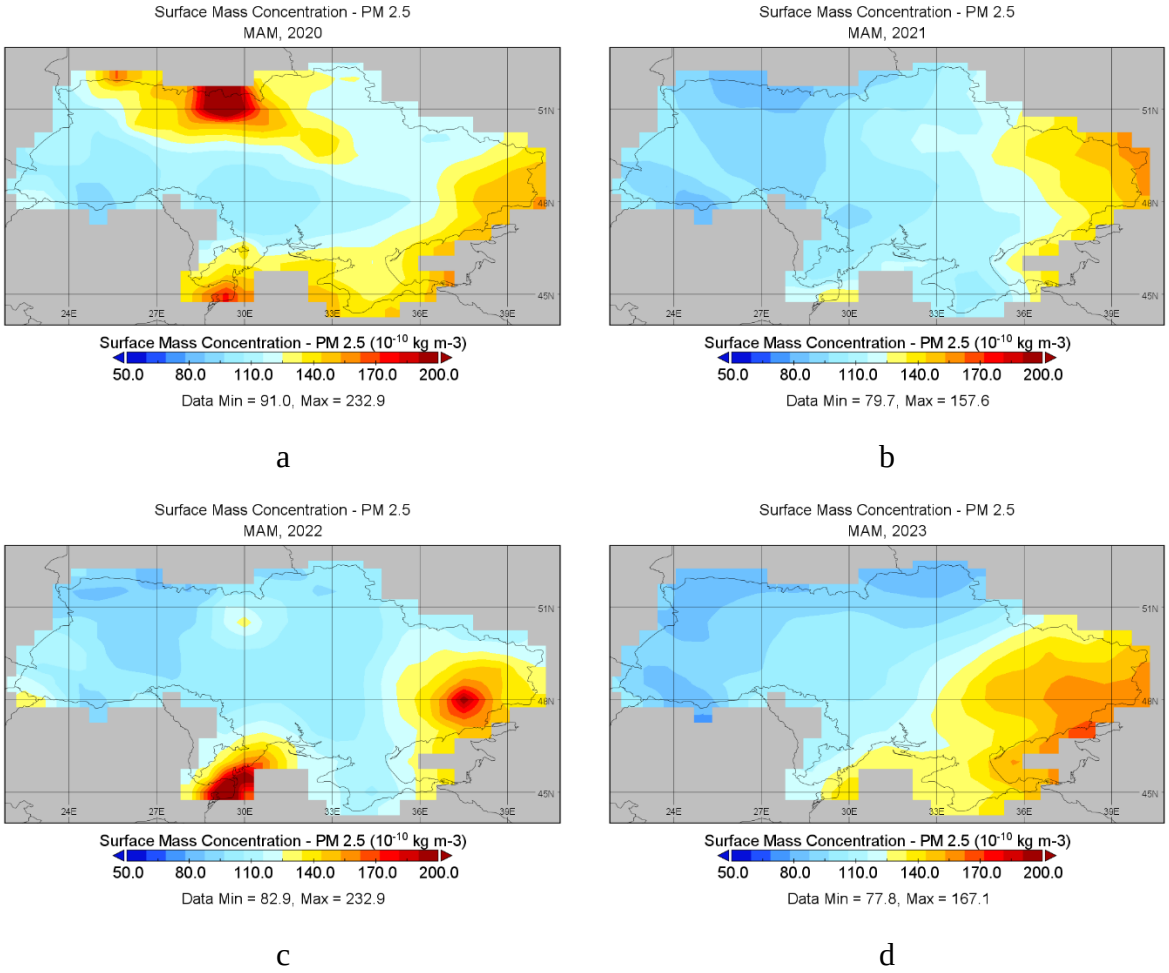

Figure 6.13. Time-averaged surface mass concentration of $PM_{2.5}$ in the atmosphere over Ukraine during a) spring 2020, b) spring 2021, c) spring 2022 and d) spring 2023. The abbreviation MAM represents the months: March, April, and May. Modeling was provided using the MERRA-2 program. Data were obtained from the GIOVANNI platform. The unit of the color scale is 10^{-10} kg m^{-3}.

During summer, lower concentrations of particular matter are typically observed across the territory compared to winter and spring. Throughout all years, $PM_{2.5}$ concentrations range from 7 to 12 µg m^{-3} (see Fig. 6.14). However, during the summers of 2021 and 2022, slightly higher values within the range of 12-17 µg m^{-3} were recorded in the southern and southeastern regions of Ukraine (see Fig. 6.14b,c).

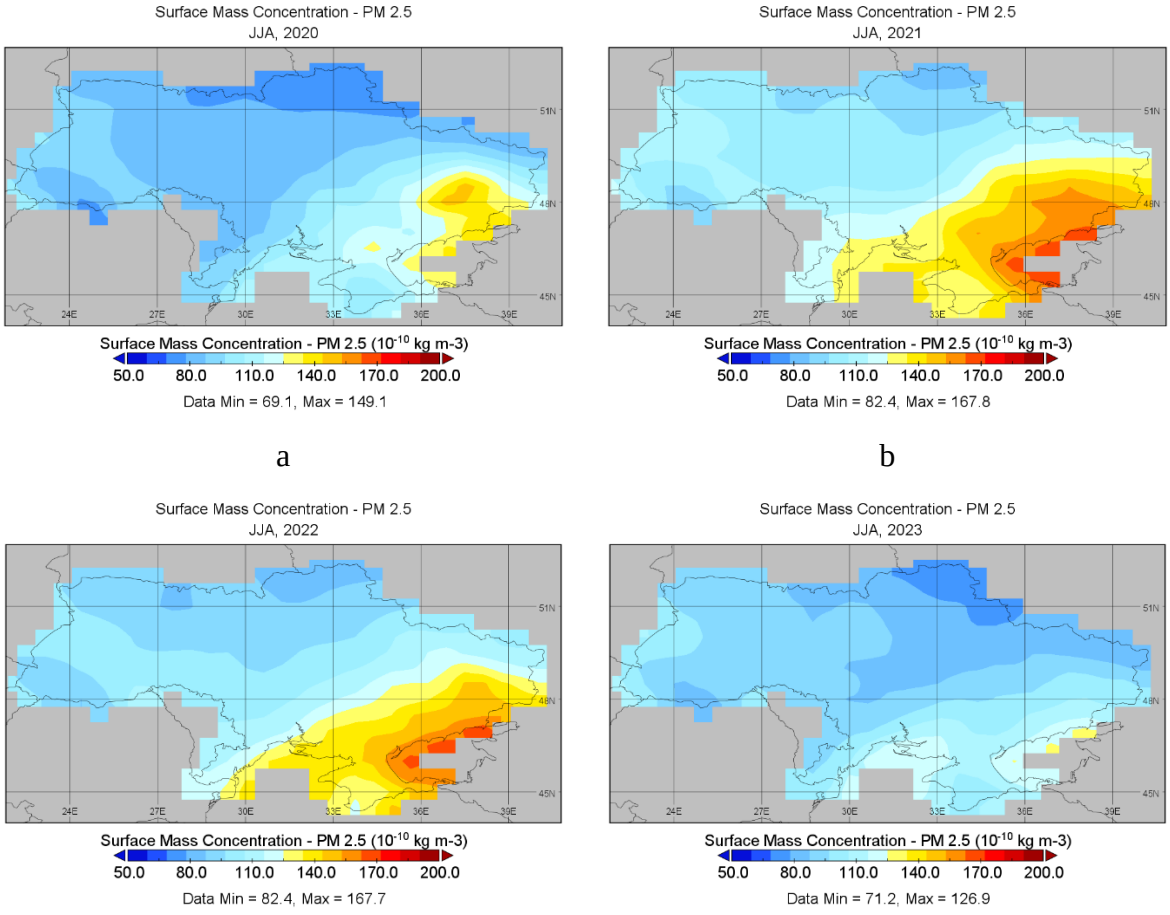

Figure 6.14. Time-averaged surface mass concentration of $PM_{2.5}$ in the atmosphere over Ukraine during a) summer 2020, b) summer 2021, c) summer 2022 and d) summer 2023. The abbreviation JJA represents the months: June, July, and August. Modeling was provided using the MERRA-2 program. Data were obtained from the GIOVANNI platform. The unit of the color scale is 10^{-10} kg m^{-3}.

The average time-averaged surface mass concentration of $PM_{2.5}$ during the autumnal period also shows considerable variation: in 2020, high concentrations ranging from 12 to 24 µg m^{-3} were observed in the eastern part of Ukraine (see Fig. 6.15a). Meanwhile, for the autumns of 2021 and 2022, the values were the lowest observed during the entire monitoring period and did not exceed 13 µg m^{-3} (see Fig. Fig. 6.15b,c).Similar results were obtained for September and October 2023: the surface mass concentration of $PM_{2.5}$ ranged from 7 to 12 µg m^{-3} (see Fig. 6.15d).

From the provided examples and findings, it can be inferred that the concentration of $PM_{2.5}$ exhibits seasonal tendencies and a dependence on the heating season: during colder months, the quantity of particulate matter increases. Regarding the impact of the full-scale

Russian invasion, a noticeable increase in $PM_{2.5}$ concentration in March 2022, even reflected in the average values for the spring season.

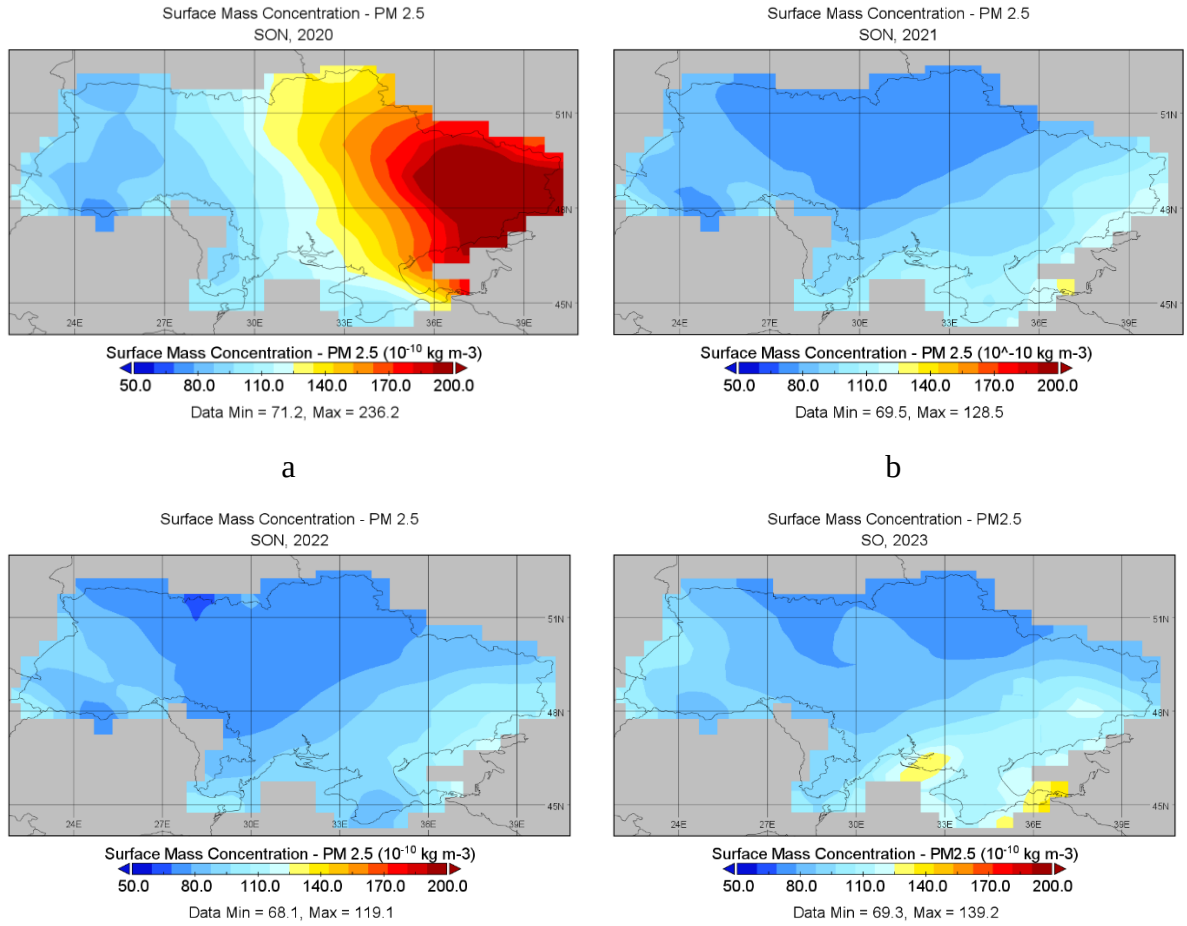

Figure 6.15. Time-averaged surface mass concentration of $PM_{2.5}$ in the atmosphere over Ukraine during a) autumn 2020, b) autumn 2021, c) autumn 2022 and c) September and October of 2023. The abbreviation SON represents the months: September, October, and November. Modeling was provided using the MERRA-2 program. Data were obtained from the GIOVANNI platform. The unit of the color scale is 10^{-10} kg m^{-3}.

6.2.3 Changes of SO_2 and SO_4

As previously mentioned, the combustion of fuel, primarily by military vehicles for transportation, as well as the occurrences of oil depot explosions, resulted in a notable escalation in atmospheric sulfate levels in some regions. For the analysis of surface mass concentration of SO_2 and SO_4 for different periods, the MERRA-2 reanalysis was used, specifically products:

"MERRA-2 tavg1_2d_aer_Nx: 2d, 1-Hourly, Time-averaged, Single-Level, Assimilation, Aerosol Diagnostics V5.12.4 (M2T1NXAER)" and "MERRA-2 tavgM_2d_aer_Nx: 2d, Monthly mean, Time-averaged, Single-Level, Assimilation, Aerosol Diagnostics V5.12.4 (M2TMNXAER)".

Thus, Figure 6.16 presents the changes in the surface mass concentration of SO_2 before and during the onset of the invasion. Before February 24, SO_2 concentrations exceeding 6.4 μg m^{-3} were exclusively in the eastern region (see Fig. 6.16a). Generally, the concentration of SO_2 across the expanse of Ukraine ranged from 1.6 to 5 μg m^{-3}. Subsequent to February 24, the zone characterized by elevated SO_2 content shifted southeastward, encompassing a relatively huge area with concentrations ranging from 6.4 to 11 μg m^{-3} (see Fig. 6.16b). In the central and northeastern regions, SO_2 concentrations witnessed a decrease, with values hovering around 3.6 – 4 μg m^{-3}. In contrast, the situation in the western region exhibited an opposing trend, with reduced concentrations recorded post-invasion in comparison to the pre-invasion period.

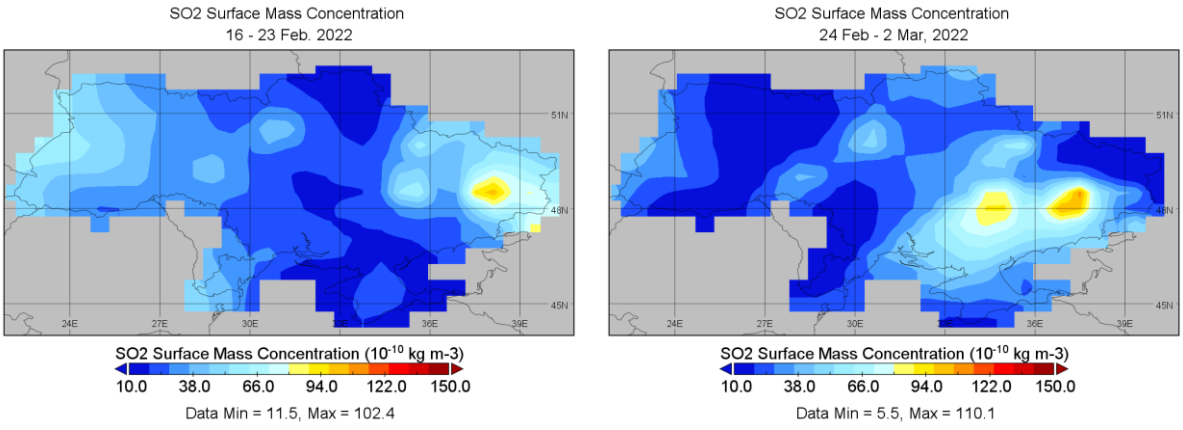

a b

Figure 6.16. Time-averaged surface mass concentrations of SO_2 in the atmosphere over Ukraine time-averaged for the periods: a) February 16–23, 2022, and b) February 24 – March 2, 2022. Modeling was provided using the MERRA-2 program. Data were obtained from the GIOVANNI platform. The unit of the color scale is 10^{-10} kg m^{-3}.

Further analysis of SO_2 concentrations for February and March between 2020 and 2023, as well as well as reviewing seasonal values during this period, did not reveal significant variations or deviations: the values consistently range from 8 to 12 μg m^{-3} across the main part of Ukraine, with slightly higher values in the east at 12 – 15 μg m^{-3}. There is a minor difference between seasons, with the lowest values characteristic of summer and the highest during winter. The results are provided in the Appendix 4.

However, it is more intriguing in this scenario to investigate how the concentration of SO_4 has changed at the onset of the conflict and over longer time spans. Therefore, an analysis of the change in the time-averaged surface mass concentration of SO_4 is warranted to understand the situation at the beginning of the full-scale Russian invasion, as shown in Fig 6.17. In this instance, the increase in SO_4 levels is notably conspicuous: shifting from a range of 1.3 – 4 μg m^{-3} prior to the invasion (Fig. 6.17a) to a range of 2.3 – 5.5 μg m^{-3} across most of Ukraine following the invasion (Fig. 6.17b). Additionally, in certain eastern regions, values exceed 5.5 μg m^{-3}.

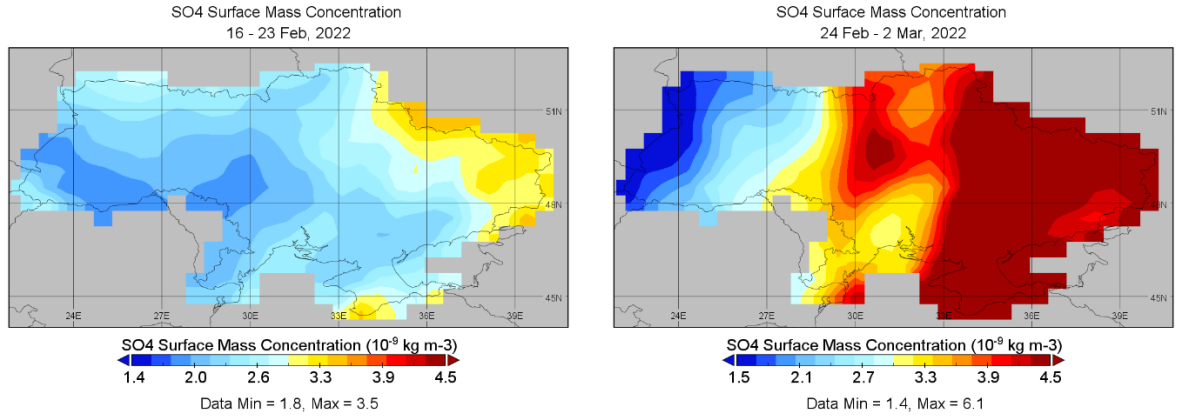

a b

Figure 6.17. Time-averaged surface mass concentration of SO_4 in the atmosphere over Ukraine during a) February 16–23, 2022, and b) February 24 – March 2, 2022. Modeling was provided using the MERRA-2 program. Data were obtained from the GIOVANNI platform. The unit of the color scale is 10^{-9} kg m^{-3}.

There is also the presence of SO_4 pollution in the Kyiv region (4.2 – 5.2 μg m^{-3}), which experienced significant advancement of enemy forces and intense shelling during that period (see Fig. 6.17). Although SO_4 particles can be formed from SO_2, the maps of their average distribution do not correlate strongly. This may be attributed to the peculiarities of chemical transformations of these substances and the consideration of weather conditions (such as wind direction).

The next step involves investigating whether Russian aggression has impacted the monthly variations of SO_4 during February and March of 2022 and 2023. Initially, the focus will be directed towards analyzing the average monthly concentrations of SO_4 for the last winter month over the past four years (from 2020 to 2023 inclusive), as depicted in Figure 6.18. The week of the invasion did not notably influence the overall concentration of SO_4 for February

2022 (see Fig. 6.18c). During this period, the values were relatively lower compared to other studied periods, ranging from 1.5 to 3.8 μg m^{-3}, with the highest concentrations observed in Eastern Ukraine. Similar patterns were observed for February 2020, although the concentrations in Eastern Ukraine ranged from 3.2 to 4.3 μg m^{-3} (see Fig. 6.18a). In 2023, SO_4 concentrations varied from 2.3 to 4.3 μg m^{-3}, with higher levels not only in the east but also in the north of the country (see Fig. 6.18d). February 2021 depicted the most intricate scenario, with SO_4 levels ranging from 3.3 to 6.2 μg m^{-3} across nearly the entire territory of Ukraine (see Fig. 6.18b). Further investigation is required to understand the underlying reasons for this distribution.

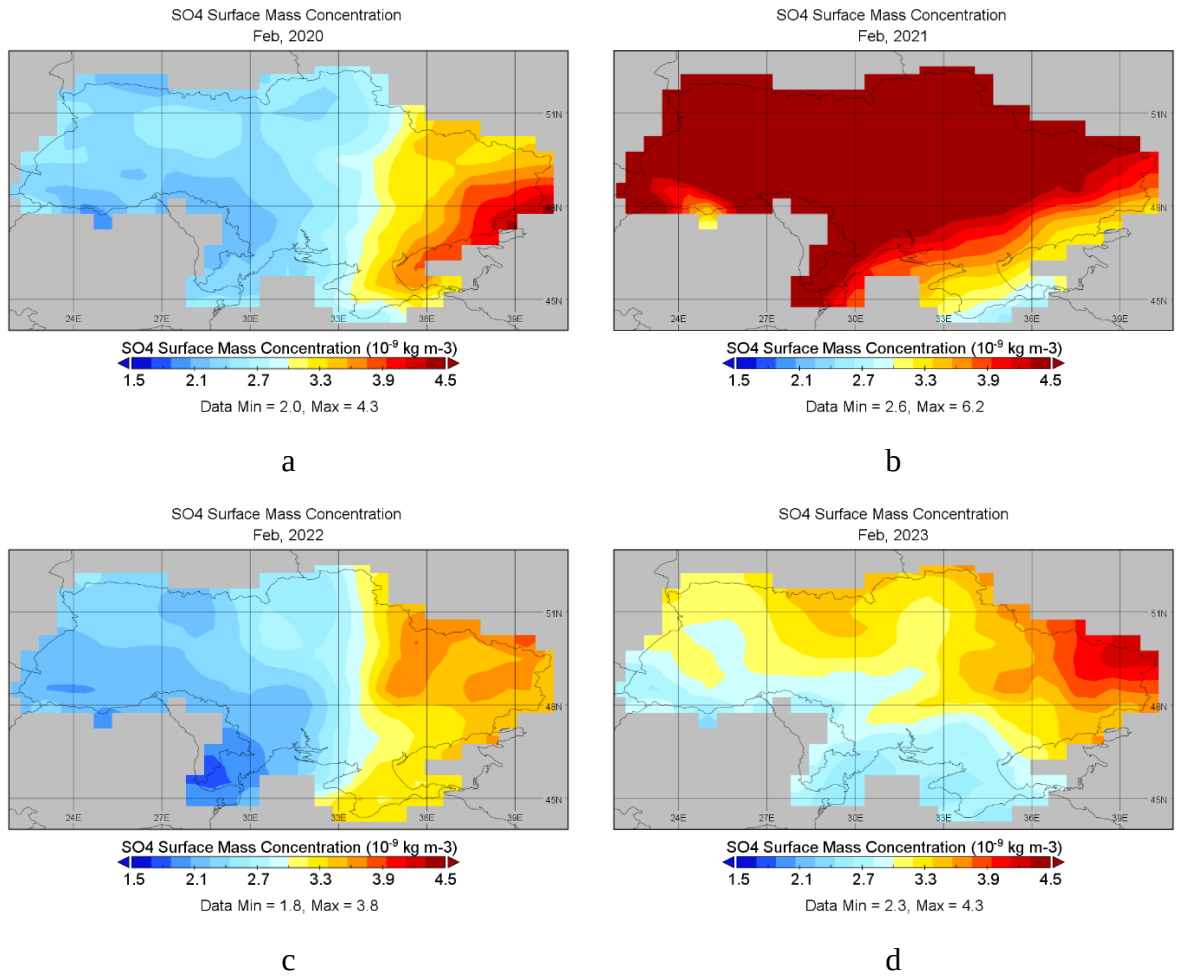

Figure 6.18. Time-averaged surface mass concentration of SO_4 in the atmosphere over Ukraine during a) February 2020, b) February 2021, c) February 2022 and d) February 2023. Modeling was provided using the MERRA-2 program. Data were obtained from the GIOVANNI platform. The unit of color scale is 10^{-9} kg m^{-3}.

The situation for analysis in March also appears to be intricate. Over recent years, these data show significant spatial variability (see Fig. 6.19). In March 2020, the concentration of SO_4 fell within the range of 2.2 – 3.5 μg m^{-3} compared to other years (see Fig. 6.19a). The

subsequent March of 2021 notably featured SO_4 spanning from 3.2 – 4.7 μg m^{-3} across nearly the entire territory of Ukraine, with values exceeding 4 μg m^{-3} in the central and northern parts of the country (see Fig. 6.19b). March during the first year of the Russian invasion also portrayed similar SO_4 concentrations across the entire territory, except for the West, where values were between 2.1 – 2.8 μg m^{-3} (see Fig. 6.19c). In 2023, once again, SO_4 concentrations varied from 2.6 to 4.2 μg m^{-3} across Ukraine, with higher levels in the east and southeast (see Fig. 6.19d).

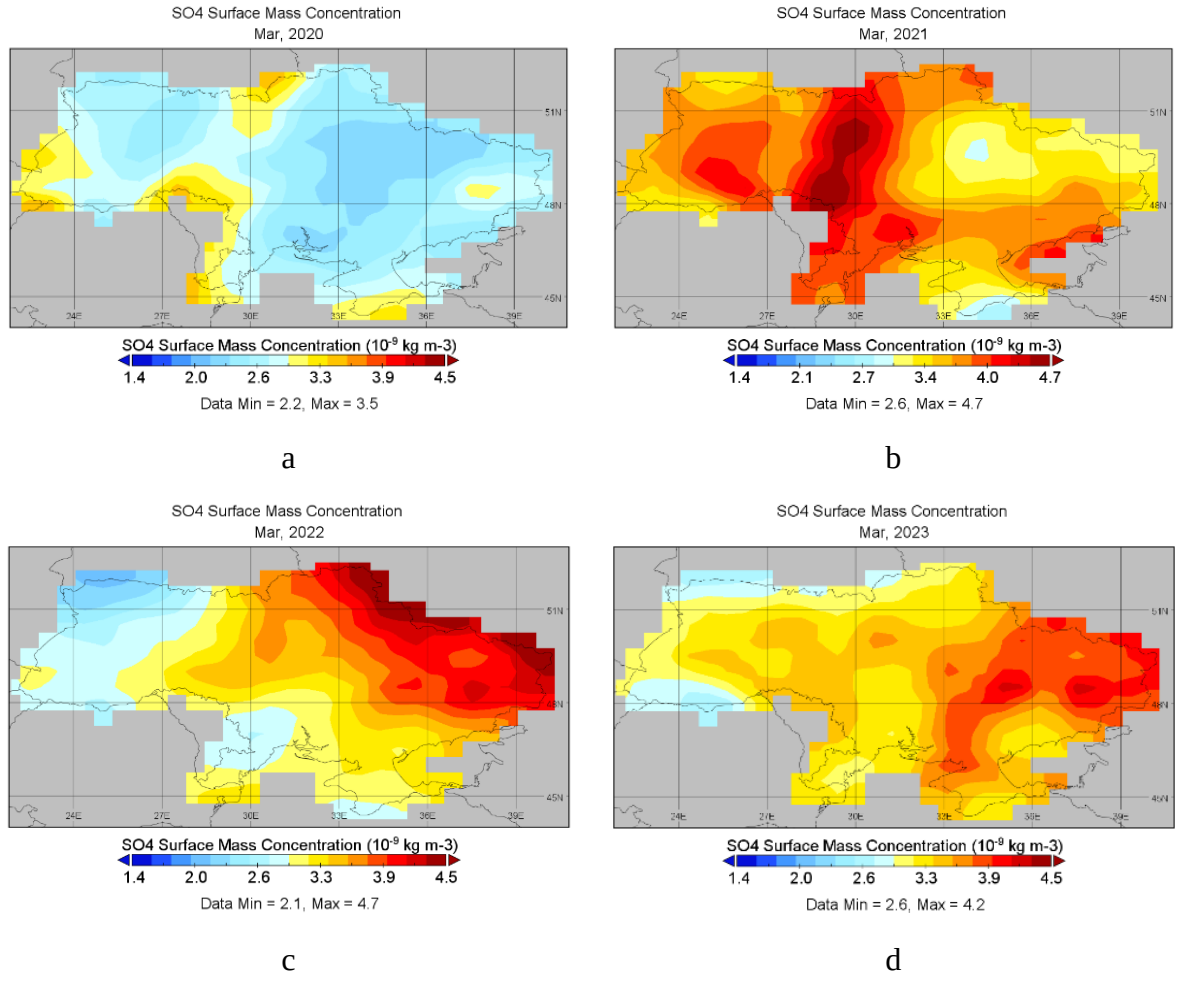

Figure 6.19. Time-averaged surface mass concentration of SO_4 in the atmosphere over Ukraine during a) March 2020, b) March 2021, c) March 2022 and d) March 2023. Modeling was provided using the MERRA-2 program. Data were obtained from the GIOVANNI platform. The unit of the color scale is 10^{-9} kg m^{-3}.

When considering winter variations in SO_4 surface concentrations (see Fig. 6.20), a similar trend is seen like in the February months (see Fig. 6.18). During the winters of 2020 and 2022, SO_4 peaks are situated in the east and northeast of Ukraine, with values ranging from 1.9 to 4 μg m^{-3} (see Fig. 6.20,c). In March 2023, SO_4 concentrations range from 3.1 to 3.4 μg m^{-3},

predominantly notable in the north and northeast, with lower values in other regions (see Fig. 6.20d). The winter of 2021 is characterized by relatively high SO_4 concentrations across Ukraine: 2.4 – 4.8 μg m^{-3} (see Fig. 6.20b).

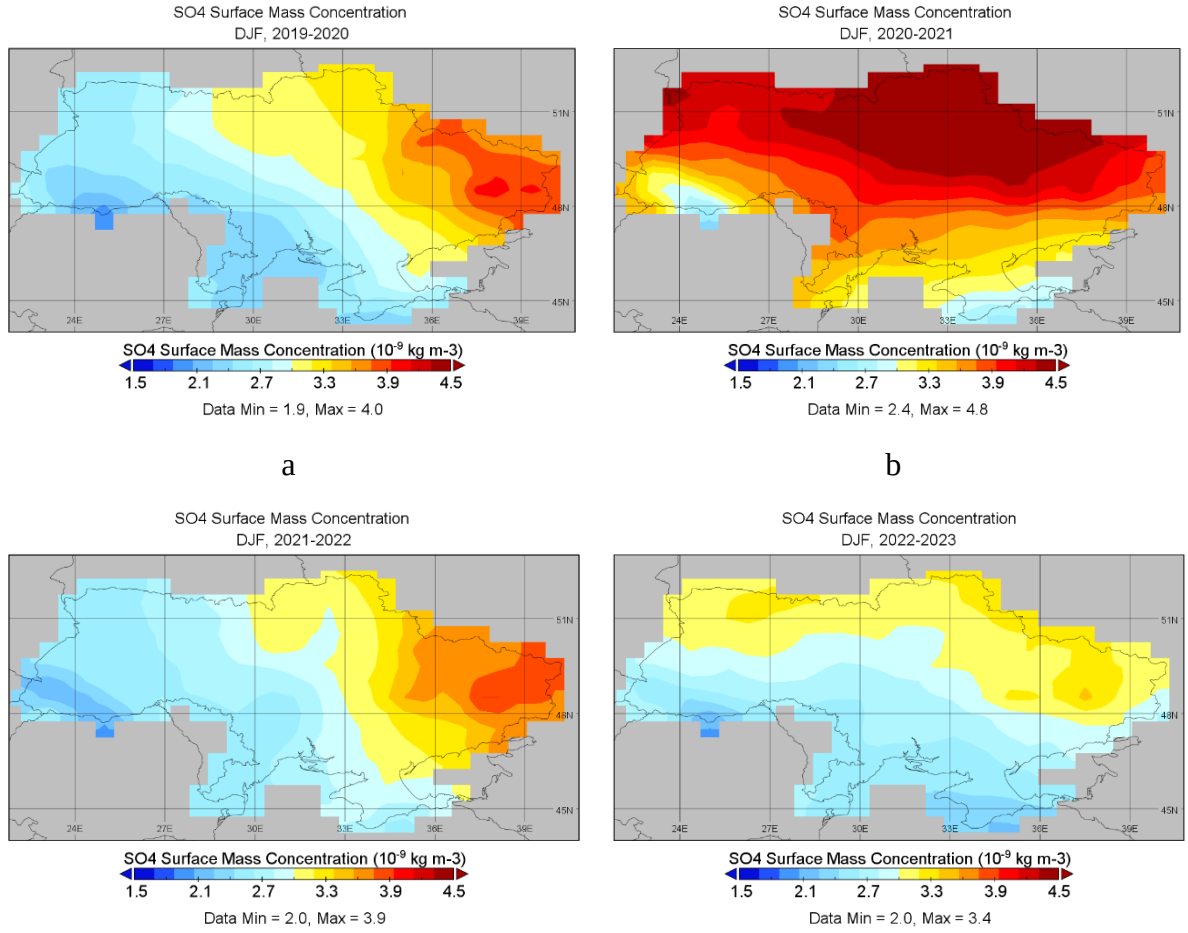

Figure 6.20. Time-averaged surface mass concentration of SO_4 in the atmosphere over Ukraine during a) winter 2019 – 2020, b) winter 2020 – 2021, c) winter 2021 – 2022 and d) winter 2022 – 2023. The abbreviation DJF represents the months: December, January, and February. Modeling was provided using the MERRA-2 program. Data were obtained from the GIOVANNI platform. The unit of the color scale is 10^{-9} kg m^{-3}.

In reviewing the springtime changes in SO_4 concentration, the following pattern emerges. The lowest values were noted in the spring of 2020 (see Fig. 6.21a), ranging from 2.2 to 3.2 μg m^{-3} across the entire territory of Ukraine. Conversely, in the subsequent spring of 2021, the situation shifts remarkably: higher values persisting throughout the period, ranging from 2.8 to 4 μg m^{-3} (see Fig. 6.21b). In 2022, the maximum reached 4.2 μg m^{-3} in the east (see Fig. 6.21c), similar to 2023; however, during the spring of that year, values were only less than 2.9 μg m^{-3} in the north (see Fig. 6.21d).

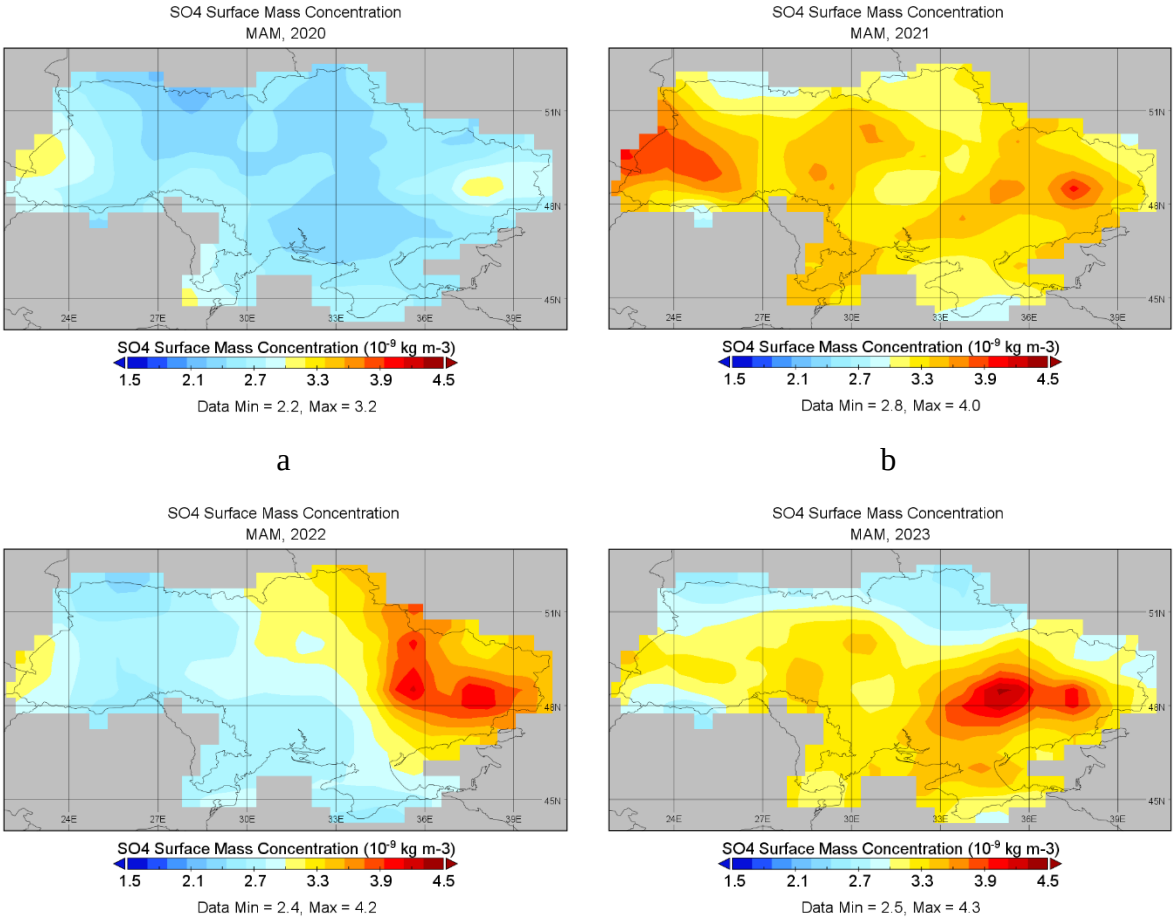

Figure 6.21. Time-averaged surface mass concentration of SO_4 in the atmosphere over Ukraine during a) spring 2020, b) spring 2021, c) spring 2022 and d) spring 2023. The abbreviation MAM represents the months: March, April, and May. Modeling was provided using the MERRA-2 program. Data were obtained from the GIOVANNI platform. The unit the color scale is 10^{-9} kg m^{-3}.

During summer, the concentration of SO_4 decreases across the entire territory of Ukraine and ranges between 2.1 to 3.7 μg m^{-3} in 2020, 2022, and 2023 (see Fig. 6.22a,c,d). In the summer of 2021, SO_4 levels were higher in the south and southeast, as well as in the western part, ranging from 3.1 to 3.9 μg m^{-3} (see Fig. 6.22b). It is noteworthy that in 2020 and 2023, values in the western region were also higher compared to the rest of Ukraine (see Fig. 6.22a,d).

Higher concentrations of SO_4 in Western Ukraine were also observed during the autumn of 2020 and 2022 within the ranges of 3.1 – 4.3 μg m^{-3} and 3.1 – 3.9 μg m^{-3}, respectively (see Fig. 6.23a, c). Similar values were detected in central and eastern Ukraine in 2022. As for 2021, unexpectedly low SO_4 values were recorded during that autumn (compared to previous seasons when the concentrations of this and other parameters were often higher compared to other years)

ranging from 2.2 to 3.3 μg m^{-3} (see Fig. 6.23b). In regard to September and October 2023, the surface mass concentration of SO_4 remains relatively low, ranging from 1.9 to 2.9 μg m^{-3} across the entire country (see Fig. 6.23d).

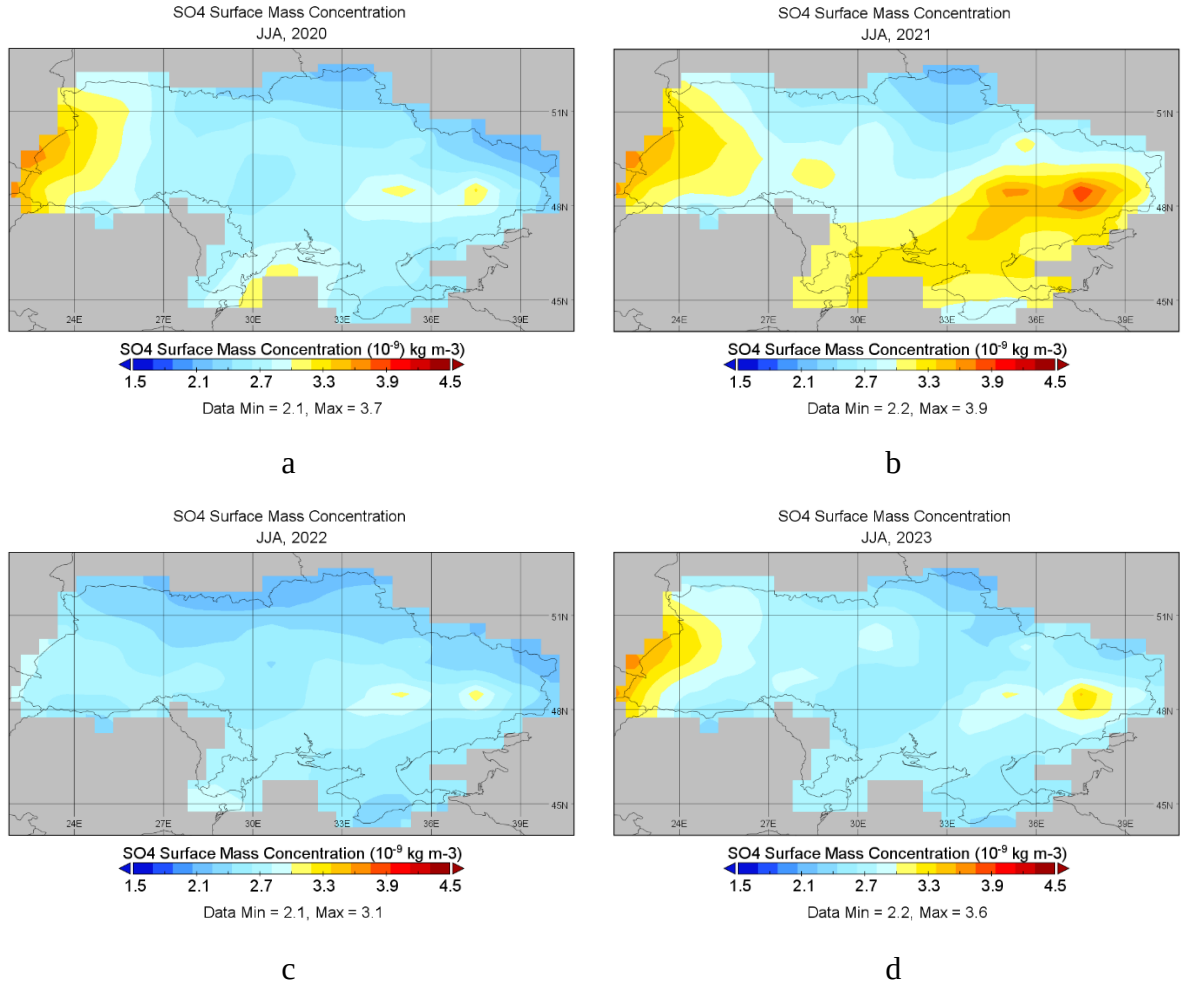

Figure 6.22. Time-averaged surface mass concentration of SO_4 in the atmosphere over Ukraine during a) summer 2020, b) summer 2021, c) summer 2022 and d) summer 2023. The abbreviation JJA represents the months: June, July, and August. Modeling was provided using the MERRA-2 program. Data were obtained from the GIOVANNI platform. The unit of the color scale is 10^{-9} kg m^{-3}.

It is noteworthy that the data for this season may yet undergo alterations with the inclusion of November's data. The data presented for the surface mass concentration of SO_4 and SO_2 exhibit considerable spatial variations of these substances across different seasons and years. In the week following the full-scale invasion, the concentration of SO_2 remained relatively stable. The investigations showed no substantial deviations in SO_2 concentrations across February, March, and the seasonal periods between 2020 and 2023. Concerning SO_4, a notable increase occurred in regions affected by active combat. March 2022 analysis indicated

elevated values in the eastern part of Ukraine; however, these values were not significantly different from the results of the previous two years. According to seasonal analysis, a noticeable difference exists between values in the winter–spring and summer–autumn periods.

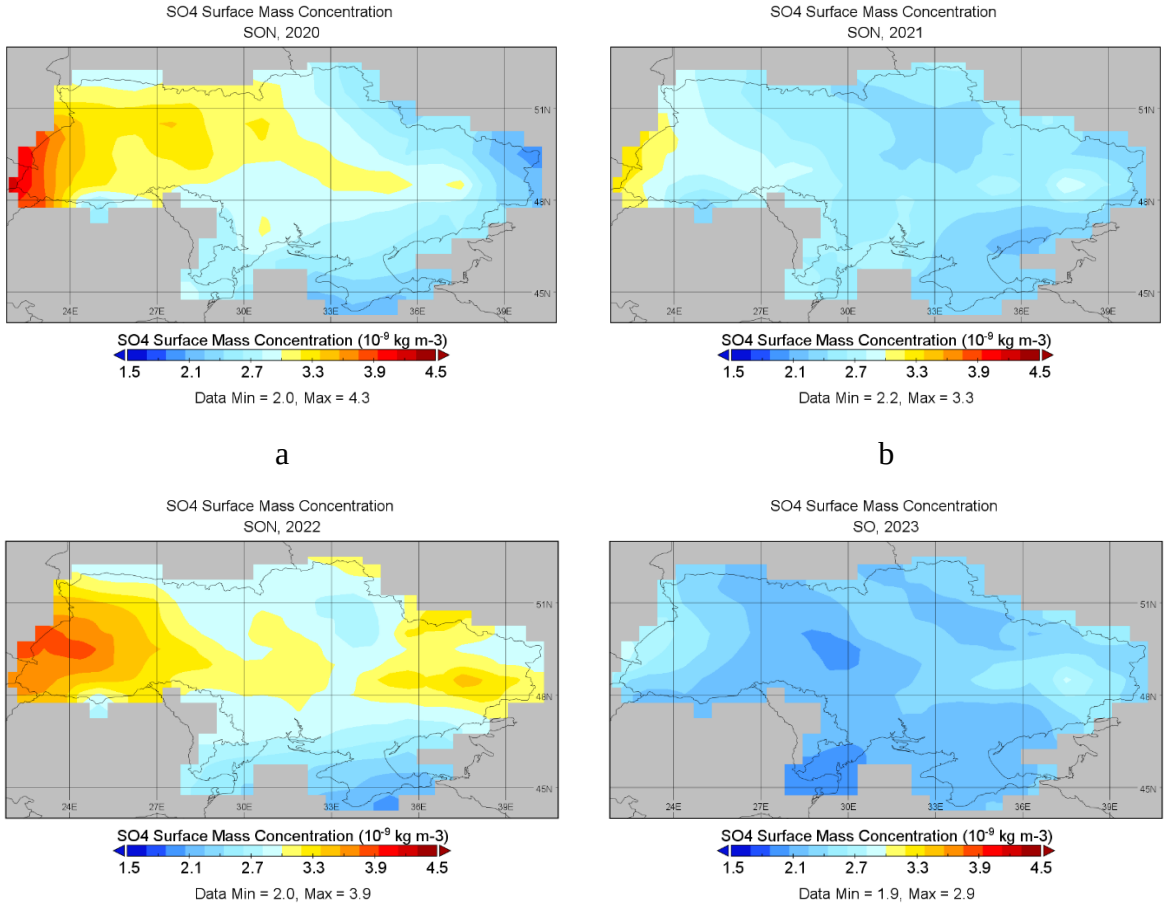

Figure 6.23. Time-averaged surface mass concentration of SO_4 in the atmosphere over Ukraine during a) autumn 2020, b) autumn 2021, c) autumn 2022 and c) September and October of 2023. The abbreviation SON represents the months: September, October, and November. Modeling was provided using the MERRA-2 program. Data were obtained from the GIOVANNI platform. The unit of the color scale is 10^{-9} kg m^{-3}.

6.3 The impact of war on aerosol characteristics in Kyiv

This section describes the changes in aerosol characteristics in 2022 and 2023 during the full-scale Russian-Ukrainian war compared to previous years (2019 – 2021). Variations in Aerosol Optical Depth, Angstrom Exponent, Single Scattering Albedo, fine and coarse

fractions, and complex refractive index are analyzed based on AERONET observations in Kyiv. The impact of the invasion on air quality and $PM_{2.5}$ concentration is also considered using data from the AirVisual network.

6.3.1 Changes in aerosol optical depth and particle sizes

To explore the alterations in aerosol properties induced by the Russian-Ukrainian conflict, comparative analyses were performed on monthly averaged particle characteristics throughout 2022 and 2023 in contrast to observations from preceding years, specifically 2019, 2020, and 2021. As the year 2020 was marked by the COVID-19 pandemic and lockdown measures were also implemented in 2021, the comparison of not pandemic year of 2019 is included for reference. Figure 6.24 illustrates the monthly average changes in AOD (see Fig 6.24a) and AE (see Fig 6.24b) from 2019 to 2023 based on observations from the AERONET station in Kyiv. Also, the number of used measurements is indicated (see Fig 6.24c).

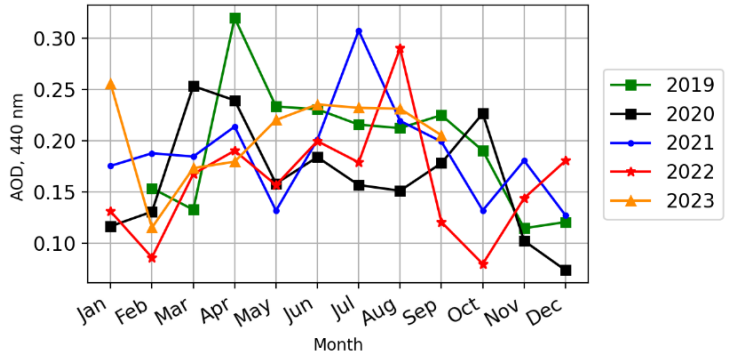

a

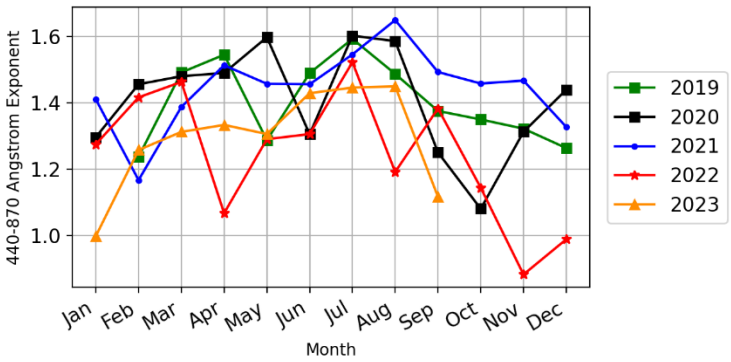

b

Figure 6.24. Changes in a) Aerosol Optical Depth (AOD) at a wavelength of 440 nm and b) Ångström Exponent (AE) at wavelengths of 440–870 nm during 2019–2023. Data monthly averaged. Observations from the AERONET station in Kyiv. Years of observation are indicated by colors. Data level 1.5.

Due to the unavailability of AERONET level 2.0 data since 2020 (owing to the inability to transport the sun photometer for calibration), in order to enhance the credibility of the results from level 1.5 data, a filtration process will be applied under specific conditions. Particularly for AOD and AE, observations were selected at sun zenith angles greater than 50 degrees ($\theta_s > 50°$) to ensure higher data reliability.

The AOD values for the years 2022 and 2023 do not demonstrate a distinct upward or downward trend. Notably, the seasonal peaks observed in AOD align closely with those observed in previous years (see Fig 6.24a). This result indicates the presence of aerosols in the atmosphere over Kyiv and suggests that the conflict has had minimal impact on their quantity. However, it is clear that sources have changed during this period, with the addition of various pollutants. Therefore, it is necessary to pay attention to other aerosol characteristics. Notably, significant changes are observed in the annual dynamics of the AE for the year 2022 and 2023 (see Fig 6.24b).

The monthly average values from January to March exhibit minimal variations in comparison to 2020 and 2021. Nevertheless, it's noteworthy that the values of 1 for January 2023 and 1.2 for April 2022 represent the lowest recorded figures for those respective months within the five-year observation period. From April to May, the overall AE ranges from 1.3 to 1.5, and on average, it is lower by 0.1 to 0.2 compared to previous years. More noticeable differences are observed after October: in 2022, the AE decreases, and in November and December, it is less than 1, while in previous years, it varied from 1.2 to 1.5 during this period. Therefore, the study of AE indicates that this parameter was lower in 2022 and 2023 compared to previous years. Moreover, the Figure 6.25 illustrates the number of measurements utilized to compute the average values of AOD and AE, along with their standard deviation. Due to the similarity in the magnitude range of AOD and AE values, the representation of standard deviations directly on the graph alongside AOD and AE complicates the readability of the plot. When assessing the number of measurements (see Fig. 6.25a), it's clear that the quantity of measurements for 2022 and 2023 shows no significant deviation from those in previous years.

This suggests that in 2022 and 2023, the atmosphere over Kyiv was predominantly influenced by aerosols characterized by larger particle sizes, particularly in the coarse mode. To confirm this hypothesis, it is recommended to analyze the variations of coarse mode AOD and the proportion of fine mode particles within the overall aerosol composition (see Fig. 6.26a, b).

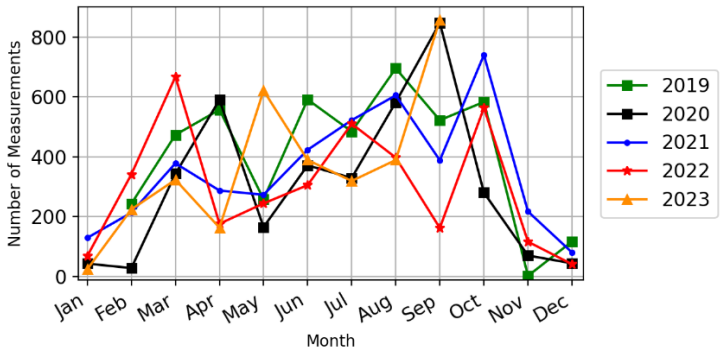

a

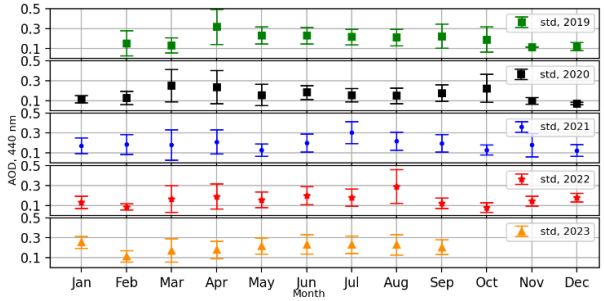

b

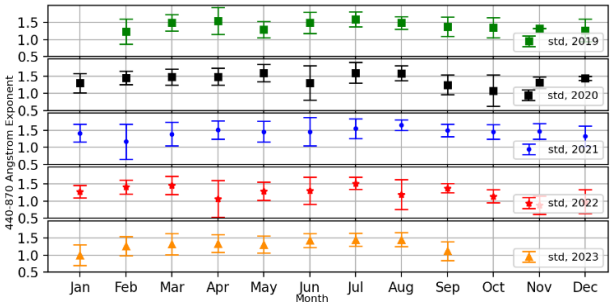

c

Figure 6.25. a) Number of measurements used for averaging AOD and AE (see Fig. 6.24) during the years 2019–2023. Standard deviation of b) Aerosol Optical Depth (AOD) (440 nm) and c) Ångström Exponent (AE) (440–870 nm). Data of AERONET Kyiv, with different colors indicating the respective years of observation. Data level 1.5.

Furthermore, apart from the condition $\theta_s > 50°$ as in the previous case, there is an inclusion of the condition AOD>0.4. This approach helps to avoid inaccurate data and is employed for the analysis of fine fraction, coarse AOD, and refractive index. With the exception of two notable peaks of coarse mode AOD observed in April and August 2022, values from March to September ranging from 0.1 to 0.3, which is a bit higher that values recorded in previous years (see Fig. 6.26a). In addition, there is a significant increase coarse mode AOD in September and October. As for the year 2023, the coarse mode AOD values exhibit differences

compared to the 2022 results. They are generally lower and closely align with values from previous years, without distinct peaks or deviations.

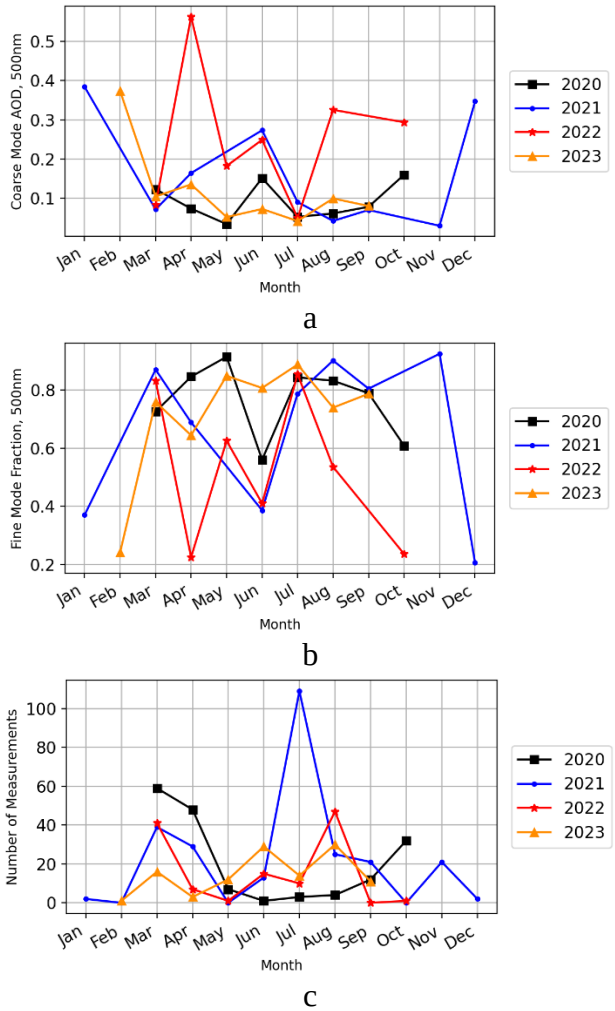

Figure 6.26. Changes of a) Coarse Mode Aerosol Optical Depth (coarse mode AOD, 500 nm); b) Fine Fraction Mode (500 nm) and c) number of used measurements, 2019–2023. Data monthly averaged. Observations from the AERONET station in Kyiv. Years of observation are indicated by colors. Data level 1.5.

The changes in particle size become noticeable when considering the monthly changes in the fine mode fraction, as depicted in Figure 6.26b. Observations show that the data curve for 2022 consistently features smaller values when compared to the results for 2020 and 2021. In April, the fraction of fine mode aerosols reached approximately 0.2, marking the lowest value for this time of the year (see Fig. 6.26). In April 2022, many regions experienced delayed agricultural activities due to the Russian invasion, making it an active month for initiating or continuing these activities. From May to September in 2022, the fraction of fine particles ranged from 0.5 to 0.8, aligning with values observed in previous years. Additionally, starting from August, the fraction of fine particles in 2022 significantly decreased compared to the typical

values for this period in 2020 and 2021. The standard deviation for the coarse mode and fine mode fractions is displayed in the following figure (see Fig. 6.27).

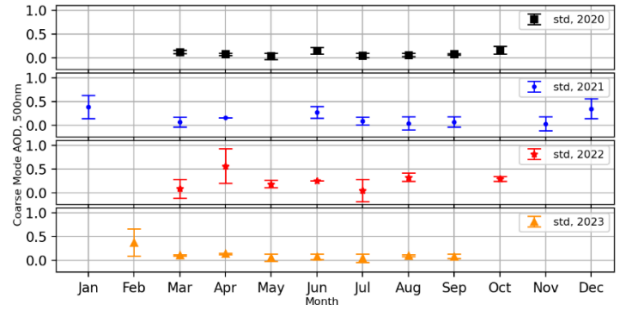

a

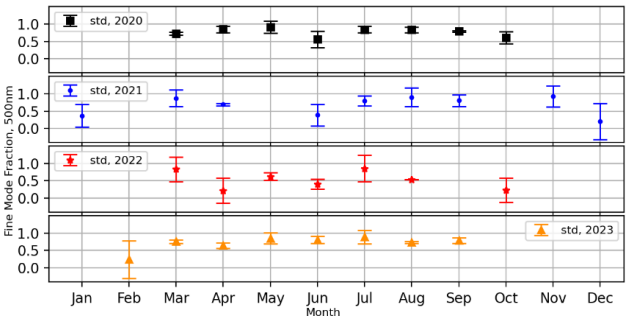

b

Figure 6.27. Standard deviation of a) Coarse Mode Aerosol Optical Depth (AOD) at a wavelength of 500 nm; b) Fine Mode Fraction at a wavelength of 500 nm (see Fig. 6.26). Observations from the AERONET station in Kyiv. Years of observation are indicated by colors. Data level 1.5.

Concerning coarse mode AOD, conspicuous peaks were identified in April and August 2022, with values from March to September slightly elevated compared to previous years. However, in 2023, the coarse mode AOD closely mirrored previous years' patterns without notable peaks or deviations. Conversely, the fine mode fraction showed discernible changes, consistently displaying lower values in 2022 than in 2020 and 2021. Although from May to September in 2022, the fine particle fraction was in line with previous years, a substantial decline compared to 2020 and 2021 occurred from August onwards.

6.3.2 Variations of the complex refractive index

The complex refractive index of aerosols is a property closely linked to the chemical composition of aerosols, and its change can indicate shifts or predominance of specific aerosol

types. Figure 6.28 depicts the monthly average variations in the real part of the complex refractive index from 2020 to 2023, along with the number of measurements utilized, based on observations obtained from the AERONET Kyiv station.

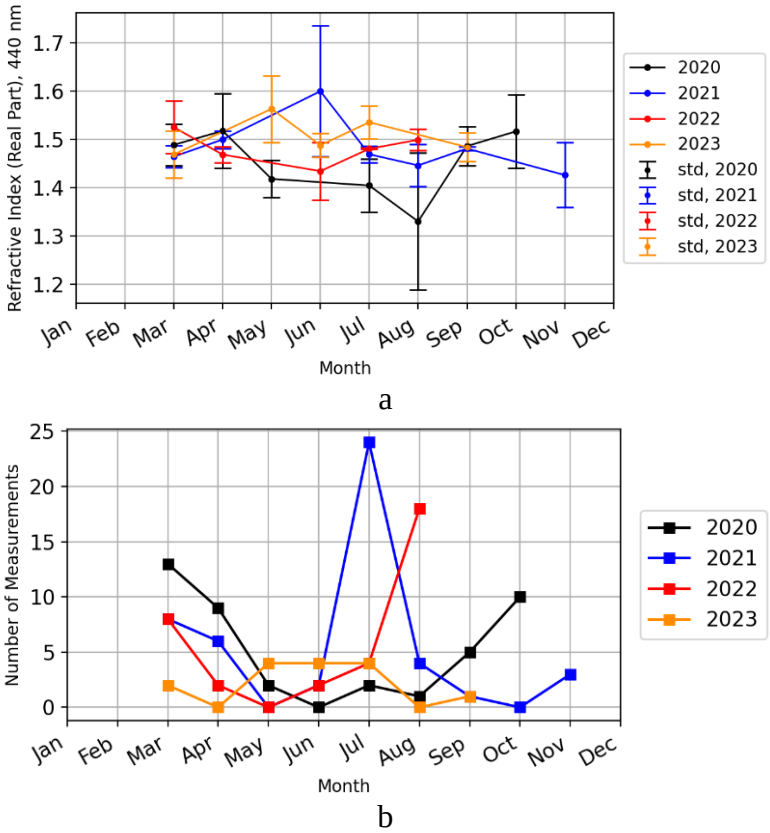

Figure 6.28. a) Changes of the real part of the complex refractive index at wavelength 440 nm with standard deviation and b) number of used measurements, 2019–2023. Data monthly averaged. Observations from the AERONET station in Kyiv. Years of observation are indicated by colors. Data level 1.5.

In general, the real part of the complex refractive index exhibits minimal variation among different aerosol types across various wavelength ranges, as reported by Zhang et al. (2017). Therefore, observations at 440 nm were chosen for analysis (see Fig. 6.28a). The available dataset for analysis is limited (see Fig. 6.28b) but meets the criteria for data quality; nevertheless, data are available for each of the selected years. The data selection criteria have been previously mentioned in the preceding paragraph: the conditions $\theta_s > 50°$ i AOD>0.4. As observed, the values of the real part of the refractive index range from 1.33 to 1.6. Notably, the values for 2022 and 2023 do not deviate significantly from those in 2020 and 2021. The Appendix 5 also includes a graph incorporating data from 2016 and 2017, which fall within the same range of values and measurement quantity. From the obtained results, it can be concluded that the chemical composition of aerosols, which influences their reflective properties, has

remained relatively stable in the years 2022 and 2023. In contrast to the real part of the refractive index, there are certain variations in behavior throughout the year for 2022 and 2023 (see Fig. 6.29) in the case of the imaginary part. The graph is shown for a wavelength of 440 nm, and the number of measurements used for calculation is the same to the previous case (see Fig. 6.28c). In 2022, higher values of the imaginary part were observed in July and August compared to the corresponding period in previous years.

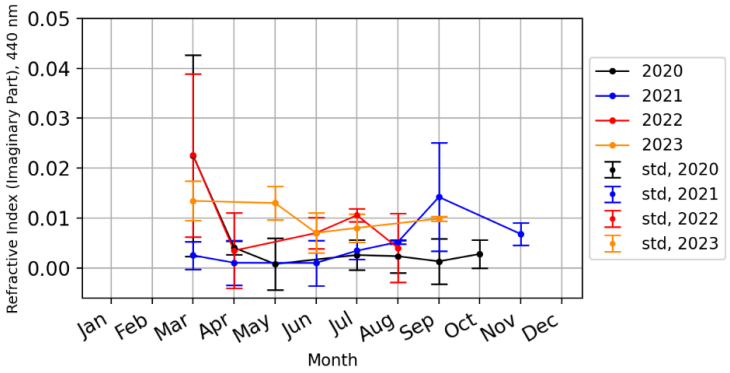

Figure 6.29. Changes of the imaginary part of the complex refractive index at wavelengths 440 nm with standard deviation, 2019–2023. Data monthly averaged. Observations from the AERONET station in Kyiv. Years of observation are indicated by colors. Data level 1.5.

A similar situation occurred in 2023, with higher values than in 2020 and 2021 observed in March, May, June, and July. A comparison with 2016 and 2017 yielded the same results (where the values of the imaginary part did not exceed 0.01, these data are presented in the Appendix 5). Although the imaginary part of the refractive index, based on the results, falls within the range of 0 to 0.025 for a wavelength of 440 nm, this component directly influences the absorbing properties of aerosol particles. Based on the obtained results, it can be concluded that the impact of this component increased in the atmosphere above Kyiv in 2022 and 2023. In addition, Appendix 5 shows the changes in SSA during 2022–2023.

6.4. The impact of the war on the chemical composition of aerosols in the atmosphere above Kyiv

As mentioned in earlier sections of this study, the war has significantly impacted the chemical composition of aerosols in the atmosphere above Kyiv. Specifically, changes in the

coarse and fine aerosol modes and noticeable alterations in the imaginary part of the refractive index were observed. This aerosol properties are particularly helpful in directly obtaining information about the chemical composition of aerosols and their respective types.

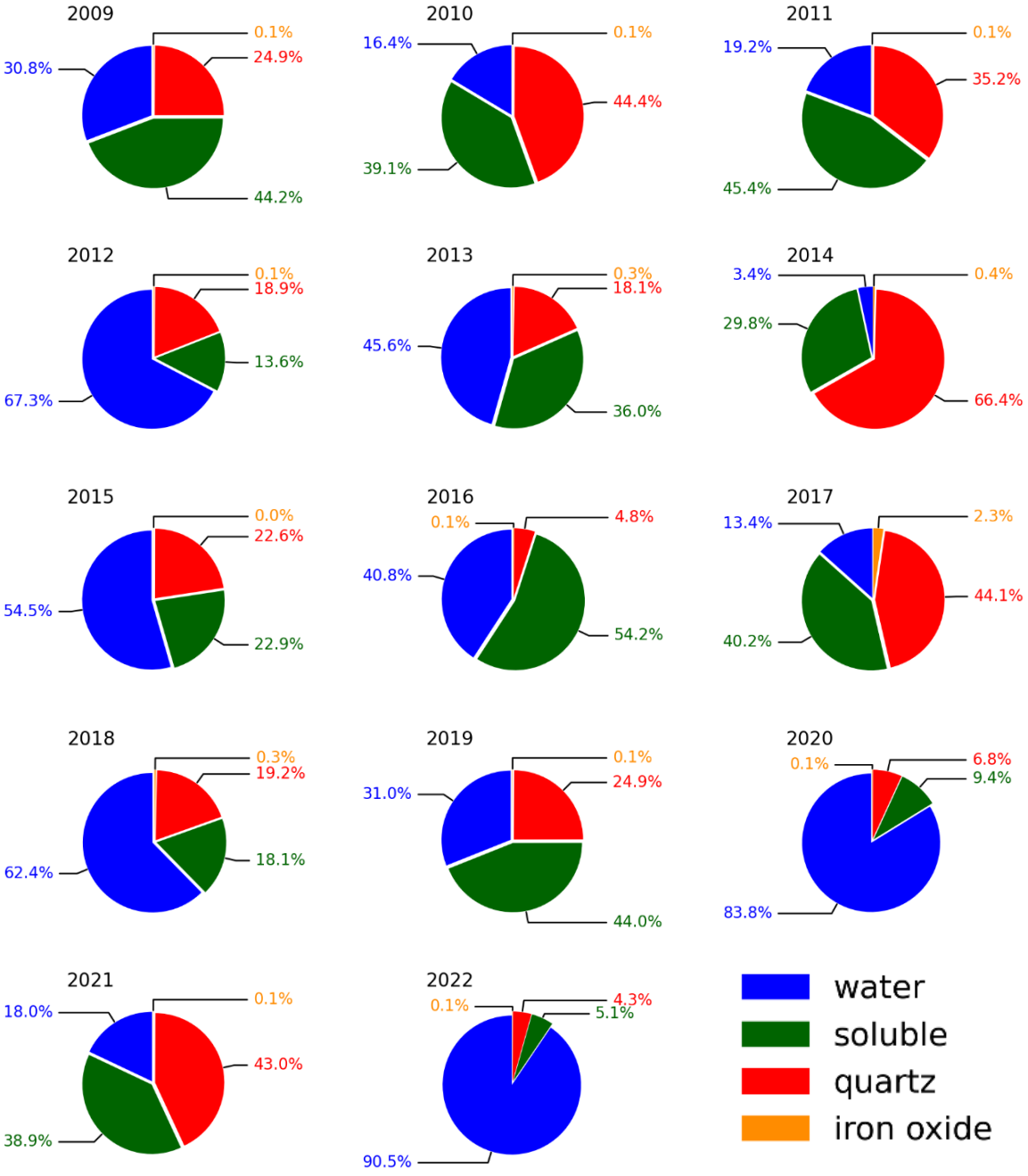

Figure 6.30. Changes in the chemical composition of coarse mode of aerosols in the atmosphere over Kyiv during 2009–2022. GRASP data for Kyiv.

Using the GRASP/Components algorithm applied to measurements of the sun photometer of the AERONET Kyiv station, aerosols' chemical composition over Kyiv from 2009 to 2022 were analyzed. It is worth noting that, despite GRASP employing a different

approach to data processing, it shows good agreement with optical characteristics derived by the operational AERONET algorithm. For instance, in the study by Li et al. (2019), the GRASP algorithm was evaluated using actual AERONET measurements, and the results exhibited substantial consistency with the standard AERONET product, particularly for locations where mineral dust, biomass burning, or a combination of both types of aerosols prevailed. The GRASP algorithm provides information about water (coarse and fine), soluble (coarse and fine) and non-absorbing, absorbing insoluble materials that are approximated by refractive indices of quartz (coarse and fine), black carbon, brown carbon, and iron oxide.

Figure 6.30 illustrates variations in different particle types for the coarse mode of aerosols. The presented data reveal significant fluctuations in the specified substances from 2009 to 2023. The water fraction, in general, fluctuates between 17 and 16 percent, with only 3.4% observed in 2014. In contrast, in 2020 and 2022, it accounts for 83.8% and 90.5%, respectively. Soluble aerosols on average constitute a third part, as does mineral dust (quartz). Regarding iron oxide, it comprises only 2.3% of the total coarse mode in 2017. For all other years, the value does not exceed 0.4%. Upon more detailed analysis, 2022 does not show significant deviations from previous years. A similar situation with a high water content was already observed in 2020 and 2018 and is unrelated to military actions. There is also no noticeable correlation between other components; for example, changes in the percentage of water do not lead to proportional changes in the quantity of soluble aerosols or mineral dust. Therefore, based on the analysis by the GRASP algorithm, it can be concluded that anomalies in the coarse mode of aerosols were not observed in 2022.

Changes in the fine mode of aerosols also present considerable complexity for analysis (see Fig. 6.31). Numerous years where a significant portion of the fine mode is occupied by water were observed (2015, 2018, 2020, and 2022). There are also years dominated by mineral dust, notably 2009, 2010, and 2019. Regarding soluble aerosols, significant variations are again observed from year to year. This situation may be linked to the fact that increased humidity could facilitate the formation of aerosol particles from gaseous substances; for example, ammonia may condense and generate aerosol particles in humid atmospheric conditions. Humidity levels can impact chemical processes within the atmosphere, including aerosol reactions with other substances. However, it's essential to highlight that the quantity and characteristics of soluble aerosols in the atmosphere are influenced by various other factors, such as sources of pollution, particle size, meteorological conditions, among others. Consequently, these patterns can be intricate and contingent on specific contexts. Another

substance representative of the fine mode is brown carbon, the values of which have not exceeded 0.2% throughout all the years.

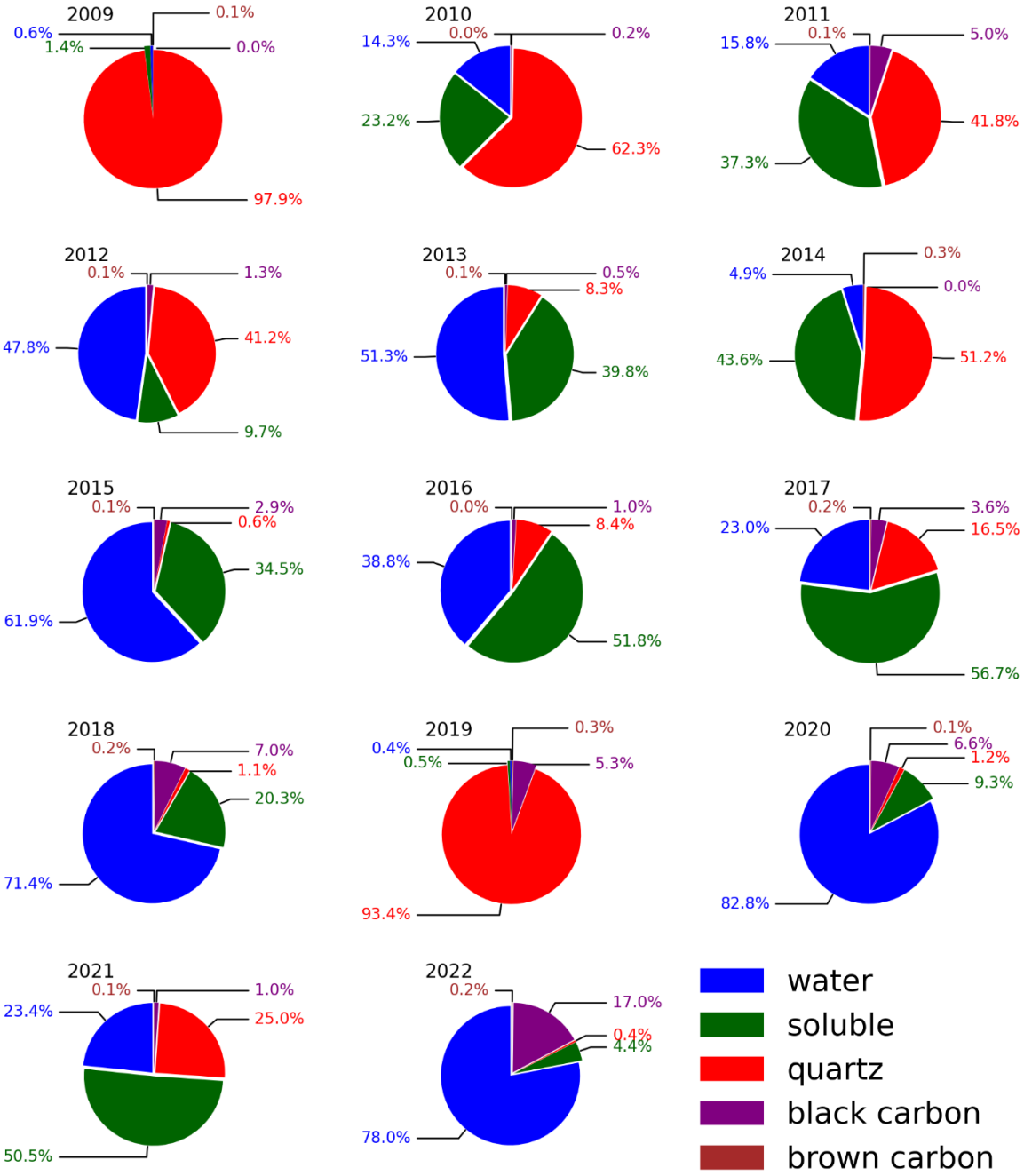

Figure 6.31. Changes in the chemical composition of fine mode of aerosols in the atmosphere over Kyiv during 2009–2022. GRASP data for Kyiv.

Consequently, following the analysis of the overall chemical composition trends, attention will now be directed to the observed changes in 2022 (see Fig. 6.31). The sole indicator that has significantly increased compared to last years is black carbon, which constituted 17% in 2022. In comparison to the maximum value of 7% in 2018, this figure has substantially risen.

Sources of black carbon were previously mentioned in connection with the impact of military actions on its increase. Before the commencement of the full-scale Russian invasion, black carbon does not exceed of 7% of the total aerosol content in the atmosphere over Kyiv, but in 2022, this species increased by a few times.

6.5 War and $PM_{2.5}$ Concentration in Kyiv

Measurements of air quality monitoring stations in the city of Kyiv did not stop after the full-scale Russian invasion. Observations from the Chornobylska and Nauky stations are available for the first half of 2022, while observations from the Trosyanetska and Golosiiv stations are available at the beginning of 2023 (detailed measurements of each station are discussed in Section 5.3, see Fig. 5.6). The impact of military actions on the territory of Ukraine on $PM_{2.5}$ concentration and air quality index will be analyzed. This analysis involves describing the monthly variations of particulate matter as presented in Figure 6.32. The reasons for higher $PM_{2.5}$ levels during the cold season, resulting in poorer air quality, have already been discussed in previous sections.

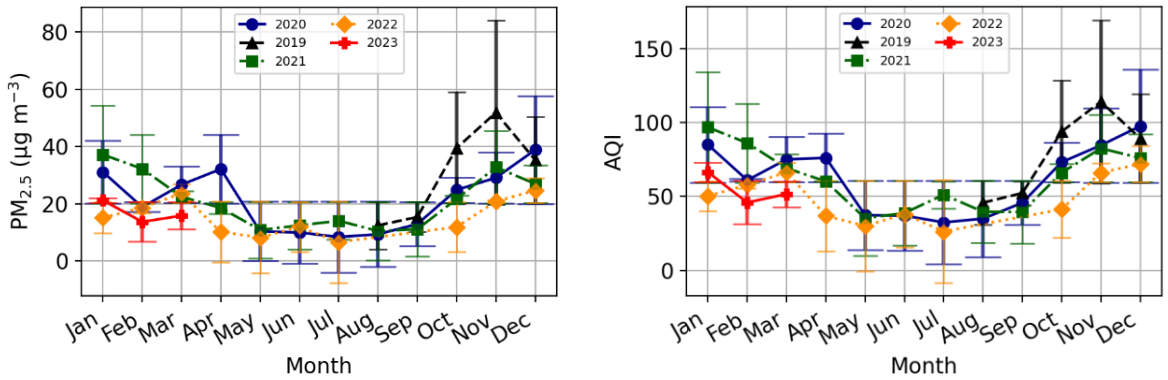

Figure 6.32. Monthly variations of (a) $PM_{2.5}$ concentration and (b) Air Quality Index (AQI) for Kyiv during 2019–2023. Measurements by AirVisual, monthly averaged. Years of observation are indicated by colors.

The highest $PM_{2.5}$ values were observed during the autumn months of 2019 (see Fig. 6.32). Regarding 2020 and 2021, the dynamics and magnitudes are very similar. For 2022, it was expected to obtain data that exceeded the observations of 2020 and 2021 due to the impact of bombings, shelling, extensive fires, increased use of generators during power outages, and

increased wood heating during the autumn and winter. However, as we can see from Figure 6.32, the observations show the opposite trend.

In January 2022, the $PM_{2.5}$ concentration was the lowest among the observed years (see Fig. 6.32a). In February, $PM_{2.5}$ levels were consistent with the overall pattern (since the invasion occurred at the end of February, its impact on the monthly average was not significant). The March $PM_{2.5}$ level is directly associated with military actions: rocket shelling of Kyiv, fires, and the occupation of a significant territory of the Kyiv region. During this period, many enterprises were closed, and the traffic volume significantly decreased due to the exodus of many residents from the capital. These factors, along with the de-occupation of territories near Kyiv and the region, contributed to low $PM_{2.5}$ values in April and May. June and July observations show little difference compared to 2020 and 2021, while from October 2022 to March 2023, these values are significantly lower (see Fig. 6.32a). However, even with the decrease in $PM_{2.5}$ concentration, the AQI remains above the WHO recommended level and exceeds 50 during the cold season (see Fig. 6.32b).

The changes of $PM_{2.5}$ concentration during the seasons of 2019–2023 are presented in Figure 6.33. The smallest values for all years are observed during the summer period, with $PM_{2.5}$ ranging from 20–30 μg m^{-3} in the first half of June 2022, and subsequently not exceeding 10 μg m^{-3} until the end of July, closely matching the patterns of previous years (see Fig. 6.33a). Autumn observations in late October and November 2022 do not exceed 50 μg m^{-3} and are relatively consistent, whereas in 2019, 2020, and 2021, numerous peaks with higher concentrations were observed. It is due to the absence of a large number of polluted days that the monthly average $PM_{2.5}$ concentrations for this period are lower (see Fig. 6.33b).

Winter observations for the years 2022–2023 are more comprehensive compared to the summer and autumn seasons (see Fig. 6.33c). The variations in $PM_{2.5}$ for the year 2023 show little difference from the corresponding season in 2021–2022. However, both winters have lower $PM_{2.5}$ levels than the previous ones, ranging from 10 to 50 μg m^{-3} for the winters of 2021–2022 and 2022–2023, compared to 20–70 μg m^{-3} for the previous years of 2019–2020 and 2020–2021 (see Fig. 6.33c).

Spring monitoring by AirVisual also includes a complete set of measurements for the spring of 2022, and measurements for March 2023 are available at the time of writing (see Fig. 6.33d). $PM_{2.5}$ concentrations above 50 μg m^{-3} are only observed in the second half of March 2022, while remaining within even lower levels than typical (see Fig. 6.33d). For March 2023,

the dynamics and concentration of $PM_{2.5}$ show no significant deviations (see Fig. 6.33d). From the presented data, one might mistakenly assume that the air quality improved significantly over a large territory of Ukraine with the onset of the full-scale invasion, leading to a decrease in $PM_{2.5}$ content. Number of measurement and standard deviation are presented in Appendix 3.

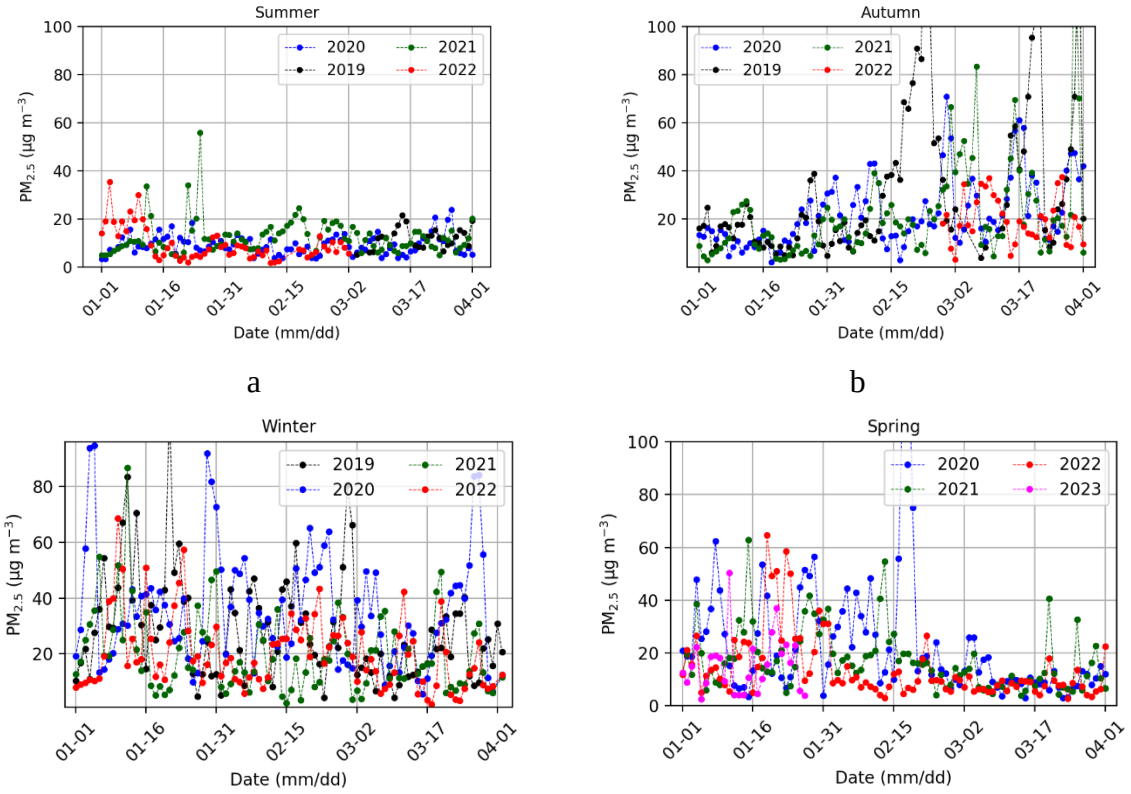

Figure 6.33. Seasonal variations of $PM_{2.5}$: (a) summer (June, July, August); (b) autumn (September, October, November); (c) winter (December, January, February); and (d) spring (March, April, May) in the atmosphere of Kyiv during 2019–2023. Measurements by AirVisual, daily averaged. Years of observation are indicated by colors.

6.6 Conclusions for Chapter 6

In this chapter, the changes in aerosol properties resulting from the Russian invasion and military actions are investigated. This was accomplished by analyzing observations from the AERONET station by AERONET and GRASP methods, variations in $PM_{2.5}$ concentrations based on measurements from the AirVisual network and using data from MERRA-2 reanalysis.

The main results of Chapter 6 are as follows:

1) The average surface concentrations of BC, $PM_{2.5}$, SO_2, and SO_4 were analyzed for the period of February 16–23 and February 24 – March 2, 2022, using MERRA-2 reanalysis. It was shown that before February 24 (from February 16 to 23). Regarding the obtained results, all the aforementioned substances exhibited alterations in their concentrations, notably increasing in areas with active military operations. Additionally, a comparison of changes in these substances during February and March over the past four years was conducted, while seasonal variations were also considered. A rise in the values during March 2022 was noted, attributed to the war actions.

2) Based on AERONET observations, significant alterations in the annual patterns of the Ångström Exponent for the year 2022 were detected. The AE values for that year were lower compared to previous years. This decrease was associated with a reduction in the fine aerosol fraction, while the coarse mode became more dominant.

3) Observations from the AirVisual network did not reveal abnormal increases in $PM_{2.5}$ concentrations during 2022 and early 2023. High $PM_{2.5}$ values were characteristic of March and April 2022 due to active military actions, fires, and other factors. Despite the decrease in $PM_{2.5}$ concentrations during these months, the Air Quality Index remained above the recommended WHO level and exceeded 50 during the cold season. According to the AirVisual monitoring, it may initially appear that air quality improved significantly across a substantial area of Ukraine with the onset of the full-scale invasion, and $PM_{2.5}$ levels decreased. However, previous subsections of this study indicate a tendency towards an increase in aerosol particle sizes in 2022.

4) The war has resulted in significant changes in the chemical composition of atmospheric aerosols over Kyiv, as indicated by GRASP retrievals. The percentage of black carbon in 2022 significantly increased compared to previous years.

Chapter 7

7. CONCLUSIONS AND PERSPECTIVES

The thesis presents research findings concerning the evolution of aerosol properties in the atmosphere above Kyiv and Ukraine. The study encompasses both short-term and long-term analyses of observations and modeling. The air above Kyiv is impacted by diverse aerosol sources, arising from urban emissions and remote origins as air masses shift. The city can receive biomass burning products from suburbs or distant regions, and there can be a significant increase in mineral dust due to agricultural activities. Seasonal variations are also influenced by forest fires (typically occurring in mid-spring and early autumn), farming practices, vegetation cover, the heating season, and other factors. Ukraine's expansive territory encompasses three natural zones (forests, forest-steppe, and steppe), a southern coastline, and varying levels of infrastructure, with predominantly heavy industry in the east. All these factors contribute to the diversity of aerosol particles in the atmosphere over the country.

Short-term increases in aerosols in the atmosphere over Kyiv can lead to reduced visibility, smog, and adverse effects on the health and well-being of residents. Such occurrences are explored in this study, focusing on notable increases in aerosol concentrations during peat and forest fires in autumn 2015 and spring 2020. Detailed analyses were carried out to analyze changes in aerosol properties, including Single Scattering Albedo, Complex Refractive Index, Fine Mode Fraction, Coarse AOD, variations in radiative forcing, and effective radiative forcing. The analysis involved data from the AERONET Kyiv sun photometer network and lidar observations done during the field lidar campaign in Kyiv in 2015, backed by support from the Laboratoire d'Optique Atmospherique, Université de Lille. The study also incorporated measurements of $PM_{2.5}$ concentrations and the Air Quality Index based on the AirVisual network data. Additionally, the use of HYSPLIT backward trajectories calculation enabled a more precise localization of aerosol particle sources. It also allowed an investigation into the factors influencing the evolution of aerosol properties, including potential transport times, altitude, and the areas traversed by the air mass pathways.

This work also included the long-term changes in Aerosol Optical Depth, Angstrom Exponent, Radiative Forcing, and concentrations of atmospheric components like black carbon, organic carbon, SO_2, SO_4, $PM_{2.5}$, and CO across the Kyiv and Ukraine. To analyze changes in aerosol properties and their impact on the energy balance over Kyiv, observations from the sun photometer at the AERONET Kyiv station were used, providing continuous data for almost 15 years (since 2008). Additionally, data on $PM_{2.5}$ concentration changes have been available for Kyiv since 2019, derived from AirVisual. These AirVisual data were also employed to describe the changes occurring during this period. Modeling results from MERRA-2 were used to investigate the AOD, AE, and variations in other atmospheric components (black carbon, organic carbon, SO_2, SO_4) over the Ukrainian territory.

In addition to short-term and long-term variations, the study investigates the impact of the Russian-Ukrainian war on BC, SO_2, SO_4, $PM_{2.5}$ concentrations, air quality, and aerosol properties. It describes the changes that occurred immediately following the full-scale invasion, as well as their monthly, seasonal, and annual effects.

The main results of the thesis are as follows:

1) The findings from Ukraine's first lidar field campaign are showcased. Prior to this endeavor, no comparable investigation had been conducted in Kyiv or the surrounding region. The observations explored the spatial distribution of aerosols under various conditions.

2) An intense aerosol layer over Kyiv region, resulting from forest fires in various parts of Ukraine in September 2015, was investigated. The using of the CE 370 aerosol lidar enabled the study of aerosol particle distribution with height and the calculation of mass concentration for the first time in Ukraine. A comparison of the obtained data with AERONET observations allowed for the estimation of aerosol particle parameters. Satellite image obtained through the MODIS instrument aided in locating the fire origins that caused such pollution and assessing the extent of atmospheric smoke.

3) September 3rd marked the day when the extinction coefficient exceeded 0.3 km^{-1}, reaching its peak concentration of 250 μg m^{-3} at an altitude of approximately 4 km. This coincided with an indication from the Angstrom Exponent, pointing to an abundance of small-sized particles associated with biomass burning. The notably high ratio of extinction to backscattering coefficient further indicated the prevalence of these aerosol particles.

4) The first results of air quality monitoring in Kyiv using $PM_{2.5}$ concentration measurements are presented. The findings from AirVisual, APDA–371 HORIBA Popudrenka, and AERONET Kyiv stations were analyzed, revealing significant air pollution by aerosol particles during forest fires in March – April 2020. The properties of aerosol particles were also studied, allowing conclusions to be drawn regarding their nature and composition. Specific characteristics of biomass burning aerosols in the region were identified.

5) Based on observations from the AERONET Kyiv station, seasonal variations in AOD over Kyiv were found, which are linked to agricultural activities and climatic factors. The overall trend during the observation period indicated a decrease in AOD and Angstrom Exponent. The observations also revealed the influence of aerosol particles on the energy balance and heating of the atmosphere.

6) Analysis of data using the GIOVANNI platform and MERRA-2 modeling showed that AOD and AE values vary depending on the season and aerosol components over Ukraine. Changes in the concentrations of black carbon, $PM_{2.5}$, CO, SO_2, SO_4, and organic carbon in the atmosphere over the territory of Ukraine were determined over a 15-year period. It was found that the highest concentrations were observed during the winter season and the heating season, while the lowest concentrations occurred during the summer for almost all components (organic carbon as an exception).

7) Due to the MERRA-2 reanalysis data, a low average concentration of $PM_{2.5}$ particles were observed in Ukraine until February 24, 2022. However, after this date, a significant change occurred, and the average $PM_{2.5}$ concentration nearly doubled. An increase in the average mass concentration of sulfates in the atmosphere was also noted after the full-scale invasion. While providing a seasonal analysis, a notable significant influence on these atmospheric components was evident in March 2022.

8) An analysis of aerosol properties was also provided to identify the impact of the Russian-Ukrainian war on atmospheric aerosol characteristics above Ukraine. Research based on AERONET observations indicates changes in the aerosol composition of the atmosphere in 2022: the fine particle fraction decreased, while the coarse particle fraction became more prominent. The increase in the aerosol optical depth indicates a shift in the dominant aerosol type. Assessment of radiative forcing showed more noticeable changes at the top of the atmosphere, while significant anomalies were not detected at the bottom.

9) The impact of war on Kyiv's atmospheric aerosols, as inferred from GRASP retrievals, was evident in substantial alterations in chemical composition. Particularly, the proportion of black carbon significantly surged in 2022 in contrast to prior years, highlighting the tangible influence of invasion on atmospheric components.

10) According to the AirVisual network data, no abnormal increases in $PM_{2.5}$ concentrations were observed during the second half of 2022 and the beginning of 2023. High $PM_{2.5}$ levels were recorded in March and April 2022 due to military activities and fires. Despite the decrease in $PM_{2.5}$ concentrations during these months, the air quality index remained above the recommended WHO level, exceeding 50 units during the cold season.

Perspectives:

The outcomes of this study can be applied in further research on aerosols over Kyiv, both in the short and long term. Specifically, the results obtained for biomass burning aerosols delineate aerosol properties for particles of diverse origins that are representative of this category. This information will aid in more accurately distinguishing between aerosol types over Kyiv and the surrounding region.

A long-term analysis of aerosols and other atmospheric components revealed seasonal trends that could also be used in identification of aerosol types. Additionally, a trend towards a reduction in both AOD and AE has been observed, showing certain changes in the chemical composition of aerosols, which could be further investigated. Moreover, specific anomalies in seasonal values of BC, SO2, and SO4 were identified, offering potential paths for further study

Furthermore, the study shows the impact of the Russian invasion on aerosol parameters and the concentrations of other atmospheric components. These data can also be applied for a more detailed analysis, serving as an illustration of changes occurring in the atmosphere due to the influence of war. The GRASP analysis revealed alterations in the chemical composition of aerosols, particularly a noticeable increase in black carbon. The data obtained from the algorithm's output will be further employed in computing substance concentrations and for a more detailed exploration of the war's influence on the chemical composition of aerosols.

BIBLIOGRAPHY

Abera, A.; Mattisson, K.; Eriksson, A.; Ahlberg, E.; Sahilu, G.; Mengistie, B.; Bayih, A.G.; Aseffaa, A.; Malmqvist, E.; Isaxon, C. (2020). Air pollution measurements and land-use regression in urban Sub-Saharan Africa using low-cost sensors – possibilities and pitfalls. *Atmosphere*, 11, 1357. doi:10.3390/atmos11121357

AERONET (AErosol RObotic NETwork). Available online: http://aeronet.gsfc.nasa.gov/ (accessed on 6 March 2023)

AERONET. Available online: https://aeronet.gsfc.nasa.gov/new_web/data_description_AOD_V2.html (accessed on 6 March 2023)

AirVisual. Available online: https://www.airvisual.com/invitation/T8nZek2N2 (accessed on 2 February 2023)

Alados-Arboledas, L.; Müller, D.; Guerrero-Rascado, J.L.; Navas-Guzmán, F.; Pérez-Ramírez, D.; Olmo, F.J. (2011). Optical and microphysical properties of fresh biomass burning aerosol retrieved by Raman lidar, and star- and sun-photometry. *Geophys. Res. Lett.*, *38*, L01807. doi:10.1029/2010GL045999.

Amaral, S.S.; de Carvalho, J.A., Jr.; Martins Costa, M.A.; Pinheiro, C. (2015). An Overview of Particulate Matter Measurement Instruments. *Atmosphere*, 6, 1327–1345. doi:10.3390/atmos6091327

Angstrom A. (1929) On the atmospheric transmission of sun radiation and on dust in the air. *Geogr Ann*,12, 130–59

Arias, P.A., N. Bellouin, E. Coppola, R.G. Jones, G. Krinner, J. Marotzke, V. Naik, M.D. Palmer, G.-K. Plattner, J. Rogelj, M. Rojas, J. Sillmann, T. Storelvmo, P.W. Thorne, B. Trewin, K. Achuta Rao, B. Adhikary, R.P. Allan, K. Armour, G. Bala, R. Barimalala, S. Berger, J.G. Canadell, C. Cassou, A. Cherchi, W. Collins, W.D. Collins, S.L. Connors, S. Corti, F.A. Cruz, F.J. Dentener, C. Dereczynski, A. Di Luca, A. Diongue-Niang, F.J. Doblas-Reyes, A. Dosio, H. Douville, F. Engelbrecht, V. Eyring, E. Fischer, P. Forster, B. Fox-Kemper, J.S. Fuglestvedt, J.C. Fyfe, N.P. Gillett, L. Goldfarb, I. Gorodetskaya, J.M. Gutiérrez, R. Hamdi, E. Hawkins, H.T. Hewitt, P. Hope, A.S. Islam, C. Jones, D.S. Kaufman, R.E. Kopp, Y. Kosaka, J. Kossin, S. Krakovska, J.-Y. Lee, J. Li, T. Mauritsen,

T.K. Maycock, M. Meinshausen, S.-K. Min, P.M.S. Monteiro, T. Ngo-Duc, F. Otto, I. Pinto, A. Pirani, K. Raghavan, R. Ranasinghe, A.C. Ruane, L. Ruiz, J.-B. Sallée, B.H. Samset, S. Sathyendranath, S.I. Seneviratne, A.A. Sörensson, S. Szopa, I. Takayabu, A.-M. Treguier, B. van den Hurk, R. Vautard, K. von Schuckmann, S. Zaehle, X. Zhang, and K. Zickfeld. (2021). Techincal summary. In Climate Change 2021: The Physical Science Basis. Contribution of Working Group I to the Sixth Assessment Report of the Intergovernmental Panel on Climate Change. V. Masson-Delmotte, P. Zhai, A. Pirani, S.L. Connors, C. Péan, S. Berger, N. Caud, Y. Chen, L. Goldfarb, M.I. Gomis, M. Huang, K. Leitzell, E. Lonnoy, J.B.R. Matthews, T.K. Maycock, T. Waterfield, O. Yelekçi, R. Yu, and B. Zhou, Eds., *Cambridge University Press*, pp. 33-144, doi:10.1017/9781009157896.002

Bergstrom, R. W., Pilewskie, P., Russell, P. B., Redemann, J., Bond, T. C., Quinn, P. K., and Sierau, B. (2007). Spectral absorption properties of atmospheric aerosols, *Atmos. Chem. Phys.*, 7, 5937–5943, doi:10.5194/acp-7-5937-2007

Boucher, O., D. Randall, P. Artaxo, C. Bretherton, G. Feingold, P. Forster, V.-M. Kerminen, Y. Kondo, H. Liao, U. Lohmann, P. Rasch, S.K. Satheesh, S. Sherwood, B. Stevens, and X.Y. Zhang (2013). Clouds and aerosols. In *Climate Change 2013: The Physical Science Basis. Contribution of Working Group I to the Fifth Assessment Report of the Intergovernmental Panel on Climate Change*. T.F. Stocker, D. Qin, G.-K. Plattner, M. Tignor, S.K. Allen, J. Doschung, A. Nauels, Y. Xia, V. Bex, and P.M. Midgley, Eds., Cambridge University Press, pp. 571-657, doi:10.1017/CBO9781107415324.016.

Boulon, J., Sellegri, K., Hervo, M., & Laj, P. (2011). Observations of nucleation of new particles in a volcanic plume. *Proceedings of the National Academy of Sciences*, 108 (30), 12223–12226. doi:10.1073/pnas.1104923108

Bovchaliuk V. (2016). Aerosols properties as retrieved from the GARRLIC synergetic approach applied to multi wavelength Raman LiDAR observations performed over Lille and Dakar sites. Laboratoire d'Optique Atmosphèrique, France. 153 p.

Bovchaliuk V., Milinevsky G., Danylevsky V., Goloub Ph., Sosonkin M., Yukhimchuk Yu., Podvin T. (2017). Aerosol properties in atmosphere over Kyiv using lidar and sun-photometer observations. Kosm. nauka tehnol. Space Science and Technology, 23(4).

Bovchaliuk, A. (2013). The spatial variability of $PM_{2.5}$ over Europe using satellite POLDER-3/PARASOL data. *Adv. Astron. Space Phys.*, 3, 102–108. Available online: http://aasp.kiev.ua/volume3/102-108-BovchaliukA.pdf (accessed on 25 January 2023).

California Air Resources Board. Available online: https://ww2.arb.ca.gov/resources/inhalable-particulate-matter-and-health (accessed on 26 January 2023)

Che, Z., Purushotham, S., Cho, K. et al. (2018). Recurrent Neural Networks for Multivariate Time Series with Missing Values. *Sci Rep*, 8, 6085. doi:10.1038/s41598-018-24271-9

Chin, M., Diehl, T., Tan, Q., Prospero, J. M., Kahn, R. A., Remer, L. A., ... & Holben, B. N. (2014). Multi-decadal aerosol variations from 1980 to 2009: a perspective from observations and a global model. *Atmos. Chem. Phys*., 14, 3657–3690. doi:10.5194/acp-14-3657-2014

Chin, M., Ginoux, P., Kinne, S., Torres, O., Holben, B. N., Duncan, B. N., Martin, R. V., Logan, J. A., Higurashi, A., & Nakajima, T. (2002). Tropospheric Aerosol Optical Thickness from the GOCART Model and Comparisons with Satellite and Sun Photometer Measurements, *Journal of the Atmospheric Sciences*, 59(3), 461-483.

Chu Y.; Liu, Y.; Li, X.; Liu, Zh.; Lu, H.; Lu, Y.; Mao, Z.; Chen, X.; Li, N.; Ren, M.; et al. (2016). A review on predicting ground $PM_{2.5}$ concentration using satellite aerosol optical depth. *Atmosphere*, 7, 129-1–129-25, doi:10.3390/atmos7100129

CIMEL. Available online: www.cimel.fr (accessed on 30 January 2023)

Climate Data for Cities Worldwide. Available online: https://en.climate-data.org/ (accessed on 25 January 2023).

Connolly, P. J., Möhler, O., Field, P. R., Saathoff, H., Burgess, R., Choularton, T., and Gallagher, M. (2009). Studies of heterogeneous freezing by three different desert dust samples, *Atmos. Chem. Phys*., 9, 2805–2824, doi:10.5194/acp-9-2805-2009.

DeMott, P.J.; Sassen, K.; Poellot, M.R.; Baumgardner, D.; Rogers, D.C.; Brooks, S.D.; Prenni, A.J.; Kreidenweis, S.M. (2003). African dust aerosols as atmospheric ice nuclei. *Geophys. Res. Lett*., 30, 1732. doi:10.1029/2003GL017410

Draxler, R.R. & Hess, G.D. (1998). An overview of the HYSPLIT 4 modeling system for trajectories, dispersion, and deposition. *Aust. Meteor. Mag*., *47*, 295–308.

Dubovik, O., & King, M. D. (2000). A flexible inversion algorithm for retrieval of aerosol optical properties from Sun and sky radiance measurements. Journal of Geophysical Research: Atmospheres, 105(D16), 20673-20696. doi:10.1029/2000JD900282

Dubovik, O., A. Sinyuk, T. Lapyonok, B.N. Holben, M. Mishchenko, P. Yang, T.F. Eck, H. Volten, O. Muñoz, B. Veihelmann, W.J. van der Zande, J.-F. Leon, M. Sorokin, and I. Slutsker. (2006). Application of spheroid models to account for aerosol particle nonsphericity in remote sensing of desert dust. *J. Geophys. Res.*, 111, D11208, doi:10.1029/2005JD006619.

Dubovik, O., A. Smirnov, B. N. Holben, M. D. King, Y. J. Kaufman, T. F. Eck, and I. Slutsker. (2000). Accuracy assessments of aerosol optical properties retrieved from Aerosol Robotic Network (AERONET) Sun and sky radiance measurements, J. Geophys. Res., 105(D8), 9791–9806, doi:10.1029/2000JD900040.

Dubovik, O., Herman, M., Holdak, A., Lapyonok, T., Tanré, D., Deuzé, J. L., ... & Lopatin, A. (2011). Statistically optimized inversion algorithm for enhanced retrieval of aerosol properties from spectral multi-angle polarimetric satellite observations. Atmospheric Measurement Techniques, 4(5), 975. doi:10.5194/amt-4-975-2011

Dubovik, O., Holben, B. N., Lapyonok, T., Sinyuk, A., Mishchenko, M. I., Yang, P., and Slutsker, I. (2002b). Non-spherical aerosol retrieval method employing light scattering by spheroids, Geophys. Res. Lett., 29, 541–544, https://doi.org/10.1029/2001GL014506.

Dubovik, O., Holben, B., Eck, T. F., Smirnov, A., Kaufman, Y. J., King, M. D., Tanré, D., & Slutsker, I. (2002). Variability of Absorption and Optical Properties of Key Aerosol Types Observed in Worldwide Locations. *Journal of the Atmospheric Sciences*, 59(3), 590-608. doi:10.1175/1520-0469(2002)059<0590:VOAAOP>2.0.CO;2

Dubovik, O., Holben, B., Eck, T. F., Smirnov, A., Kaufman, Y. J., King, M. D., Tanré, D., and Slutsker, I. (2002a). Variability of Absorption and Optical Properties of Key Aerosol Types Observed in Worldwide Locations, J. Atmos. Sci., 59, 590–608.

Dubovik, O., Lapyonok, T., Litvinov, P., Herman, M., Fuertes, D., Ducos, F., Torres, B., Derimian, Y., Huang, X., Lopatin, A., Chaikovsky, A., Aspetsberger, M., and Federspiel, C. (2014). GRASP: a versatile algorithm for characterizing the atmosphere, SPIE Newsroom, 2–5, https://doi.org/10.1117/2.1201408.005558

EARTHDATA. Visible Infrared Imaging Radiometer Suite (VIIRS). Available online: https://www.earthdata.nasa.gov/learn/find-data/near-real-time/viirs (accessed on 2 February 2023)

Encyclopedia Britannica. Available online: https://www.britannica.com/place/Ukraine/Plant-and-animal-life (accessed on 6 March 2023)

EOSDIS NASA Worldview. Available online: https://worldview.earthdata.nasa.gov/ (accessed on 6 March 2023).

European Aerosol Research Lidar Network. Available online: www.earlinet.org (accessed on 25 January 2023)

European Aerosol Research Lidar Network. Homepage. Available online: https://www.earlinet.org/index.php?id=earlinet_homepage (accessed on 2 February 2023)

European commission. Available online: https://commission.europa.eu/index_en (accessed on 27 January 2023)

European Commission. Available online: https://health.ec.europa.eu/scientific-committees_en (accessed on 25 January 2023)

European Environment Agency. Available online: https://www.eea.europa.eu/ (accessed on 26 January 2023)

Evangeliou, N.Y.; Balkanski, Y.; Cozic, A.; Hao, W.M.; Mouillot, F.; Thonicke, K.; Paugam, R.; Zibtsev, S.; Mousseau, T.A.; Wang, R.; et al. (2015). Fire evolution in the radioactive forests of Ukraine and Belarus: Future risks for the population and the environment. *Ecol. Monogr*., 85, 49–72. doi:10.1890/14-1227.1

Evironmental Expert. Available online: https://www.environmental-expert.com/products/horiba-model-apda-371-ambient-dust-monitor-151228 (accessed on 2 February 2023)

Fattoruso, G.; Nocerino, M.; Toscano, D.; Pariota, L.; Sorrentino, G.; Manna, V.; De Vito, S.; Cartenì, A.; Fabbricino, M.; Di Francia, G. (2020). Site suitability analysis for low cost sensor networks for urban spatially dense air pollution monitoring. *Atmosphere*, 11, 1215. doi:10.3390/atmos11111215

Fernald, F.G. (1984). Analysis of atmospheric LIDAR observations: Some comments. *Appl. Opt.*, *23*, 652–653. doi:10.5194/acp-9-9249-2009

FIRMS: Fire Information for Resource Management System of NASA's Earth Observing System Data and Information System (EOSDIS). Available online: https://earthdata.nasa.gov/firms (accessed on 6 March 2023).

Gao, C.; Zhang, X.; Wang, W.; Xiu, A.; Tong, D.Q.; Chen, W. (2018). Spatiotemporal distribution of satellite-retrieved ground-level $PM_{2.5}$ and near real-time daily retrieval algorithm development in Sichuan Basin, China. *Atmosphere*, 9, 78. doi:10.3390/atmos9020078

García, O. E., Díaz, J. P., Expósito, F. J., Díaz, A. M., Dubovik, O., Derimian, Y., Dubuisson, P., and Roger, J.-C. (2012). Shortwave radiative forcing and efficiency of key aerosol types using AERONET data, *Atmos. Chem. Phys*., 12, 5129–5145. doi:10.5194/acp-12-5129-2012.

García, O. E., et al. (2008), Validation of AERONET estimates of atmospheric solar fluxes and aerosol radiative forcing by ground-based broadband measurements, *J. Geophys. Res*., 113, D21207, doi:10.1029/2008JD010211

Generalized Retrieval of Atmosphere and Surface Properties. Available online: https://www.grasp-sas.com/ (accessed on 2 February 2023)

Giles, D. M., Sinyuk, A., Sorokin, M. G., Schafer, J. S., Smirnov, A., Slutsker, I., Eck, T. F., Holben, B. N., Lewis, J. R., Campbell, J. R., Welton, E. J., Korkin, S. V., and Lyapustin, A. I. (2019). Advancements in the Aerosol Robotic Network (AERONET) Version 3 database – automated near-real-time quality control algorithm with improved cloud screening for Sun photometer aerosol optical depth (AOD) measurements, *Atmos. Meas. Tech.*, 12, 169–209, doi:10.5194/amt-12-169-2019

Global Data Assimilation System (GDAS). National Oceanic and Atmospheric Administration. Available online: https://www.ncei.noaa.gov/products/weather-climate-models/global-data-assimilation (accessed on 6 March 2023).

Global Modeling and Assimilation Office (GMAO) (2015), MERRA-2 tavgM_2d_aer_Nx: 2d, Monthly mean, Time-averaged, Single-Level, Assimilation, Aerosol Diagnostics V5.12.4, Greenbelt, MD, USA, Goddard Earth Sciences Data and Information Services Center (GES DISC), Accessed: [Data Access Date], 10.5067/FH9A0MLJPC7N

Global Modeling and Assimilation Office (GMAO) (2015), MERRA-2 tavg1_2d_aer_Nx: 2d,1-Hourly, Time-averaged, Single-Level, Assimilation,Aerosol Diagnostics V5.12.4, Greenbelt, MD, USA, Goddard Earth Sciences Data and Information Services Center (GES DISC), Accessed: [Data Access Date], 10.5067/KLICLTZ8EM9D

Goddard Earth Sciences Division Projects. Available online: https://earth.gsfc.nasa.gov/climate/data/deep-blue/science (accessed on 27 January 2023)

Government of Canada: (https://www.canada.ca/en.html). (accessed on 27 January 2023)

Haënninen, O.O.; Salonen, R.O.; Koistinen, K.; Lanki, T.; Barregard, L.; Jantunen, M. (2009). Population exposure to fine particles and estimated excess mortality in Finland from an East European wildfire episode. *J. Expo. Sci. Environ. Epidemiol.*, 19, 414–422. doi:10.1038/jes.2008.31

Hinds, W.C. (1999) Aerosol Technology, Properties, Behaviour, and Measurement of Airborne Particles. *John Wiley & Sons Inc., New York*.

Holben B.N.; Kim, J.; Sano, I.; Mukai, S.; Eck, T.F.; Giles, D.M.; Schafer, J.S.; Sinyuk, A.; Slutsker, I.; Smirnov, A.; et al. (2018). An overview of mesoscale aerosol processes, comparisons, and validation studies from DRAGON networks. *Atmos. Chem. Phys.*, 18, 655–671, doi:10.5194/acp-18-655-2018

Holben, B.N., Tanre, D., Smirnov, A., Eck, T.F., Slutsker, I., Abuhassan, N., Newcomb, W.W., Schafer, J.S., Chatenet, B., Lavenu, F., Kaufman, Y.J., Castle, J.V., Setzer, A., Markham,

B., Clark, D., Frouin, R., Halthore, R., Karneli, A., O'Neill, N.T., Pietras, C., Pinker, R.T., Voss, K. and Zibordi, G. (2001). An Emerging Ground Based Aerosol Climatology: Aerosol Optical Depth from AERONET. *Journal of Geophysical Research — Atmospheres*, 106, 12067-12097. doi:10.1029/2001JD900014

Holben, B.N.; Eck, T.F.; Slutsker, I.; Tanré, D.; Buis, J.P.; Setzer, A.; Vermote, E.; Reagan, J.A.; Kaufman, Y.J.; Nakajima, T.; et al. (1998). AERONET-A Federated Instrument Network and Data Archive for Aerosol Characterization. *Remote Sens. Environ.*, 66, 1–16. doi:10.1016/S0034-4257(98)00031-5

Huang, K.; Xiao, Q.; Meng, X.; Geng, G.; Wang, Y.; Lyapustin, A.; Gu, D.; Liu, Y. (2018). Predicting monthly high-resolution $PM_{2.5}$ concentrations with random forest model in the North China Plain. *Environ. Pollut.*, 242, 675–683. doi:10.1016/j.envpol.2018.07.016

HYSPLIT Website Service, NOAA Air Resources Laboratory. Available online: https://www.ready.noaa.gov/HYSPLIT.php (accessed on 6 March 2023).

IPCC, 2014: Climate Change 2014: Synthesis Report. Contribution of Working Groups I, II and III to the Fifth Assessment Report of the Intergovernmental Panel on Climate Change [Core Writing Team, R.K. Pachauri and L.A. Meyer (eds.)]. IPCC, Geneva, Switzerland, 151 pp. (accessed on 25 January 2023).

IPCC, 2021: Climate Change 2021: The Physical Science Basis. Contribution of Working Group I to the Sixth Assessment Report of the Intergovernmental Panel on Climate Change [Masson-Delmotte, V., P. Zhai, A. Pirani, S.L. Connors, C. Péan, S. Berger, N. Caud, Y. Chen, L. Goldfarb, M.I. Gomis, M. Huang, K. Leitzell, E. Lonnoy, J.B.R. Matthews, T.K. Maycock, T. Waterfield, O. Yelekçi, R. Yu, and B. Zhou (eds.)]. *Cambridge University Press*, Cambridge, United Kingdom and New York, NY, USA, In press, doi:10.1017/9781009157896

IPCC. Anthropogenic and Natural Radiative Forcing. Available online: https://www.ipcc.ch/report/ar5/wg1/anthropogenic-and-natural-radiative-forcing/ (accessed on 27 January 2023)

IQAir AirVisual Platform. Available online: https://www.iqair.com/us/ (accessed on 27 January 2023)

Janhäll, S.; Andreae, M.O.; Pöschl, U. (2010). Biomass burning aerosol emissions from vegetation fires: Particle number and mass emission factors and size distributions. *Atmos. Chem. Phys.*, *10*, 1427–1439. doi:10.5194/acp-10-1427-2010

Kaskaoutis D. G. and Kambezidis H. D. (2006). Investigation into the Wavelength Dependence of the Aerosol Optical Depth in the Athens Area. *Journal of the Royal Meteoro-logical Society*, 132, 620, 2217-2234. doi:10.1256/qj.05.183

Khamala Geoffrey W., Makokha John W., Boiyo Richard, Kumar Kanike Raghavendra. (2023). Spatiotemporal analysis of absorbing aerosols and radiative forcing over environmentally distinct stations in East Africa during 2001–2018, *Science of The Total Environment,* 864, 161041, doi:10.1016/j.scitotenv.2022.161041

Khan, R., Kumar, K.R., Zhao, T.L., (2019). The climatology of aerosol optical thickness and radiative effects in Southeast Asia from 18-years of ground-based observations. *Environ. Pollut.* 254, 113025. doi: 10.1016/j.envpol.2019.113025

Klett, J. D. (1981). Stable analytical inversion solution for processing lidar returns. Applied optics, 20(2), 211-220.

Klett, J. D. (1985). Lidar inversion with variable backscatter/extinction ratios. Applied Optics, 24(11), 1638-1643.

Krueger, A. J., & Minzner, R. A. (1976). A mid-latitude ozone model for the 1976 US Standard Atmosphere. *Journal of Geophysical Research*, 81(24), 4477-4481. doi:10.1029/JC081i024p04477

Kucbel, M.; Corsaro, A.; Švédová, B.; Raclavská, H.; Raclavský, K.; Juchelková, D. (2017). Temporal and seasonal variations of black carbon in a highly polluted European city: apportionment of potential sources and the effect of meteorological conditions. *J. Environ. Manage*, *203*, 1178–1189, doi:10.1016/j.jenvman.2017.05.038.

Lack, D.A., Cappa, C.D. (2010). Impact of brown and clear carbon on light absorption enhancement, single scatter albedo and absorption wavelength dependence of black carbon. *Atmos. Chem. Phys*. 10, 4207–4220. doi:10.5194/acp-10-4207-2010.

Lanzinger, S.; Schneider, A.; Breitner, S.; Stafoggia, M.; Erzenc, I.; Dostal, M.; Pastorkova, A.; Bastian, S.; Cyrys, J.; Zscheppang, A.; et al. (2016). Associations between ultrafine and fine particles and mortality in five central European cities-Results from the UFIREG study. *Environ. Int.*, 88, 44–52. doi:10.1016/j.envint.2015.12.006

Lennartson, E.M.; Wang, J.; Gu, J.; Garcia, L.C.; Ge, C.; Gao, M.; Choi, M.; Saide, P.E.; Carmichael, G.R.; Kim, J.; et al. (2018). Diurnal variation of aerosol optical depth and PM2:5 in South Korea: A synthesis from AERONET, satellite (GOCI), KORUS-AQ observation, and the WRF-Chem model. *Atmos. Chem. Phys*., 18, 15125–15144. doi:10.5194/acp-18-15125-2018

Leon, J.-F.; Derimian, Y.; Chiapello, I.; Tanre, D.; Podvin, T.; Chatenet, B.; Diallo, A.; Deroo, C. (2009). Aerosol vertical distribution and optical properties over M'Bour (16.96°W; 14.39°N), Senegal from 2006 to 2008. *Atmos. Chem. Phys.*, *9*, 9249–9261. doi:10.5194/acp-9-9249-2009

Levin, E.J.T., McMeeking, G.R., Carrico, C.M., Mack, L.E., Kreidenweis, S.M., Wold, C.E., Moosmüller, H., Arnott, W.P., Hao, W.M., Collett, J.L., Malm, W.C. (2010). Biomass burning smoke aerosol properties measured during fire laboratory at missoula experiments (FLAME). *J. Geophys. Res*. 115. doi:org/10.1029/2009JD013601

Li Tao, Rong Hu, Zi Chen, Qiyuan Li, Shouxiong Huang, Zhou Zhu, Lin-Fu Zhou. (2018). Fine particulate matter (PM2.5): The culprit for chronic lung diseases in China. *Chronic Diseases and Translational Medicine Volume*, 4, 3, 139-204. doi:10.1016/j.cdtm.2018.07.002

Li, L., Dubovik, O., Derimian, Y., Schuster, G. L., Lapyonok, T., Litvinov, P., Ducos, F., Fuertes, D., Chen, C., Li, Z., Lopatin, A., Torres, B., and Che, H. (2019). Retrieval of aerosol components directly from satellite and ground-based measurements, *Atmos. Chem. Phys*., 19, 13409–13443, doi:10.5194/acp-19-13409-2019

Li, L.; Mahowald, N.M.; Miller, R.L.; Pérez García-Pando, C.; Klose, M.; Hamilton, D.S.; Gonçalves Ageitos, M.; Ginoux, P., Balkanski, Y.; Green, R.O.; et al. (2021). Quantifying the range of the dust direct radiative effect due to source mineralogy uncertainty. *Atmos. Chem. Phys*., 21, 3973–4005. doi:10.5194/acp-21-3973-2021

Li, L.; Sokolik, I.N. (2018). The Dust Direct Radiative Impact and Its Sensitivity to the Land Surface State and Key Minerals in the WRF-Chem-DuMo Model: A Case Study of Dust Storms in Central Asia. J. *Geophys. Res. Atmos*., 123, 4564–4582. doi:10.1029/2017JD027667

Lohmann, U. and Feichter, J. (2005). Global indirect aerosol effects: a review, *Atmos. Chem. Phys*., 5, 715–737, doi:10.5194/acp-5-715-2005

Lopatin, A. (2013). Enhanced remote sensing of atmospheric aerosol by joint inversion of active and passive remote sensing observations (Doctoral dissertation, Lille 1).

Lopatin, A., Dubovik, O., Chaikovsky, A., Goloub, P., Lapyonok, T., Tanré, D., & Litvinov, P. (2013). Enhancement of aerosol characterization using synergy of lidar and sun-photometer coincident observations: the GARRLiC algorithm. Atmospheric Measurement Techniques, 6(8), 2065-2088. doi:10.5194/amt-6-2065-2013

Markowicz, K.M.; Chilinski, M.T.; Lisok, J.; Zawadzka, O.; Stachlewska, I.S.; Janicka, L.; Rozwadowska, A.; Makuch, P.; Pakszys, P.; Zielinski, T.; et al. (2016). Study of aerosol optical properties during long-range transport of biomass burning from Canada to Central Europe in July 2013. *J. Aerosol Sci*., 101, 156–173. doi:10.1016/j.jaerosci.2016.08.006

Milinevsky G, Yatskiv Ya, Degtyaryov O, Syniavskyi I, Mishchenko M, Rosen- bush V, Ivanov Yu, Makarov A, Bovchaliuk A, Danylevsky V, Sosonkin M, Moskalov S, Bovchaliuk V, Lukenyuk A, Shymkiv A, Udodov E. (2016). New satellite project Aerosol-UA: Remote sensing of aerosols in the terrestrial atmosphere. *Acta Astronaut*, 123:292–300. doi:10.1016/j.actaastro.2016.02.027

Milinevsky, G.; Danylevsky, V.; Bovchaliuk, V.; Bovchaliuk, A.; Goloub, Ph.; Dubovik, O.; Kabashnikov, V.; Chaikovsky, A.; Miatselskaya, N.; Mishchenko, M.; Sosonkin, M. (2014). Aerosol seasonal variations over urban–industrial regions in Ukraine according to AERONET and POLDER measurements. *Atmos. Meas. Tech.*, 7, 1459–1474, doi:10.5194/amt-7-1459-2014

Moderate Resolution Imaging Spectroradiometer. Available online: https://modis.gsfc.nasa.gov/about (accessed on 2 February 2023)

Mortier, A. (2013). Tendances et Variabilites de l'aerosol Atmospherique a l'aide du Couplage Lidar. Photometre sur les Sites de Lille et Dakar. *Ph.D. Thesis, University of Lille*, Lille, France.

Mortier, A., Goloub, P., Podvin, T., Deroo, C., Chaikovsky, A., Ajtai, N., ... & Derimian, Y. (2013). Detection and characterization of volcanic ash plumes over Lille during the Eyjafjallajökull eruption. Atmospheric Chemistry & Physics, 13(7). doi:10.5194/acp-13-3705-2013

Müller D., Jungandreas A., Koch F., Schierhorn F. Impact of Climate Change on Wheat Production in Ukraine. (2016). *Report for the Agrarpolitischer Dialog (APD) Ukraine*. Available online: https://www.researchgate.net/publication/307569914_Impact_of_climate_change_on_wheat_production_in_Ukraine (accessed on 3 March 2023)

Myhre, G., Myhre, C. E.L., Samset, B. H. & Storelvmo, T. (2013) Aerosols and their Relation to Global Climate and Climate Sensitivity. Nature Education Knowledge 4(5):7

NAAPS: Navy Aerosol Analysis and Prediction System. Naval Research Lab Monterey ICAP Multi-Model Ensemble. Available online: https://www.nrlmry.navy.mil/aerosol_web/Docs/nrlmryonrprop.html (accessed on 6 March 2023).

NASA (National Aeronautics and Space Administration). Available online: https://www.nasa.gov/multimedia/imagegallery/image_feature_2393.html (accessed on 2 February 2023)

NASA Earth Observatory. Available online: https://earthobservatory.nasa.gov/features/UVB (accessed on 27 January 2023)

NASA Micro-Pulse Lidar Network. Available online: https://mplnet.gsfc.nasa.gov (accessed on 3 February 2023)

National Environmental Satellite, Data, and Information Service (NESDIS). Available online: https://www.nesdis.noaa.gov/current-satellite-missions/currently-flying/joint-polar-satellite-system/visible-infrared-imaging (accessed on 2 February 2023)

National Oceanic and Atmospheric Administration. Air Resources Laboratory. Available online: https://www.arl.noaa.gov/hysplit/ (accessed on 2 February 2023)

National Oceanic and Atmospheric Administration. Visible Infrared Imaging Radiometer Suite (VIIRS). Available online: https://www.ospo.noaa.gov/Products/Suites/satellite_instruments.html (accessed on 2 February 2023)

National Weather Service. Available online: https://www.weather.gov/jetstream/absorb (accessed on 27 January 2023)

New York State Department of Health. Available online: https://www.health.ny.gov/environmental/indoors/air/pmq_a.htm (accessed on 25 January 2023)

Penner, J.E., et al. (2001). Aerosols, Their Direct and Indirect Effects. In: Houghton, J.T., et al., Eds., Climate Change 2001: The Scientific Basis, Contribution of Working Group I to the Third Assessment Report of the Intergovernmental Panel on Climate Change, *Cambridge University Press*, Cambridge and New York, 289-348.

Petty, Grant W. (Grant William). (1958). A first course in atmospheric radiation. *Madison, Wis.: Sundog Pub*., c2006.

Pitz M., Cyrys J., Karg E., Wiedensohler A., Wichmann H-E., Heinrich J. (2003). *Environmental Science & Technology*. 37 (19), 4336-4342. doi:10.1021/es034322p

Platnick, S., P. Hubanks, K. Meyer, and M. D. King. (2015). MODIS Atmosphere L3 Monthly Product (08_L3). NASA MODIS Adaptive Processing System, Goddard Space Flight Center.

Putaud, J.-P.; Van Dingenen, R.; Alastuey, A.; Bauer, H.; Birmili, W.; Cyrys, J.; Flentje, H.; Fuzzi, S.; Gehrig, R.; Hansson, H.C.; et al. (2010). A European aerosol phenomenology-3:

Physical and chemical characteristics of particulate matter from 60 rural, urban, and kerbside sites across Europe. *Atmos. Environ*., 44, 1308–1320. doi:10.1016/j.atmosenv.2009.12.011.

Racioppi, F., Rutter, H., Nitzan, D., Borojevic, A., Carr, Z., Grygaski, T. J., ... & Kluge, H. H. P. (2022). The impact of war on the environment and health: implications for readiness, response, and recovery in Ukraine. *The Lancet*, 400(10356), 871-873. doi: 10.1016/s0140-6736(22)01739-1

Rasch, P. J., Barth, M. C., Kiehl, J. T., Schwartz, S. E., and Benkovitz, C. M. (2000). A description of the global sulfur cycle and its controlling processes in the National Center for Atmospheric Research Community Climate Model, Version 3, *J. Geophys. Res.*, 105(D1), 1367– 1385, doi:10.1029/1999JD900777.

Reid, J.S.; Koppmann, R.; Eck, T.F.; Eleuterio. D.P. (2005). A review of biomass burning emissions part II: Intensive physical properties of biomass burning particles. *Atmos. Chem. Phys*., 5, 799–825. doi:10.5194/acp-5-799-2005

Rosenfeld D, Lohmann U, Raga GB, O'Dowd CD, Kulmala M, Fuzzi S, Reissell A, Andreae MO. (2008). Flood or drought: how do aerosols affect precipitation? *Science*, 5; 321(5894), 1309-13. doi:10.1126/science.1160606

Samek, L.; Turek-Fijak, A.; Skiba, A.; Furman, P.; Styszko, K.; Furman, L.; Stegowski, Z. (2020). Complex characterization of fine fraction and source contribution to PM2.5 mass at an urban area in Central Europe. *Atmosphere*, 11, 1085. doi:10.3390/atmos11101085

Sapkota, A.; Symons, J.M.; Kleissl, J.; Wang, L.; Parlange, M.B.; Ondov, J.; Breysse, P.N.; Diette, G.B.; Eggleston, P.A.; Buckley, T.J. (2005). Impact of the 2002 Canadian forest fires on particulate matter air quality in Baltimore city. *Environ. Sci. Technol*., *39*, 24–32. doi:10.1021/es035311z. PMID: 15667071.

Sayer, A.M.; Hsu, N.C.; Eck, T.F.; Smirnov, A.; Holben, B.N. (2014). AERONET-based models of smoke-dominated aerosol near source regions and transported over oceans, and implications for satellite retrievals of aerosol optical depth. *Atmos. Chem. Phys*., *14*, 11493–11523. doi:10.5194/acp-14-11493-2014.

Schaap, M.; Apituley, A.; Timmermans, R.M.A.; Koelemeijer, R.B.A.; de Leeuw, G. (2009). Exploring the relation between aerosol optical depth and PM2.5 at Cabauw, the Netherlands. *Atmos. Chem. Phys*., 9, 909–925. doi:10.5194/acp-9-909-2009

Schuster, G. L., Dubovik, O., and Arola, A. (2016a). Remote sensing of soot carbon – Part 1: Distinguishing different absorbing aerosol species, Atmos. Chem. Phys., 16, 1565–1585, https://doi.org/10.5194/acp-16-1565-2016.

Schuster, G. L., Lin, B., and Dubovik, O. (2009). Remote sensing of aerosol water uptake, Geophys. Res. Lett., 36, L03814, https://doi.org/10.1029/2008GL036576

Seinfeld, J. H., Carmichael, G. R., Arimoto, R., Conant, W. C., Brechtel, F. J., Bates, T. S., Cahill, T. A., Clarke, A. D., Doherty, S. J., Flatau, P. J., Huebert, B. J., Kim, J., Markowicz, K. M., Quinn, P. K., Russell, L. M., Russell, P. B., Shimizu, A., Shinozuka, Y., Song, C. H., Tang, Y., Uno, I., Vogelmann, A. M., Weber, R. J., Woo, J., & Zhang, X. Y. (2004). ACE-ASIA: Regional Climatic and Atmospheric Chemical Effects of Asian Dust and Pollution, *Bulletin of the American Meteorological Society*, 85(3), 367-380. doi:10.1175/BAMS-85-3-367

Shanghai Expat Health and Safety. Available online: https://healthandsafetyinshanghai.com/ (accessed on 2 May 2023)

Shelestov, A.; Kolotii, A.; Borisova, T.; Turos, O.; Milinevsky, G.; Gomilko, I.; Bulanay, T.; Fedorov, O.; Shumilo, L.;Pidgorodetska, L.; et al. (2020). Essential variables for air quality estimation. *Intern. J. Digital Earth*, 13, 278–298. doi:10.1080/17538947.2019.1620881

Shi S., Cheng T., Gu X., Guo H., Wu Y., Wang Y. (2019). Biomass burning aerosol characteristics for different vegetation types in different aging periods. *Environment International*, 126, 504–511, doi:10.1016/J.ENVINT.2019.02.073

Shin, S.K., Tesche, M., Noh, Y., Muller, D., (2019). Aerosol type classification based on AERONET version3 inversion products atmos. *Meas. Tech. Discuss*. 12, 3789–3803. doi:10.5194/amt-12-3789-2019.

Sinyuk, A., Holben, B. N., Eck, T. F., Giles, D. M., Slutsker, I., Korkin, S., Schafer, J. S., Smirnov, A., Sorokin, M., and Lyapustin, A. (2020). The AERONET Version 3 aerosol retrieval algorithm, associated uncertainties and comparisons to Version 2, Atmos. Meas. Tech., 13, 3375–3411, doi:10.5194/amt-13-3375-2020

Sokolik, I.N.; Toon, O.B. (1996). Direct radiative forcing by anthropogenic airborne mineral aerosols. *Nature*, 381, 681–683.

Sówka, I.; Chlebowska-Styś, A.; Pachurka, Ł.; Rogula-Kozłowska, W.; Mathews, B. (2019). Analysis of particulate matter concentration variability and origin in selected urban areas in Poland. *Sustainability, 11*, 5735, doi:10.3390/su11205735.

Stein, A. F., Draxler R. R., Rolph G. D., Stunder B. J. B., Cohen M. D., and Ngan F. (2015). NOAA's HYSPLIT Atmospheric Transport and Dispersion Modeling System. *Bulletin of the American Meteorological Society*, 96, 12, 2059-2077. doi:10.1175/BAMS-D-14-00110.1

Stier, P., Feichter, J., Kinne, S., Kloster, S., Vignati, E., Wilson, J., Ganzeveld, L., Tegen, I., Werner, M., Balkanski, Y., Schulz, M., Boucher, O., Minikin, A., and Petzold, A. (2005). The aerosol-climate model ECHAM5-HAM, *Atmos. Chem. Phys.*, 5, 1125–1156, doi:10.5194/acp-5-1125-2005

Stohl, A. (1998). Computation, accuracy and applications of trajectories: A review and bibliography. *Atmos. Environ.*, *32*, 947–966. doi:10.1016/S1352-2310(97)00457-3.

Technical Assistance Document for the Reporting of Daily Air Quality – the Air Quality Index (2018). Available online: https://www.airnow.gov/sites/default/files/2020-05/aqi-technical-assistance-document-sept2018.pdf (accessed on 26 January 2023)

Turos, O., Maremukha, T., Petrosian, A., Mykhina, L., Morhulova, V. (2019). Integral indicators as tools for air quality assessment. *Environment & Health*, *1*(*90*), 51–55. doi:10.32402/dovkil2019.01.051

U.S. Environmental Protection Agency. Available online: https://www.epa.gov/ (accessed on 27 January 2023)

U.S. Environmental Protection Agency. Available online: https://www.epa.gov/ground-level-ozone-pollution/health-effects-ozone-pollution (accessed on 27 January 2023)

van Donkelaar, A.; Martin, R.V.; Levy, R.C.; da Silva, A.M.; Krzyzanowski, M.; Chubarova, N.E.; Semutnikova, E.; Cohen, A.J. (2011). Satellite-based estimates of ground-level fine particulate matter during extreme events: A case study of the Moscow fires in 2010. *Atmos. Environ.*, 45, 6225–6232. doi:10.1016/j.atmosenv.2011.07.068

Verma, S., Prakash, D., Soni, M. and Ram, K. (2019). Atmospheric Aerosols Monitoring: Ground and Satellite-Based Instruments. Advances in Environmental Monitoring and Assessment. *IntechOpen.* doi:10.5772/intechopen.80489

Weitkamp, C. (Ed.). (2006). Lidar: range-resolved optical remote sensing of the atmosphere (Vol. 102). *Springer Science & Business*.

WHO global air quality guidelines. Particulate matter ($PM_{2.5}$ and PM_{10}), ozone, nitrogen dioxide, sulfur dioxide and carbon monoxide. Geneva: World Health Organization; 2021. Licence: CC BY-NC-SA 3.0 IGO. Available online: https://iris.who.int/bitstream/handle/10665/345329/9789240034228-eng.pdf (accessed on 8 April 2024)

World Air Quality Report 2021 (2021). Available online: https://www.iqair.com/world-air-quality-report (accessed on 26 January 2023)

World Health Organization (WHO). Available online: https://www.who.int/health-topics/air-pollution#tab=tab_1 (accessed on 25 January 2023)

World Health Organization (WHO). Map Gallery. Available online: https://www.who.int/data/gho/map-gallery (accessed on 26 January 2023)

Yang, S.H.; Jeong, J.I.; Park, R.J.; Kim, M.J. (2020). Impact of Meteorological Changes on Particulate Matter and Aerosol Optical Depth in Seoul during the Months of June over Recent Decades. *Atmosph*ere, 11, 1282. doi:10.3390/atmos11121282

Yatskiv, Y. A., and S Milinevsky, G. P. (2015). Information About Fire Smoke in Kyiv Atmosphere. Report of National Academy of Sciences of Ukraine. 10, 25–30.

Yatskiv, Y. S., Mishchenko, M. I., Rosenbush, V. K., Shakhovskoy, D. N., Sinyavsky, I. I., Milinevsky, G. P., et al. (2012). Satellite project "AEROSOL-UA": remote sensing of aerosols in the Earth's atmosphere. *Kosm. Nauka Tehnol*. 18, 3–15. doi: 10.15407/knit2012.04.003

Yukhymchuk, Y.; Milinevsky, G.; Syniavskyi, I.; Popovici, I.; Unga, F.; Sciare, J.; Marenco, F.; Pikridas, M.; Goloub, P. (2022) Atmospheric Aerosol Outbreak over Nicosia, Cyprus, in April 2019: Case Study. Atmosphere 2022. – 13, 1997. https://doi.org/10.3390/atmos13121997

Zalakeviciute, R., Mejia, D., Alvarez, H., Bermeo, X., Bonilla-Bedoya, S., Rybarczyk, Y., & Lamb, B. (2022). War Impact on Air Quality in Ukraine. Sustainability, 14(21), 13832. doi:10.3390/su142113832

Zanatta, M.; Gysel, M.; Bukowiecki, N.; Müller, T.; Weingartner, E.; Areskoug, H.; Fiebig, M.; Yttri, K.E.; Mihalopoulos, N.; Kouvarakis, G.; et al. (2016). A European aerosol phenomenology-5: climatology of black carbon optical properties at 9 regional background sites across Europe. *Atmos. Environ.*, *145*, 346–364, doi:10.1016/j.atmosenv.2016.09.035.

Zhang C, Shulga V, Milinevsky G, Danylevsky V, Yukhymchuk Y, Kyslyi V, Syniavsky I, Sosonkin M, Goloub P, Turos O, Simon A, Choliy V, Maremukha T, Petrosian A, Pysanko, V, Honcharova A, Shulga D, Miatselskaya N, Morhuleva V. (2022) Spring 2020 Atmospheric Aerosol Contamination over Kyiv City. *Atmosphere*. – 13(5), 687. doi:10.3390/atmos13050687

Zhang, Q., Jimenez, J. L., Canagaratna, M. R., Allan, J. D., Coe, H., Ulbrich, I., Alfarra, M. R., Takami, A., Middlebrook, A. M., Sun, Y. L., Dzepina, K., Dunlea, E., Docherty, K., DeCarlo, P. F., Salcedo, D., Onasch, T., Jayne, J. T., Miyoshi, T., Shimono, A., ... Worsnop, D. R. (2007). Ubiquity and dominance of oxygenated species in organic aerosols in anthropogenically-influenced Northern Hemisphere midlatitudes. *Geophysical Research Letters*, *34*(13), [L13801]. doi:10.1029/2007GL029979

Zhang, Y., Li, Z., Zhang, Y., Li, D., Qie, L., Che, H., and Xu, H. (2017). Estimation of aerosol complex refractive indices for both fine and coarse modes simultaneously based on AERONET remote sensing products, *Atmos. Meas. Tech*., 10, 3203–3213, doi:10.5194/amt-10-3203-2017

Zhao, F.; Liu, Y.; Shu, L.; Zhang, Q. (2020). Wildfire Smoke Transport and Air Quality Impacts in Different Regions of China. *Atmosphere*, 11, 941. doi:10.3390/atmos11090941

ZoomEarth: NOAA/NESDIS/STAR, EUMETSAT, JMA/NOAA/CIRA Global Weather Satellite Images. Available online:https://zoom.earth/ (accessed on 6 March 2023).

Appendix 1

Table 1. Parameters of the aerosol particles columnar size distribution in the atmosphere over the Kyiv AERONET site during the days with significant aerosol contamination in March and April 2020.

Date	Time	Fine mode parameters			Coarse mode parameters			AOD (440 nm)	AE(440–870 nm)
		R_{eff}, μm	R_{Med}, μm	STD	R_{eff}, μm	R_{Med}, μm	STD		
28.03.2020	12:05	0.133	0.149	0.479	1.878	2.486	0.755	0.38	1.20
28.03.2020	13:05	0.112	0.122	0.432	1.932	2.567	0.737	0.38	1.15
28.03.2020	14:15	0.113	0.126	0.493	1.800	2.374	0.740	0.47	1.33
29.03.2020	08:04	0.110	0.121	0.467	1.779	2.229	0.672	0.50	1.11
29.03.2020	09:04	0.114	0.126	0.484	1.800	2.271	0.680	0.56	1.15
29.03.2020	10:04	0.092	0.100	0.463	1.791	2.219	0.653	0.43	0.91
29.03.2020	11:05	0.112	0.124	0.472	1.773	2.240	0.682	0.47	1.07
29.03.2020	12:04	0.111	0.122	0.471	1.833	2.363	0.704	0.48	1.05
29.03.2020	13:04	0.113	0.124	0.467	1.883	2.409	0.692	0.56	1.16
29.03.2020	14:17	0.113	0.123	0.434	1.947	2.477	0.684	0.60	1.23
29.03.2020	**14:59**	**0.126**	**0.135**	**0.382**	**1.906**	**2.365**	**0.653**	**0.54**	**1.16**
30.03.2020	**05:49**	**0.147**	**0.162**	**0.456**	**1.952**	**2.448**	**0.679**	**0.77**	**1.67**
30.03.2020	08:04	0.143	0.157	0.439	1.897	2.399	0.699	0.71	1.70
30.03.2020	09:04	0.144	0.156	0.392	1.782	2.385	0.758	0.76	1.66
30.03.2020	10:04	0.154	0.168	0.418	1.984	2.531	0.704	0.76	1.67
30.03.2020	11:04	0.162	0.178	0.470	2.079	2.528	0.644	0.98	1.72
17.04.2020	04:39	0.187	0.220	0.601	2.285	2.745	0.632	1.46	1.67
17.04.2020	11:59	0.135	0.149	0.471	1.828	2.676	0.837	0.63	1.38
17.04.2020	13:39	0.120	0.132	0.456	1.939	2.731	0.798	0.69	1.52
18.04.2020	06:17	0.192	0.213	0.453	1.669	2.286	0.826	1.60	1.41
18.04.2020	11:59	0.184	0.226	0.683	2.913	3.446	0.571	0.51	1.31
18.04.2020	14:49	0.176	0.223	0.711	3.575	4.183	0.532	0.47	1.41
19.04.2020	04:35	0.132	0.143	0.425	1.451	1.897	0.754	0.42	1.69
19.04.2020	06:15	0.159	0.176	0.476	1.706	2.249	0.765	0.46	1.73
19.04.2020	06:57	0.130	0.141	0.420	1.427	1.966	0.824	0.36	1.81
19.04.2020	07:05	0.149	0.172	0.582	2.180	2.677	0.647	0.34	1.80

Appendix 2

The impact of mineral dust transport in the atmosphere above Nicosia

1. The impact of dust storms on Cyprus

The island of Cyprus is located in the Mediterranean Sea and has a Mediterranean climate with warm and dry summers and mild winters. However, in recent years, there have been some changes in the island's climate. The Eastern Mediterranean and the Middle East are projected to experience more temperature changes compared to most other places on Earth. According to research by the Cyprus Institute, the projected increase in average temperature in this region will be approximately 1–3 °C over the next three decades, 3–5 °C by the middle of the century, and 3.5–7 °C by the end of the century (https://www.cyi.ac.cy/). This leads to a higher likelihood of severe heatwaves, which can have a negative impact on human and animal health, as well as on vegetation.

Additionally, climate change on the island of Cyprus is also manifested in changes in precipitation patterns. Considering the consistent decrease in precipitation observed over the past three decades, climate change in Cyprus will result in an additional reduction in rainfall by 10–15% during the period from 2020 to 2050 (https://www.cyi.ac.cy/).

Furthermore, anthropogenic activities and an increasing number of episodes of Saharan dust transport to northern parts of the region lead to an increase in the concentration of mineral dust and aerosols in the atmosphere of the island (https://www.cyi.ac.cy/). This results in an increase in respiratory diseases and is increasingly recognized as a significant health issue, particularly in Cyprus (https://www.cyi.ac.cy/).

As previously mentioned, mineral dust from the Sahara Desert can be transported over very long distances (Prospero, 1999). According to studies, Sahara dust can reach various parts of the world, including Europe, Asia, North and South America, and the Caribbean islands (refer to the works of Shao et al., 2011; Schepanski et al., 2009; Yu et al., 2015; Messager et al., 2009; Prospero & Carlson, 1972; Prospero et al., 2010).

The transport of Sahara mineral dust occurs through air currents that carry the dust from the source in the Sahara Desert to distant locations. The transportation of dust depends on two

main factors: the availability of dust sources, such as dry minerals and organic deposits, of which deserts are infinite sources, and the wind conditions that facilitate the lifting of solid particles into the troposphere and their transport. As a result, dust episodes tend to be seasonal, following changes in wind patterns (https://atmosphere.copernicus.eu/what-saharan-dust-and-how-does-it-change-atmosphere-and-air-we-breathe).

The transport of Sahara dust to the Caribbean Basin is more likely to occur during spring, summer, and early autumn when a layer of Saharan air, carrying very dry and dusty air masses, crosses the Atlantic. Early spring is the most active period for dust transport to Europe (https://atmosphere.copernicus.eu/what-saharan-dust-and-how-does-it-change-atmosphere-and-air-we-breathe).

The transport of Sahara mineral dust can have both positive and negative consequences. On the one hand, mineral dust can be beneficial for certain ecosystems, such as ocean waters or the Amazon rainforests, where it can serve as a source of nutrients for microorganisms (Swap et al., 1992; Reichholf, 1986; Koren et al., 2006; Falkowski et al., 1998). On the other hand, mineral dust can have a negative impact on human health, especially for those suffering from respiratory illnesses. Additionally, dust can affect air quality and contribute to environmental or ecosystem pollution (https://atmosphere.copernicus.eu/what-saharan-dust-and-how-does-it-change-atmosphere-and-air-we-breathe).

Based on the observations conducted at the Nicosia Atmospheric Monitoring Station (AERONET Nicosia), the highest values of Aerosol Optical Depth from 2015 to 2022 were recorded in April 2019. This increase in AOD was associated with a dust storm that occurred in the Sahara Desert and traveled towards southern Europe, including Cyprus. This storm brought a significant amount of dust and aerosol particles into the atmosphere of Cyprus, resulting in an increase in AOD values. The AERONET Nicosia website provides nearly continuous observations since February 2019. Some observations at this site are also available for March–April 2015 and April 2016. The aerosol optical depth reported by this instrument and the Ångström exponent are shown in Figure 1. Seasonal variations in AOD over Nicosia show the lowest concentration of aerosol particles during the winter season (typically less than 0.1 at a wavelength of 500 nm). From the beginning of spring, AOD values start to increase and vary until the end of autumn, reaching an average of ~0.20 (500 nm), with sporadic episodes where values reach ~0.5 (500 nm).

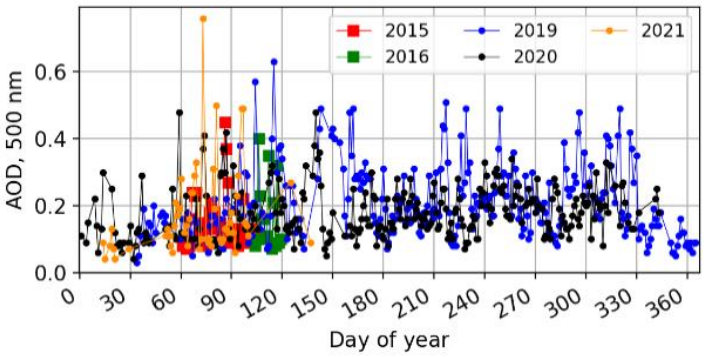

a

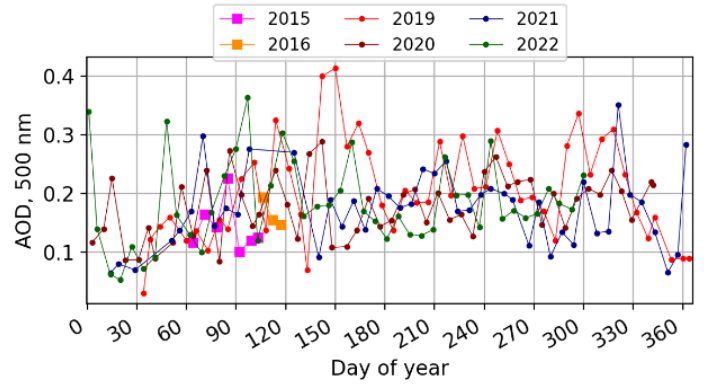

b

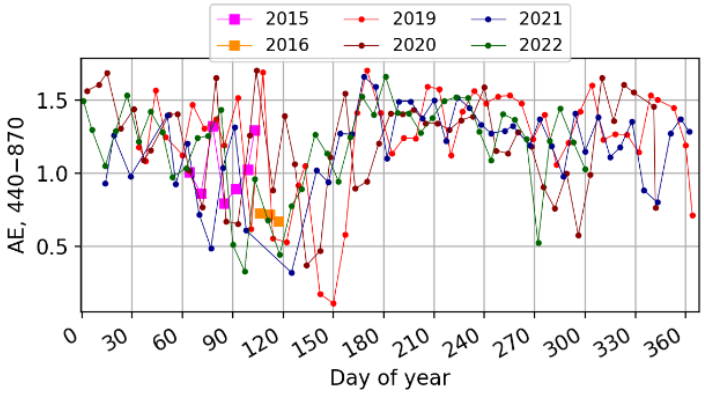

c

Figure 1. Aerosol Optical Depth (AOD) and Angstrom Exponent (AE) trends during 2015–2022: (a) AOD (500 nm), daily average data; (b) AOD (500 nm) and (c) AE (440–870 nm), weekly averaged measurements. Data obtained from the AERONET sun photometer in Kyiv. Level 2.0 for 2015–2021 and level 1.5 for 2021–2022.

In the spring months, an increase in the amount of aerosols leads to an increase in Aerosol Optical Depth to approximately 0.6–0.8 (at 500 nm), and this situation is observed almost every year. Additionally, in March-April 2015 and April 2016, the AOD values were lower (~0.15) compared to the corresponding period of 2019–2021 (~0.25). Figure 1a shows the data for 2021 at a level of 2.0 only for the winter-spring period, while for the rest of 2021 and for 2022, the available data level of 1.5 was used. Seasonal variations of the weekly average

values of Angstrom Exponent (440–870 nm) are presented in Figure 1b. Throughout 2019–2022, AOD and AE variations exhibit similar behavior with a certain seasonal dependency. The AE data demonstrate seasonal fluctuations, with a decrease in AE observed from mid-spring to early summer (Figure 1b). During this period, the transport of mineral dust from the Sahara Desert to the Eastern Mediterranean regions typically occurs in Nicosia (Amiridis et al., 2005; Papayannis et al., 2009).

Compared to other springtime aerosol enhancements, the aerosol transport event in April 2019 was one of the largest, where the AE values (470–870 nm) decreased to 0.3 in accordance with an increase in AOD (500 nm) above 0.9, indicating a significant contribution of mineral dust.

2. Observations at the AERONET station in Nicosia

a) Aerosol Optical Depth and Angstrom Exponent

On April 25, 2019, an increase in the daily average value of AOD at a wavelength of 500 nm to approximately 0.7 was observed. During April 23–25, 2019, AOD (500 nm) varied from around 0.1 to approximately 0.9. However, specific measurements on April 25 recorded higher values of aerosol optical depth, with AOD at a wavelength of 500 nm reaching values close to 0.98 (see Fig. 2a, b).

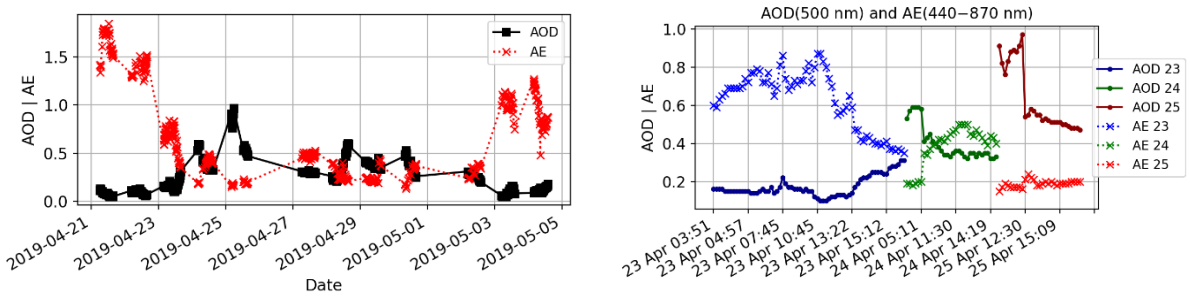

a b

Figure 2. Changes in aerosol optical depth (AOD 500 nm) and Ångström exponent (AE 470–870 nm) during (a) the 21–29 April period and (b) day time of April 23–25, 2019, Nicosia, Cyprus. Data level 2.0.

The increase in AOD and simultaneous decrease in AE indicate the influx of a significant amount of aerosols that differ in their properties from typical atmospheric particles over Nicosia. Moreover, the AE value change, which decreased from 0.7 to less than 0.2, suggests that this is due to the advection of mineral dust that started to arrive at the end of 23 April (see Fig. 2). The AE variations anticorrelate with the AOD values (see Fig. 2). The light blue line shows that the AE decreased from 0.6–0.8 to ≤0.4 on 23 April. On 25 April, a sun-photometer detected the lowest AE values of ≤0.2 (the pink curve in Fig. 2b).

b) single scattering albedo

In Figure 3, a clear transition from absorbing aerosols to predominantly scattering aerosols can be observed. The graphs present the spectral single scattering albedo from April 21 to April 25, 2019 (daily values) and specifically for April 25. The change in aerosol properties from absorbing to scattering is manifested by a smooth transition with an increase in SSA, reaching its maximum value on April 25 (see Fig. 3). On April 25, 2019, the SSA was approximately 0.99 (at wavelengths of 675–1020 nm, see Fig. 3) at 4:46 AM.

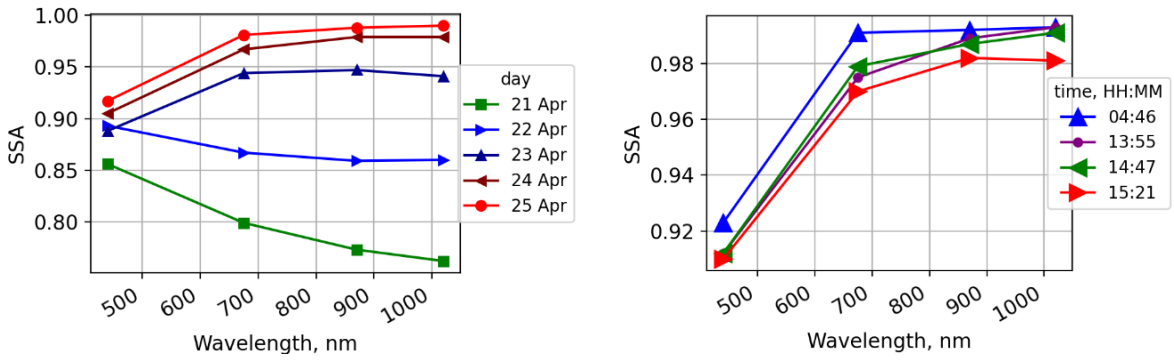

a b

Figure 3. Spectral Single Scattering Albedo (SSA) (a) from April 21 to April 25 and throughout the day (b) on April 25, 2019. Days are represented by colors in (a), while hours are indicated in (b). Data level 1.5 for (a) from April 21 to April 25 and data level 2.0 for (b) on April 25.

In Figure 3, it can be observed that the SSA curves for April 21 and 22 have a different shape compared to the SSA curves for April 23–25. This can be explained by the dominance of absorbing aerosol particles during the period from April 21 to 22, while scattering particles were predominant from April 23 to 25. The SSA curves for April 23–25 (see Fig. 3) exhibit a

typical shape for mineral dust. However, it is important to note that SSA also depends on other factors such as particle size and chemical composition, so the SSA for mineral dust can vary.

c) size distribution and complex refractive index

According to the variations in size distribution observed from April 21 to April 28, the number of coarse particles gradually increased from April 21 to 25, as seen in Figure 4a. Subsequently, a decrease in the number of these particle modes was observed from April 25 to April 27–28, as shown in Figure 4b.

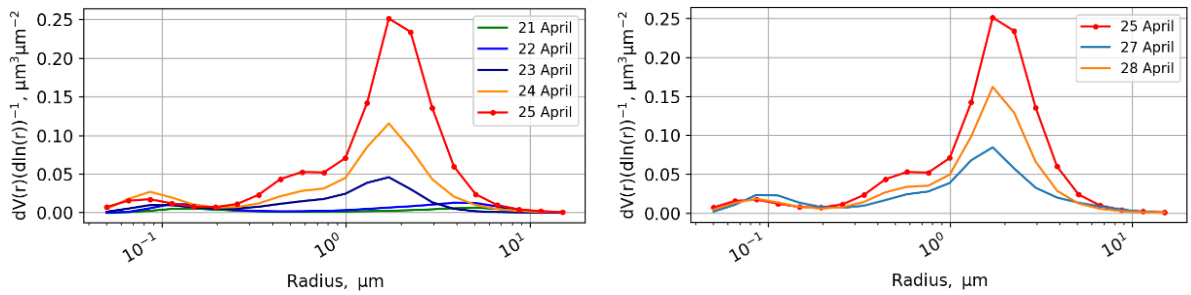

a b

Figure 4. Aerosol Size Distribution (a) from April 21 to April 25 and (b) from April 25 to April 28, 2019. Data level 2.0. Data for April 26 are not available. Days of observations are indicated by colors.

The coarse particle mode was dominant during the increase in aerosol concentration on April 25, 2019. The graphs in Figure 4 indicate that a significant fraction of aerosols varies in size from 1 to 10 µm. The highest values were recorded in the morning of April 25. According to previous studies, the characteristic size distribution for the advection of mineral dust is dominated by the coarse mode (Maring et al., 2003; Zhang et al., 2017).

Figure 5 shows the AERONET Nicosia data for both the real part of the refractive index (RI) on April 25, 2019, and the variation of the imaginary part over the period from April 21 to April 28. The real part of RI ranges from 1.43 to 1.52 (see Fig. 5a) and varies with wavelength, which is typical for mineral dust particles (Zhang et al., 2017). Similar results were obtained for the imaginary part of the refractive index. Firstly, the values of the imaginary part of RI are within the range of less than 0.04 (see Fig. 5b), which is characteristic of Saharan dust particles (Di Biagio et al., 2019). Secondly, the shape of the variation in the imaginary part of RI depends

on the wavelength and describes changes that are typical for mineral dust particles, as illustrated in similar graphs presented in Zhang et al. (2017).

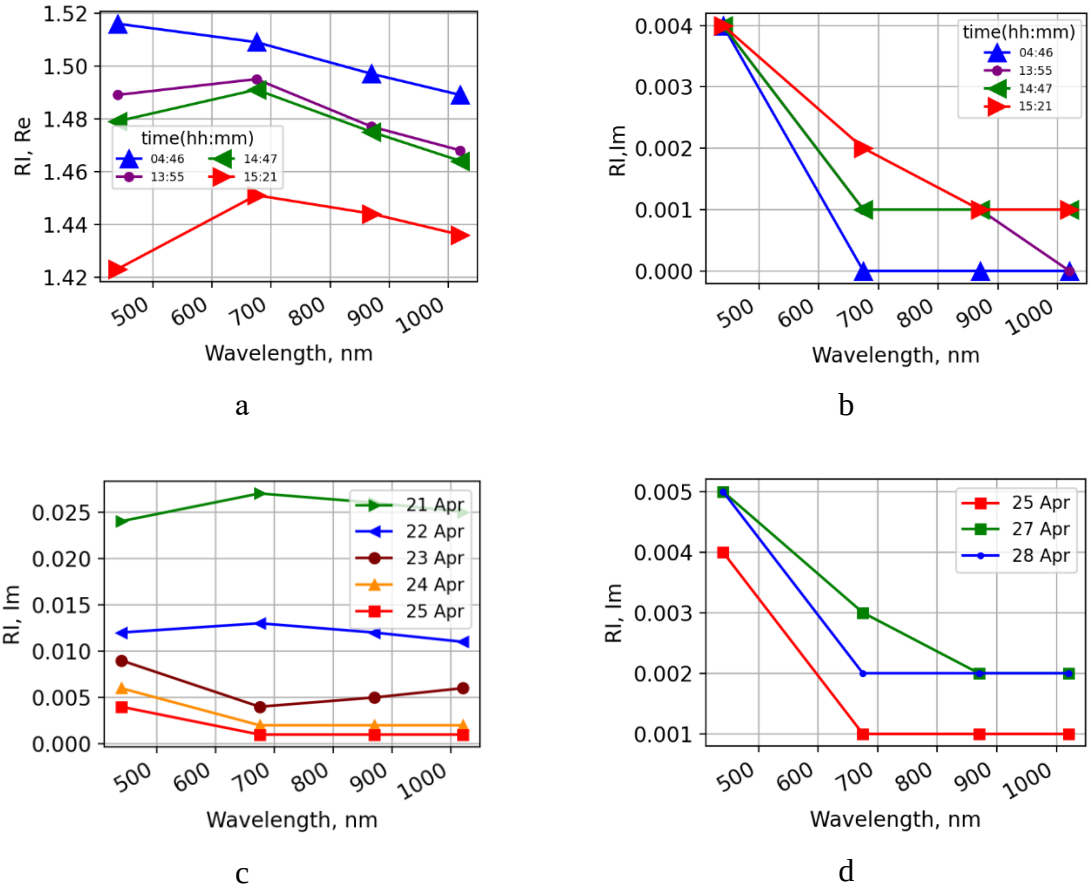

Figure 5. Complex refractive index: (a) real part, (b) imaginary part on April 25, 2019. Data level 2.0. Imaginary part for (c) April 25, 2019, and (d) April 25, 27, 28, 2019. Data level 1.5. Values for April 26, 2019, are not available.

d) Cluster Analysis for Aerosols Particle Types

The cluster analysis method allows to group data in datasets with similar characteristics. In the case of the 23–25 April events, we have enough AOD and AE measurements to provide the cluster analysis of aerosol-type particles (Omar et al., 2005; Szkop et al., 2016). The changes in aerosol types are shown in the scatter plot AOD versus AE in Figure 6.

According to Figure 6, changes in the dominant aerosol type were observed in the atmosphere above Nicosia. For two days, an anthropogenic aerosol type prevailed, but it was later replaced by an aerosol with mineral dust properties. This transition process occurred

rapidly but smoothly, indicating that the pollution did not occur spontaneously but could have been transported over Nicosia through air transport from distant sources.

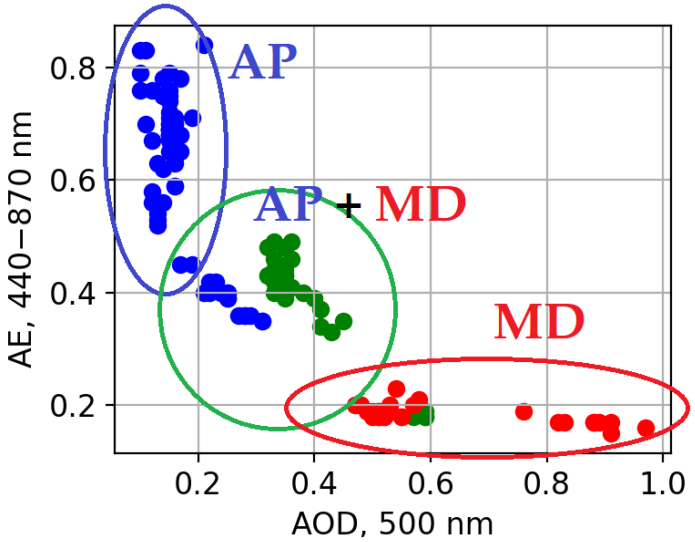

Figure 6. Scatter plot for aerosol optical depth (500 nm) versus Ångström exponent (440–870 nm) dependency during 23–25 April 2019: blue dots – 23 April, green – 24 April, and red – 25 April. AP – anthropogenic aerosol particles; MD – mineral dust. Data level 2.0.

3. Lidar observations

a) profiles of extinction and mass concentration of particles

Lidar observations provide information on the altitude distribution of aerosol particles with high spatial resolution. In contrast to AERONET observations, which retrieve aerosol characteristics for a whole atmospheric column, lidar observations allow defining the altitudes of particles' spatial structure (Papayannis et al., 2009).

This information is important for studying aerosol dynamics over some territories, aerosol properties, and sources of aerosol particles. The main part of aerosol advection is concentrated at the planetary boundary level, usually at the altitudes below 1000–2000 m, depending on the topography (Liu et al., 2010; Palm et al., 2021). The smoke and biomass burning aerosol from powerful wildfires can rise to higher altitudes, such as 4–5 km, and ash

from volcano eruptions could be able to reach the stratosphere (Papanikolaou et al., 2022; Mona et al., 2012).

In the case of Nicosia, lidar observations cover the entire year of 2019, including the period of the event of 23–25 April 2019. Based on lidar measurements and AERONET sun photometer data, we provided analysis of the aerosol dust contamination over Nicosia on 25 April 2019. As was mentioned before, the combination of sun photometer and lidar data allowed retrieving extinction, lidar ratio, and mass concentration during aerosol outbreak events. Figure 7 presents the lidar time series of range-corrected backscatter signal for Nicosia on 25 April 2019. On 23 April, the lidar observations showed a low amount of aerosol particles in the atmosphere, and on the next day, the backscatter signal increased. The maximum backscattering was detected on 25 April.

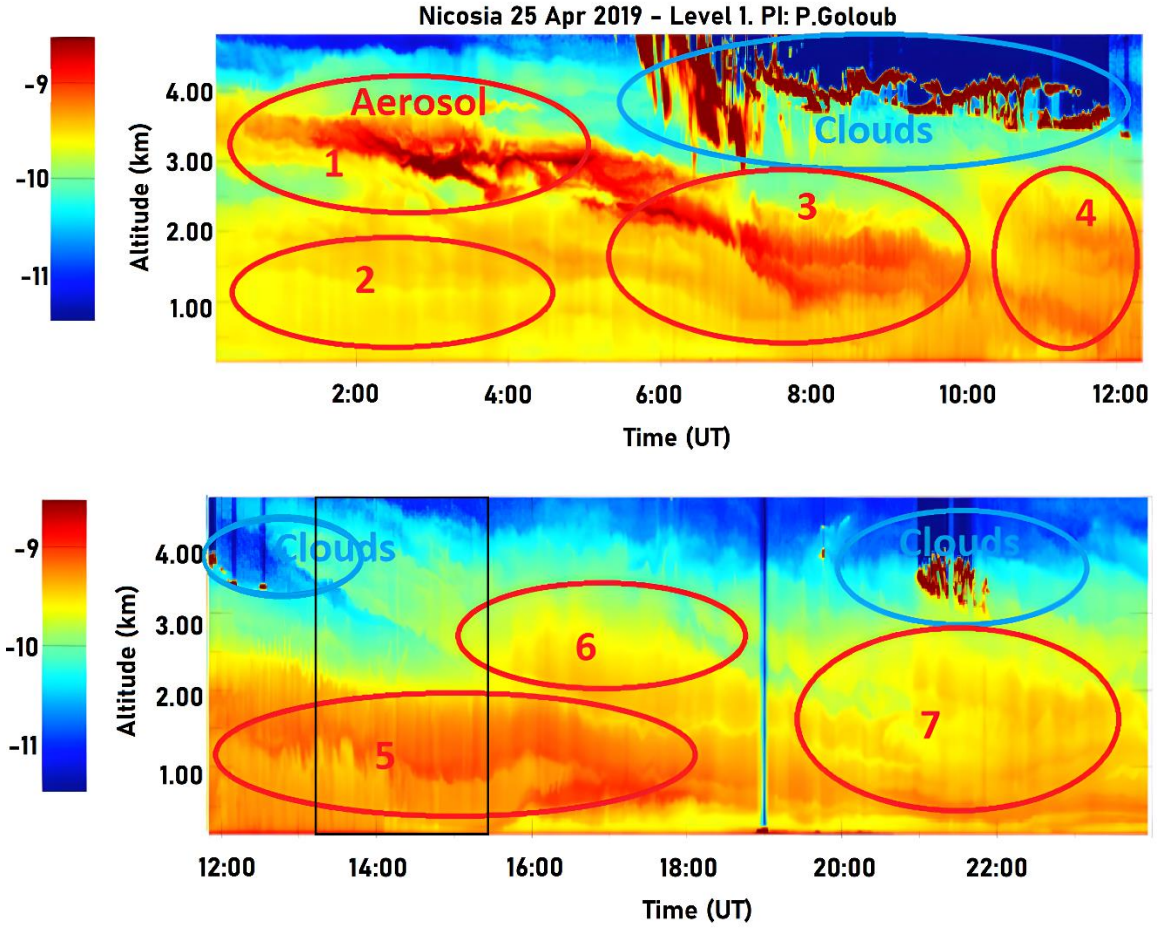

Figure 7. Lidar time series of range-corrected backscatter signal for Nicosia, Cyprus, on April 25, 2019. The color represents the natural logarithm of the height-corrected lidar signal (ln PR^2, left scale). Blue circles indicate clouds, while red circles and numbers (1–7) represent aerosol layers.

Backscatter signals according to lidar observations started to grow up on 24 April. When a new aerosol plume arrived at high altitudes (3.5 km, the layer 1 at 1 h on 25 April, see Fig. 7), there was already aerosol advection below 2 km (see Fig. 7, the layer 2). The upcoming aerosol layer 1 was located at altitudes between 3 and 4 km. At 5 h, aerosol layer 1 decreased its altitude and mixed with layer 2, forming layer 3 (see Fig. 7, the layer 3). The layer 5 (former layer 4) was dominant until 16 h. Then, it was separated into layers 6 and 7, which were less dense than layer 5 (see Fig. 7, layer 5). This atmospheric dynamic is probably due to atmospheric advection, the details of which are not a topic of this study.

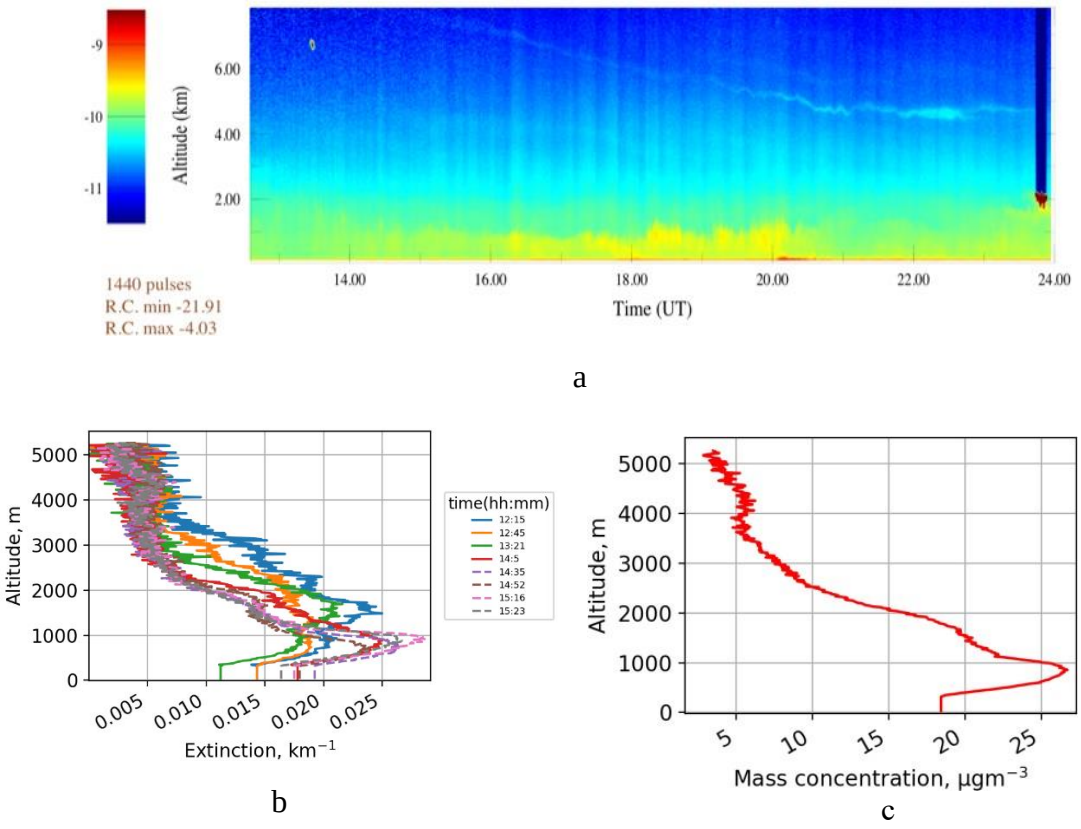

Figure 8. (a) Lidar time series of range-corrected backscatter signal for Nicosia, Cyprus, on April 21, 2019. The natural logarithm of the height-corrected signal (ln PR^2, left scale) is shown in color. (b) Altitude profile of extinction for April 21 from 12:15 to 15:23 UT (measurement time indicated in color) and the corresponding (c) profile of average mass concentration in the atmosphere above Nicosia.

In order to determine the aerosol vertical profile of the extinction coefficient and mass concentration using lidar data, the different models of aerosol types and their size distribution should be used. In the AERONET retrieval algorithm, aerosol types are modeled by several modes with a certain aerosol particle size distribution, where each mode is a mixture of

homogeneous spherical particles and randomly oriented spheroids (http://aeronet.gsfc.nasa.gov/, Dubovik et al., 2002). Retrieval of extinction profile and effective lidar ratio (the extinction to backscattering ratio) are performed during daytime using methodology Leon et al. (2009), that is based on the Klett and Fernald solution (Klett et al., 1981; Fernald et al., 1984) using the BASIC algorithm (Mortier et al., 2013; Mortier, 2013), and it includes the use of the accurate AOD measurements, such as AERONET. The other AERONET observed aerosol characteristics are the particle diameter (for two modes), the proportion of fine and coarse mode, particle density, and real and imaginary parts of the refractive index, which, in synergy with the extinction profile, could be used for the calculation of aerosol mass concentration (Mortier et al., 2013).The lidar retrieval algorithm allows choosing the aerosol type model based on the above-mentioned aerosol properties: biomass burning, ash, urban–industrial, dust, sea salt, or manually defining.

Extinction profiles for April 25, 2019, are presented in Figure 9a. Results for April 21 are provided for comparison (see Fig. 8). Extinction profiles with minimal cloud influence were considered for calculating the mass concentration. On April 25, the extinction coefficient varied from 0.05 to 0.2 km^{-1}.

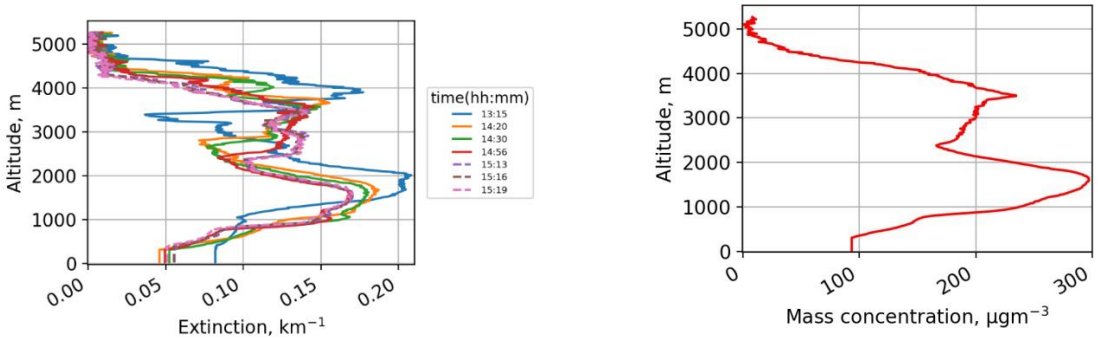

a b

Figure 9. (a) Altitude profile of extinction for April 25 from 13:15 to 15:19 UT (measurement time indicated in color) and the corresponding (b) profile of average mass concentration in the atmosphere above Nicosia.

For the calculation of mass concentration for this day, the following assumptions and observations were used: (1) the refractive index from AERONET observations (see Fig. 5); (2) the density of mineral dust is approximately 2.6 g cm^{-3} (Linke et al., 2006; Kandler et al., 2011), and urban aerosol according to the AERONET model is 1.7 g cm^{-3}; (3) the mineral dust model for the aerosol size distribution (based on AERONET observations of size distribution presented in Figure 4, the mineral dust model is the most suitable for this case); and (4) lidar

measurements of the extinction coefficient. The resulting aerosol mass concentration corresponding to an extinction of 0.6 is over 1000 μg m^{-3}. Assuming an average particle radius of 1.3 μm (see Fig. 4), the calculated average mass concentration falls within the range of 100–300 μg m^{-3} (see Fig. 9b). Compared to the "background" day on April 21, the highest mass concentration value on April 25 exceeds the background by more than 10 times (see Fig. 8c, 27 μg m^{-3}). Two peaks in mass concentration at approximately ~1.5 km and ~3.5 km (see Fig. 9b) correspond to aerosol plumes in layers 5 and 6 in Figure 7.

b) Influence of atmospheric mass transport on the transport of mineral dust

For air mass movement calculation, the HYSPLIT model uses meteorological data files from the Global Data Assimilation System (GDAS), which includes a variety of data from different instruments and sources of data: satellite, ground-based, and aircraft measurements (https://www.emc.ncep.noaa.gov/gmb/gdas/).

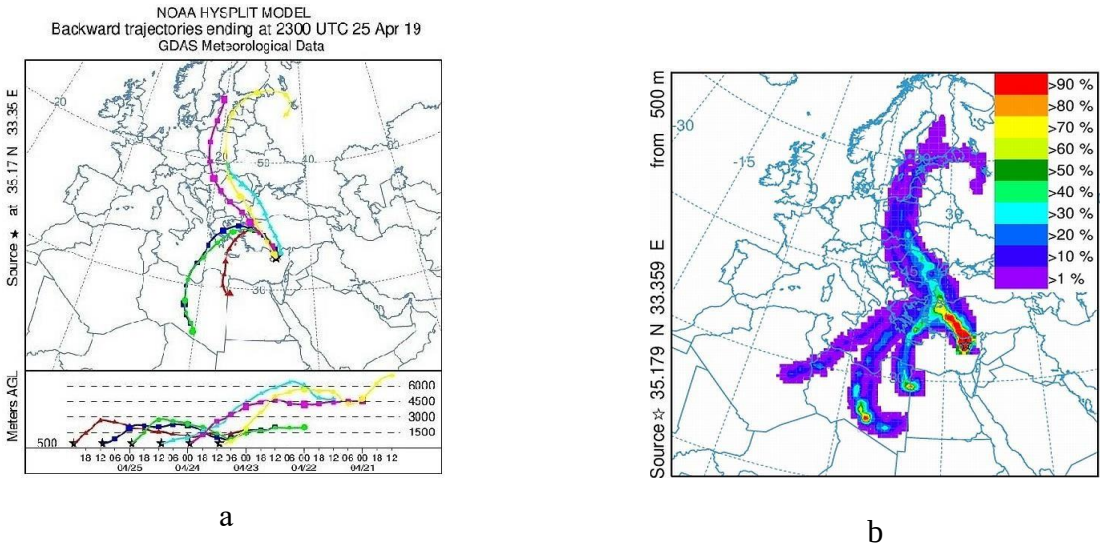

a b

Figure 10. (a) Backward trajectory of the air mass at 23 UTC and (b) trajectory frequency (b) on 25 April 2019, Nicosia, Cyprus. HYSPLIT calculation. Different colors at the bottom scale of vertical air movements at (a) correspond to different air mass trajectory for a particular day that comes from a calculated altitude to altitude of 500 m (AGL). For example, the yellow line shows air moving from an altitude above 6000 m (AGL) that comes by trajectory (marked on the map the same color) and was detected at Nicosia at an altitude of 500 m AGL at 12 h on 23 April. Red color corresponds to 00 h on 26 April, blue – to 12 h on 25 April, green – to 00 h on 25 April, light blue – to 12 h on 24 April, and pink – to 00 h on 24 April.

To study the impact of air mass transport from different regions to Nicosia, the calculations of backward trajectories for different periods and trajectory frequency have been provided. The 6-day backward trajectories are presented in Figure 10a. The trajectory starts every 12 h and runs for 72 h. That means the latest curve (red) starts at the same time when the earliest (yellow) ends. The altitude for calculation is 500 m above ground level (AGL). The results show the changes in the air mass transport direction from East Europe on 21–24 April to North Africa on 24–25 April. The frequency calculation provides specific information about dominant wind directions and air mass movements over Nicosia. The trajectory frequency option starts a trajectory from a single location (Nicosia) at the height of 500 m AGL every 3 h. The duration of 72 h in 3 days for every trajectory is the same as in the previous backward trajectory calculation (see Fig. 10b).

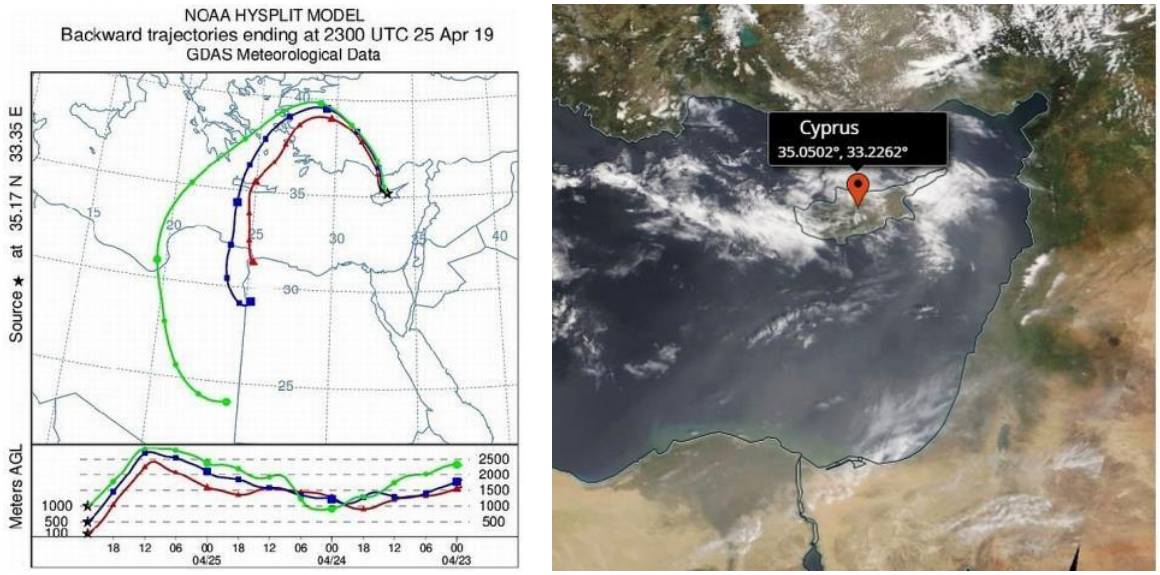

a b

Figure 11. (a) Backward trajectories of air masses at 23:00 UTC: the red trajectory represents the transport of air masses starting at an altitude of 1500 m above ground level at midnight from April 22 to April 23 and ending at an altitude of 100 m (above ground level) in Nicosia at 23:00 on April 25, 2019. The trajectories that terminated at different altitudes are indicated by different colors. The time is indicated in UTC. The map shows the horizontal movement, and the scale at the bottom represents the vertical movements of air masses. (b) Aqua/MODIS image of Cyprus, Eastern Mediterranean on April 25, 2019 (https://worldview.earthdata.nasa.gov/).

The main part of the upcoming aerosol particles was located at an altitude of less than 4 km. Figure 11a presents the backward trajectories for three different altitudes: 100, 500, and 1000 m AGL. The red and blue lines correspond to 100 and 500 m, accordingly, almost

matching the results in Figure 3.10a. For higher altitudes (1000 m, green line, see Fig. 10a), the trajectory is located at the western part in comparison with the 100 and 500 m trajectories. Trajectories for the 3 previous days before 25 April start over Libya and Egypt, which include the territory of the Sahara Desert (see Fig. 10 and 11a).

In the Aqua/MODIS satellite image (see Fig. 11b), the haze of the dust is visible over the territory of Egypt and the eastern part on the Mediterranean Sea including Cyprus. This haze corresponds to mineral dust particles transported from the Sahara Desert. Comparison with the results of the HYSPLIT calculation confirmed that mineral dust came to Nicosia with air masses transported from the Sahara Desert region.

c) radiative forcing and efficiency of radiative forcing

Average daily values of RF and Eff RF were obtained from the AERONET website for the period of April 21–29, when atmospheric pollution occurred over Nicosia due to aerosol particles (http://aeronet.gsfc.nasa.gov/). At the top of the atmosphere, changes in RF and Eff RF exhibit similar dynamics: in both cases, they begin to decrease after April 21 (see Fig. 12a). The RF values ranged from ~0 W m^{-2} on April 21 to –38 W m^{-2} on April 25, and then slightly increased to approximately –20 W m^{-2}.

In the case of Eff RF, on April 21, the value of approximately –21 W m^{-2} changed to less than –60 W m^{-2} during the subsequent days of increased aerosol concentration events. Thus, in both cases, the presence of mineral dust in the atmosphere over Nicosia contributed to the reduction of RF and Eff RF. Therefore, it can be argued that the increase in aerosol concentration in the air (in this case, the presence of coarse mode particles) leads to cooling of the upper atmosphere by reducing radiative forcing and its efficiency.

Changes in the Efficiency of Radiative Forcing at the bottom of the atmosphere follow a similar dynamic to the TOA (see Fig. 12b). At the boundary of the bottom atmosphere, the values of Eff RF changed from over –250 W m^{-2} to –125 W m^{-2} on the day of the highest aerosol concentration, April 25, 2019 (see Fig. 12). The event of mineral dust transport resulted in a reduction of energy influx from the upper layers of the atmosphere due to air pollution, leading to a change in Eff RF and cooling. As Eff RF is dependent on the aerosol concentration in the atmosphere, an increase in the concentration of mineral dust can lead to a decrease in the

efficiency of radiative forcing. This implies that the atmosphere becomes less transparent to solar radiation penetration as mineral dust absorbs and scatters a portion of the incoming solar radiation entering the atmosphere.

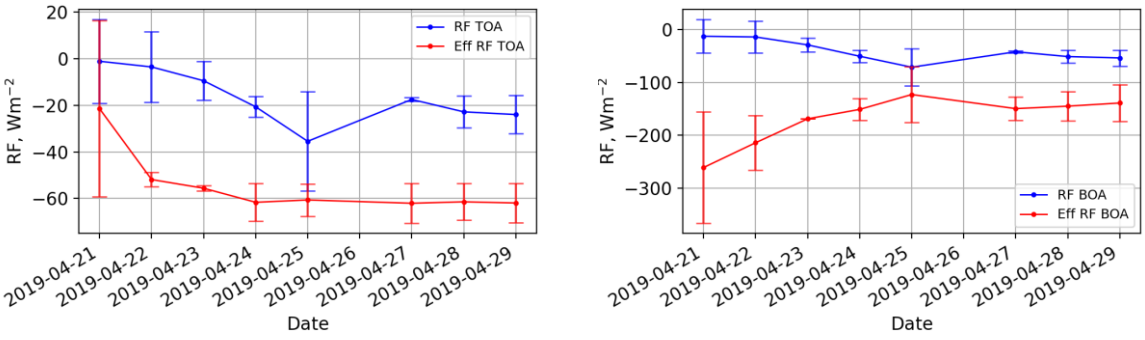

a b

Figure 12. Radiative Forcing (RF) and Efficiency of Radiative Forcing (Eff RF) in (a) the top of the atmosphere (TOA) and (b) the bottom of the atmosphere (BOA). Average daily data for the period of April 21–29 from the AERONET station in Nicosia. AERONET data level 2.0.

However, in the case of RF at the boundary of the bottom atmosphere, it exhibits following behavior: on April 25, it reaches values greater than –50 W m^{-2}, while in previous days, the values were around –10 W m^{-2}. The presence of mineral dust in the lower atmosphere can lead to a change in RF due to additional scattering and absorption of solar radiation. Mineral dust can also absorb solar radiation. This effect can be enhanced when the dust has a darker color and larger particle sizes, increasing its ability to absorb solar radiation. Therefore, the increase in RF in the bottom atmosphere in the presence of mineral dust depends on the balance between light scattering and absorption by the mineral dust, which, in turn, is influenced by dust properties such as color and size.

4. **Conclusions**

The results of detailed analysis of the intensive aerosol plume event over Nicosia, Cyprus in the Eastern Mediterranean in April 2019 are presented in this paper. The characteristics of aerosol particles during the high atmospheric aerosol contamination event are considered. For analysis, the data from the sun-photometer Nicosia AERONET station, the ground-based automatic micro-lidar, and the HYSPLIT back trajectories were used. We compare the aerosol characteristics during the April 2019 event with aerosol parameters outside

of this period of strong contamination AOD (500 nm), AOD (440 nm), and AE (440–870 nm) on the basis of the available AERONET data in the years 2015–2022. This comparison reveals that a similar event takes place almost every spring, and the considered aerosol outbreak was one of the strongest. The AOD exhibits seasonal variation, with the lowest concentration of aerosol particles during the winter season (AOD < 0.1) and increasing values in spring. Day-by-day analysis several days before, during, and after the outbreak event shows gradual changes in aerosol characteristics—AE, SSA, aerosol size distribution and refractive index (see Fig. 2–5) from fine-mode to coarse-mode particles, and from absorbing to mostly scattering aerosols. The scatter plot of AOD versus AE values also shows transition from the mostly anthropogenic type of aerosol to mineral dust (Fig. 6).

According to lidar data, the extinction altitude profiles and average mass concentration altitude profiles have been changed dramatically from "background" conditions to the event of aerosol contamination (Fig. 8,9). The largest value of mass concentration during the event by lidar profiles is about 300 μg m^{-3}, which exceeds background data by more than 10 times, and two peaks in the mass concentration profile are seen at ~1.5 and ~3.5 km instead of the usual single, much smaller maximum below ~1.0 km. All these aerosol parameters, AOD, Ångström exponent, single-scattering albedo, refractive index, and size distribution, suggest the arrival in the atmosphere over Nicosia in April 2019 of the large amount of mineral dust particles, with AOD at least five times larger (~0.9 at 500 nm) than background values (~0.2). The backward trajectory analysis clearly shows that the mineral dust arrived from the Sahara Desert region and Egypt. The mineral dust aerosol properties in the extreme event of 25 April 2019 were confirmed by lidar measurements and retrievals, scatter plot analysis, and aerosol volume size distribution.

The aerosol conditions in the region around Cyprus were studied in previous works (Kaduk (2015), Gong et al. 2019, Calmer et al 2019, Retalis et al 2010). Our analysis and previous studies show that the mineral dust of the Saharan Desert from the southwest and of the Arabian Peninsula Desert from the southeast was often transported to the atmosphere over Cyprus in several events since 2015. The 23–25 April 2019 event was one of the extreme aerosol outbreaks by mineral dust from the Saharan Desert in the atmosphere over Cyprus. We evaluated the assumption of how this type of aerosol outbreak can impact radiative forcing in the region using the AERONET approach. Results show noticeable reduction in the effective radiative forcing caused by increasing aerosol amounts during the outbreak. These results can

be used to quantify the impact of aerosol dust as a forcing agent that induces rapid changes in regional radiative forcing in the atmosphere.

References

Amiridis, V.; Balis, D.; Kazadzis, S.; Giannakaki, E.; Papayannis, A.; Zerefos, C. (2005). Four years aerosol observations with a Raman lidar at Thessaloniki, Greece, in the framework of European Aerosol Research Lidar Network (EARLINET). *J. Geophys. Res.*, 110, D21203. doi:10.1029/2005JD006190

Calmer, R.; Roberts, G.C.; Sanchez, K.J.; Sciare, J.; Sellegri, K.; Picard, D.; Vrekoussis, M.; Pikridas, M. Aerosol–cloud closure study on cloud optical properties using remotely piloted aircraft measurements during a BACCHUS field campaign in Cyprus. Atmos. Chem. Phys. 2019, 19, 13989–14007. doi.org/10.5194/acp-19-13989-2019

Di Biagio, C.; Formenti, P.; Balkanski, Y.; Caponi, L.; Cazaunau, M.; Pangui, E.; Journet, E.; Nowak, S.; Andreae, M.O.; Kandler, K.; et al. (2019). Complex refractive indices and single-scattering albedo of global dust aerosols in the shortwave spectrum and relationship to size and iron content. *Atmos. Chem. Phys.*, *19*, 15503–15531. doi:10.5194/acp-19-15503-2019

Dubovik, O., Holben, B., Eck, T. F., Smirnov, A., Kaufman, Y. J., King, M. D., Tanré, D., & Slutsker, I. (2002). Variability of Absorption and Optical Properties of Key Aerosol Types Observed in Worldwide Locations. *Journal of the Atmospheric Sciences*, 59(3), 590-608. doi:10.1175/1520-0469(2002)059<0590:VOAAOP>2.0.CO;2

Falkowski, P. G., Barber, R. T., and Smetacek, V. (1998). Biogeochemical Controls and Feedbacks on Ocean Primary Production, Science, 281, 200–206. doi: 10.1126/science.281.5374.200.

Fernald, F.G. (1984). Analysis of atmospheric LIDAR observations: Some comments. *Appl. Opt.*, *23*, 652–653. doi:10.5194/acp-9-9249-2009

Gong, X.; Wex, H.; Müller, T.; Wiedensohler, A.; Höhler, K.; Kandler, K.; Ma, N.; Dietel, B.; Schiebel, T.; Möhler, O.; et al. Characterization of aerosol properties at Cyprus, focusing on cloud condensation nuclei and ice-nucleating particles. Atmos. Chem. Phys. 2019, 19, 10883–10900. doi.org/10.5194/acp-19-10883-2019

Kaduk, C. Characterization of the Optical Properties of Complex Aerosol Mixtures Observed with a Multiwavelength-Raman- Polarization Lidar during the 6-Weeks BACCHUS Campaign in Cyprus in Spring 2015. Fakultät für Physik und Geowis- senschaften der Universität Leipzig Studiengang Meteorologie, Masterarbeit 2017. Available online: https://www.tropos.de/ fileadmin/user_upload/Institut/Abteilungen/Fernerkundung/Daten_PDF/MA_Clara_Kaduk.pdf (accessed on 22 April 2022).

Kandler, K.; Lieke, K.; Benker, N.; Emmel, C.; Küpper, M.; Müller-Ebert, D.; Ebert, M.; Scheuvens, D.; Schladitz, A.; Schütz, L.; et al. (2011). Electron microscopy of particles collected at Praia, Cape Verde, during the Saharan Mineral Dust Experiment: Particle chemistry, shape, mixing state and complex refractive index. *Tellus Ser. B Chem. Phys. Meteorol*., 63, 475–496. doi:10.1111/j.1600-0889.2011.00550.x

Klett, J. D. (1981). Stable analytical inversion solution for processing lidar returns. Applied optics, 20(2), 211-220.

Koren, I., Kaufman, Y. J., Rosenfeld, D., Remer, L. A., and Rudich, Y. (2005). Aerosol invigoration and restructuring of Atlantic convective clouds, Geophys. Res. Lett., 32, LI4828, doi:10.1029/2005GL023187

Leon, J.-F.; Derimian, Y.; Chiapello, I.; Tanre, D.; Podvin, T.; Chatenet, B.; Diallo, A.; Deroo, C. (2009). Aerosol vertical distribution and optical properties over M'Bour (16.96°W; 14.39°N), Senegal from 2006 to 2008. *Atmos. Chem. Phys.*, *9*, 9249–9261. doi:10.5194/acp-9-9249-2009

Linke, C.; Möhler, O.; Veres, A.; Mohácsi, Á.; Bozóki, Z.; Szabó, G.; Schnaiter, M. (2006). Optical properties and mineralogical composition of different Saharan mineral dust samples: A laboratory study. *Atmos. Chem. Phys*., 6, 3315–3323. doi.org/10.5194/acp-6-3315-2006

Liu, S.; Liang, X.-Z. (2010). Observed diurnal cycle climatology of planetary boundary layer height Shuyan. *J. Clim.*, *23*, 5790–5809. doi:10.1175/2010JCLI3552.1

Maring, H.; Savoie, D.L.; Izaguirre, M.A.; Custals, L.; Reid, J.S. (2003). Mineral dust aerosol size distribution change during atmospheric transport. *J. Geophys. Res. Atmos.*, *108*, 8592. doi:10.1029/2002JD002536

Messager, C., Parker, D. J., Reitebuch, O., Agusti-Panareda, A., Taylor, C. M., and Cuesta, J. (2009). Structure and dynamics of the Saharan atmospheric boundary layer during the West African monsoon onset: observations and analyses from the research flights of 14 and 17 July 2006, *Q. J. R. Meteorol. Soc.*, 136, 107–124, doi:10.1002/qj.469

Mona, L.; Amodeo, A.; D'Amico, G.; Giunta, A.; Madonna, F.; Pappalardo, G. (2012). Multi-wavelength Raman lidar observations of the Eyjafjallajökull volcanic cloud over Potenza, southern Italy. *Atmos. Chem. Phys.*, *12*, 2229–2244. doi:10.5194/acp-12-2229-2012

Mortier, A. (2013). Tendances et Variabilites de l'aerosol Atmospherique a l'aide du Couplage Lidar. Photometre sur les Sites de Lille et Dakar. *Ph.D. Thesis, University of Lille*, Lille, France.

Mortier, A., Goloub, P., Podvin, T., Deroo, C., Chaikovsky, A., Ajtai, N., ... & Derimian, Y. (2013). Detection and characterization of volcanic ash plumes over Lille during the Eyjafjallajökull eruption. Atmospheric Chemistry & Physics, 13(7). doi:10.5194/acp-13-3705-2013

Omar, A.H.; Won, J.-G.; Winker, D.M.; Yoon, S.-C.; Dubovik, O.; McCormick, M.P. (2005). Development of global aerosol models using cluster analysis of Aerosol Robotic Network (AERONET) measurements. *J. Geophys. Res.*, *110*, D10S14. doi:10.1029/2004JD004874

Palm, S.P.; Selmer, P.; Yorks, J.; Nicholls, S.; Nowottnick, E. (2021). Planetary Boundary Layer Height Estimates From ICESat-2 and CATS Backscatter Measurements. *Front. Remote Sens.*, *2*, 716951. doi.org/10.3389/frsen.2021.716951

Papanikolaou, C.-A.; Papayannis, A.; Mylonaki, M.; Foskinis, R.; Kokkalis, P.; Liakakou, E.; Stavroulas, I.; Soupiona, O.; Hatzianastassiou, N.; Gavrouzou, M.; et al. (2022). Vertical Profiling of Fresh Biomass Burning Aerosol Optical Properties over the Greek Urban City of Ioannina, during the PANACEA Winter Campaign. *Atmosphere*, *13*, 94. doi:10.3390/atmos13010094

Papayannis, A.; Mamouri, R.E.; Amiridis, V.; Kazadzis, S.; Perez, C.; Tsaknakis, G.; Kokkalis, P.; Baldasano, J.M. (2009). Systematic lidar observations of Saharan dust layers over Athens, Greece in the frame of EARLINET project (2004–2006). *Ann. Geophys.*, 27, 3611–3620. doi:10.5194/angeo-27-3611-2009

Prospero, J. M. and Carlson, T. N. (1972). Vertical and areal distribution of Saharan dust over the western equatorial North Atlantic Ocean, *J. Geophys. Res.*, 77, 5255–5265, doi:10.1029/JC077i027p05255

Prospero, J. M., Landing, W. M., and Schulz, M. (2010). African dust deposition to Florida: Temporal and spatial variability and comparisons to models, J. Geophys. Res., 115, D13304, https://doi.org/10.1029/2009jd012773

Prospero, J.M. (1999). Long-term measurements of the transport of African mineral dust to the southeastern United States: Implications for regional air quality. *J. Geophys. Res.*, 104, 15917–15927. doi:10.1029/1999JD900072

Reichholf, J. H. (1986). Is Saharan Dust a Major Source of Nutrients for the Amazonian Rain Forest?, *Studies on Neotropical Fauna and Environment*, 21:4, 251-255, doi:10.1080/01650528609360710

Retalis, A.; Hadjimitsis, D.G.; Michaelides, S.; Tymvios, F.; Chrysoulakis, N.; Clayton, C.R.I.; Themistocleous, K. Comparison of aerosol optical thickness with in situ visibility data over Cyprus. Nat. Hazards Earth Syst. Sci. 2010, 10, 421–428. doi.org/10.5194/nhess-10-421-2010

Schepanski, K., Tegen, I., and Macke, A. (2009). Saharan dust transport and deposition towards the tropical northern Atlantic, *Atmos. Chem. Phys.*, 9, 1173–1189, doi:10.5194/acp-9-1173- 2009

Shao, Y., Wyrwoll, K.-H., Chappell, A., Huang, J., Lin, Z., McTainsh, G. H., Mikami, M., Tanaka, T. Y., Wang, X., and Yoon, S. (2011). Dust cycle: an emerging core theme in Earth system science, *Aeolian Res.*, 2, 181–204, doi:10.1016/j.aeolia.2011.02.001

Swap, R., Garstang, M., Greco, S., Talbot, R., and Kallberg, P. (1992). Saharan dust in Amazon basin, *Tellus 44B*, 133–149

Szkop, A.; Pietruczuk, A.; Posyniak, M. (2016). Classification of aerosol over Central Europe by cluster analysis of aerosol columnar optical properties and backward trajectory statistics. *Acta Geophys.*, *64*, 2650–2676. doi:10.1515/acgeo-2016-00112

Yu, H., Chin, M., Yuan, T., Bian, H., Remer, L. A., Prospero, J. M., Omar, A., Winker, D., Yang, Y., Zhang, Y., Zhang, Z., and Zhao, C. (2015). The fertilizing role of African dust in the Amazon rainforest: A first multiyear assessment based on data from Cloud-Aerosol Lidar and Infrared Pathfinder Satellite Observations, *Geophys. Res. Lett*., 42, 1984–1991, doi:10.1002/2015gl063040

Zhang, Y., Li, Z., Zhang, Y., Li, D., Qie, L., Che, H., and Xu, H. (2017). Estimation of aerosol complex refractive indices for both fine and coarse modes simultaneously based on AERONET remote sensing products, *Atmos. Meas. Tech*., 10, 3203–3213, doi:10.5194/amt-10-3203-2017

Appendix 3

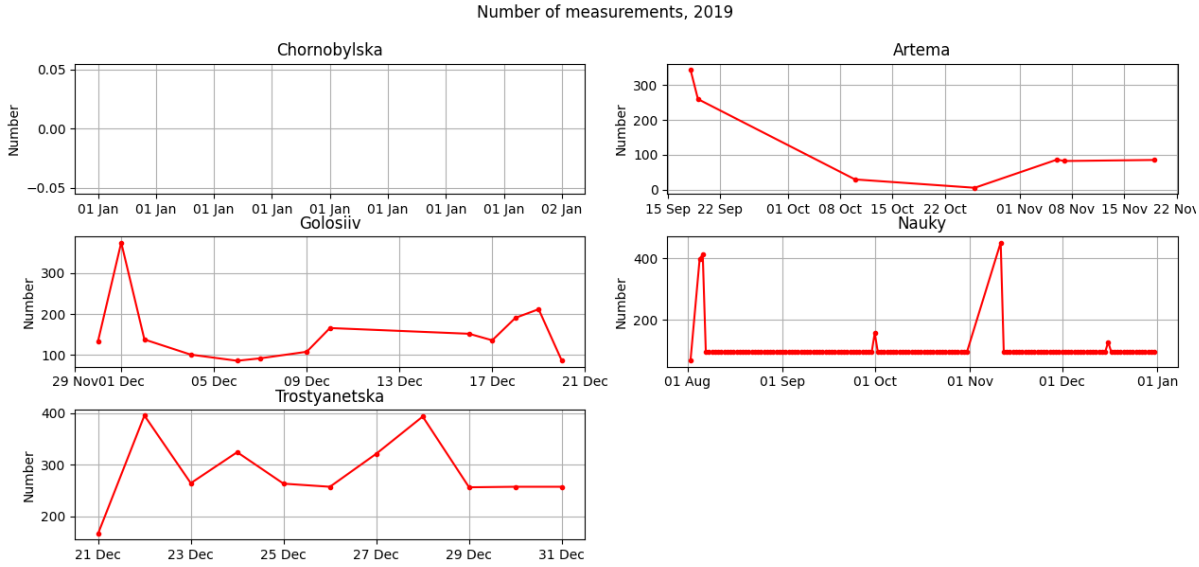

Figure 13. The number of measurements per day from the AirVisual network at the Chornobylska, Artema, Golosiiv, Nayky, and Trostyanetska stations for the year 2019.

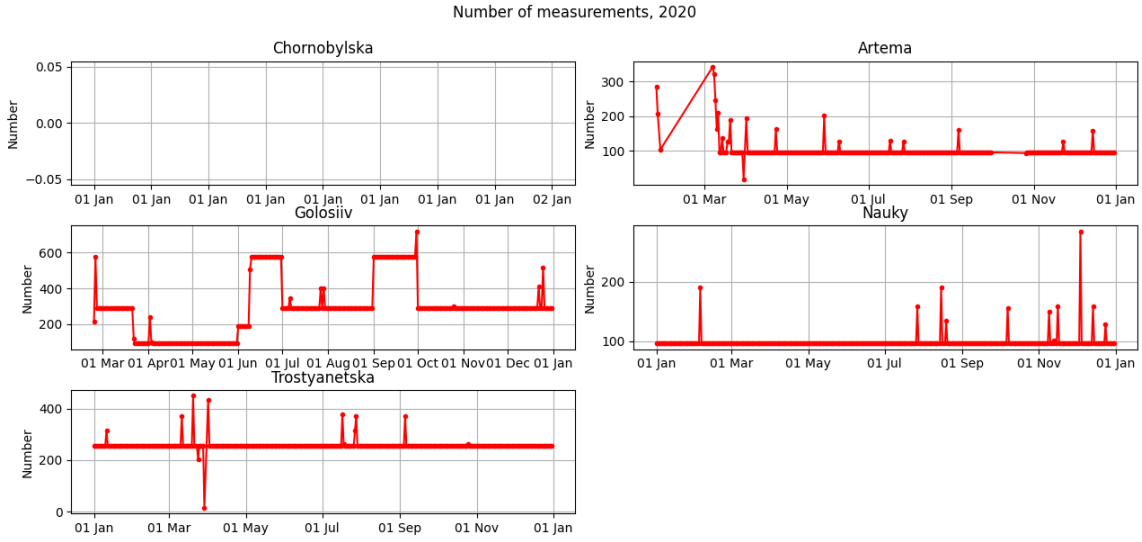

Figure 14. The number of measurements per day from the AirVisual network at the Chornobylska, Artema, Golosiiv, Nayky, and Trostyanetska stations for the year 2020.

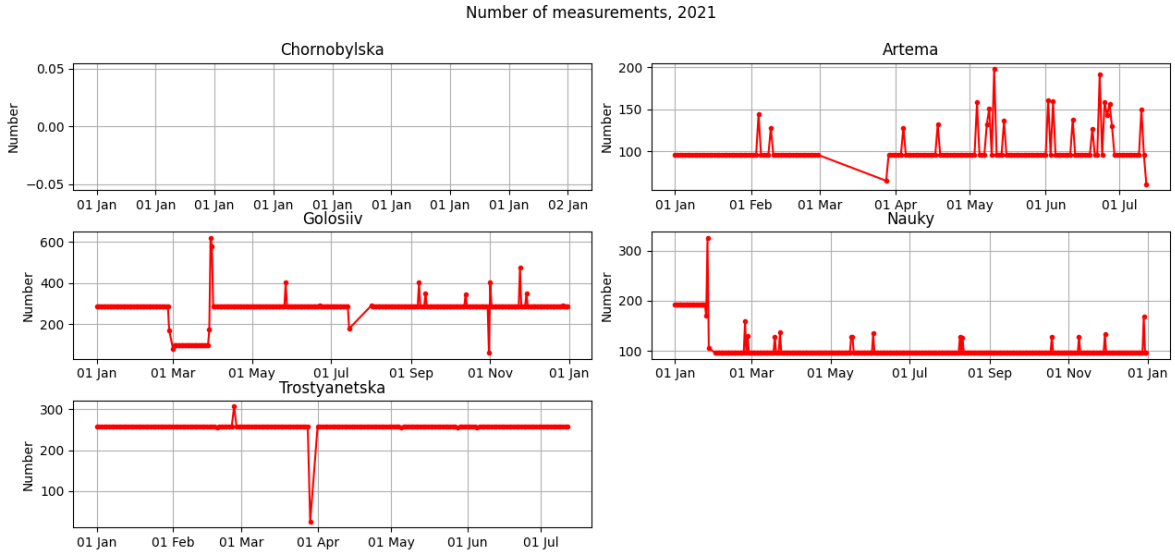

Figure 15. The number of measurements per day from the AirVisual network at the Chornobylska, Artema, Golosiiv, Nayky, and Trostyanetska stations for the year 2021.

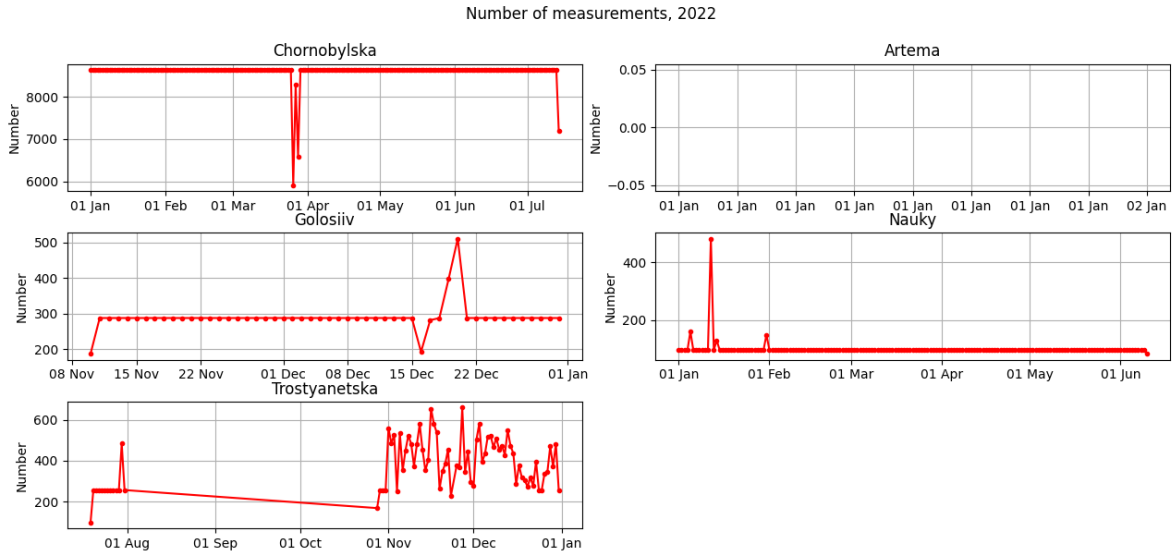

Figure 16. The number of measurements per day from the AirVisual network at the Chornobylska, Artema, Golosiiv, Nayky, and Trostyanetska stations for the year 2022.

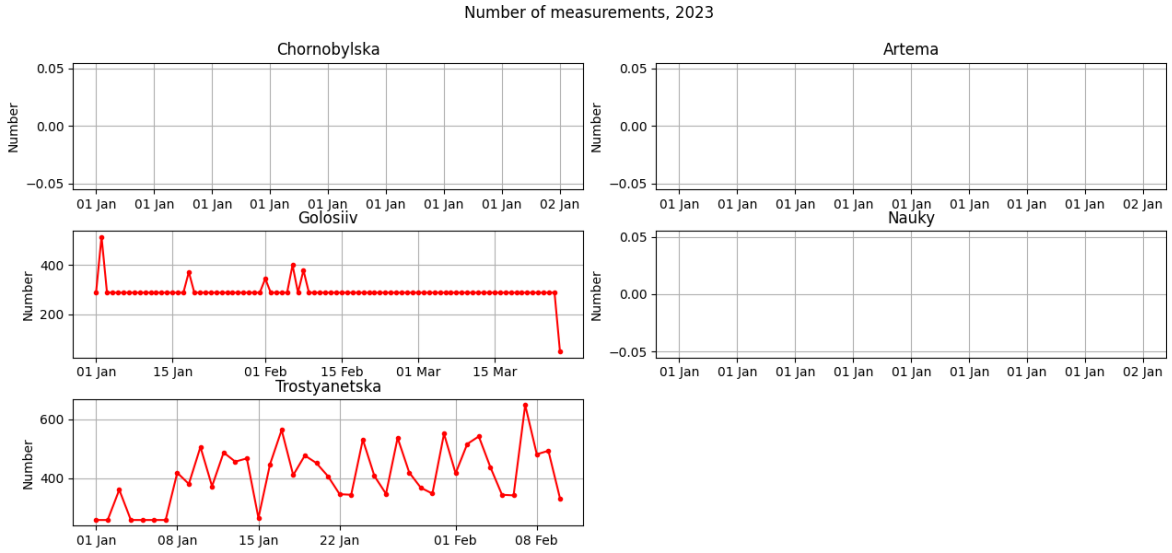

Figure 17. The number of measurements per day from the AirVisual network at the Chornobylska, Artema, Golosiiv, Nayky, and Trostyanetska stations for the year 2023.

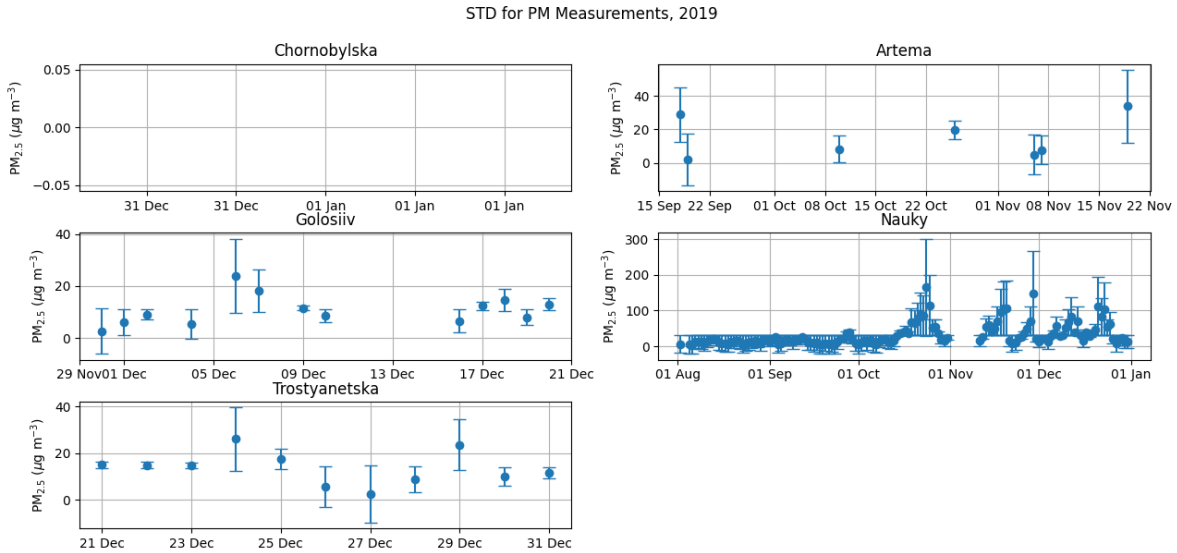

Figure 18. Standard deviation for $PM_{2.5}$: Data from the AirVisual network at the Chornobylska, Artema, Golosiiv, Nayky, and Trostyanetska stations for the year 2019, based on daily averaged data.

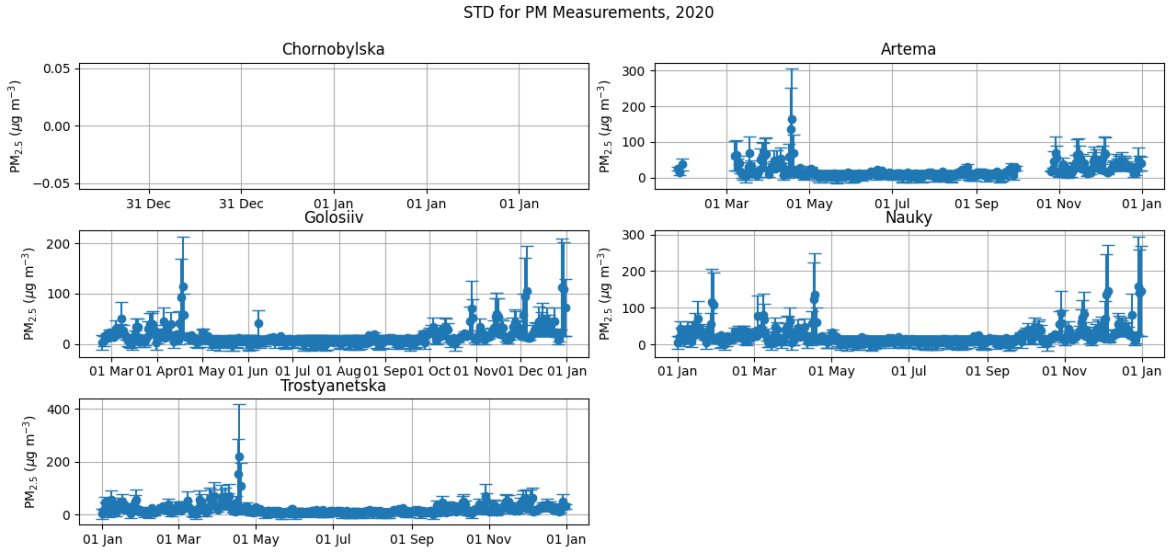

Figure 19. Standard deviation for $PM_{2.5}$: Data from the AirVisual network at the Chornobylska, Artema, Golosiiv, Nayky, and Trostyanetska stations for the year 2020, based on daily averaged data.

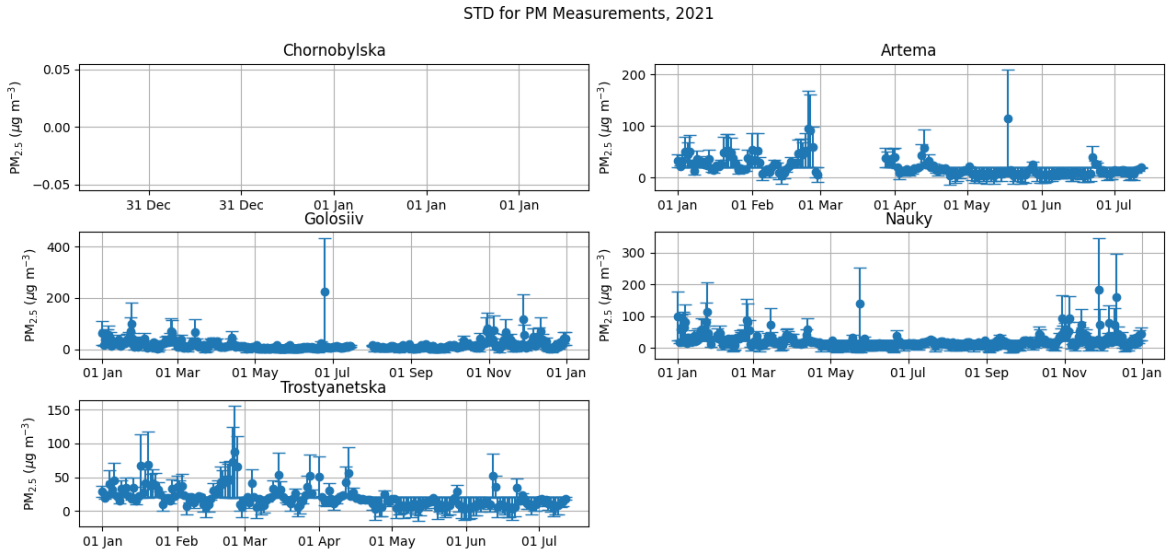

Figure 20. Standard deviation for $PM_{2.5}$: Data from the AirVisual network at the Chornobylska, Artema, Golosiiv, Nayky, and Trostyanetska stations for the year 2021, based on daily averaged data.

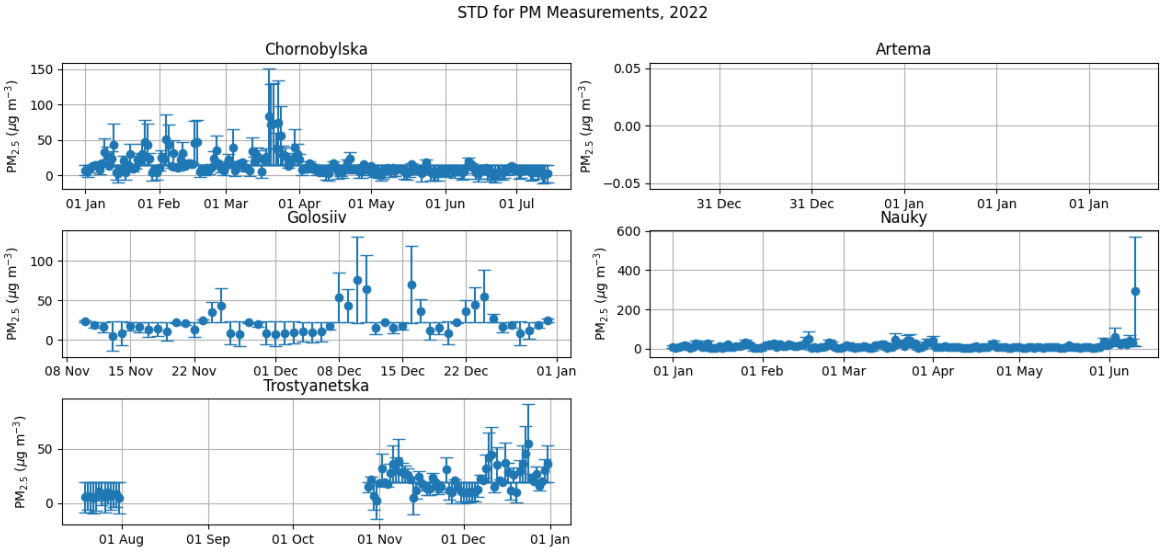

Figure 21. Standard deviation for $PM_{2.5}$: Data from the AirVisual network at the Chornobylska, Artema, Golosiiv, Nayky, and Trostyanetska stations for the year 2022, based on daily averaged data.

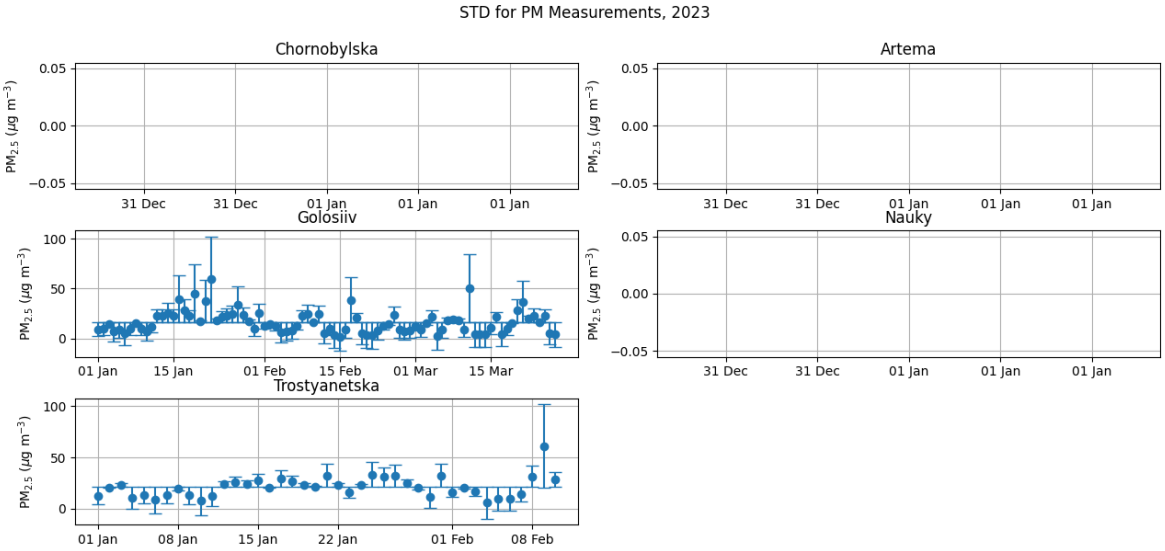

Figure 22. Standard deviation for $PM_{2.5}$: Data from the AirVisual network at the Chornobylska, Artema, Golosiiv, Nayky, and Trostyanetska stations for the year 2023, based on daily averaged data.

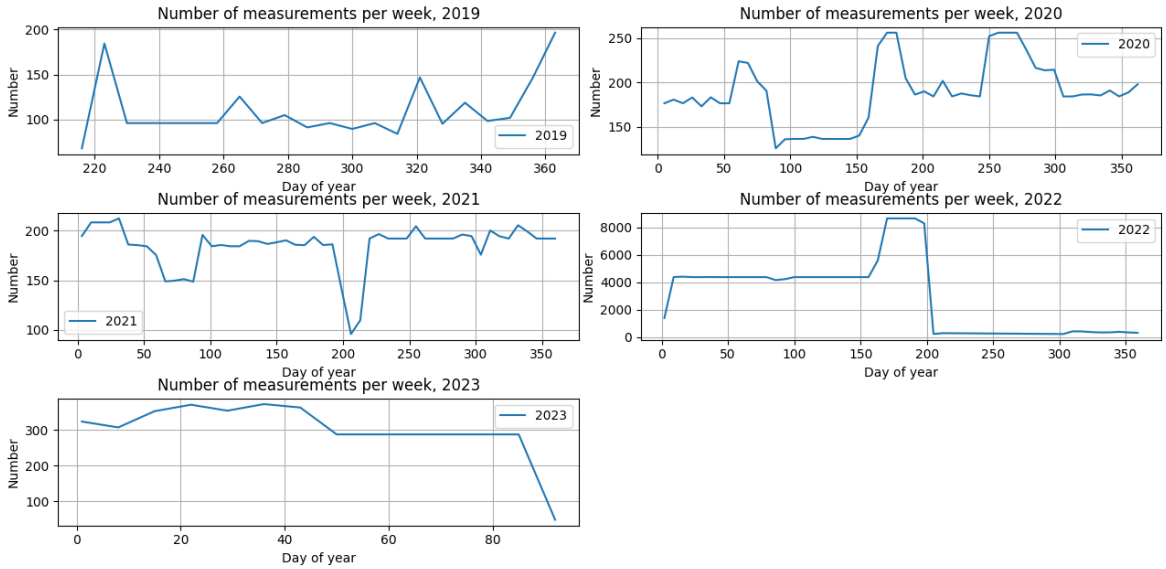

Figure 23. Number of measurements from the AirVisual network at the Chornobylska, Artema, Golosiiv, Nayky, and Trostyanetska stations for the years 2019 – 2023, weekly averaged data.

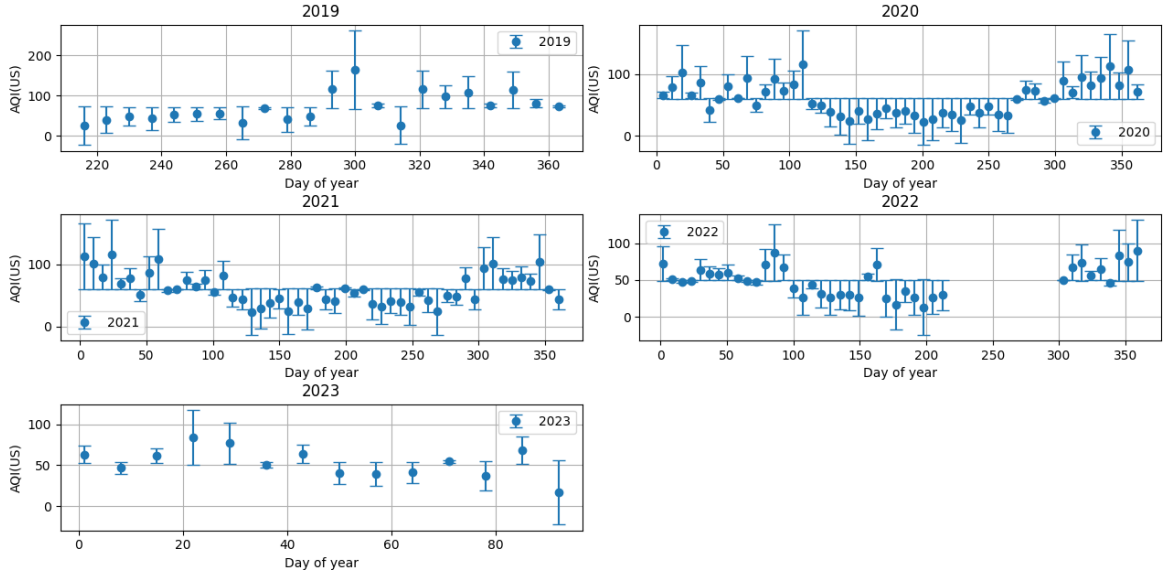

Figure 24. Standard deviation for AQI: Data from the AirVisual network at the Chornobylska, Artema, Golosiiv, Nayky, and Trostyanetska stations for the years 2019 – 2023, based on weekly averaged data.

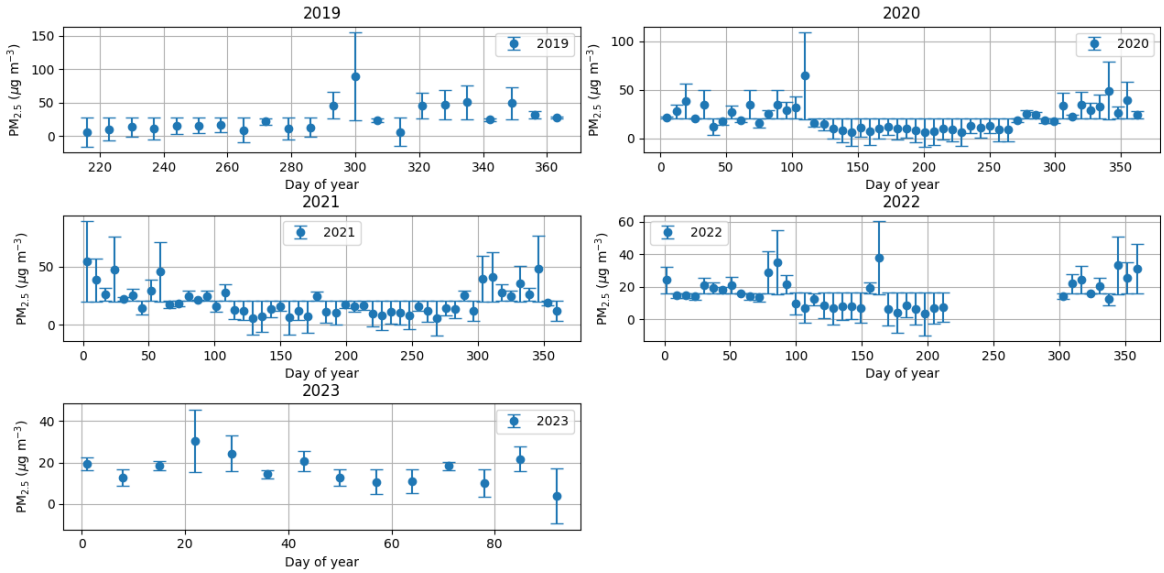

Figure 25. Standard deviation for $PM_{2.5}$: Data from the AirVisual network at the Chornobylska, Artema, Golosiiv, Nayky, and Trostyanetska stations for the years 2019 – 2023, based on weekly averaged data.

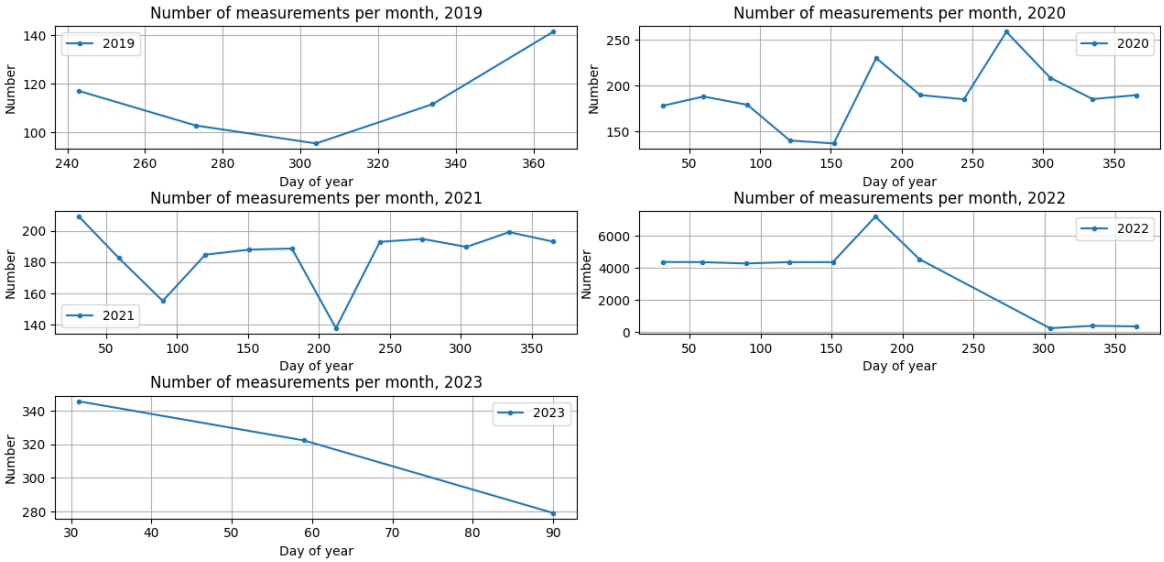

Figure 26. Averaged number of measurements from the AirVisual network at the Chornobylska, Artema, Golosiiv, Nayky, and Trostyanetska stations for the years 2019 – 2023, monthly averaged data.

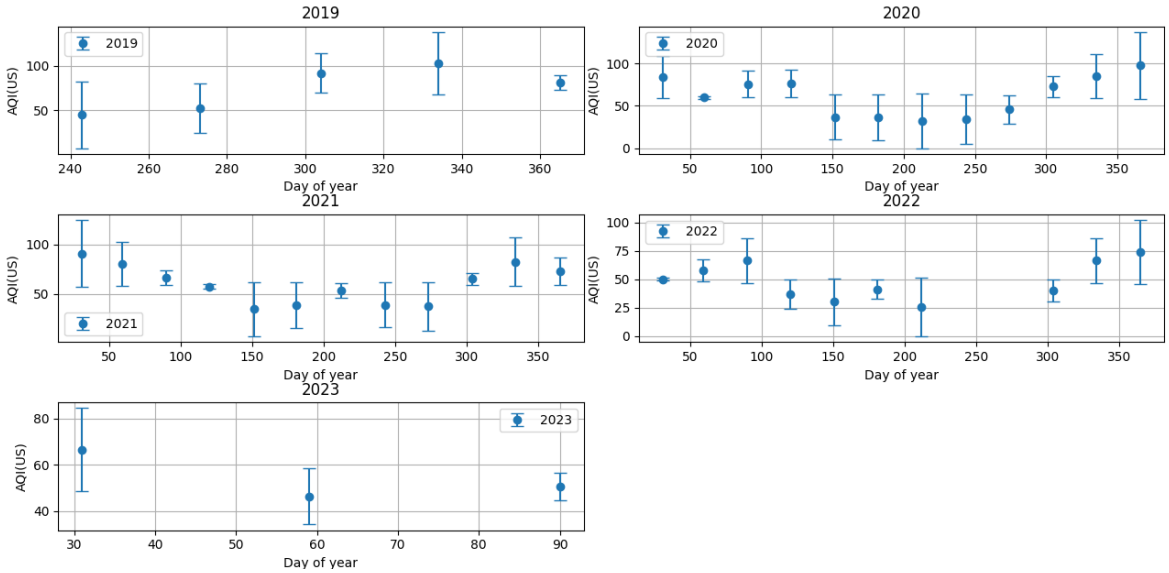

Figure 27. Standard deviation for AQI: Data from the AirVisual network at the Chornobylska, Artema, Golosiiv, Nayky, and Trostyanetska stations for the years 2019 – 2023, based on monthly averaged data.

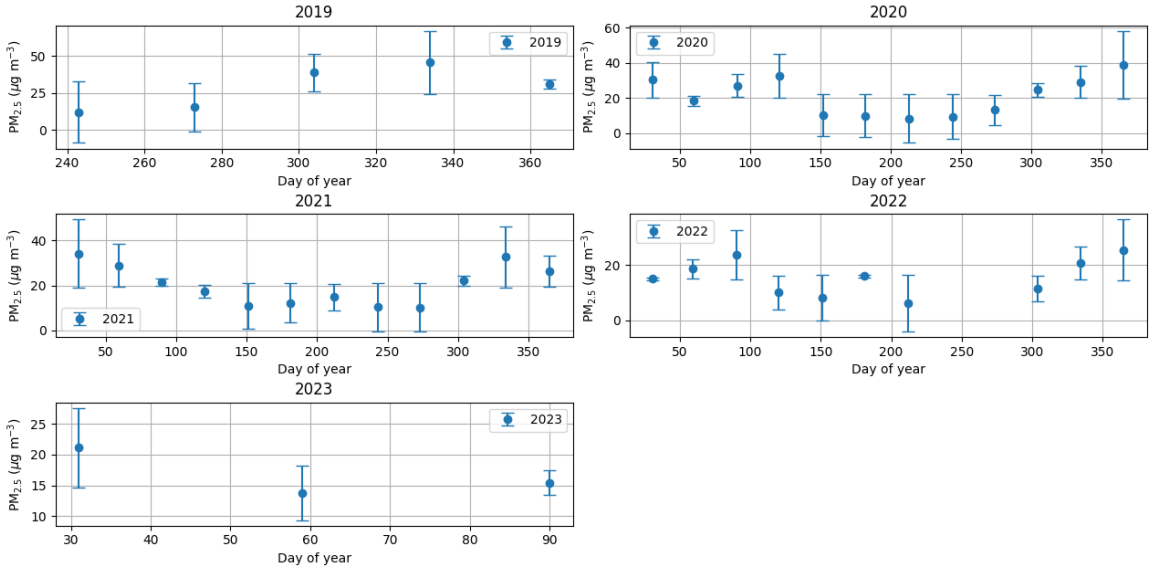

Figure 28. Standard deviation for $PM_{2.5}$: Data from the AirVisual network at the Chornobylska, Artema, Golosiiv, Nayky, and Trostyanetska stations for the years 2019 – 2023, based on monthly averaged data.

Appendix 4

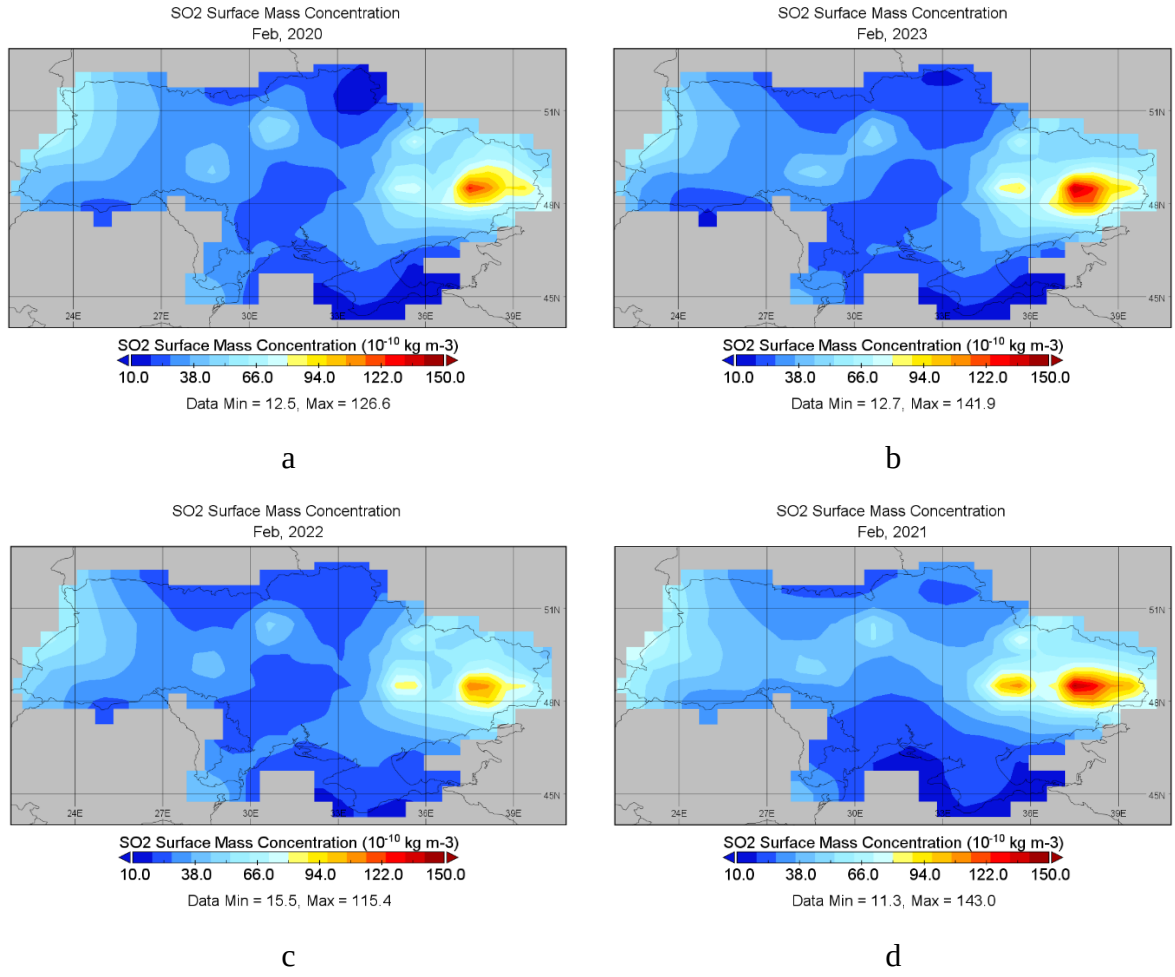

Figure 29. Time-averaged surface mass concentration of SO_2 in the atmosphere over Ukraine during a) February 2020, b) February 2021, c) February 2022 and d) February 2023. Modeling was provided using the MERRA-2 program. Data were obtained from the GIOVANNI platform. The unit of color scale is 10^{-10} kg m^{-3}.

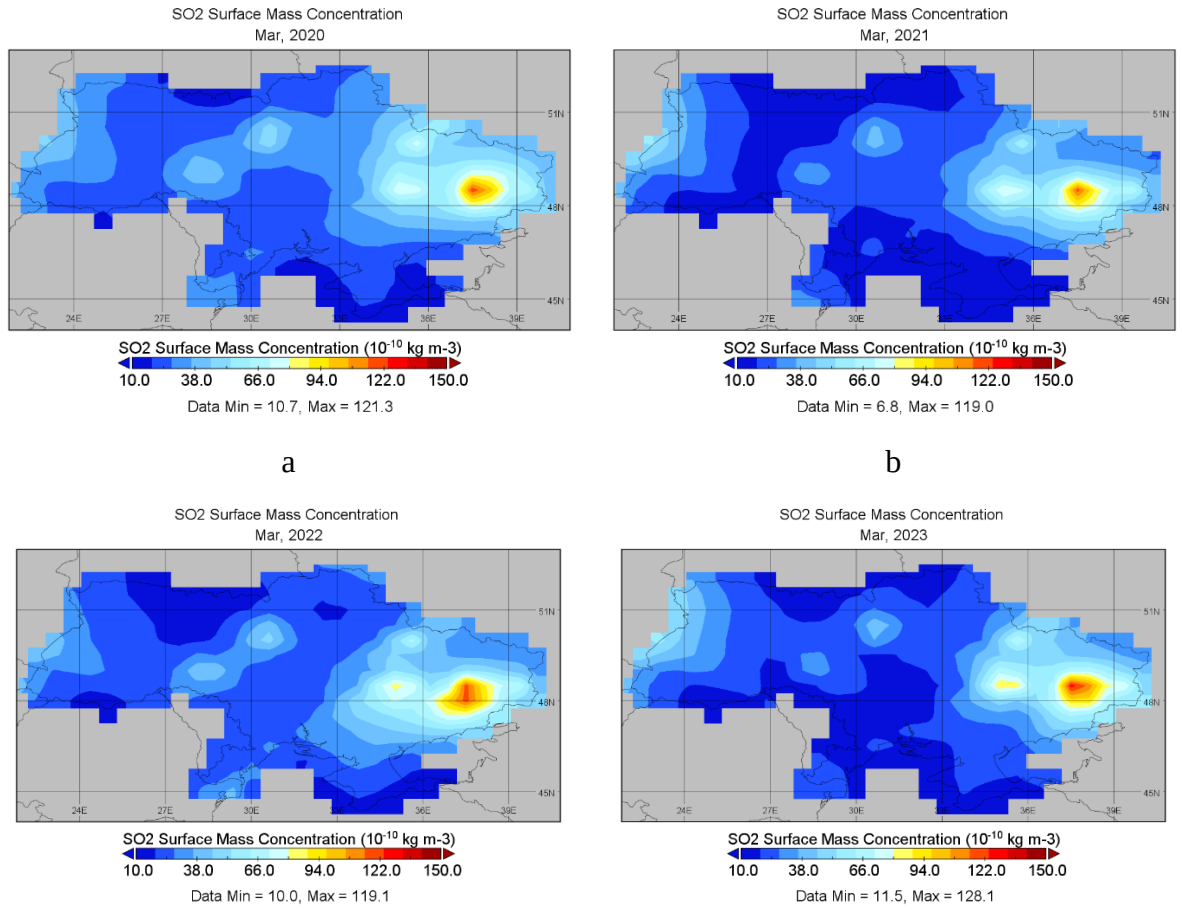

Figure 30. Time-averaged surface mass concentration of SO_2 in the atmosphere over Ukraine during a) March 2020, b) March 2021, c) March 2022 and d) March 2023. Modeling was provided using the MERRA-2 program. Data were obtained from the GIOVANNI platform. The unit of the color scale is 10^{-10} kg m^{-3}.

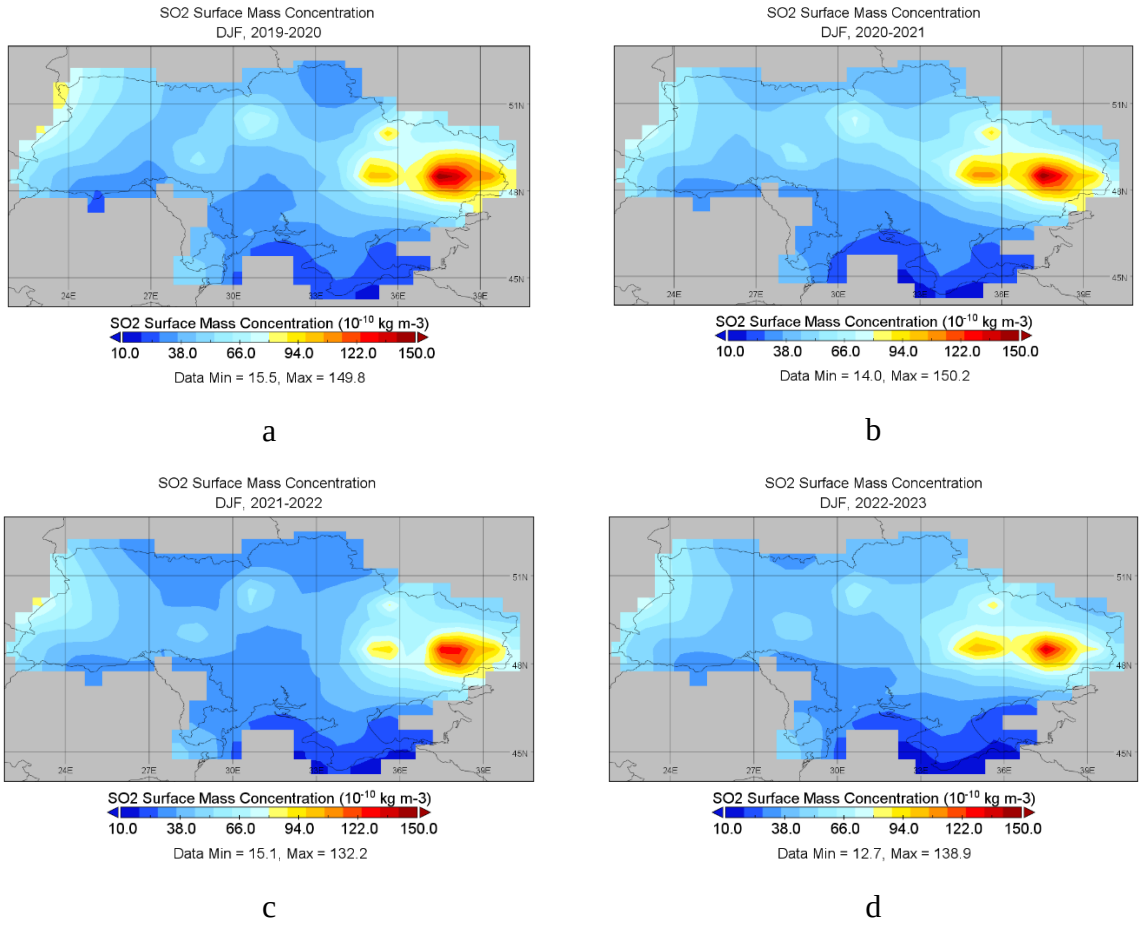

Figure 31. Time-averaged surface mass concentration of SO_2 in the atmosphere over Ukraine during a) winter 2019 – 2020, b) winter 2020 – 2021, c) winter 2021 – 2022 and d) winter 2022 – 2023. The abbreviation DJF represents the months: December, January, and February. Modeling was provided using the MERRA-2 program. Data were obtained from the GIOVANNI platform. The unit of the color scale is 10^{-10} kg m^{-3}.

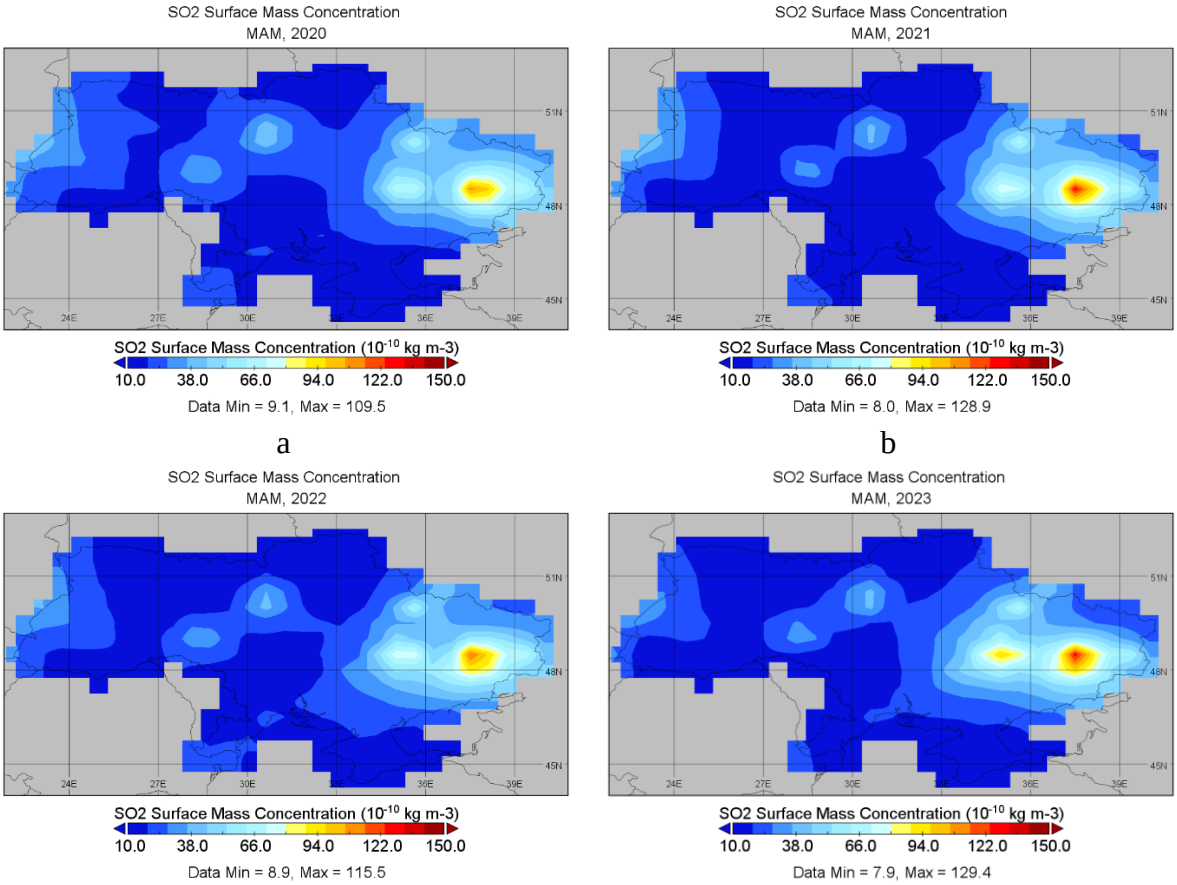

Figure 32. Time-averaged surface mass concentration of SO_2 in the atmosphere over Ukraine during a) spring 2020, b) spring 2021, c) spring 2022 and d) spring 2023. The abbreviation MAM represents the months: March, April, and May. Modeling was provided using the MERRA-2 program. Data were obtained from the GIOVANNI platform. The unit the color scale is 10^{-10} kg m^{-3}.

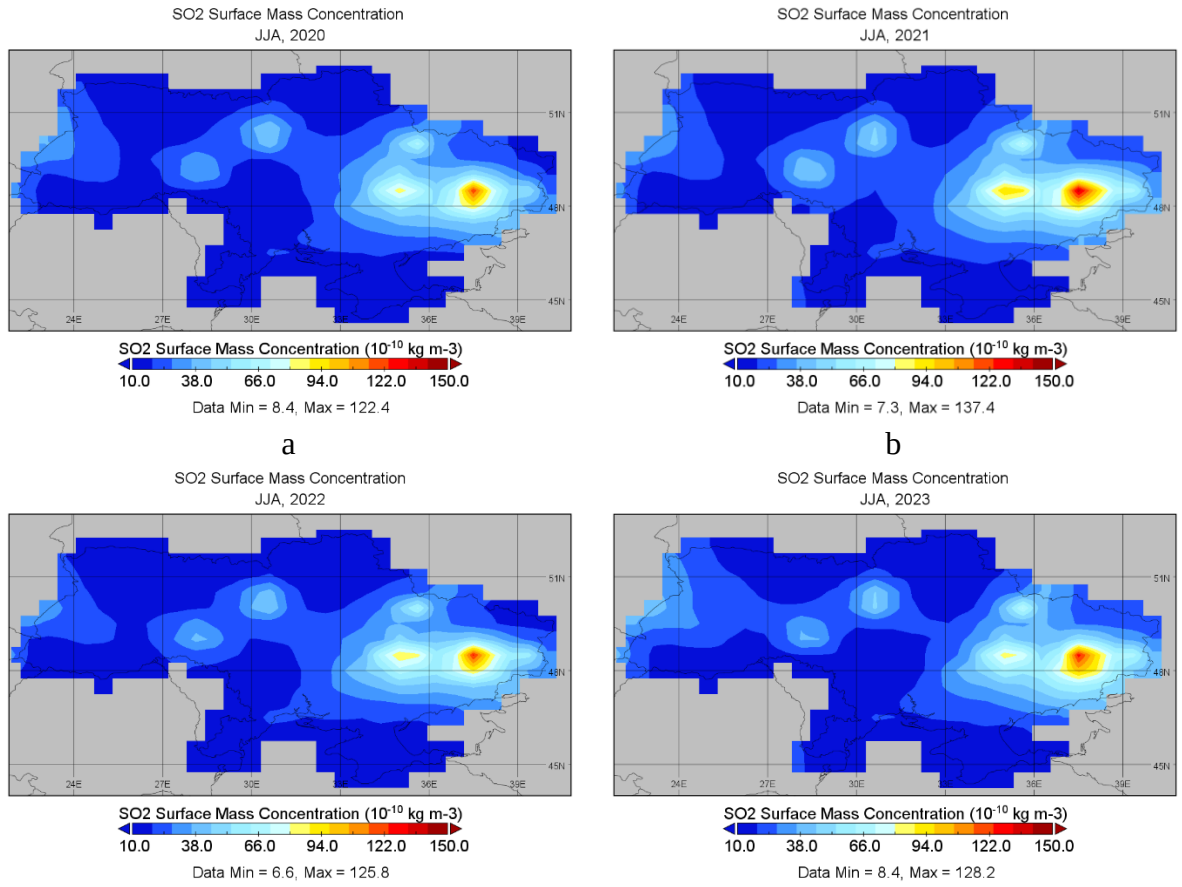

Figure 33. Time-averaged surface mass concentration of SO_2 in the atmosphere over Ukraine during a) summer 2020, b) summer 2021, c) summer 2022 and d) summer 2023. The abbreviation JJA represents the months: June, July, and August. Modeling was provided using the MERRA-2 program. Data were obtained from the GIOVANNI platform. The unit of the color scale is 10^{-10} kg m^{-3}.

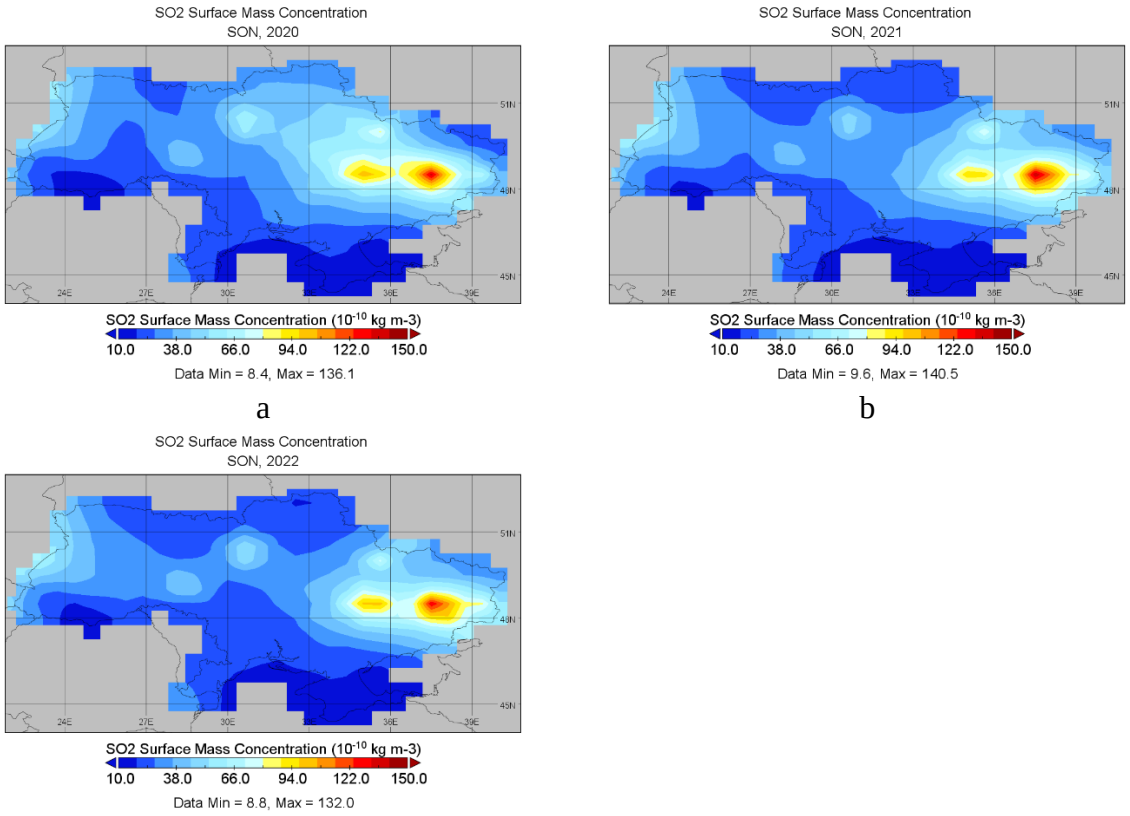

Figure 34. Time-averaged surface mass concentration of SO_2 in the atmosphere over Ukraine during a) autumn 2020, b) autumn 2021, c) autumn 2022 and c) September and October of 2023. The abbreviation SON represents the months: September, October, and November. Modeling was provided using the MERRA-2 program. Data were obtained from the GIOVANNI platform. The unit of the color scale is 10^{-10} kg m^{-3}.

Appendix 5

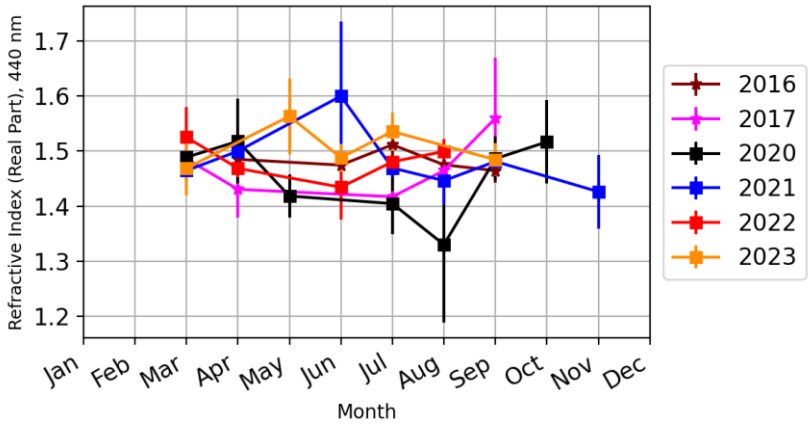

a

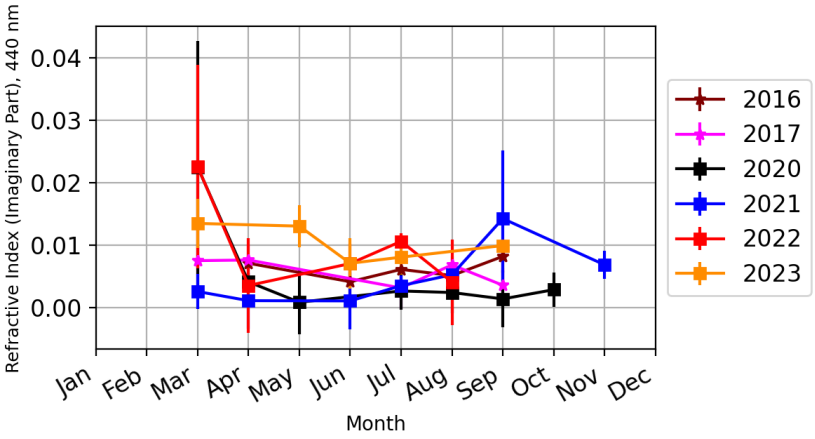

b

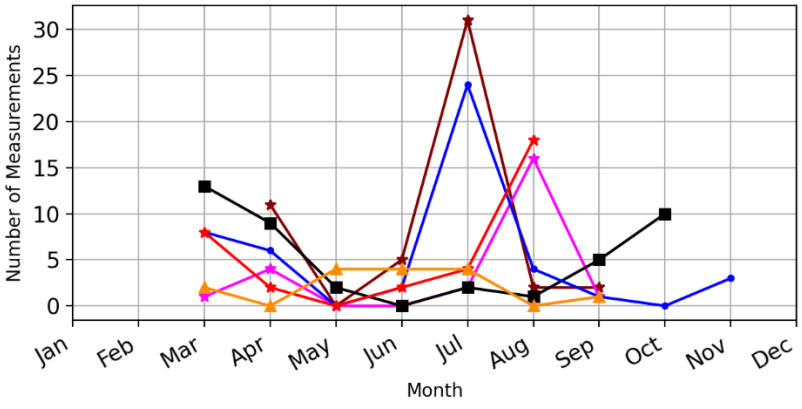

c

Figure 1. a) Changes of the real part of the complex refractive index at wavelength 440 nm with standard deviation, b) the imaginary part of the complex refractive index at wavelengths 440 nm with standard deviation and c) number of used measurements, 2016, 2017, 2019–2023. Data monthly averaged. Observations from the AERONET station in Kyiv. Years of observation are indicated by colors. Data level 1.5.

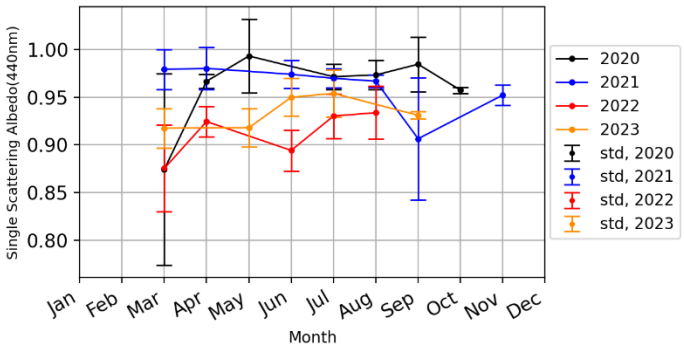

a

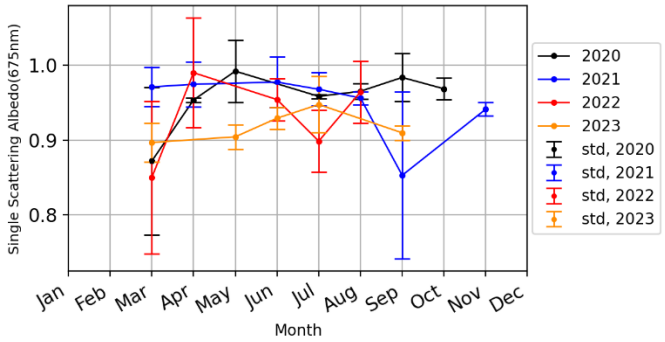

b

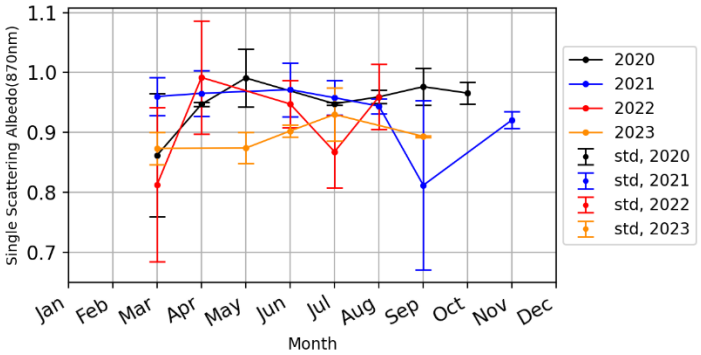

c

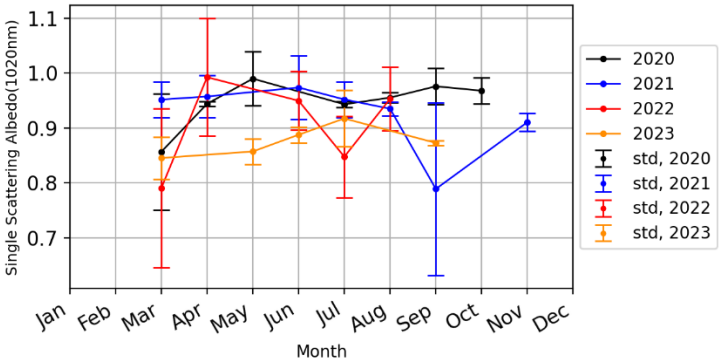

d

Figure. 2. Changes of the Single Scattering Albedo wavelength a) 440 nm, b) 677 nm, c) 870 nm and d) 1020 nm with standard deviation during 2020–2023. Data monthly averaged. Observations from the AERONET station in Kyiv. Years of observation are indicated by colors. Data level 1.5.